

Design and optimization of a space camera with application to the PHI solar magnetograph

Von der Fakultät für Elektrotechnik, Informationstechnik, Physik
der Technischen Universität Carolo-Wilhelmina zu Braunschweig
zur Erlangung der Würde
eines Doktor-Ingenieurs (Dr.-Ing.)
genehmigte Dissertation

von Juan José Piqueras Meseguer
aus Molina de Segura, Murcia, Spanien

eingereicht am: 19. März 2013

mündliche Prüfung am: 3. Mai 2013

1. Referent: Prof. Dr.-Ing. Harald Michalik

2. Referent: Prof. Dr. Sami K. Solanki

Bibliografische Information der Deutschen Nationalbibliothek

Die Deutsche Nationalbibliothek verzeichnet diese Publikation in der Deutschen Nationalbibliografie; detaillierte bibliografische Daten sind im Internet über <http://dnb.d-nb.de> abrufbar.

ISBN 978-3-942171-72-4

uni-edition GmbH 2013

<http://www.uni-edition.de>

© Juan José Piqueras Meseguer



This work is distributed under a
Creative Commons Attribution 3.0 License

Printed in Germany

Contents

List of Figures	vi
List of Tables	viii
Summary	ix
Kurzfassung	xi
1 Introduction	1
1.1 Objectives	3
1.2 Outline	4
2 Background	7
2.1 Solar magnetographs	7
2.2 Scientific cameras	13
2.2.1 Image sensors	14
2.2.2 Front-End electronics	16
2.2.3 Specifications	17
2.3 Space radiation environment	20
2.3.1 Sources	20
2.3.2 Effects	21
2.3.3 Mitigation and testing	24
2.4 Field Programmable Gate Arrays	25
3 Requirements of the camera	31
3.1 The Solar Orbiter mission	31
3.2 Mission driven camera requirements	34
3.2.1 Radiation	34
3.2.2 Thermal and vacuum	36
3.3 The PHI instrument	37
3.4 Instrument driven camera requirements	41
3.4.1 Photon budget	41
3.4.2 Synchronization strategies	46
3.4.3 Shutter implications	51
3.4.4 Discussion	53
3.5 Summary	55

4	Selection of the image sensor	57
4.1	State-of-the-art	57
4.2	Assessment of alternatives	62
4.3	Decision and sensor description	64
5	Design of the camera electronics	67
5.1	Functionality and architecture	67
5.2	Digital control electronics	70
5.2.1	FPGA device	70
5.2.2	Architecture	71
5.2.3	Critical points	72
5.2.4	Limitations	81
5.3	Enhanced functionality	84
5.3.1	Image sensor protection	84
5.3.2	Snapshot shutter operating mode	85
5.4	Assessment of radiation effects	86
5.4.1	Long-term effects	86
5.4.2	Single event effects	88
5.4.3	Mitigation techniques	89
5.5	Conclusions	90
6	Camera tests and space qualification	93
6.1	Electrical tests	93
6.1.1	Camera read noise and pixel sampling	93
6.1.2	Data acquisition and synchronization	97
6.1.3	Power consumption	99
6.2	Electro-optical characterization	100
6.2.1	Conversion gain and linearity	100
6.2.2	Dark current and offset FPN	101
6.2.3	Sensitivity and PRNU	104
6.3	Overall qualification strategy	106
6.4	Image sensor radiation tests	106
6.4.1	Campaigns	106
6.4.2	Results	108
6.5	Discussion	117
6.5.1	Comparison with scientific cameras in space	119
7	Concluding remarks	123
A	Detailed specification of PHI	127
	Acronyms	131
	Bibliography	133
	Acknowledgements	143
	Curriculum Vitae and publications	145

List of Figures

1.1	Solar storm and impact on Earth: space weather	2
2.1	Polarization module: typical arrangements	8
2.2	Example of solar magnetograph output	10
2.3	Summary of magnetograph operation	11
2.4	Basic architecture of a camera electronics	13
2.5	CCD and CMOS sensors: functional differences	15
2.6	Shutter types based on functionality: snapshot or rolling	18
2.7	Radiation sources in the Solar System interplanetary space	21
2.8	Ionizing and non-ionizing effects on electronics: mechanisms	23
2.9	Basic FPGA architecture and main blocks	27
3.1	Orbit of Solar Orbiter	34
3.2	Radiation environment of Solar Orbiter	36
3.3	Overview of the PHI instrument	38
3.4	Operation flowchart of PHI	40
3.5	Influence of frame rate and full well charge on cycle time	46
3.6	Influence of sensitivity, read noise, and dark current on cycle time	46
3.7	Cycle time and number of accumulations: dependence on exposure time	47
3.8	Fast polarization tuning mode	48
3.9	Fast wavelength tuning mode	48
3.10	Intermediate tuning mode	49
3.11	Acquisition modes	49
3.12	Cycle time and modulation period versus tuning mode	50
3.13	Cycle time and modulation period versus acquisition mode	50
3.14	Polarization modulation packages: transitions	52
3.15	Polarimetric efficiency in continuous mode with snapshot shutter	52
3.16	Polarimetric efficiency in continuous mode with rolling shutter	53
4.1	4T CMOS sensor: pixel architecture	59
4.2	Influence of image sensor alternatives on instrument performance	63
4.3	ISPHI sensor architecture and pictures	65
5.1	Block diagram of the camera electronics	69
5.2	Pictures of the camera electronics: electrical model	69
5.3	Reduced block diagram of the FPGA design	72
5.4	Tunable sampling point: concept	74

5.5	Tunable sampling point: schematic	74
5.6	Simple and proposed solutions for ADCs clocking: comparison	75
5.7	Sampling clock and ADC data delays	76
5.8	Data synchronization using mesochronous structure	78
5.9	Data synchronization using double flopping	79
5.10	Data synchronization using dual-port memory	80
5.11	Power-on reset policy	82
5.12	Image sensor protection against SEU: remote TMR	84
6.1	ISPFI star-target image versus sampling instant	94
6.2	Effect of temperature on the optimum sampling point	95
6.3	Interpretation of the temperature effect on the sampling point	96
6.4	Digitization noise versus sampling scheme	97
6.5	Overall camera read noise versus frequency	98
6.6	Acquisition of digitized pixels	98
6.7	Photon transfer curves and conversion gain	102
6.8	Saturation curves and linearity	102
6.9	Dark current and DCNU versus temperature	103
6.10	Offset fixed pattern noise versus temperature	104
6.11	Sensitivity versus wavelength and PRNU	105
6.12	Total ionizing dose radiation campaign: setup	109
6.13	Displacement damage radiation campaign: setup	109
6.14	Single event effects radiation campaign: setup	110
6.15	Image appearance after TID irradiation	111
6.16	Dark current after TID irradiation	111
6.17	Signal level under flat illumination after TID irradiation	112
6.18	Power consumption after TID irradiation	112
6.19	Dark current after proton irradiation	114
6.20	Dark current after proton irradiation versus temperature	114
6.21	Read noise after proton irradiation	115
6.22	PRNU and sensitivity after proton irradiation	115
6.23	Single event upset test: dark mean value	116
6.24	Single event upset test: power consumption	117
6.25	PHI performance before, during, and after IS irradiation	119
A.1	Profile of the FeI spectral line used by PHI	129

List of Tables

2.1	Selection of current solar magnetographs: main features	12
2.2	Comparison of CCD/CMOS imagers: summary	16
2.3	Main characteristics of cameras	18
2.4	Cameras: basic performance parameters	19
2.5	Interplanetary space: radiation sources and their main emissions	22
2.6	Comparison of digital technologies: ASIC, FPGA, and generic processor	26
2.7	FPGA types based on programming technology	28
2.8	Main specifications and performance parameters for FPGAs	28
3.1	Payload of Solar Orbiter: List of scientific instruments	33
3.2	Solar EM flux received by the SO mission	35
3.3	Thermal and vacuum requirements	37
3.4	Performance specifications of PHI	39
3.5	Camera and instrument parameters assessed by the photon budget	45
3.6	Requirements of the image sensor affecting instrument performance	54
3.7	Requirements of the camera electronics affecting instrument performance	55
3.8	Optimum operating mode of the PHI instrument	56
4.1	Comparison of CISs typical pixel architectures	58
4.2	Selection of potential CMOS sensors for PHI	61
4.3	Image sensors employed in current solar magnetographs	62
4.4	Comparison of sensor alternatives: technical, risk, cost, time, and logistics.	65
5.1	Goal performance parameters for the camera electronics considering instrument and ISPHI requirements	68
5.2	List of digital control electronics tasks	70
5.3	Result of the Static Timing Analysis for the proposed FPGA design	82
5.4	Digital control electronics design area and pin occupation	83
5.5	Rolling and snapshot shutter with 4T pinned-photodiode pixels: steps	86
6.1	Camera power consumption	99
6.2	Electro-optical characterization: summary of measurements	100
6.3	Summary of Solar Orbiter radiation specification	107
6.4	Overview of radiation campaigns	108
6.5	Camera and IS performance: Comparison with requirements	118
6.6	Characteristics of other space cameras	121

List of Tables

A.1	Transmissions of the PHI optical subsystems	127
A.2	Spectral tuning of PHI	128
A.3	Polarimetric tuning of PHI	128

Summary

A camera based on a customized Active Pixel Sensor (APS) has been designed, characterized, and qualified for application in space. The camera was optimized for its implementation in solar magnetographs, with the intention of being employed in the Polarimetric and Helioseismic Imager (PHI) aboard the Solar Orbiter mission.

The designed camera has its control electronics implemented in a Field Programmable Gate Array (FPGA). Optimizations added to the control electronics minimize the camera noise at high readout speeds and under variable operating conditions such as temperature gradients. In addition, the control module protects the image sensor against single event effects (SEEs) caused by space radiation.

Characterization results of both image sensor and camera reveal their electrical and electro-optical performances. Moreover, three radiation campaigns have allowed studying the tolerance of the customized detector against ionizing doses, non-ionizing doses, and single event effects. Radiation, especially non-ionizing doses, significantly increases the dark current of the sensor and provokes smaller effects in other parameters. Post-irradiation tests demonstrate that those effects can be partly overcome, thus not endangering the scientific accomplishments, if proper in-flight annealing and operating temperatures are guaranteed. The implemented protection of the detector against SEEs successfully avoids permanent functional failures of the camera.

An application analysis shows how the camera characteristics as well as its combined operation with the rest of the instrument units influence the polarimetric and timing performance of the PHI magnetograph. This analysis results in both, a definition of the minimum camera requirements and an optimum strategy to jointly operate polarization, spectral, and imaging modules. The instrument demands a resolution of 2048×2048 pixels, fast readout, and large full well capacity from the camera. In turn, the challenging orbit of the mission imposes harsh thermal and radiation environments on all onboard subsystems. The camera electronics and APS sensor have surpassed these derived minimum performances and operating conditions.

Solar Orbiter is a space mission that will study the Sun, the heliosphere, and how they relate to each other. The spacecraft will approach the Sun much closer than any previous space mission. The PHI magnetograph, as part of the Solar Orbiter payload, will measure magnetic fields and gas flow velocities in the Sun's visible surface: the photosphere.

Most of this work, including the requirements study, camera design solutions, and radiation evaluation of the image sensor, can be either applied to future solar observatories or directly used in other scientific cameras for space.

Kurzfassung

Eine Kamera, die auf einem speziell entwickelten Active Pixel Sensor (APS) basiert, ist im Rahmen dieser Arbeit entworfen, charakterisiert und für Anwendungen im Weltraum qualifiziert worden. Die Kamera wurde für eine Implementierung in einen Sonnenmagnetographen optimiert, insbesondere mit der Absicht später im Polarimetric and Helioseismic Imager (PHI) an Board der Solar Orbiter Mission zum Einsatz zu kommen.

Die entworfene Steuerelektronik der Kamera ist in einem Field Programmable Gate Array (FPGA) implementiert. Optimierungen in der Steuerelektronik minimieren das Rauschen der Kamera bei hohen Auslesegeschwindigkeiten und unter veränderlichen Betriebsbedingungen, z.B. Temperaturgradienten. Außerdem schützt das Steuermodul den Bildsensor vor Single Event Effects (SEEs), die durch kosmische Strahlung verursacht werden.

Die Ergebnisse der Charakterisierung von Bildsensor und Kamera offenbaren die elektrische und elektro-optische Leistungsfähigkeit. Darüber hinaus ermöglichten drei Strahlungs-Testkampagnen, die Toleranz des speziell entwickelten Sensors gegenüber ionisierende Strahlung und nicht-ionisierender Strahlung sowie SEEs zu untersuchen. Insbesondere nicht ionisierende Strahlung steigert den Dunkelstrom des Bildsensors erheblich und bewirkt auch bei anderen Parametern kleinere Änderungen. Tests nach der Bestrahlung demonstrieren, dass diese Effekte teilweise beseitigt werden können und somit die Erfüllung der wissenschaftlichen Aufgaben nicht gefährden, insofern ein Ausheilen von Defekten durch Erwärmen des Sensors (*annealing*) während des Fluges durchgeführt sowie gewisse Betriebstemperaturen eingehalten werden. Der Schutz des Detektors vor SEEs, der in der FPGA implementiert ist, kann ein dauerhaftes Versagen der Kamera mit Erfolg verhindern.

Eine Anwendungsanalyse zeigt, wie die Kameraeigenschaften sowie ihr kombinierter Betrieb mit den restlichen Instrumenteinheiten die polarimetrische und zeitliche Performance des PHI Magnetographen beeinflusst. Diese Analyse führt zu einer Definition der minimalen Anforderungen, die an das Design der Kamera gestellt werden und zu einer optimalen Strategie, um gemeinsam die Module zur Messung von Polarisations-, Spektral- und Bildaten zu betreiben. Das Instrument benötigt eine Auflösung von 2048×2048 Pixeln, eine hohe Ausleserate und eine große Kapazität für Ladungsträger (*full well capacity*). Aus der anspruchsvollen Umlaufbahn resultieren jedoch schwierige Umgebungsbedingungen hinsichtlich Temperatur und Strahlungsbelastung für alle Subsystem an Board. Die Kameraelektronik und der APS Sensor haben die abgeleiteten minimalen Anforderungen bei repräsentativen Betriebsbedingungen übertroffen.

Solar Orbiter ist eine Weltraummission mit dem Ziel, die Sonne, die Heliosphäre, und ihre Verbindung zueinander zu studieren. Die Raumsonde wird sich der Sonne deutlich näher als jede vorangegangene Mission zuvor annähern. Der PHI Magnetographen, der

Bestandteil der Nutzlast sein wird, soll Magnetfelder und Strömungsgeschwindigkeiten des Gas auf der sichtbaren Oberfläche der Sonne – der Photosphäre – messen.

Ein Großteil der Arbeit, einschließlich der Studie der Kamera Anforderungen und verschiedener Konstruktionslösungen sowie die Bewertung der Strahlungshärte des Bildsensors kann sowohl bei der Auslegung zukünftiger Sonnenobservatorien als auch wissenschaftlicher Kamerasystem für die Raumfahrt angewendet werden.

1 Introduction

Most scientific instruments in astronomy employ cameras. In contrast to commercial imagers, scientific cameras normally demand exceptional performance and operate under arduous conditions. Hence, they require special designs optimized for their needs and meticulous characterizations, in particular, when intended for space applications.

Interplanetary space missions experience especially harsh radiation and thermal environments that affect the performance of cameras and can endanger the fulfillment of the mission's goals. Image sensors are particularly susceptible to space radiation. Among the main types of sensor technologies, charge-coupled devices (CCDs) degrade strongly when exposed to radiation but they can be built with very high performance characteristics. On the other hand, CMOS image sensors (CISs) – also known as active pixel sensors (APSs) – are more robust in irradiated environments but their imaging performance is slightly worse. Past missions have extensively used CCDs, yet they had to add dedicated protective shielding against radiation, e.g., Keller et al. (2007) or Sierks et al. (2011). As mission orbits get more ambitious, the mass of the shielding has a higher impact on cost. At the same time, CMOS imagers have significantly improved their performance characteristics and, thus, become a veritable alternative for scientific imagers (Theuwissen 2008). To date, very few scientific missions have employed this imaging technology. PROBA-2, an ESA technology demonstrator that was launched in 2009, included the first APS camera used for space solar observations. That camera was implemented aboard the SWAP extreme-ultraviolet imager within the satellite payload (De Groof et al. 2008). The success of this demonstrator reinforces the use of CISs for future missions. However, since its heritage is limited, using this technology still requires passing specific qualification processes. As for the camera electronics, severe changes of the environmental conditions like, e.g., temperature variations, can degrade their normal functionality because of deviations of components operational parameters.

Among the numerous cameras used in space science, a significant fraction is devoted to solar observations. The Sun is a normal, middle aged star. However, it presents a unique characteristic: the Sun is the closest star to Earth. As such, it is the only one on which we can resolve spatial structures and analyze in depth fundamental astrophysical processes. Moreover, the Sun provides almost all energy to Earth and influences life on our planet. Therefore, understanding the Sun means understanding our major source of energy.

The Sun is active and hence continuously changing. Atmospheric eruptions, irradiance variations, sunspots, or the 11-years solar cycle are examples of solar activity that produces phenomena such as aurora borealis, modifies the Earth's upper atmosphere, and threatens spacecrafts and polar-route aircrafts (Fig. 1.1). All solar activity emanates from the Sun's magnetic field (Stix 2002, Ch. 8). Much about how this field originates and



Figure 1.1. Solar storm and impact on Earth: space weather. Sun's eruptions massively release plasma and charged particles into the solar wind that travels to the Earth. This shapes the Earth's magnetic shield (magnetosphere), creating a bow shock between Sun and Earth (top image). The planetary magnetic field deflects the charged particles onto the polar regions, where they can produce aurora borealis (bottom image). Note that objects are not drawn to scale. *Source: Solar and Heliospheric Observatory (SOHO), URL: <http://sohowww.nascom.nasa.gov/home.html>.*

evolves, and how it forms the corona, is still unknown. In particular, current predictions of solar eruptive events or duration of solar cycles do not properly match the observed solar behaviors (Müller et al. 2012, Sect. 3.4).

To study the magnetic field on the solar surface, where it first manifests itself, we use spectro-polarimeters that measure the polarization of solar light in specific spectral lines. That polarized light contains imprints of the magnetic activity (Del Toro-Iniesta 2003, Sect. 1.3). Current solar polarimeters pursue four main performance characteristics: temporal resolution to track fast evolution of magnetic fields, spatial resolution to sample fine magnetic structures while covering large areas of the solar surface, accuracy to sense small field gradients, and sensitivity to discern weak fields. These solar instruments can be located either on ground or can be operated in space. Space observatories present some advantages with respect to terrestrial measurements at the expense of cost, risk, and development time. First, observations are not distorted by the Earth's atmosphere. Second, the whole spectrum, e.g. the extreme ultraviolet (EUV) region, is observable because atmospheric absorption is not present. And third, spacecraft can get close to the target and observe regions not visible from Earth. In consequence, contemporary solar physics research pushes towards more challenging space instrumentation.

Cameras, together with polarizers and filtergraphs, accomplish an essential part of the solar polarization measurements. The elevated temporal and spatial resolution that polarimeters require translate into large image arrays and high frame rate cameras, hence

into fast sensor readout schemes. This complicates the design of image sensor and camera electronics as well as their synchronization with polarizers and filtergraphs. Particularly, noise figures deteriorate as readout speed increases and temporal resolution depends on the ability to synchronize the key subsystems. In addition, polarimetric accuracy needs large signal capacity and moderate noise levels on the camera. Therefore, camera high-speed design and instrument operation become critical.

The Solar Orbiter¹ mission will observe the Sun from a heliocentric orbit that will bring the spacecraft closer to the star than any previous space probe and it will provide observations from high solar latitudes. This orbit imposes radiation and thermal requirements to the onboard instrumentation that are much more severe than those of past solar observatories, e.g., *Solar Dynamics Observatory* (Drobnes et al. 2012) or *Solar-B* (Kosugi et al. 2007).

Within Solar Orbiter, the polarimetric and helioseismic imager (PHI) is the magnetograph (spectro-polarimeter) that will measure magnetic fields on the solar surface. The readout speed requirements of the PHI camera are well beyond the specifications of previous space solar magnetographs, e.g., Schou et al. (2012) or Tsuneta et al. (2008).

1.1 Objectives

This thesis seeks to match state-of-the-art space cameras with the needs of solar instruments to develop a new camera able to expand the capabilities of future instrumentation. It focusses on the particular case of the PHI magnetograph aboard the Solar Orbiter space probe. The general goals of the work carried out by the author are:

- (g1) Identify the instrument's requisites and convert them into a set of camera specifications.
- (g2) Define a strategy to jointly operate camera and the rest of subsystems within the instrument. It shall guarantee the demanded performance.
- (g3) Study image sensor options and support the development of an appropriate sensor that fulfills the derived camera specifications.
- (g4) Design and develop the digital control electronics of the camera to interface the selected image sensor.
- (g5) Characterize the performance of both image sensor and camera.
- (g6) Assess the radiation tolerance of the image sensor as well as the hazards of radiation on the camera electronics at the dose levels of the mission environment.

Several open questions arise from the above list of goals. Firstly, how does the camera performance and its combination with polarization and spectrograph modules influence the accuracy and temporal resolution with which the instrument measures the polarization of the solar light, thus the magnetic fields in the surface of the Sun. Then, how significant is the impact of the variable thermal and radiation environments of the mission on the

¹<http://www.solarorbiter.org/>

camera parameters, especially for recent technologies such as active pixel sensors. In particular, drifts in the camera noise level can degrade the dynamic range and therefore the scientific results. In that context, the primary contributions of the thesis and that are the outcome of the author's work follow:

- (c1) *Optimum strategy to synchronize camera, filtergraph, and polarizers.* This strategy defines the mode of operation of the instrument. It aims at guaranteeing the required polarimetric properties while minimizing the overall measuring time. (c1) is linked with (g1) and (g2).
- (c2) *Reduction of camera noise at high readout frequencies in variable radiation and thermal environments.* It assures that the noise performance does not exceed the requirements even if environmental conditions change. (c2) is linked with (g4) and (g5).
- (c3) *Protection of the camera against functional interruptions caused by space radiation.* It is implemented in the control electronics and corrects upsets affecting the unprotected CMOS image sensor. (c3) is linked with (g4) and (g6).
- (c4) *Testing and analysis of radiation effects on custom CMOS image sensor.* This assesses how each sensor parameter degrades with radiation, as well as the impact of that degradation on camera and instrument performances. (c4) is linked with (g6).

1.2 Outline

The remainder of the thesis is structured as follows:

Chapter 2 reviews the main concepts and literature of the subjects this work is based on. It covers the scientific instrument (solar magnetograph), the subsystem (science camera), the environmental hazards (space radiation), and the technology of the camera control electronics (field programmable gate array).

Chapter 3 presents the Solar Orbiter mission and the set of environmental requirements that its orbit inflicts on the PHI camera. The chapter introduces the PHI instrument together with its major performance specifications. Based on those specifications, the influence of every camera parameter is analyzed to define an explicit list of requirements. Strategies to synchronize the camera with both filtergraph and polarizer while maximizing the instrument's outcome are proposed and discussed.

Chapter 4 uses the camera requirements derived in chapter 3 to study the state-of-the-art of CMOS image sensors and evaluate the alternatives available to fulfill the camera needs. Lastly, an image sensor solution is proposed, described, and justified.

Chapter 5 tackles the design of the camera front-end electronics and its interface to the image sensor selected in Chapter 4. Following to the definition of specifications, the overall camera architecture is presented, with the focus put on the digital control electronics. The critical parts of the design are discussed with emphasis on optimizations to improve the overall camera performance. The limitations of the

design are discussed and a couple of extra functionalities are proposed as solutions to enhance the reliability and performance of the image sensor. The last section deals with the impact of space radiation on the digital control electronics.

Chapter 6 describes the process and results of the camera and image sensor characterization. During this characterization, we pay special attention to the critical points of the design introduced in Chapter 5 and to the minimum camera performance derived in Chapter 3, as well as to the comparison of image sensor results with the expected specifications from Chapter 4. After that, the space qualification of the image sensor is discussed, focussing on the plan, development, and results of the radiation tests. The last section compiles the characterization and qualification results and compares them to existing scientific cameras.

Chapter 7 discusses the contributions and main results of the thesis. An outlook for future camera applications is given.

2 Background

Space instrumentation embraces diverse fields of study. Understanding any piece of the development process necessitates an overview of the instrument's concept and goals, its subsystems, the environment it must withstand, and the technologies that make it work.

This chapter provides such an overview, together with definitions and basic concepts, for the aimed camera development. First, solar magnetographs, as the type of instrument in which the studied camera must operate, are introduced (Section 2.1). Second, Section 2.2 covers scientific cameras, which are the targeted subsystem. The space environmental conditions are considered in Section 2.3 and, finally, the technology employed for the camera control electronics, field programmable gate array (FPGA), is presented in Section 2.4.

2.1 Solar magnetographs

The solar dynamo, the magnetic field it produces, and its interaction with solar convection are the source of all solar activity and that is causing the structure of the Sun's magnetic fields and its evolution in time like, e.g., the creation of sunspots, the activity cycle, eruptions, and the solar wind that fills our Solar System. The variations of the magnetic field influence every object of the Solar System, including the Earth and space missions. Therefore, by studying the solar magnetic field we may understand the dynamic activities of the Sun, and become able to predict phenomena that have an impact on Earth.

Magnetometers measure strength and direction of magnetic fields. A necessary condition for a magnetometer to operate is that it has to be in contact with the field it measures, i.e., it provides in-situ measurements. This condition cannot be satisfied in the Sun because of the inhospitable habitat it presents. Instead, all measurements shall be retrieved from the emitted solar radiation. Fortunately, the solar magnetic field imprints its signature on the state of polarization of the emitted light via the Zeeman effect (Del Toro-Iniesta 2003, Ch. 8). When no magnetic field is present, the solar spectrum presents a set of absorption and emission lines. These lines appear due to atomic transitions, within allowed energy levels, that occur after atoms absorb or emit photons. If a magnetic field is applied to these atoms, most of the energy levels split, which results in a splitting of the previous spectral lines. Moreover, light emitted at these split spectral lines, i.e. the part of the light not absorbed, is now polarized, with its polarization state depending on the applied magnetic field. Magnetographs employ this principle to extract magnetic field information from polarized light.

In consequence, magnetographs need capabilities to both, select individual spectral lines and measure the state of polarization of light. These two features define them as

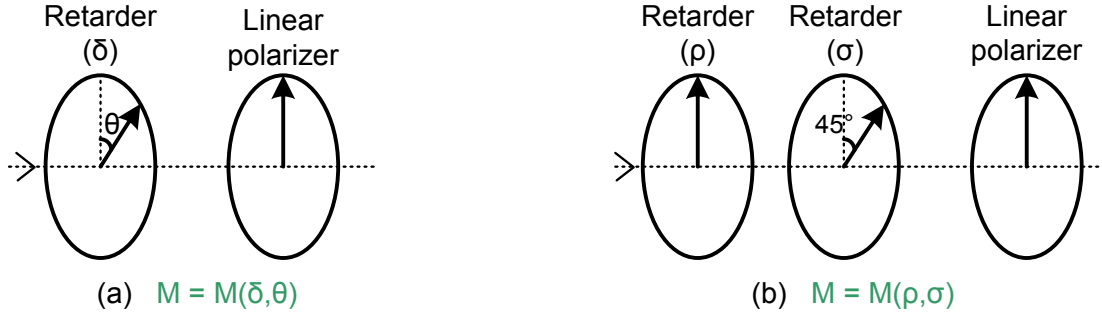


Figure 2.1. Polarization module: typical arrangements. The first option (a) presents a Mueller matrix that is function of the retarder orientation angle θ and retardance δ . In the second case (b), orientations are fixed but both retarders can vary their retardances ρ and σ . Both cases assume that the light travels from left to right.

spectro-polarimeters. Spectral selection is achieved using a filter that blocks any input wavelength except for the desired line, or part of it. Polarization measurement is harder because photon sensors can only detect intensity, not polarization. Therefore, the polarization information shall be converted into intensity through a process called modulation. This conversion requires a polarization module, which allows selecting a specific state of polarization, plus a detector that measures the intensity of that state. If an appropriate set of polarization states is selected, their intensity differences contain the desired polarization measurement.

The Stokes parameters describe the polarization state of an electromagnetic wave as the four elements vector $\vec{S} = (I, Q, U, V)^T$, with I representing the intensity, Q and U the linearly polarized components, and V the circularly polarized radiation. This notation is especially convenient because the output of any optical system relates to its input following

$$\vec{S}_{\text{out}} = \mathbf{M} \cdot \vec{S}_{\text{in}}, \quad (2.1)$$

with \mathbf{M} being the 4×4 Mueller matrix associated with the optical system (see Shurcliff 1962, Ch. 8; Del Toro-Iniesta 2003, Ch. 4). Mueller matrices can describe any linear change in the polarization state of light. The polarization module that selects a polarization state typically comprises one or two optical retarders plus a linear polarizer (Fig. 2.1). A retarder is an optical element that divides the input beam into two orthogonal components (fast and slow axis), adds a phase shift (retardance) between those components, and reunites them back (Shurcliff 1962, Ch. 7). A linear polarizer selects the linearly polarized part of the input light that is parallel to its axis. Changing either retardances or orientations in the setups of Fig. 2.1, and restricting to the intensity Stokes parameter, which sensors can detect, Eq. (2.1) leads to a set of n relations as follows

$$I_{\text{out},k} = M_{1,1}(\delta_k, \theta_k) \cdot I_{\text{in}} + M_{1,2}(\delta_k, \theta_k) \cdot Q_{\text{in}} + M_{1,3}(\delta_k, \theta_k) \cdot U_{\text{in}} + M_{1,4}(\delta_k, \theta_k) \cdot V_{\text{in}}, \quad (2.2)$$

where $k = \{1, \dots, n\}$, and $M_{1,m}(\delta_k, \theta_k)$ is the $\{1, m\}$ component of the polarization module's Mueller matrix with configuration (δ_k, θ_k) . If one can find, at least, four (δ_k, θ_k) combinations that result in linearly independent equations like (2.2), then a modulation matrix \mathbf{O} ,

containing the $M_{1,m}$ components of each combination, can be built. A similar modulation matrix can be defined with four (ρ_k, σ_k) combinations if the setup of Fig. 2.1 (b) is used. The set of combinations is called modulation scheme, and the modulation matrix fulfills

$$\vec{I}_{\text{out}} = \begin{pmatrix} I_{\text{out},1} \\ I_{\text{out},2} \\ \dots \\ I_{\text{out},n} \end{pmatrix} = \mathbf{O} \cdot \vec{S}_{\text{in}}. \quad (2.3)$$

Provided that the combinations in the chosen scheme are linearly independent and matrix \mathbf{O} is invertible, the demodulation matrix $\mathbf{D} = \mathbf{O}^{-1}$ allows retrieving the desired Stokes parameters from the measured intensities as

$$\vec{S}_{\text{in}} = \mathbf{D} \cdot \vec{I}_{\text{out}}. \quad (2.4)$$

Ideally, the retrieved Stokes vector after demodulation equals the input one as in Eq. (2.4). However, in reality several noise contributions disturb this measurement. Del Toro-Iniesta and Collados (2000) and Collados (1999) derive the optimum modulation matrix in terms of noise propagated to the measured Stokes parameters, and define the polarimetric efficiency as the vector $\vec{\epsilon} = (\epsilon_I, \epsilon_Q, \epsilon_U, \epsilon_V)^T$, or $\vec{\epsilon} = (\epsilon_1, \epsilon_2, \epsilon_3, \epsilon_4)^T$, with

$$\epsilon_i = \left(n \sum_{j=1}^n D_{i,j}^2 \right)^{-1/2}, \quad (2.5)$$

where n is the number of combinations of the modulation scheme, and $i = \{1, 2, 3, 4\}$. Higher efficiencies lead to lower noise contributions transferred to the measured Stokes parameters through the modulation/demodulation processes. The ideal efficiency is $\vec{\epsilon} = (1, 1/\sqrt{3}, 1/\sqrt{3}, 1/\sqrt{3})^T$ (Del Toro-Iniesta and Collados 2000). Therefore, the signal to noise ratio of the Stokes measurement can be increased in three ways: minimizing the noise contributions, such as spurious polarizations or non-uniformities, increasing the retrieved signal, and optimizing the polarimetric efficiencies.

Two options to modulate the input Stokes parameters as intensities are possible: temporal and spatial. Spatial modulation acquires two or more modulated intensities $I_{\text{out},k}$ in parallel, which requires the use of beam splitters and more than one detection area. The main advantage is the speed, but it suffers from spurious signals coming from the detection areas non-uniformities or differences between detection systems. On its part, temporal modulation consists of sensing the modulated intensities sequentially. This option has the disadvantage of taking longer, which may blur the measurements due to temporal evolution of the Sun, spacecraft or telescope jitter, or seeing induced image variations for ground-based observatories. However, it minimizes the problem of detection disparities. Independently of the modulation option, the filter-detector configuration determines whether the instrument takes two-dimensional maps of a defined field of view at a single wavelength, which is then varied sequentially, or it takes intensity measurements in one dimension and simultaneously all spectral information in the other. In the last case, the intensity dimension can be shifted sequentially to scan spatial structures.

As a final step to turn polarization measurements into useful data, one shall post-process the retrieved Stokes parameters to derive the magnetic field information and generate a magnetogram (Fig. 2.2). This operation is known as inversion. Whether the inver-

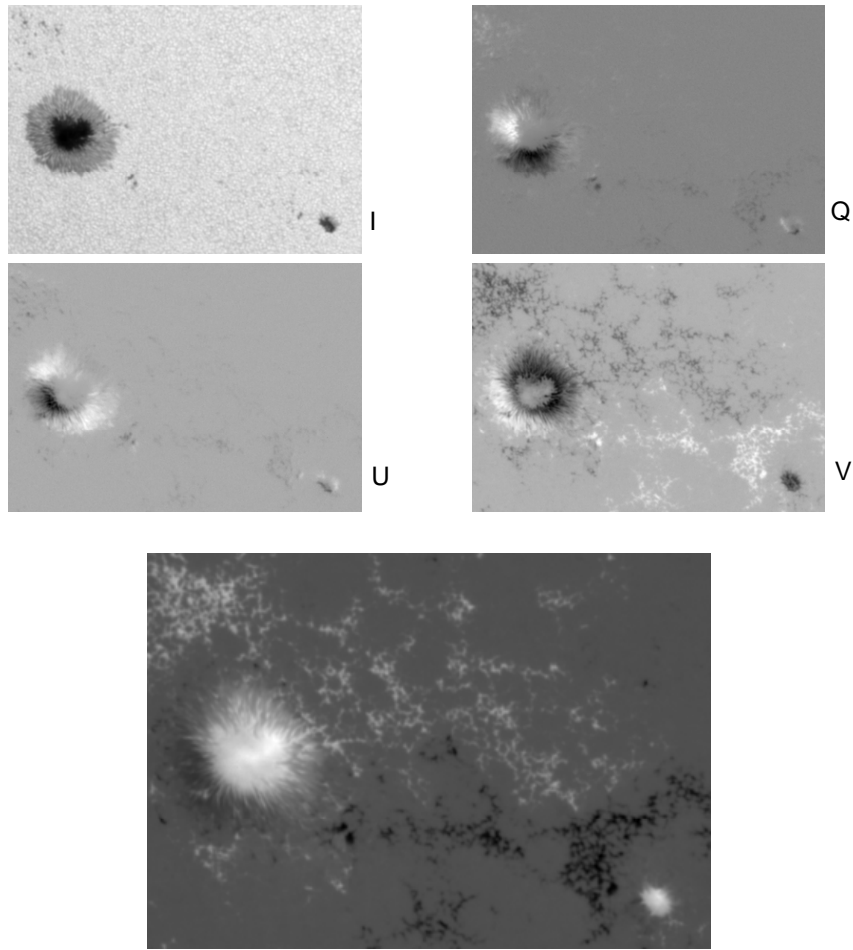


Figure 2.2. Example of solar magnetograph output taken with the HMI instrument on 2nd August 2012. The first four images represent the Stokes parameters (I , Q , U , V) of a solar active region, sunspot, in a fixed wavelength of the 617.3 nm spectral line. Lighter shade of the gray scale corresponds to higher values. In the intensity image (I) one observes the sunspot umbra and penumbra, surrounded by the granulation of the quiet Sun. The bottom image shows the line-of-sight magnetogram obtained after inversion of Stokes parameters above as well as their counterpart at other wavelength positions within the line. White color represents positive magnetic field, pointing out of the image, and black color negative one, pointing towards the image plane. The magnetic field strength is clearly concentrated in the active region, located at the sunspots and the surrounding plage, while the quiet Sun's magnetic field is very small along the line of sight.

sion leads to a vector magnetic field (strength and direction) or to a longitudinal measurement within the line-of-sight depends on the number of independent intensities (n) the instrument can provide. A vector magnetograph is capable of measuring all four Stokes parameters. Del Toro-Iniesta (2003), in Chapters 9 and 11, explains different inversion techniques to process solar spectro-polarimeters' datasets. Figure 2.3 summarizes how a solar magnetograph works, from the physical source to the final results.

Table 2.1 lists some magnetographs that are presently used in space or at ground observatories. Newer instruments tend towards increasing spatial resolution to allow resolving smaller features on the Sun, even if it is at the expense of reducing the field of

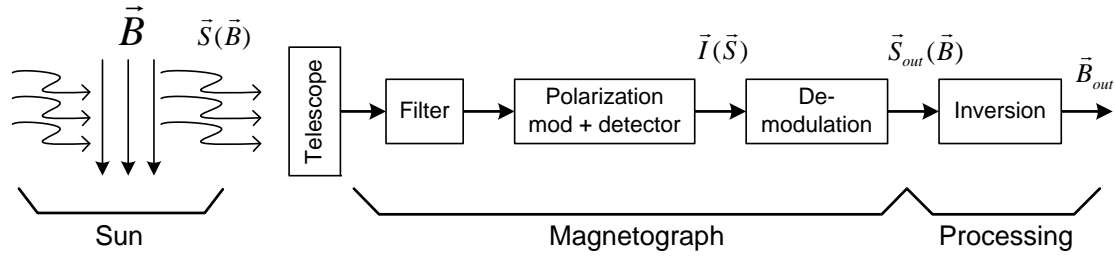


Figure 2.3. Summary of magnetograph operation. Polarized light from the Sun is collected by a telescope, tuned to a single spectral line by a filter, and modulated by a polarization module that encodes all polarization information in intensities ($\vec{I}(\vec{S})$). These intensities are analyzed by a demodulation stage to derive the Stokes parameters ($\vec{S}_{out}(\vec{B})$). The magnetic field vector is determined by an inversion process.

view (e.g., CRISP or IMAx). In theory, ground and balloon-borne observatories produce better spatial resolutions than space ones because they employ larger telescopes. However, space-borne telescopes are not affected by atmospheric conditions and, thus, do not suffer from air turbulences or balloon instabilities. Most magnetographs employ visible spectral lines, while only a few are working in the infrared and ultraviolet. The visible lines usually provide a view of the lowest layer of the solar atmosphere (photosphere), whereas infrared and ultraviolet lines normally make accessible the higher solar strata, e.g., the chromosphere. However, there are also chromospheric lines in the visible as well as photospheric lines in the infrared and ultraviolet regions. The latter spectral ranges are technically more challenging, apart from the wavelength dependency of the Zeeman splitting (Sasso et al. 2006; Socas-Navarro et al. 2004).

Table 2.1. Selection of current magnetographs that operate in the main solar observatories: main features. A number of other magnetographs not in the list, such as ZIMPOL-II (Gandorfer et al. 2004) or SVM/SOLIS (Henney et al. 2006), are also in use or have been used before. MDI is already out of operation but has been included because it represents a milestone in solar magnetographs. Type column specifies whether the instrument takes two dimensional maps, or it devotes one dimension to wavelength scanning. HR stands for high resolution mode, whereas FD means full disk. Note that the given FOVs and resolutions, expressed in arcsec, can be directly compared with each other because all these observatories are at about the same distance to the Sun. Detailed descriptions of the listed instruments can be found in Scherrer et al. (1995) for MDI, Collados et al. (2007) for TIP-II, Tsuneta et al. (2008) for SP, Ortiz and Voort (2010) for CRISP, Martínez-Pillet et al. (2011) for IMAx, and Schou et al. (2012) for HMI.

Name	Site	Mission / Telescope	Year	Type	Band (nm)	Spatial resolution (arcsec)	Field of view (arcsec)
Michelson Doppler Imager (MDI)	space	SOHO	1995	2D	676.8	1.25 3.96	624.6 (HR) 2027.5 (FD)
Tenerife Infrared Polarimeter II (TIP-II)	ground	VTT	2005	1D	1000-1800	0.36	77 (HR)
Stokes Polarimeter (SP)	space	Hinode SoT	2006	1D	630.15-630.25	0.32	163.8 (HR)
CRisp Imaging Spectro-polarimeter (CRISP)	ground	SST	2008	2D	630.2	0.13	70 (HR)
Imaging Magnetograph eXperiment (IMaX)	balloon	Sunrise	2009	2D	525.02	0.11	50 (HR)
Helioseismic and Magnetic Imager (HMI)	space	SDO	2010	2D	617.3	1.01	2068.5 (FD)

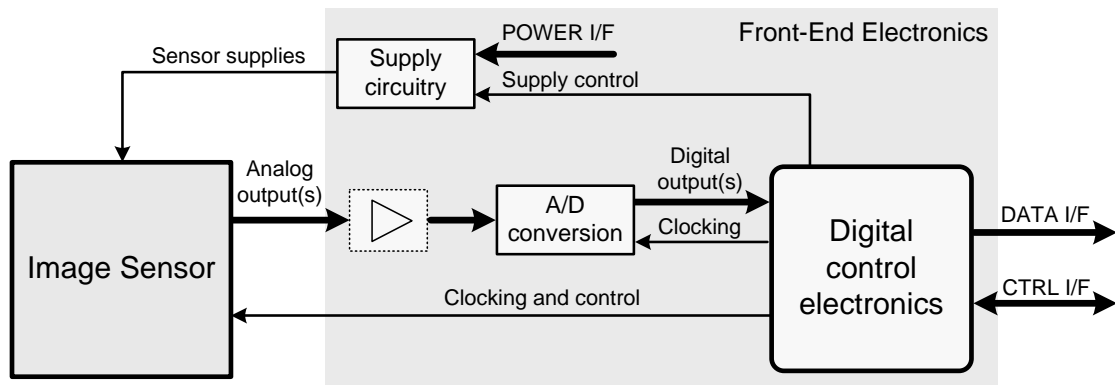


Figure 2.4. Basic architecture of a camera electronics. Depending on the specific image sensor and camera design, some blocks may be optional, embedded in others, or just omitted.

2.2 Scientific cameras

Digital cameras are involved in many aspects of everyday life, ranging from mobile devices or surveillance systems to professional photography or science. Regardless of its application, all cameras share the same operating principle. Scientific cameras, especially those used in astronomy, differ from the rest in the set of very demanding performance specifications they must demonstrate, which regularly bring technology at its cutting-edge. In particular, astronomical applications often require low noise, specific spectral ranges, high sensitivity, and/or operation under severe environmental conditions.

The basic block diagram of a camera comprises two main parts: image sensor (IS) and front-end electronics (FEE), also simply known as camera electronics (Fig. 2.4). The image sensor converts the incoming light per pixel into electrical signals, whereas the front-end electronics controls, clocks, and supplies the sensor, digitizes its analog data outputs, manages the digital data stream, and communicates with the camera external interfaces. Some cameras include analog pre-amplifiers before the analog to digital converters (ADCs), while others hold the ADCs integrated into the sensor. The supply circuitry receives the main voltages from the external power interface and provides all the required sensor supplies. It usually consists of DC/DC converters and digital to analog converters (DACs). On its part, the digital control electronics generates all signals and clocks the sensor requires, commands the supply circuitry, provides the sampling clocks for the ADCs, acquires the digital image data, and is the data link to the external interface. Depending on the type of camera and sensor, additional components may be required to, for example, adjust the voltage level of the clocks.

Section 2.2.1 introduces the types of image sensors, explains their operating principles, and presents their strengths and weaknesses. Section 2.2.2 briefly comments on possible FEE architectures and on the implementation of their main blocks. Finally, Section 2.2.3 identifies the set of parameters that defines the performance and characteristics of a scientific camera.

2.2.1 Image sensors

Charge-coupled devices (CCDs) and CMOS image sensors (CISs) establish the two big groups of digital detector technologies. In astronomy, CCDs have been the chosen technology since they delivered the first astronomical image in 1975 (Janesick and Blouke 1987). Only recently, CMOS sensors have overcome major performance difficulties to become a serious competitor for scientific applications. Literature provides extensive reviews of CCDs, see Janesick (2001) or Howell (2006), and CMOS imagers, see Bigas et al. (2006) or Hoffman et al. (2005); as well as explicit comparisons between them, see Magnan (2003) or Janesick et al. (2007).

The operation of an image sensor comprises five principal steps: convert photons into electrons via the photoelectric effect (charge generation), accumulate those electrons in every pixel during exposure (charge collection), convert accumulated electrons per pixel into signal (charge to voltage conversion), read pixel values (readout), and, optionally, translate them into digital numbers (DN). A CCD (Fig. 2.5, top) consists of an array of pixels and an output circuitry. Every pixel includes a photodiode together with a storage element (capacitor) to generate and collect photoelectrons during exposure. Once exposure finishes readout starts, with charge being transferred vertically from row to row and loaded into an output shift register, which in turn shifts the charge horizontally to get a pixel by pixel output. This output feeds a charge to voltage conversion stage and an amplifier. Finally, the stream of pixels exits the CCD chip and additional post-processing steps, such as correlated double sampling (CDS) to reduce noise¹ or analog to digital conversion, follow. In case the CCD presents more than one output stage (shift register, voltage conversion, and amplifier), charge is transferred in opposite directions for different array areas, so that every pixel reaches its closer output. The basic architecture of a CCD can be modified to optimize certain performance parameters, leading to particular CCD types (frame transfer, interline, orthogonal transfer, etc.). Howell (2006) gives in Chapter 2 a concise description of those types.

A CMOS image sensor (Fig. 2.5, bottom) shows a different approach to carry out the same five basic steps. Every pixel in the array contains not only a photodiode plus a storage element for charge generation and collection, but also the charge to voltage conversion stage plus a buffer or amplifier. This means that the pixel complexity is higher but the charge transfer step is by-passed. The readout phase simply requires multiplexing the pixel values into a common bus followed by an amplifier. Whether there is a single or several common buses, and the multiplexing is performed in one or more steps depend on the specific design of the sensor. Since CISs complete a manufacturing process that benefits from the advances of standard CMOS processes (Hoffman et al. 2005), it is possible to integrate additional on-chip circuitry, such as CDS or analog to digital conversion. These sensors are also known as APSs because most of them include an active amplifier within the pixel. A common way of classifying CISs is as a function of their pixel architecture. The variety of pixel architectures ranges from the simplest 3-transistors (3T) photodiode pixel to the 4-transistors (4T) photogate, 5T, 6T, and so on. More transistors per pixel pro-

¹CDS consists of sampling the reset, *zero*, level of each pixel just before starting every exposure. After exposing, this reset level is subtracted from the read pixel value to reduce reset and kTc noise. In case the sampled reset value is not taken just before starting the exposure, the process is called uncorrelated double sampling, and the noise reduction is lower (Janesick 2001, Sect. 6.4).

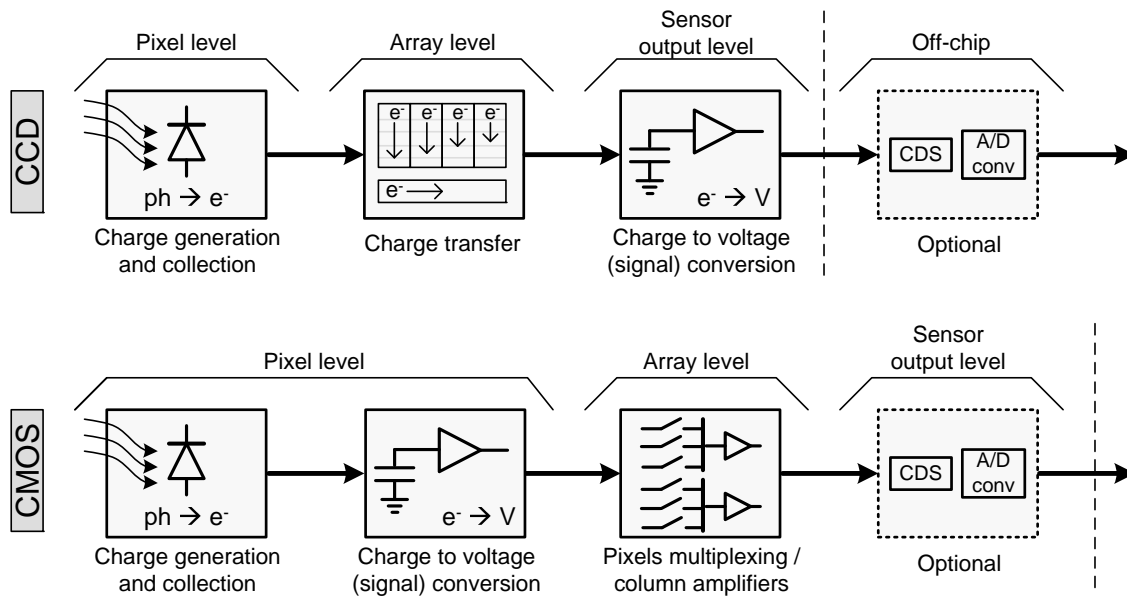


Figure 2.5. CCD and CMOS sensors: functional differences. Diagrams show the basic steps required to convert photons into digital images in a CCD (top) and a CIS (bottom).

vide the sensor with additional features. For example, a 4T pixel allows on-chip reduction of noise contributions, and a 5T pixel permits performing a global reset of the pixel array (Janesick et al. 2002).

The spectral range in which a sensor can detect photons depends on the semiconductor material used to manufacture its photosensitive area, and on its properties: mainly band-gap and thickness. Silicon is the material used in CCDs, which results in a range covering from ultraviolet (UV) to near infrared (NIR) (typically 300 – 1100 nm). Some particular CCDs have been manufactured with other materials, for example Germanium, to extend the range towards the infrared band. However, those fabrication processes present some performance drawbacks (Janesick 2001, Sect. 1.2.2.1). CMOS imagers can be monolithic or hybrid. Monolithic CISs are entirely manufactured using a CMOS process, therefore their photosensitive area is Silicon. Hybrid CMOS sensors presents two separate layers that are coupled together. The first layer contains the array of sensitive pixels without any additional circuitry, whereas the second layer, the readout integrated circuit (ROIC), includes additional CMOS circuitry, as in a monolithic CIS. Both layers are usually connected pixel by pixel via indium bumps. This hybrid approach permits manufacturing the sensitive layer with a material different to the Silicon ROIC (Beletic et al. 2008; Simms 2010). Hybrid sensors achieve good sensitivities at wavelengths beyond 10 μm .

Sensors can be either front- or back-side illuminated. In front-side devices, light enters from the top part of the sensor, where electrodes, gate contacts, and other pixel circuitry are placed. Therefore, the effective photosensitive area is reduced with respect to the physical size of the pixel (fill factor is lower than 100 %). On the other hand, back-side illuminated sensors collect photons from the bottom, thus presenting a 100 % of fill factor and maximizing sensitivity. Manufacturing processes are more complex for back-side imagers. In both cases, a coating can be added to the illuminated interface to reduce reflectivity at certain wavelengths of interest.

Table 2.2. Comparison of CCD/CMOS imagers: summary.

	Advantages	Disadvantages
CCD	Low noise Good linearity Charge binning Long heritage	Mechanical shutter High power cons. Radiation susceptibility
CMOS	On-chip circuitry Low power cons. Radiation tolerance Electronic shutter	Higher noise (typical) Non-linearity

Table 2.2 lists the main advantages and disadvantages of CCDs and CISs. In general, charge-coupled devices show better performance with respect to noise and linearity. Moreover, the charge transfer step allows performing binning in the charge domain, which reduces the accumulated noise. Non-linearity is significant in CMOS imagers mainly because the charge to voltage conversion shows a dependence on the integrated signal level, thus degrading the linearity of gain with signal (Janesick et al. 2006; Janesick 2007, Ch. 7). This dependence vanishes in sensors that isolate photodiode and sense node with a transfer gate (Janesick et al. 2006). Noise in CISs presents a larger contribution from offset fixed pattern noise (FPN), i.e., pixels exhibit different offset levels, because each pixel includes its own charge to voltage conversion, which leads to small differences across the pixel array (Janesick 2007, Ch. 11). The operation of a CCD, especially the charge transfer, requires relatively high voltages, thus a higher power consumption. Contrarily, CISs work with standard CMOS low voltages. As for the shutter, scientific CCDs² require a synchronized mechanical shutter to block its exposure to light, whereas CMOS sensors perform this operation electronically. Regarding radiation tolerance, CCDs are especially susceptible because the charge transfer process is affected by radiation-induced traps that reduce the transfer efficiency (Dale et al. 1993).

2.2.2 Front-End electronics

Three approaches are possible to implement a front-end electronics: single chip, discrete electronics, or ASIC (Hoffman et al. 2005). All of them share the same basic functionality (Fig. 2.4), but differ in the concept. The first option consists of embedding all the electronics on-chip together with the image sensor. It is only an option for CISs because CCDs do not allow on-chip circuitry. This solution is compact and consumes low power. However, it is difficult to optimize the performance of all on-chip components and the cost is high. The discrete electronics approach is the most widely used in CCDs, where each component is placed in a separate part of one or more printed circuit boards (PCBs). This option allows individual choice of each camera component but usually results in higher size, mass, and power consumption. Finally, ASICs permit to design the complete electronics on a single chip, so that the camera is reduced to two components. This solution

²Some special CCD types, e.g., interline CCDs, can provide an electronic shutter but they are not common in scientific applications because some specifications, such as sensitivity or resolution, are degraded.

allows optimizing not only performance but also size, mass, and power. However, the cost is much higher than the second approach, the development time is longer, and it is less flexible. Loose et al. (2003) show an example of the third approach.

A/D conversion and digital control are the principal elements of the front-end electronics. ADCs are characterized by their resolution in bits, maximum sampling rate, and noise contributions. Conversion architectures and specifications have been largely studied elsewhere, e.g. Kester (2005). Digital control electronics, independently of the FEE architecture, can be implemented using different technologies: microcontroller/microprocessor, FPGA, or digital ASIC. The first option consists of running a program that controls the camera using a fixed processing architecture. It provides flexibility but normally shows speed and I/O limitations. FPGAs offer the possibility of implementing customized high-speed architectures while still being flexible, especially at design stage, and with low cost (Section 2.4). Finally, a digital ASIC allows fully customizing the hardware architecture, which results in the best performance and lower power consumption, but significantly increases costs and reduces flexibility.

2.2.3 Specifications

We distinguish two types of specifications for the camera system: characteristics (Table 2.3) and performance parameters (Table 2.4). Characteristics are those specifications that are fixed at design level, while performance parameters are aimed at design level but only confirmed after measuring them in the real camera.

On the image sensor side, the list of characteristics includes its format in number of rows and columns (pixels), the physical pixel size (pitch), and the spectral range in which it shows sensitivity. The frame rate depends on the maximum working speed of sensor, ADCs, and control electronics. Two kinds of shutter exist: snapshot and rolling (Fig. 2.6). In snapshot mode, all pixels of the sensor are exposed to light at the same time. On the other hand, a rolling shutter exposes rows from top to bottom sequentially. In both cases, the total exposure time is the same for every pixel in the array. However, rolling shutter may cause smearing on the final image. This classification attends to the operation and not to the shutter implementation, which may be mechanical or electronic. A mechanical shutter, as the one commonly used with CCDs, presents a snapshot exposure, while electronic shutters can be snapshot or rolling depending both on the sensor design and the digital control electronics. Finally, the ADC stage defines the bit resolution of every digitized pixel.

The quantum efficiency and the fill factor define how sensitive the camera is to light of a certain wavelength. The first factor stands for the amount of incident photons that are able of interacting and generate photoelectrons, whereas the fill factor indicates the portion of pixel area that is photosensitive. In general, the signal level at the output of the sensor follows

$$S = C \cdot t_{\text{exp}}^{\gamma}, \quad (2.6)$$

where C is a proportionality constant, t_{exp} the exposure time, and γ indicates how linear the sensor response is. Assuming that the digitization process does not add non-linearities and adjusting C accordingly, S in Eq. (2.6) may be expressed both in e^- or DN. The linearity

Table 2.3. Main characteristics of cameras. Last column identifies which camera components influence each feature.

Characteristic	Symbol	Unit	Associated component(s)
Format	$N_{\text{row}} \times N_{\text{col}}$	pixels	Image sensor
Pixel size	A_{pixel}	μm^2	Image sensor
Spectral range	λ_{range}	nm	Image sensor
Frame rate	$1/T_{\text{acq}}$	fps	Image sensor A/D conversion Control elect.
Shutter type	–	–	Image sensor Control elect.
Pixel resolution	N_{bits}	bits	A/D conversion

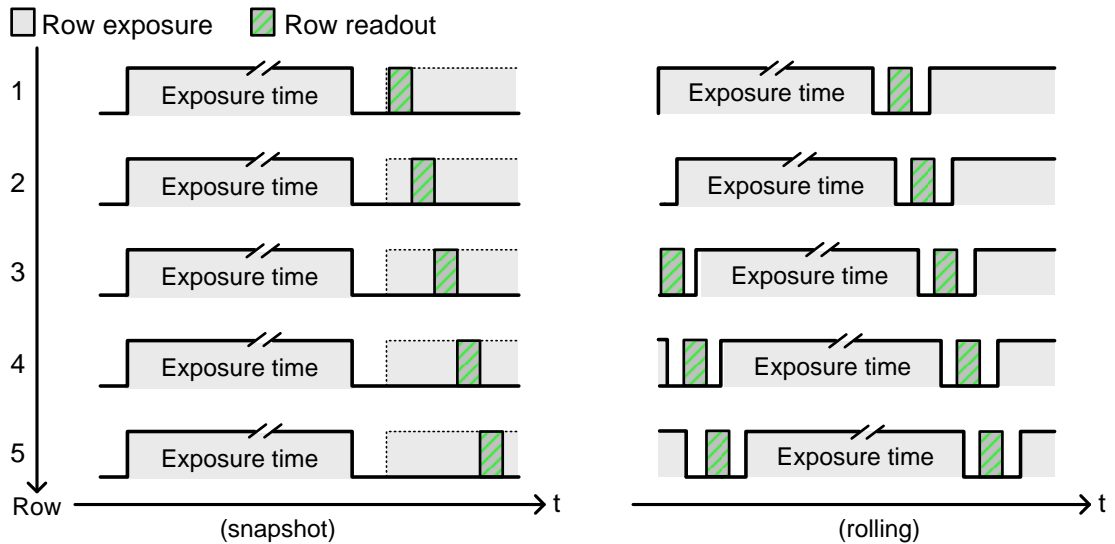


Figure 2.6. Shutter types based on functionality: snapshot (left) or rolling (right). The shown snapshot scheme assumes that exposing the next frame while reading out the current one is possible. Otherwise, the frame rate would be reduced to half. Drawing adapted from Hoffman et al. (2005).

specification measures how linear the signal value varies as a function of the exposure time. Non-linearity at a certain signal level S can be quantified via comparison with the level in a defined linear region (Janesick 2001, Sect. 2.2.7). Full well charge specifies the maximum amount of electrons that a pixel can collect before reaching saturation, with saturation defined as the point at which an increase in exposure time does not increase the signal level. Linear full well is usually defined in terms of non-linearity as the signal level at which NL exceeds certain value.

A key set of performance specifications arises from noise sources and non-uniformities.

Table 2.4. Cameras: basic performance parameters. Last column identifies which camera components are responsible for each feature.

Parameter	Symbol	Unit	Associated component(s)
Sensitivity	$QE \times FF$	%	Image sensor
Non-linearity	NL	%	Image sensor
Full well charge	FWC	e^-	Image sensor
Read noise	σ_{read}	e^-	Image sensor Control elect.
Digitization noise	σ_{ADC}	e^-	A/D conversion Control elect.
Dark current	D_c	e^-/s	Image sensor
Dark current non-uniformity	$DCNU$	%	Image sensor
Pixel response non-uniformity	$PRNU$	%	Image sensor
Crosstalk	X_{talk}	%	Image sensor
Image lag	Lag	%	Image sensor
Conversion gain	CG	e^-/DN	Image sensor Amplification A/D conversion
Power consumption	P_{cons}	mW	All
Radiation tolerance	<i>(see Section 2.3)</i>		All

Read noise, also known as temporal dark noise, encompasses any noise contribution that is not a function of the signal level. Therefore, it includes sources ranging from pixel reset to control electronics noise. One particularly important contributor to the read noise is the digitization noise. This source corresponds to the noise introduced by the A/D conversion stage, and depends on the converters as well as on the digital control electronics, which generates the sampling clocks. Dark current represents the level of thermally generated electrons, which increases with exposure time and temperature. It has two contributions, one is the actual level of dark current that is added to the signal and the other is the dark current shot noise, which varies as the square root of the dark current level and adds to the read noise. Moreover, dark current also shows spatial variations from pixel to pixel, resulting in dark current non-uniformity (DCNU). In the same way, the individual pixel response is not constant across the sensor array, which produces pixel response non-uniformity (PRNU). Crosstalk indicates the amount of spurious charge that couples from one pixel to its neighbors, while image lag is the amount of charge or signal that remains from one image to the consecutive one.

The conversion gain is the overall gain factor of the camera, which allows converting from electrons to digital numbers and viceversa. Finally, the camera power consumption and radiation tolerance also correspond to important camera specifications.

2.3 Space radiation environment

The space age started with the launch of the first artificial satellite around Earth (Sputnik 1) in 1957. From this moment on, space technology has notably evolved to face new challenges, as well as to widen the scope of space applications. At present, areas of applicability include, among others, space science, communication, navigation, and Earth observation. The success of space missions greatly depends on their capacity to operate under space environmental conditions. These conditions cover ambient factors, such as temperature, pressure, or atomic oxygen concentration, as well as gravitation, radiation, and others like micro-meteoroids or orbital debris. Data from previous missions evidence that the majority of spacecraft anomalies related to space environment are caused by radiation effects (Velazco et al. 2007, Ch. 3).

A mission's characteristics determine how the radiation environment of a spacecraft will be. In particular, the orbit, or trajectory, and the time-frame of the mission are highly influencing factors. For instance, a spacecraft orbiting the Earth may encounter an environment affected by the Van Allen radiation belts and protected by the Earth's magnetosphere, whereas other planets present orbits with totally different properties. This section focusses on interplanetary radiation environments, which cover missions such as Solar Orbiter, that travel between planets of the Solar System.

The subsequent discussion splits up into three parts. Section 2.3.1 identifies the interplanetary radiation sources and specifies the type of radiation they emit. Section 2.3.2 introduces the effects that radiation causes on electronics, with emphasis on CMOS technology and image sensors. Finally, Section 2.3.3 deals with how these effects can be mitigated and explains the basic concepts of radiation testing.

2.3.1 Sources

Interplanetary radiation primarily originates in two places: the Sun and outside the Solar System. Secondarily generated radiation and, in minor degree, other planetary sources may also contribute to the interplanetary environment (Fig. 2.7).

In first place, the Sun emits a continuous flux of electromagnetic radiation with energies up to the X -ray band. The γ -rays produced in the solar core are not directly emitted because they are absorbed and re-emitted as lower energy photons before reaching the solar surface. The solar cycle modulates the solar irradiance intensity, so that solar activity maxima result in stronger electromagnetic fluxes. High energy photons, from UV to X -rays, are the ones of concern for a missions' safety. Secondly, the Sun generates the solar wind, which is a stream of charged particles in the form of plasma that fills the interplanetary space. These particles are mostly protons and electrons of energies below 10 keV. Solar activity also influences the density and other properties of the solar wind. Lastly, the Sun produces occasional events, such as solar flares or coronal mass ejections (CMEs), that result in eruptions of energetic particles, mainly protons and heavy ions (HIs), and electromagnetic radiation from radio waves to γ -rays. Again, solar cycles modulate the rate at which these events occur.

Galactic cosmic rays (GCRs) are the most significant contribution to radiation from outside the Solar System. They are generated in our galaxy and result in a low but continuous flux of ions. Their composition includes protons, α -particles, and very energetic

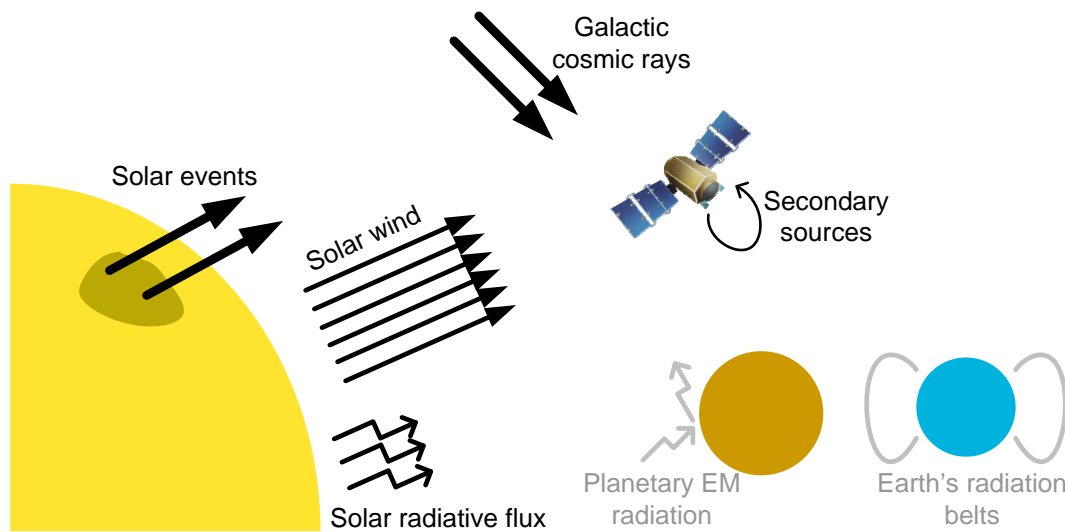


Figure 2.7. Radiation sources in the Solar System interplanetary space. Note that sizes are not to scale.

heavy ions, which are the most hazardous despite having the lowest density. The continuous flux of cosmic rays is anti-correlated with the solar activity, so that during solar maxima the more dense solar wind plasma acts as a shielding, thus reducing the flux of cosmic rays into the interplanetary region.

Secondary radiation arises from the interaction of primary environmental components with spacecraft materials. In particular, the most significant secondary source, called *Bremsstrahlung*, produces γ /*X*-rays when other particles, mainly electrons, decelerate during their interaction with matter, e.g., spacecraft structure. In addition, other nuclear interaction mechanisms may also generate neutrons. Finally, two planetary radiation sources play a minor role in the interplanetary environment: planetary electromagnetic radiation and Earth's radiation belts. Planetary EM radiation comes from the albedo resulting after solar light is reflected in a planet's surface. The Earth's radiation belts, which are vital to Earth's orbiting missions, are of concern only during the launch phase of interplanetary spacecrafts.

Table 2.5 summarizes the main emissions of the different radiation sources. In order to calculate an environmental specification for a particular interplanetary mission, these sources shall be combined with specific mission characteristics, such as orbit details, duration, solar activity during main phases, and even spacecraft design features. Several models have been developed to allow those calculations (ESA PA 1993, Sect. 3.8; Holmes and Adams 2002, Ch. 12).

2.3.2 Effects

Radiation that interacts with a material may cause damage to it. In case the material constitutes a more complex device, whether it is electronics, optics, or of any other nature, this device may suffer from performance degradation.

Attending to the response mechanism, radiation effects are classified as ionizing and non-ionizing. Ionizing effects include total ionizing dose (TID) and single event ef-

Table 2.5. Interplanetary space: radiation sources and their main emissions. Emission column includes those particles and high energy electromagnetic radiation of most concern for space missions.

Source	Emission	Comments
Solar EM flux	UV, X-rays	$3.1 \text{ eV} < E < 1.24 \text{ keV}$
Solar wind	Plasma	$p^+, He^{++}, e^-; E < 10 \text{ keV}$
Solar events	$p^+, HI, \gamma/X\text{-rays}$	E_{p^+} up to 100's MeV
Galactic cosmic rays	HI, p^+, α	E_{HI} in the GeV range
Secondary sources	$\gamma/X\text{-rays}, n$	Depends on s/c materials

fect (SEE), whereas non-ionizing ones comprise displacement damage (DD). Some of them produce long-term damage (TID and DD), while others are transients (SEE). The specific effect after interaction depends on the type of radiation, energy, flux, type of material (semiconductor, dielectric, conductor), and device properties (geometry, process, structure). Therefore, complex devices on mixed environments may be subjected to more than one degradation mechanism.

Ionizing effects are related to the process of removing electrons from materials' atoms, thus producing electron-hole pairs that can move through the material generating additional pairs and contributing to the current conduction. The long-term ionizing effect, characterized by the total (accumulated) ionizing dose, causes device degradation, and is mainly produced by protons, electrons, and high energy EM radiation. It is quantified by the dose as the energy absorbed by the material through ionization per unit mass, typically measured in rad referred to the material, e.g., rad(Si). The ionizing degradation process in semiconductors differs from the one in insulators. In semiconductors, some electrons of the valence band are excited to the conduction band, so that the electrical current level is higher than in normal conditions. The exact level depends on the total dose and rate. In dielectrics, such as oxides, the process is similar but has a more severe effect because they are supposed to be electrical insulators. After the generation of electron-hole pairs and temporal conduction due to radiation, some electrons recombine, while others, depending on the applied electric field, are capable of escaping the insulator. The same applies to holes, but they move slower, which makes it less likely for them to escape from the dielectric material. As a result, the insulator gets positively charged and presents trapped holes or defects. Due to biasing, some of the trapped holes can drift towards the interface of the material and lead to a localized charged area. In addition, radiation can alter the chemical bonds that join insulators and semiconductors in complex devices, thus generating undesired interface states (Fig. 2.8, a).

In contrast to long-lived phenomena, single event effects are ionizing transients. They are caused by single, high energetic, ions that cross a sensitive region of the irradiated material creating a linear ionization path. Through this ionizing track, charge is deposited in a very localized region, where the effect takes place (Fig. 2.8, b). The type of particle, which can be either heavy ions or high energy protons, its properties (atomic number and energy), and those of the material determine the characteristics of the event. The linear energy transfer (LET) quantifies the amount of energy that particles deposit during the

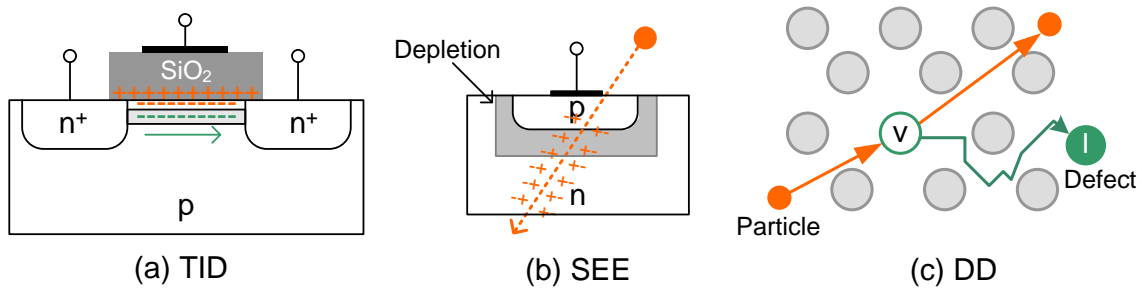


Figure 2.8. Ionizing and non-ionizing effects on electronics: mechanisms. (a) Long-term effect due to accumulated ionizing dose in a typical NMOS structure (transistor). Oxide gets positively charged due to holes traps that are shifted to the interface, and negative charge is confined in the oxide-semiconductor interface because of interface defects. (b) Ionizing transient effect on a p-n junction. Incident particle creates a charged track through its trajectory. (c) Non-ionizing damage produced by the displacement of an atom after colliding with an incident particle. The atom leaves a vacancy and an interstitial is created (defect). Drawings (a) and (c) are adapted from Mohammadzadeh et al. (2003).

event, which is a function of the distance they travel through the material. Two parameters indicate the device sensitivity to SEEs. The threshold linear energy transfer (LET_{th}) gives the minimum energy deposition required to produce a SEE, whereas the saturation cross section marks the point (LET_{sat}) at which every incident particle would trigger an event. LETs above the saturation do not increase the number of events. Several types of events can be triggered by SEE, with single event upset (SEU), single event transient (SET), and single event latch-up (SEL) being the most common ones. Single event upsets occur when the deposited charge ends in a critical node of a digital circuit, such as a flip-flop or a memory cell, and changes its logic level. If the bit-flip requires powering down and up the complete system to recover, then a single event functional interruption (SEFI) is registered. SETs provoke temporal pulses or glitches in analog or digital circuits, which may affect the overall functionality. In digital circuits, if the SET is latched by a sequential unit, then a SEU happens. Finally, latch-ups consist of activating, with the event, the parasitic p-n-p-n thyristor structure created in some CMOS circuits. This activation results in a low impedance path between power supply rails that may destroy the device.

Lastly, displacement damage takes place when an atom in a solid is displaced from its equilibrium position by an incident particle. Provided that the colliding particle has enough energy, the momentum exchange makes the atom leave its original position. As a result, a vacancy and an interstitial atom appear (Fig. 2.8, c). After that first process, if the particle energy is high enough, the displaced atom can collide with more atoms and lead to a cascade of displacements. Then, each displaced atom can either recombine and come back to its original position, which would make the lattice defect to disappear, or rest in an interstitial state (defect). Defects induced in devices' materials can interfere with their normal operation in several ways, such as trapping charge, modifying carriers mobility, or generating additional electron-hole pairs. Particles capable of producing displacement damage are protons, electrons, and neutrons, with the amount of displacements depending on the energy these particles transfer to the colliding atom. This fraction of particle energy involved in the atomic collision is called non-ionizing energy loss (NIEL). In principle, displacement damage effects may affect any material. However, the effect is of

more concern in semiconductors because other materials, such as insulators or glasses, do not present a well defined crystal structure, which means that defects exist even before irradiation. Those materials are dominated by ionizing effects (Mohammadzadeh et al. 2003).

CMOS circuitry is susceptible to total ionizing dose and single event effects. Displacement damage, though existent, does not play a significant role in regular CMOS electronics devices (Ma and Dressendorfer 1989, Ch. 1). Main effects in CMOS circuits after ionizing irradiation are the shift of the threshold voltage in transistors, change in the carriers' mobility, and increase of leakage currents. Consequently, the power consumption increases due to leakages, input range in digital devices and noise margin are reduced because of threshold change, and propagation delays increase as a result of mobility degradation.

Image sensors, both CCDs and CISs, are sensitive to all kinds of radiation effects: TID, SEE, and DD. Since the objective of these sensors is to detect and collect photoelectrons from low energy EM radiation, they are especially susceptible to radiation damage. The principal radiation effects on image sensors are:

- Increase in power consumption because of induced leakage currents.
- Increase in dark current due to voltage threshold shifts and interface states after TID, and to lattice defects after DD.
- Decrease in sensitivity.
- Charge transfer efficiency degradation, only in CCDs.
- Other parameters affected: Read noise, random telegraph signal, and hot pixels.

Effects of radiation on CISs will be covered in more detail in Chapter 6.

2.3.3 Mitigation and testing

Several methods and techniques help to either protect components against radiation, or to heal them from previous radiation damage. The simplest approach is to shield the component with a material of certain thickness that blocks or attenuates the incident radiation. Appropriate shielding would allow using commercial or soft devices on environments they were not designed for. Holmes and Adams (2002), in Chapter 11, provide a detailed discussion about shielding. The second alternative consists of either designing the component to be radiation hard, which involves employing a set of preventing techniques and special manufacturing processes, or applying high level protection measures, such as redundancy. Velazco et al. (2007), in Chapter 7, review hardening methodologies for ASICs, and in Chapter 8 cover the fault tolerance of programmable circuits. Finally, the last strategy, annealing, tries to heal partly-damaged devices. This method aims at removing trapped charge and defects from irradiated devices by heating them up. Annealing has effect from room to high temperatures (100 °C or more), but the effectiveness strongly depends on the specific component technology and structure. Holmes and Adams (2002), in Section 4.6, analyze the impact of annealing in MOS devices.

Subjecting space components to the radiation conditions they are expected to encounter during their mission is mandatory to guarantee survivability. These radiation tests shall be performed for every manufacturing lot because radiation tolerance is sensitive not only to technology and design, but also to process variations. The testing procedure for each of the possible radiation effects requires the following basic steps:

1. Select ground radiation sources to properly emulate the space environment.
2. Define irradiation conditions (dose/fluence, rate/flux, energy, temperature, biasing, etc.).
3. Identify critical component parameters to be monitored.
4. Pre-measure, measure during irradiation, and post-measure critical parameters.
5. Anneal the devices to both, compensate for high rate irradiation and check for post-recovering.
6. Data analysis and results.

Guidelines and basic specifications are available regarding the definition and plan of radiation tests (ESCC22900 2007; ESCC25000 2002). Additionally, literature provides reviews of testing alternatives and procedures (Velazco et al. 2007, Ch. 10; Holmes and Adams 2002, Ch. 13).

2.4 Field Programmable Gate Arrays

FPGAs are silicon devices that designers can configure to implement custom digital circuits. They allow parallel performing of basic and complex functions, and regularly provide re-programmability. The first commercial version of these devices appeared in 1984 (Carter et al. 1986), and filled the gap between very simple programmable devices, such as programmable logic arrays (PLAs), and fully customizable circuits (ASICs). Nowadays, FPGAs are one of the most used technology for high demanding applications aiming at small volumes, as well as for prototyping of large productions.

Any application requiring a digital system finds a wide range of available technologies that may fulfill its needs. They include custom software running on multi-purpose hardware, custom hardware, and custom software running on a custom hardware platform. Multi-purpose hardware with custom software, such as μ processors or μ controllers, allows fast development of user applications, and offers high flexibility to change the user design. On the other hand, the hardware architecture cannot be optimized and performance is limited because only a limited number of tasks are executed at a time, usually one for single core architectures. Some specific-purpose processors, for example digital signal processors (DSPs), are optimized to improve their performance in particular applications. On its part, custom hardware comprises application-specific integrated circuits (ASICs) and programmable logic devices (PLDs). The first ones can be fully customized, which allows optimizing performance and minimizing power consumption. Moreover, they can combine analog and digital circuitry. However, ASIC design demands a high effort, thus a

Table 2.6. Comparison of digital technologies: ASIC, FPGA, and generic processor. Custom refers to the level of customization allowed on the design, whereas flexible indicates how easy is to change the design or functionality on late stages. Cost is evaluated for small volumes.

	Strengths	Weaknesses
ASIC	fully custom high performance low power	design effort non-flexibility high cost
FPGA	flexibility half custom cost	power limited resources
μ Processor	low design effort high flexibility cost	fixed architecture lower performance power

long development time, incurs high manufacturing costs, and does not provide flexibility after being manufactured. This technology is only justified when very high performance is required, or large production volumes are aimed. PLDs show some degree of customization on a pre-manufactured architecture. FPGAs are the most complex PLD. They provide a trade-off between flexibility and performance, and offer customization at the expense of a higher power consumption and limited resources. On average, an ASIC can be 40 times smaller than a typical FPGA, and can run 3.2 times faster while consuming 12 times less dynamic power (Kuon and Rose 2007; Kuon et al. 2008, Ch. 7). Finally, custom hardware can embed processors, which add the flexibility of executing time critical tasks on hardware, while the rest run on software. Embedded architectures implemented using FPGA configurable logic (soft-processors) perform behind those implemented in ASICs, or pre-manufactured on the FPGA (Wong et al. 2011). Table 2.6 summarizes the advantages and disadvantages of using FPGAs instead of ASICs or generic processing units.

As programmable devices, FPGAs consist of well-arranged sets of blocks that can be interconnected to form circuits (Fig. 2.9). The peripheral area of the array contains interface blocks connected to user pins, which can be configured as inputs or outputs. Logic blocks accommodate the basic components to implement almost any digital circuitry: look-up tables (LUTs), multiplexers, and flip-flops (FFs). Special blocks are dedicated subcomponents that may hold internal memory, logic for arithmetic functions, embedded processors, clock management resources, etc. All these three basic parts are interconnected via a flexible routing network that covers the complete array. The routing interconnections are configured via switch cells. Those cells allow combining logic, special, and input/output blocks to implement the designer desired functions. Since any block operates independently, FPGA designs can be highly parallelized. The specific implementation of the blocks, distribution, and number vary among manufacturers and particular devices.

Attending to the technology of the configurable switch cells, FPGAs classify as antifuse, SRAM, or flash (Table 2.7). Antifuse devices are one-time programmable (OTP) because switch cells are fuses that after being programmed become permanent connections. This fact eliminates one of the main advantages of FPGAs: flexibility. However,

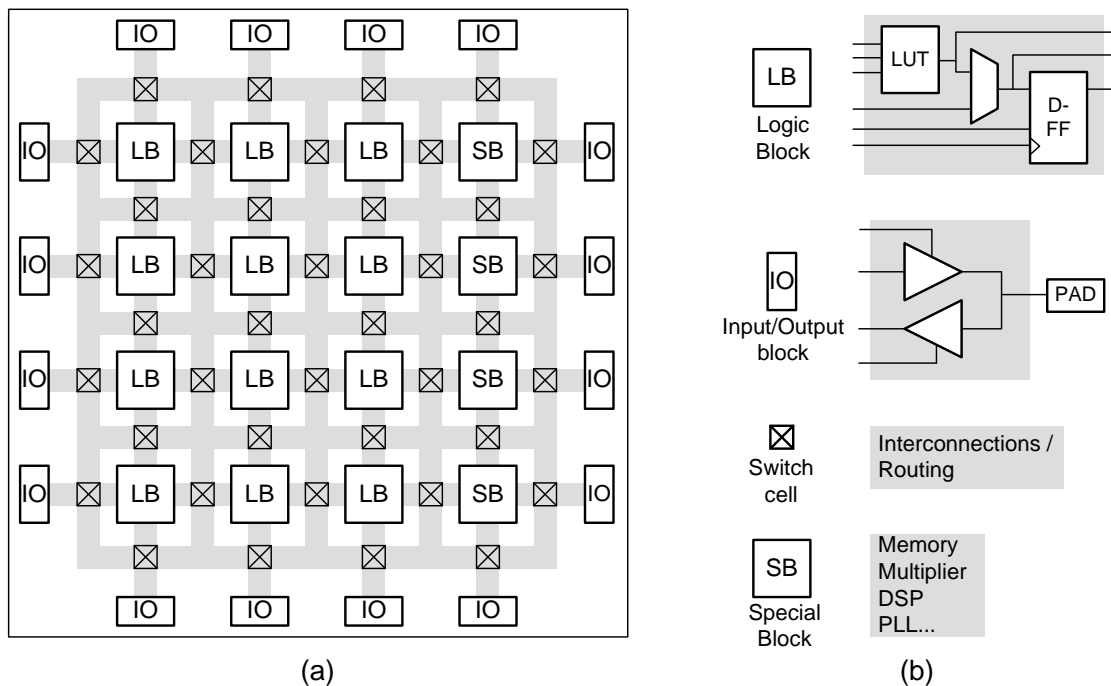


Figure 2.9. Basic FPGA architecture (a) and main blocks (b). Drawing based on Kuon et al. (2008).

permanent switches enhance the design performance, provide low impedance inter-block connections, reduce size and power consumption, and make the configuration cells immune to radiation. SRAM parts can be re-configured an unlimited number of times because the switch cells are values stored on a volatile configuration memory. Furthermore, the programming voltage is the same than the chip operating one. On the down side, the design must be loaded into the configuration memory every time the FPGA is turned on, and the size of the switches is large. Power consumption is higher than for antifuse, partly due to the switches resistance, and radiation tolerance is lower. In particular, their switches show the same tolerance against TID than standard CMOS circuits, and are susceptible to single event upsets as the SRAM memories are. This susceptibility requires the use of counter-measures, such as scrubbing, which will be explained later in this section. Finally, the use of flash memory to store the configuration data provides a limited re-programmability (about 1000 times) combined with non-volatile cells. The size of the configuration cells lies between the SRAM and antifuse ones, and the radiation tolerance is the lowest with respect to TID, and better than SRAM regarding single event upsets. Detailed discussions on FPGA types can be found elsewhere (e.g., Kuon et al. 2008, Ch. 3; Maxfield 2004, Ch. 2).

A set of specification and performance parameters permits to compare the vast variety of field programmable gate arrays available on the market (Table 2.8). The specifications refer to the number and characteristics of the main blocks, and to the number of equivalent ASIC gates of the available logic resources. Moreover, the speed grade indicates how fast a device of the same family is. Propagation and routing delays, together with power consumption define the primary performance of the device.

Current FPGAs tend to embed faster transceivers, more powerful processing archi-

Table 2.7. FPGA types based on programming technology. Radiation tolerance refers to configuration switches, not to user logic. *Require user measures to reduce SEU sensitivity.

	Antifuse	SRAM	Flash
Reprogrammable	No	Yes	Yes
Reconfiguration	N/A	Fast Unlimited	Slow Limited
Programming voltage	High	V _{cc}	High
Volatile	No	Yes	No
Switch resistance (Ω)	20-100	500-1000	500-1000
Switch capacitance (fF)	<1	1-2	1-2
Process	Special	Standard CMOS	Flash
Radiation tol. (TID)	Immune	High	Low
Radiation tol. (SEU)	Immune	Low*	Medium*
Size (switch cell)	Small	Large	Medium
Power consumption	Low	Medium	Medium

Table 2.8. Main specifications and performance parameters for FPGAs. Environmental conditions and other manufacturing parameters, such as the process size, are also relevant.

Specification	
Number of logic blocks	Amount, organization and composition of the logic blocks. It defines the capacity of the FPGA
Number of gates	From the previous specification, one can calculate an equivalent number of ASIC gates
Internal memory	Organization, capacity and maximum operating frequency of the available memory
Special blocks	They can include PLLs, multipliers, DSPs, high-speed transceivers, embedded processors, etc.
Number of IOs	Amount of user available input/outputs
IO technologies	Supported IOs: voltage, single-ended/differential, etc.
Speed grade	It classifies the devices with respect to speed
Performance	
Propagation delays	Includes propagation of combinatorial components, as well as timing of flip-flops
Routing timing	Delays associated to routing resources
Power consumption	Includes static (stand-by) and dynamic consumption

tures, and even analog interface modules (Microsemi SF datasheet 2012). Furthermore, the amount of logic cells and internal memory continue growing to overcome the technology-inherent limitation of resources. The process size follows the general miniaturization trend (see Kuon et al. (2008), Section 8.1, for a discussion on miniaturization).

In general, FPGAs are susceptible to total ionizing dose and single event effects. As summarized in Table 2.7, the tolerance of the switch cells highly depends on the device type, with some technologies being immune. Contrarily, logic and other blocks are to some extent susceptible to radiation, independently of the array type. TID causes long term degradation and mainly affects power consumption and propagation delays. Furthermore, transition times, input thresholds, output levels, and duty cycles can be affected (Wang 2003; Kastensmidt et al. 2011). State-of-the-art space FPGAs withstand, with minor degradation, TID doses up to 300 krad(Si) for antifuse and SRAM types (Huang and Wang 2012; Xilinx 2010), and up to 40 krad(Si) for flash devices (Microsemi 2010). Probability of single event latch-ups in modern FPGAs is very low because smaller processes and isolation techniques provide LET_{th} above $100 \text{ MeV} \cdot \text{cm}^2/\text{mg}$. In opposition, SEUs and SETs represent the most significant threat to modern FPGAs. Single event upsets modify the design configuration if they occur in SRAM and flash switch cells, and can alter flip-flop values in the logic cells of any FPGA type, as well as bits stored in embedded memories. These upsets can lead to complete malfunctioning of the design, thus to critical system failures. On its part, single event transients become upsets if the induced pulse width is long enough as to be latched by a FF. Since operating frequencies tend to increase in recent designs, shorter glitches provoke SEUs (Rezgui et al. 2009; Manuzzato 2009, Ch. 4). Moreover, SETs taking place in clock networks may induce additional edges on clocks, thus making all FFs triggered by those clocks change their registered values (Wang 2003, Section B.3).

Mitigating SEU and SET radiation effects requires the use of appropriate techniques at design level. The most common methods follow:

- Scrubbing is used in SRAM and flash FPGAs to prevent, or minimize, the effects of upsets in switch cells. It consists of keeping a safe copy of all configuration cells, and periodically updating the cells states. Consequently, any induced upset error presents a limited life-time given by the scrubbing period. If this period is high enough, upset rate can be minimized. The disadvantage of this technique lies on the necessity of a controller to carry out the scrubbing process.
- Triple modular redundancy (TMR) protects registers on logic blocks against upsets via triplicating them and adding a majority voter that compares their outputs. If an upset occurs in one of the registers, the voter will still resolve that the correct value is the one given by the unaffected registers. The main drawback of this technique is the additional area required for its implementation. Some FPGAs, mainly antifuse ones, include triplicated FFs in the pre-manufactured array, before user design. The concept can be extended to triplicate complete logic blocks (global TMR). In that case, the system would also be protected against SETs in the combinatorial logic. However, the area penalty and complexity grow significantly.
- Temporal redundancy allows filtering transient glitches (SETs) by way of replicating logic FFs and clocking them with progressively delayed versions of the main

clock. Therefore, a pulse of width w could be induced and propagated to the FF clocked at t_0 , but will not be propagated into a FF clocked by a delayed $t_0 + \Delta t$ clock if $\Delta t > w$. This technique increases the area utilization of the FPGA and reduces the maximum operating frequency.

- Error detection and correction (EDAC) algorithms, such as bit parity or checksums, guarantee integrity of data stored in memory cells. They require extra memory bits to store the detection and correction codes.
- Finite state machines (FSM) implement sequential logic circuits. Each state is encoded as a bit pattern, with one state being active at a time. An upset may change the bit pattern of the active state and permit another valid state to be selected, thus provoking a failure. A proper state encoding, such as *one-hot*, forces the FSM to move into an illegal state if a single bit is upset. Therefore, it facilitates failures detection and prevents malfunctioning. Safe codifications require more resources to be implemented.

Details on these techniques can be found in several bibliographic sources, e.g., ESCC-HB 2011, Ch. 10,12; Velazco et al. 2007, Ch. 7; Stettler et al. 2004; Fernández-León et al. 2002.

3 Requirements of the camera

As one of the key subunits, the scientific cameras play a major role in the accomplishment of instrument and mission goals. In consequence, every camera requirement shall harmonize with both mission and instrument.

This chapter starts by presenting the Solar Orbiter mission and identifying the set of requirements it imposes upon the PHI instrument, and specifically upon its cameras. Next, the PHI instrument is introduced along with its top-level specifications. Starting from these specifications, the impact of the main camera parameters on the instrument performance follows. Furthermore, a series of approaches to synchronize the camera with the rest of the instrument are proposed and analyzed. As a result, in Section 3.4.4 we recommend a set of desired parameters and an optimum synchronization strategy. Finally, both mission and instrument driven camera requirements are summarized.

The author original contributions to this chapter emanate from Sections 3.4 and 3.5, where goals (g1) and (g2) of the thesis and major contribution (c1) are covered (see Section 1.1).

3.1 The Solar Orbiter mission

The heliosphere is the extended atmosphere of the Sun, being the region of space through which the solar wind¹ extends and through which the Sun exerts a magnetic influence. It covers space reaching well beyond the orbits of the solar system planets. Solar Orbiter is a joint ESA-NASA mission which aims at exploring the Sun and the heliosphere. It consists of a spacecraft orbiting the Sun from the inner-heliosphere, passing closer to the star than any previous space probe. Three main features characterize the mission:

- The unique combination of in-situ and remote-sensing instruments
- The closest proximity to the Sun provided by the orbit, which will be less than one third the average Earth-Sun distance
- The availability of high latitude observing points that will permit observations of the solar poles

From the scientific viewpoint, the mission searches for answers to the fundamental question: *How does the solar system work?* (Bignami et al. 2005, Ch. 2). The objective is to study how the Sun creates and controls the heliosphere, relating the measurements in the heliosphere back to their origins in the Sun. The combination of in-situ

¹The solar wind is a continuous flow of charged particles ejected from the Sun into interplanetary space (Murdin 2001, *article: Solar Wind*).

and remote-sensing instruments provides the capability of simultaneously measuring solar wind properties and observing their source regions. For its part, the inner orbit allows both, the sampling of the heliospheric properties before being degraded by propagation and the accurate observation of the Sun at high and low latitudes. In particular, the mission addresses four top questions (Marsden and Müller 2011, Ch. 2):

1. *How and where do the solar wind plasma and magnetic field originate in the corona?*

The solar corona, i.e., the extended gaseous outer atmosphere of the Sun (Murdin 2001, *article: Corona*), expands and evolves into a supersonic wind that fills the solar system. The mechanism through which the solar wind is accelerated and escapes from the corona is unknown. This is partly because key features of the corona cannot be resolved from the usual distances of about 1 AU (Astronomical Unit)².

2. *How do solar transients drive heliospheric variability?*

The Sun is dynamic and thereby shows numerous types of transient phenomena. The largest transients are the coronal mass ejections (CMEs), which are vast structures of magnetic field and material that the Sun ejects at very high speeds. These phenomena influence the entire heliosphere and have an effect on Earth (power stations, satellite communications, etc.), giving rise to the concept of space weather. The propagation from the source to Earth distorts the current measurements of those transients, making unreliable their analysis and prediction.

3. *How do solar eruptions produce energetic particle radiation that fills the heliosphere?*

Solar energetic particles (SEPs) fill part of the heliosphere with ionizing radiation. These particles come from the Sun, which acts as an effective particle accelerator, and endanger onboard space units, radio communications, and commercial flights routed over polar regions. Measurements made from a distance of 1 AU do not allow discerning the turbulence properties that control the transport and scattering of particles in the inner heliosphere. Therefore, those mechanisms together with the generation one are not well understood.

4. *How does the solar dynamo work and drive connections between the Sun and the heliosphere?*

The solar magnetic field governs most of the observed effects happening on the Sun and connects its interior with interplanetary space. This magnetic field varies according to an 11-year cycle that modulates the shape of the heliosphere and influences the space weather. Though it is known that the solar dynamo generates this field, how that dynamo operates and why it produces a near periodicity in solar activity are unsolved questions. The possibility of observing solar high latitudes, which was not possible before, may bring insights into these points.

The Solar Orbiter payload includes four in-situ instruments, which are in contact with the medium they are measuring, and six remote-sensing instruments to observe physical processes on the Sun. Table 3.1 lists and classifies the onboard instrumentation.

²1 AU = 149.6 · 10⁶ km

Table 3.1. Payload of Solar Orbiter: List of In-Situ and Remote-Sensing instruments (left column), and main objectives (right column). Information taken from Marsden and Müller (2011), Ch. 4.

In-Situ instruments	
Solar Wind Analyser (SWA)	Ion and electron bulk properties of the solar wind
Energetic Particle Detector (EPD)	Composition, timing and distribution function of energetic particles
Magnetometer (MAG)	Heliospheric magnetic field with high resolution
Radio and Plasma Wave analyser (RPW)	Magnetic and electric field at high time resolution in the solar wind
Remote-Sensing instruments	
Polarimetric and Helioseismic Imager (PHI)	High resolution and full disk measurements of the photospheric magnetic field and gas flow velocity
EUV full-Sun and high-resolution Imager (EUI)	EUV image sequences of the solar atmospheric layers above the photosphere
EUV spectral Imager (SPICE)	EUV spectroscopy of the solar atmosphere and low corona
X-ray spectrometer/telescope (STIX)	Spectroscopy of solar thermal and non-thermal X-ray emission
Coronagraph (METIS)	Simultaneous images in the visible, UV and EUV of the solar corona
Heliospheric Imager (SoloHI)	Visible light scattered by solar wind electrons

The mission is scheduled to be launched in January 2017 (with March 2017 and September 2018 being the back-ups). In any of those cases, after the launch and verification steps, the mission proceeds to three main phases: Cruise, science nominal mission, and science extended mission. During the cruise phase, which lasts about 3 years, the spacecraft makes an interplanetary journey using chemical propulsion and gravity assist maneuvers (GAMs) until it reaches the nominal orbit. In particular, the cruise phase comprises four GAMs, two with Venus and two with Earth. The nominal phase provides an orbit as depicted in Fig. 3.1 (green values), with a closest distance to the Sun (perihelion) varying between 0.28 and 0.32 AU, and a furthest distance (aphelion) between 0.87 and 0.91 AU. The nominal phase achieves maximum solar latitudes of ± 25 deg. The duration of this main stage is between 3 and 4 years, containing 8 orbits of about 150 days. In the course of this phase the journey continues with two more GAMs with Venus, which lead to the extended phase. Finally, the extended phase presents an orbit as shown in Fig. 3.1 (blue values), having a similar perihelion, a closer aphelion, and higher inclinations: ± 34 deg. The final phase lasts between 2 and 3 years, which means 6 to 8 solar orbits, depending on the launch date. Consequently, the mission has a total duration of 10-11 years.

Table 3.2. Solar EM flux received by the Solar Orbiter mission and comparison with the one found at 1 AU. The total flux corresponds to the flux integrated over the full spectrum. Additionally, spectral radiative flux is given for high energies. Spectral fluxes scale equally at different distances because the spectra does not change with distance. Flare X-rays during maxima increase more than the rest of ranges.

	Average flux (W/m^2)		Maximum flux (W/m^2)	
	SO	Earth	SO	Earth
Total	3743	1366	17348	1413
Far UV (100-150 nm)	$2.1 \cdot 10^{-2}$	$7.5 \cdot 10^{-3}$	0.19	$1.5 \cdot 10^{-2}$
EUV (10-100 nm)	$5.6 \cdot 10^{-3}$	$2 \cdot 10^{-3}$	$5 \cdot 10^{-2}$	$4 \cdot 10^{-3}$
X-Rays (1-10 nm)	$1.4 \cdot 10^{-4}$	$5 \cdot 10^{-5}$	$1.25 \cdot 10^{-3}$	$1 \cdot 10^{-4}$
Flare X-Rays (0.1-1 nm)	$2.8 \cdot 10^{-4}$	$1 \cdot 10^{-4}$	$1.25 \cdot 10^{-2}$	$1 \cdot 10^{-3}$

The second radiation source is the solar wind plasma. The journey through the inner-heliosphere makes the spacecraft come into direct contact with the solar wind, thus with the plasma found there. The solar wind varies with the orbit from aphelion to perihelion as the density of the plasma decreases with the distance from the Sun. It increases from the value found at the Earth distance of 8.7 cm^{-3} to the maximum at perihelion of 110 cm^{-3} , the mission average being 24 cm^{-3} . The effects of the plasma environment are of relevant importance for in-situ instruments, which measure the solar wind properties, and for some spacecraft subsystems. However, they are not critical for the scientific camera that is subject of this study because solar wind particles cannot penetrate the surrounding material.

Finally, the main specifications for the camera result from the energetic particle radiation. Depending on their origin, these particles are solar energetic particles, galactic cosmic-ray ions, or secondarily generated radiation. High activity solar periods lead to frequent solar eruptions, such as flares or coronal mass ejections, that produce large fluxes of solar energetic particles. For their part, galactic cosmic-ray ions consist of a continuous and slow flux of particles coming from outside the Solar System, while secondary radiation is generated after interaction of other energetic particles with materials of the spacecraft. Figure 3.2 displays the total ionizing dose (TID) and non-ionizing energy loss (NIEL) expected from the energetic particles, together with the estimated fluence of protons. The shielding of the instrument subsystems varies from the minimum of 1 mm, given by the spacecraft, to 2 – 3 mm depending on the local housing. Therefore, the accumulated TID (graph a) is 150 krad(Si) at s/c level and 75 – 50 krad(Si) on the subsystems. As for the non-ionizing energy loss, graph (b) plots the equivalent fluence of 10 MeV protons that generates the same non-ionizing energy loss as the one expected for the complete mission, including protons of any energy as well as other particles. Plot (d) shows that only protons with energy higher than 20 MeV can penetrate a 2 mm Al shielding, and how the NIEL caused by those high energy protons significantly decreases with the energy. Finally, plot (c) gives the proton fluence at every energy.

Regarding single event effects produced by heavy ions, the mission imposes a minimum linear energy transfer threshold of $60 \text{ MeVcm}^2/\text{mg}$ for single event latch-ups and

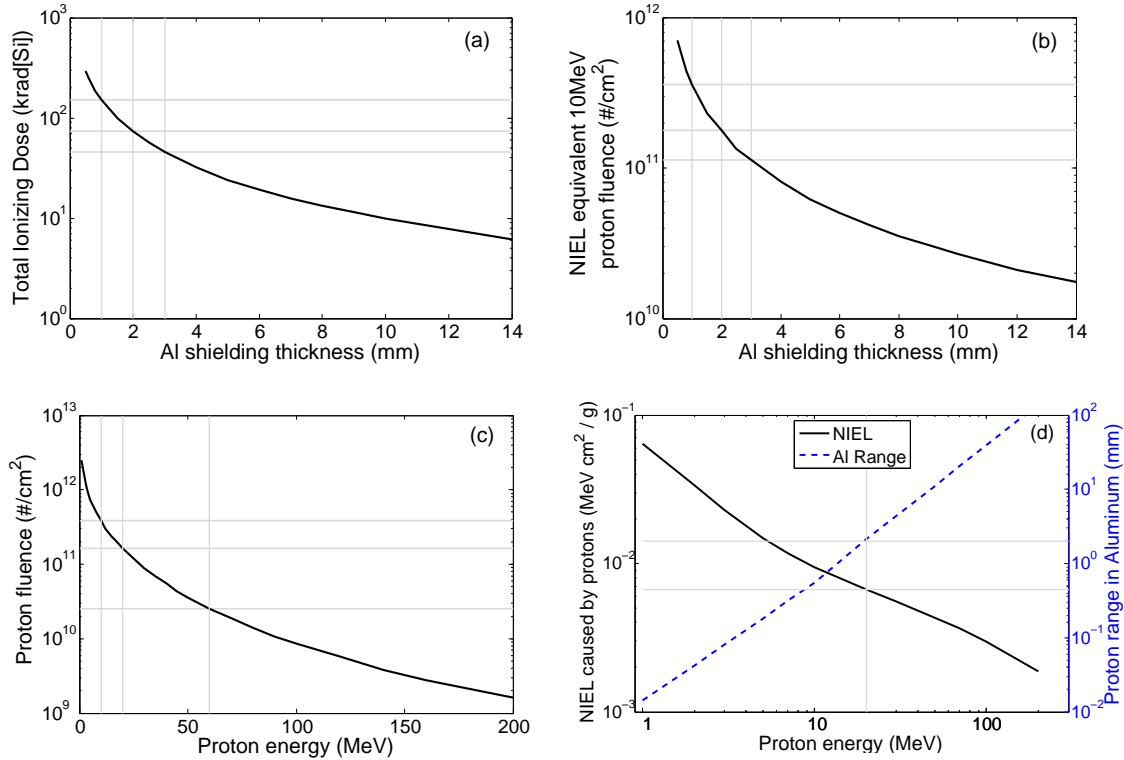


Figure 3.2. Radiation environment of Solar Orbiter: TID, NIEL, and proton fluence. Plot (a) shows the Total Ionizing Dose in silicon for the complete mission versus the thickness of the aluminum shielding. Gray lines highlight the dose at 1, 2, and 3 mm of shielding. Plot (b) represents, as a function of the shielding, the equivalent 10 MeV proton fluence required to generate the same Non-Ionizing Energy Loss that the total one received during the mission. Graph (c) shows the mission proton fluence spectrum. Fluences at 10, 20, and 60 MeV energies are emphasized. Finally, graph (d) shows the NIEL caused only by protons as a function of the proton energy, and the range of protons in Aluminum (right axis). 20 MeV energy is marked as being the minimum energy that can penetrate 2 mm Aluminum.

another minimum of 25 MeVcm²/mg for single event upsets.

3.2.2 Thermal and vacuum

The temperature range the spacecraft will experience during the mission mainly depends on its orbital position. Therefore, there are two extreme cases, which correspond to the perihelion and aphelion points. The former provides the closest distance to the Sun, known as the hot case, and the latter the furthest distance, representing the cold case. Apart from the mission's thermal environment, the instrument design and power dissipation play an important role in the operating temperatures of its subsystems. Critical components, such as the image sensor, require dedicated thermal interfaces, or cold fingers, that supply them with stable temperatures within the orbit. For the camera under study, thermal simulations (Fernández and Pérez 2012) give the results presented in Table 3.3. The sensor temperature is stable at every case whereas the electronics temperature varies within a range.

Table 3.3. Thermal and vacuum requirements for the camera electronics and the image sensor.

	Temperature ($^{\circ}C$)		Pressure (Pa)	
	Cold case	Hot case	Min	Max
Sensor	-23	-5	10^{-5}	10^5
Electronics	19 – 27	70 – 75		

In addition to the thermal requirements, Table 3.3 shows the pressure range that any onboard component must withstand. This range covers from the atmospheric pressure found before launch to the high vacuum in orbit. Moreover, the cleanliness requirements impose an outgassing demand to any material employed inside the spacecraft. Specifically, the percentage of volatile material that becomes collected by condensation (CVCM) must be lower than 0.1 %.

3.3 The PHI instrument

The success of the mission highly depends on the performance of its instrumental payload, which yields the entire scientific outcome. The remote-sensing Polarimetric and Helioseismic Imager is, conceptually, an imaging spectro-polarimeter. Attending to its scientific purpose, PHI measures vector magnetic fields and gas flow velocities in the deepest layer of the solar atmosphere: the photosphere³. The first measurement defines the instrument as a photospheric magnetograph, whereas the second allows the use of helioseismology⁴ to derive properties of the solar interior. These observables combined with other onboard-instruments' measurements at the higher atmosphere and heliosphere provide information to understand the aimed phenomena from their origins. The magnetic field at the solar surface creates most of the structures and transient events in the upper atmosphere, which in turn affects the heliosphere. Therefore, PHI will provide crucial information to answer the mission's four top science questions (Gandorfer et al. 2011). From the instrumental viewpoint, PHI embraces three functions:

- Diffraction limited imaging in the visible range
- Wavelength tuning within a selected spectral line
- Polarization sensitivity

The instrument design comprises two main units: optics and electronics; their block diagrams are shown in Fig. 3.3. The optics unit collects the incoming solar radiation, selects its desired wavelength and polarization states, and converts it into digital images. For its part, the electronics unit commands and supplies with power every subsystem,

³Layer of hundred kilometers thickness, ranging from the low atmosphere to the solar surface, where the gas changes from almost transparent to completely opaque below the surface. It is the solar layer that one observes in visible light (Stix 2002, Ch. 4).

⁴The study of the internal structure of the Sun through the analysis of solar oscillations, which are detected as small Doppler shifts in spectral lines emitted by the solar surface (Murdin 2001, *article: Helioseismology*)

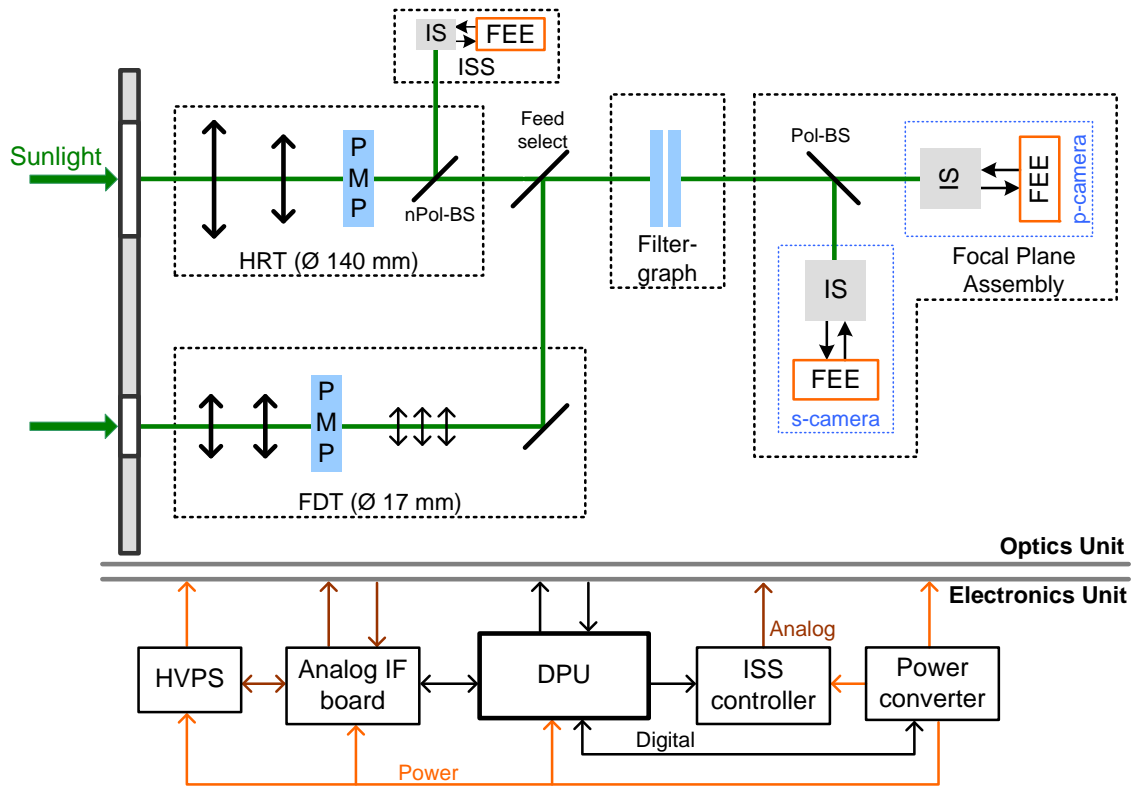


Figure 3.3. Overview of the PHI instrument: functional block diagram.

monitors the health status of the instrument, processes the retrieved image data, and communicates with the spacecraft. PHI includes two telescopes that operate in turns depending on the observing program. The high resolution telescope (HRT) allows high spatial resolution over a restricted field of view, whereas the full disk telescope (FDT) permits observing the whole solar disk but with limited spatial resolution. Each telescope, apart from mirrors and lenses, incorporates a pre-filter and a polarization modulation package (PMP), which selects a given polarization state of the collected light. The PMPs comprise two liquid crystal variable retarders (LCVRs) with an angle shift of 45° between each other, and a linear polarizer aligned with the first retarder. Next, the filtergraph tunes the desired wavelength position by high-voltage tuning of a Fabry-Pérot etalon. The focal plane assembly (FPA) holds two identical cameras that receive orthogonal beams, p- and s-polarized, extracted by the polarizing beam-splitter. An image sensor and a front-end electronics form each of the two identical cameras. These cameras are the major subject of this work. Additionally, an image stabilization system (ISS), including a third camera, guarantees stability against spacecraft vibrations. On the electronics unit side, the DPU is in charge of all the digital controlling and processing tasks, while the power converter module generates the individual low voltage supplies. A high voltage power supply (HVPS) covers the high voltage needs of the filtergraph, the analog board digitizes analog housekeepings, and the ISS controller drives the tip-tilt mirrors (not detailed in Fig. 3.3) for jitter corrections.

A set of top-level performance specifications establishes the frame to define the requirements of every subsystem. Table 3.4 lists these main specifications. The field of

Table 3.4. Performance specifications of PHI.

Parameter	Symbol	Unit	Value
Field of view (HRT)	$\alpha_{\text{FOV,HR}}$	arcmin	17
Field of view (FDT)	$\alpha_{\text{FOV,FD}}$	arcmin	120
Spatial resolution (HRT)	α_{HR}	arcsec	0.99
Spatial resolution (FDT)	α_{FD}	arcsec	3.51
Image sensor format	$N_{\text{row}} \times N_{\text{col}}$	pixels	2048×2048
Nominal wavelength	λ_0	nm	617.3341
Filter bandwidth	$\Delta\lambda$	pm	10
Spectral points	N_λ	-	6
Polarimetric SNR	$\text{SNR}(I^c)$	-	$> 10^3$
Pol. points	N_P	-	4
Pol. efficiency	$\vec{\varepsilon}$	-	$\varepsilon_1 = 1.0$ $\varepsilon_{2,3,4} > 0.45$
Cadence (Cycle)	T_{cycle}	s	< 60

views and aperture diameters describe the main telescopes properties. The nominal wavelength, bandwidth, and spectral points fix the instrument to the red part of the visible spectrum (Fe I absorption line at 617.3 nm), being quasi-monochromatic and having six possible wavelength positions. Five of the six wavelength points lie within the absorption line, whereas one, the so-called continuum, is outside the line profile. The polarizers shall select four polarization states with an objective signal-to-noise ratio and efficiencies as defined. Section 3.4 will discuss these two parameters in detail. Lastly, the cadence or cycle time of the instrument shall be lower than 1 min. A cycle is the time the instrument takes to acquire images at N_λ spectral positions and N_P polarization states with $\text{SNR}(I^c)$ and efficiencies higher than the values specified in the table, thus producing a complete set of magnetic field and flow velocity maps. $\text{SNR}(I^c)$ is the signal to noise ratio of the intensity Stokes parameter in the continuum. The given specifications define the most demanding observing mode, which imposes the hardest constraints on the subsystems. However, the instrument may also use simpler modes where some specifications are relaxed. For instance, the number of spectral points or polarization states can be reduced.

The sequence of steps PHI takes to measure magnetic fields and flow velocities based on the observed photons is depicted, for one cycle, in Fig. 3.4. The light collected by the telescope, $S(p, \lambda)$ in photons, enters the polarization package with unknown polarization state and spectral composition (p, λ) . After having passed the polarizers and the filtergraph in the iteration $\{i, j\}$, the signal has a given polarization state and wavelength component $S(P_i, \lambda_j)$ at the entrance of the polarizing beam-splitter. The splitter generates then two orthogonally polarized signals $S_P(P_i, \lambda_j)$ and $S_S(P_i, \lambda_j)$ that feed the P and S cameras, respectively. Each camera converts the input signal into two dimensional digital images, $I_P(P_i, \lambda_j, k)$ and $I_S(P_i, \lambda_j, k)$, k being the image index in a sequence. In order to

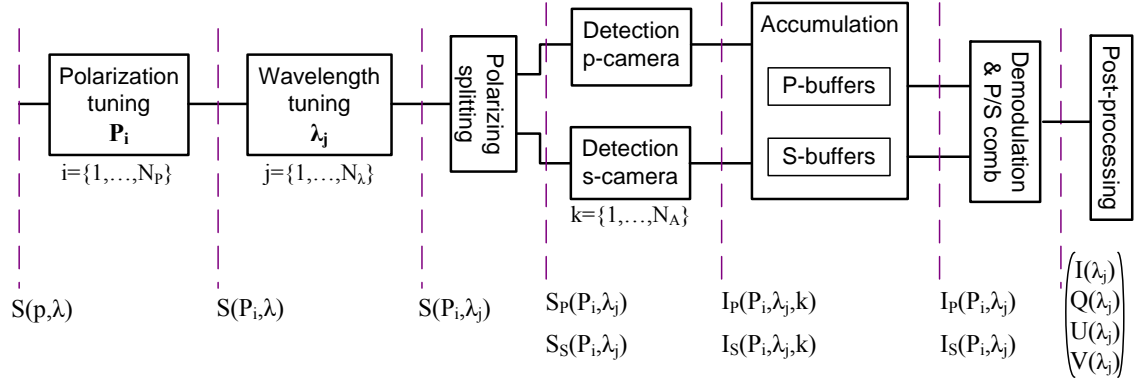


Figure 3.4. Operation flowchart of PHI: from photons to magnetic fields and flow velocities.

reach the required polarimetric signal to noise ratio, a single image per polarization and wavelength is not enough. Thus, each camera acquires N_A frames that are accumulated in a set of buffers in the following step to increase the SNR. Inputs and outputs of the accumulation block are related as

$$\begin{aligned} I_P(P_i, \lambda_j) &= \sum_{k=1}^{N_A} I_P(P_i, \lambda_j, k) \\ I_S(P_i, \lambda_j) &= \sum_{k=1}^{N_A} I_S(P_i, \lambda_j, k). \end{aligned} \quad (3.1)$$

After the accumulation of the N_P polarization states at a given wavelength λ_j , the images for each channel, $I_P(P_i, \lambda_j)$ and $I_S(P_i, \lambda_j)$, are demodulated pixel by pixel to derive the Stokes parameters, following

$$\begin{pmatrix} I(\lambda_j) \\ Q(\lambda_j) \\ U(\lambda_j) \\ V(\lambda_j) \end{pmatrix}_P = \mathbf{D}_P \cdot \begin{pmatrix} I_P(P_1, \lambda_j) \\ I_P(P_2, \lambda_j) \\ I_P(P_3, \lambda_j) \\ I_P(P_4, \lambda_j) \end{pmatrix} \quad (3.2)$$

and

$$\begin{pmatrix} I(\lambda_j) \\ Q(\lambda_j) \\ U(\lambda_j) \\ V(\lambda_j) \end{pmatrix}_S = \mathbf{D}_S \cdot \begin{pmatrix} I_S(P_1, \lambda_j) \\ I_S(P_2, \lambda_j) \\ I_S(P_3, \lambda_j) \\ I_S(P_4, \lambda_j) \end{pmatrix}, \quad (3.3)$$

where \mathbf{D}_P and \mathbf{D}_S are the demodulation matrices. Provided that the two channels, p- and s-, are exactly the same but see orthogonally polarized beams, the demodulation matrices fulfill

$$\begin{aligned} D_{S,li} &= D_{P,li} \\ D_{S,ni} &= -D_{P,ni}, \end{aligned} \quad (3.4)$$

being $n = \{2, 3, 4\}$ and $i = \{1, 2, 3, 4\}$ the components $\{n, i\}$ of the demodulation matrices. The dual channel demodulation is then combined to increase the signal to noise ratio and to suppress spurious signals as

$$\begin{pmatrix} I(\lambda_j) \\ Q(\lambda_j) \\ U(\lambda_j) \\ V(\lambda_j) \end{pmatrix} = \begin{pmatrix} I(\lambda_j) \\ Q(\lambda_j) \\ U(\lambda_j) \\ V(\lambda_j) \end{pmatrix}_P + \begin{pmatrix} I(\lambda_j) \\ Q(\lambda_j) \\ U(\lambda_j) \\ V(\lambda_j) \end{pmatrix}_S. \quad (3.5)$$

Once this flowchart iterates over the N_λ wavelength points, the post-processing step calculates the vector magnetic field and flow line-of-sight velocity $\{\vec{B}, v_{\text{LOS}}\}$.

3.4 Instrument driven camera requirements

The cameras, together with filtergraph and polarization packages, constitute the core of the instrument optics unit. The performance of PHI, which is primarily measured as the polarimetric SNR, polarization efficiency, and cadence, is thus directly affected by the properties and mode of operation of those components. This section meticulously reviews how PHI operates, assesses the influence of the cameras characteristics on the overall performance, and proposes several solutions for the synchronization of filtergraph, polarization packages, and cameras. Finally, a definition of the cameras requirements and an optimum synchronization strategy for the instrument are reached.

The analysis in this section takes into account the most stringent case. Among the variety of observing modes and configurations PHI offers, the one using the high resolution telescope operating as a vector magnetograph (four polarization states) with six spectral positions is the most demanding. Firstly, because the high resolution requires resolving smaller solar features that cross the field of view in shorter times. Secondly, more polarization states and wavelength positions need a faster system to reach the same total cadence.

Since the images taken with the s- and p- cameras are added or subtracted after demodulation (see Section 3.3), the difference between them shall come from the separate polarization components, and not from disparities of their behavior. Therefore, the same set of requirements applies to both cameras.

3.4.1 Photon budget

The photon budget plays a major role in evaluating the PHI performance. Every component inside the instrument contributes to it by its operation on the signal. The combination of all these operations relates the achieved polarimetric SNR to the properties of every subunit. One can then compare the obtained SNR to the PHI requirement and study how the camera parameters influence this top-level specification. At the same time, the analysis can include timing information, allowing an additional comparison with the cadence requirement.

The first step to calculate the photon budget is to quantify the signal coming from the target, in this case the Sun. It is known (Stix 2002, pp. 9-10) that our star irradiates in the visible range with an energy flux that approximates the one of a black-body with an

effective temperature $T_{\text{eff}} = 5778$ K. Since the nominal wavelength of PHI, λ_0 , is known (Table 3.4), the mean solar photon flux per unit time, area, wavelength interval, and solid angle follows

$$N_{\odot}(\lambda_0, T_{\text{eff}}) = \frac{2c}{\lambda_0^4} \frac{1}{e^{\frac{hc}{\lambda_0 k_B T_{\text{eff}}}} - 1}, \quad (3.6)$$

where k_B is the Boltzmann constant, h the Planck constant, and c the speed of light in vacuum. Thus, $N_{\odot}(\lambda_0 = 617.3 \text{ nm}, T_{\text{eff}} = 5778 \text{ K}) = 7.427 \cdot 10^{17} \text{ photons} \cdot \text{s}^{-1} \text{cm}^{-2} \text{sr}^{-1} \text{\AA}^{-1}$. This photon flux corresponds to the solar radiance in the continuum, where the light is not polarized. The mean number of photons reaching a single pixel on one of the cameras is then given by

$$P^c = N_{\odot} \alpha_{\text{pixel}}^2 \Delta\lambda \frac{\pi}{4} D^2 \tau t_{\text{exp}}, \quad (3.7)$$

where

$$\alpha_{\text{pixel}}^2 = \frac{\alpha_{\text{FOV}}^2}{N_{\text{row}} N_{\text{col}}} \quad (3.8)$$

is the fraction of solar solid angle seen by a single pixel, in sr, α_{FOV} being expressed in rad. $\Delta\lambda$ is the bandwidth of the filtergraph, $\frac{\pi}{4} D^2$ the collecting area of the telescope, which does not have a central obscuration,

$$\tau = \tau_{\text{window}} \tau_{\text{mirrors}} \tau_{\text{lenses}} \tau_{\text{filtergraph}} \tau_{\text{PMP}} \tau_{\text{Pol-BB}} \tau_{\text{nPol-BB}} \quad (3.9)$$

the overall transmission of the system, and t_{exp} the exposure time.

Once the incident number of photons per pixel is known, the cameras parameters provide the information needed to infer the signal to noise ratio per pixel on a single frame as

$$\text{snr}^c = \frac{S_k^c}{\sigma_k^c}, \quad (3.10)$$

where S_k^c and σ_k^c are the signal and noise levels in the single frame k . The superscript c stands for continuum. We specify for the cameras that the digitization noise must be negligible compared to the analog noise level. Hence its contribution does not affect this calculation, snr^c , being the same if signal and noise are expressed in e^- or DN. To compute the signal level (S_k^c), one starts from the number of incident photons P^c . First, only a fraction of those incident photons interacts with the silicon of the sensor and become interacting photons which, in the visible range, generate single electron-hole pairs. Second, the sensitive area of the pixels is lower than their physical area, reducing their fill factor. Consequently, the signal in electrons is given by

$$S_k^c = P^c \cdot QE \cdot FF + D_c, \quad (3.11)$$

where QE is the quantum efficiency, which relates the number of interacting photons to the number of incident ones, and FF the fill factor, which indicates the portion of physical pixel area that is sensitive. The second contribution to the signal level is the dark current D_c , which is usually subtracted via bias correction, and therefore does not influence the

signal to noise ratio. However, it still plays a role in the prediction of the charge collected by the pixels. The noise (σ_k^c) comprises shot noise, inherent to the photon rate, and read or dark temporal noise, which encompasses all noise sources that are signal independent, such as dark shot noise, reset noise, offset fixed pattern noise, etc. Since the fixed pattern noise is not random (Janesick 2007, pp. 30-33) and can be corrected via flat-fielding, it is not included. All noise sources are independent and thus added in quadrature, resulting in

$$\sigma_k^c = \sqrt{\sigma_{\text{shot}}^2 + \sigma_{\text{read}}^2}, \quad (3.12)$$

with

$$\sigma_{\text{shot}} = \sqrt{S_k^c}. \quad (3.13)$$

Up to this point we have calculated the signal to noise ratio for a single intensity image in the continuum. From Fig. 3.4, the instrument accumulates a set of N_A images for each camera at every polarization and wavelength point. Therefore, after the accumulation and including now the dependence on polarization, signal and noise levels are

$$S_I^c(P_i) = S_k^c(P_i) \cdot N_A \quad (3.14)$$

and

$$\sigma_I^c(P_i) = \sigma_k^c(P_i) \cdot \sqrt{N_A}, \quad (3.15)$$

where the units are e^- , the subscript k identifies a single frame, and the subscript I means that this signal is a digital image. The dependence on the polarization state vanishes because the light in the continuum is unpolarized. Consequently, both channels contain the same signal and noise, being

$$\begin{aligned} S_{I_p}^c(P_i) &= S_{I_s}^c(P_i) = S_I^c \\ \sigma_{I_p}^c(P_i) &= \sigma_{I_s}^c(P_i) = \sigma_I^c. \end{aligned} \quad (3.16)$$

The next step consists of demodulating and combining both channels. From Eqs. (3.2) to (3.5), (3.14), and (3.16) the Stokes parameters follow

$$\begin{aligned} I^c &= 2 \cdot N_A \cdot S_k^c \cdot \sum_{i=1}^{N_p} D_{P,1i} = 2 \cdot N_A \cdot S_k^c \\ Q^c = U^c = V^c &= N_A \cdot \sum_{i=1}^{N_p} D_{P,ni} \cdot (S_k^c - S_k^c) = 0, \end{aligned} \quad (3.17)$$

with $n = \{2, 3, 4\}$ for Stokes $\{Q, U, V\}$, and $D_{P,1i}$ the components $\{1, i\}$ of the demodulation matrix D_P . The sum of the first row components of an ideal demodulation matrix equals one by definition (Del Toro-Iniesta 2003, Ch. 4). The noise level propagated to a generic Stokes parameter I_n , with $(I, Q, U, V)^T = (I_1, I_2, I_3, I_4)^T$, from Eq. (3.15) is

$$\sigma_{I_n}^c = \sqrt{2} \cdot \sqrt{N_A} \cdot \sigma_k^c \cdot \sum_{i=1}^{N_p} D_{P,ni}^2 = \sqrt{2} \cdot \frac{\sigma_k^c}{\epsilon_n} \cdot \sqrt{\frac{N_A}{N_p}}, \quad (3.18)$$

where $n = \{1, 2, 3, 4\}$ and ϵ_n is the polarization efficiency of the Stokes parameter I_n (see Section 2.1). Finally, the polarimetric signal to noise ratio relative to the intensity in the continuum ($I^c = I_1^c$), which is the one used to define the instrument's top requirement, can be related to the signal to noise ratio of a single image as

$$SNR(I_n^c) = \frac{I_1^c}{\sigma_{I_n^c}^c} = \sqrt{2} \cdot snr^c \cdot \epsilon_n \sqrt{N_A N_P}. \quad (3.19)$$

This definition of polarimetric signal to noise ratio is the convention normally used in solar polarimetry (Del Toro-Iniesta and Martínez-Pillet 2011; Martínez-Pillet et al. 1999). Eq. (3.19), together with the requirements in Table 3.4 for $SNR(I^c)$, ϵ_n , and N_P , leads to a direct relation between the required number of accumulations and the signal to noise ratio of a single image, which mainly depends on the camera definition. Assuming that the polarization states and wavelength transitions are ideal, i.e., without delay, and that the acquisition time of a single frame is T_{acq} , the cycle time is

$$T_{cycle} = N_A \cdot N_P \cdot N_\lambda \cdot T_{acq}. \quad (3.20)$$

This time can then be compared to the cadence requirement to impose a limit on the number of accumulations and the camera minimum frame rate.

In consequence, the photon budget formulation allows the evaluation of the instrument performance versus the camera performance and various instrument parameters. Table 3.5 shows the set of camera and instrument parameters that have been assessed, together with some initial values that will be used for optimization. Given the amount of parameters to assess, a mathematical optimization of the T_{cycle} and $SNR(I^c)$ expressions with respect to the camera parameters would lead to a tedious multi-variable problem. Moreover, the outcome might result in a camera definition that may be far from a reasonable specification. Hence, we have run a set of simulations starting from a basic camera definition, and varying each parameter at a time. Figures 3.5 to 3.7 display the influence of these variations on the number of accumulations and cadence. In all the simulations, the polarimetric signal to noise ratio has been fixed to the minimum specified value of 10^3 , having N_A been calculated to reach that target value. Besides, the polarimetric efficiencies have also been fixed to their minimum specified values. Appendix A includes a detailed specification of those components of PHI that affect these calculations. As for the readout mode of the image sensor, this analysis assumes that it can be read while exposing.

Figure 3.5 (left) shows the cadence the instrument reaches as a function of the exposure time at different frame rates. The needed number of accumulated images, and thus the total time, to achieve the required signal to noise ratio decreases as the exposure time increases because the signal to noise ratio per single image improves. However, once the full well capacity of sensor is exceeded, a point which is highlighted by a vertical line, longer exposures lead to higher noise and, theoretically, the same signal level. Consequently, the cycle time increases again for longer exposures. Furthermore, at exposures longer than the acquisition time of a frame the frame time is uniquely dominated by the exposure time and not by the frame rate. This can be seen in the curve for 20 and 50 fps above 0.05 s. As for the frame rate, a faster camera takes the set of images in a shorter time, which guarantees that the observed features do not blur or even move out of the field of view. For example, a camera running at 4 fps does not fulfill the cycle time requirement at any exposure time, whereas the rest of cases complete the cycle in less than 60 s

Table 3.5. List of camera and instrument parameters assessed by the photon budget.

Camera parameters		Start value
Frame rate	$1/T_{\text{acq}}$	4 fps
Sensitivity	$QE \cdot FF$	40 %
Full well charge	FWC	80 ke ⁻
Read noise	σ_{read}	100 e ⁻
Dark current	D_c	1000 e ⁻ /s
Exposure time	t_{exp}	
Instrument parameters		
Number of accumulations	N_A	
Cadence	T_{cycle}	
Polarimetric SNR	$SNR(I^c)$	

for a variety of exposures. Although exposures closer to the full well limit provide better performance, these cases shall be avoided because non-linearities may have a higher influence there. On the right side of the same figure the maximum full well charge of the sensor varies, while the exposure time is fixed to the values that fill up to 60 % of it. At lower frame rates the full well needs to be higher, so that every single image has a higher signal to noise ratio and thus the number of accumulations decreases. As the frame rate increases, the full well requirement relaxes because, even if many frames have to be accumulated, the camera can deliver those images in a short period. In conclusion, the camera needs to reach a trade-off between the frame rate and the full well capacity. For instance, a frame rate lower than 8 fps would require a full well charge above 100 ke⁻ to be compliant with the instrument cadence with certain margin.

Apart from the frame rate and full well capacity, the sensitivity, read noise, and dark current also have an impact on the photon budget. Assuming a frame rate of 10 fps and a full well capacity of 100 ke⁻, which lead to an acceptable performance according to Fig. 3.5, Figure 3.6 displays the cycle time versus the three aforementioned parameters. Very low sensitivities require long exposures to reach adequate signal to noise ratios on single images, which negatively affect the cycle time. Once the sensitivity is high enough to lead to high cadences, the curve becomes almost constant. This is because having fixed the frame rate and full well, a higher sensitivity allows reaching the same signal to noise ratio with shorter exposures, but cannot increase it. In addition, if the exposure time is below the acquisition time, the reduction does not decrease the cycle time. As for the read noise, it affects directly the signal to noise ratio of a single frame, increasing the required number of accumulations and thus the cycle time. Finally, the dark current shows almost no impact on the performance because it can be corrected via dark subtraction. It only increases the signal level by a factor that depends on the exposure time, and adds the dark shot noise contribution to the total noise. Since the exposure times are quite low, it can be seen that even with very high dark current levels the performance is barely degraded.

Finally, Figure 3.7 displays the cycle time and number of accumulations as a function

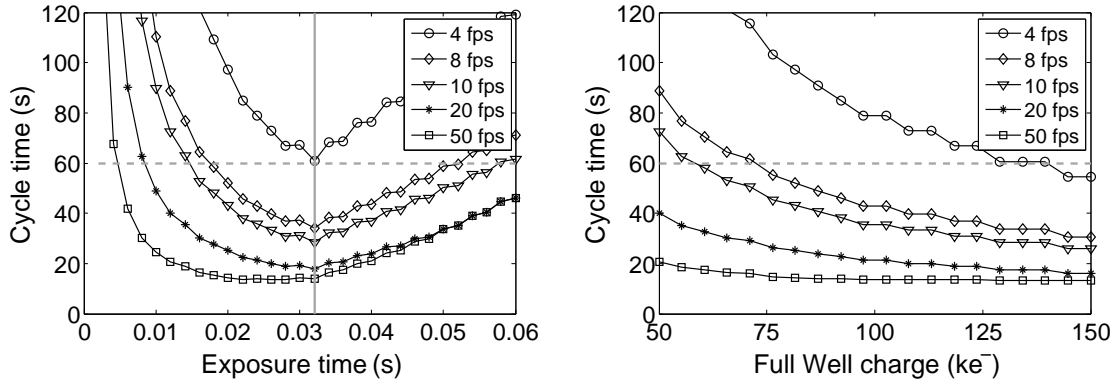


Figure 3.5. Influence of frame rate and full well charge on cycle time. Left plot shows the cycle time versus exposure at five frame rates. The vertical lighter line delimits when the full well capacity is reached and hence the sensor saturates the fixed 80 ke^- capacity. Right graph displays the cycle time versus the full well charge of the sensor for five frame rates. The horizontal dashed line is the instrument's cadence requirement. $QE \cdot FF$, σ_{read} and D_c were taken from the right column of Table 3.5, whereas the exposure time on the right side was calculated to fill 60 % of the FWC .

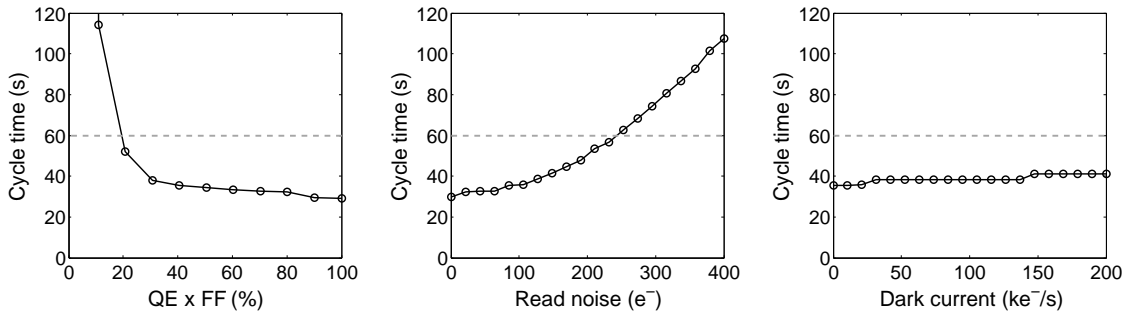


Figure 3.6. Influence of sensitivity (left), read noise (center), and dark current (right) on cycle time. The product of quantum efficiency and fill factor represents the sensitivity. The horizontal dashed line in all graphs is the instrument's cadence requirement. $FWC = 100 \text{ ke}^-$ and $1/T_{\text{acq}} = 10 \text{ fps}$ were used, whereas the exposure time follows the same criteria as in Fig. 3.5 (right).

of the exposure time for $FWC = 100 \text{ ke}^-$ and $1/T_{\text{acq}} = 10 \text{ fps}$. The optimum exposure time is highlighted as the one filling 60 % of the full well capacity. It can be seen that, in this case, $N_A = 12$ accumulations are required to give a cadence of 35.6 s.

3.4.2 Synchronization strategies

Previous section analyzed the influence of the cameras on the instrument's cadence and signal to noise ratio for an ideal case. This ideal scenario assumes that the filtergraph and PMP have zero response times, leading to a simple synchronization situation. However, the non-zero delay on the polarization and wavelength tuning creates the necessity of defining a synchronization strategy for filtergraph, PMP, and cameras. The adopted strategy has an impact on the already assessed cycle time and signal to noise ratio, as well as on the polarimetric efficiency, modulation period, and onboard memory requirements.

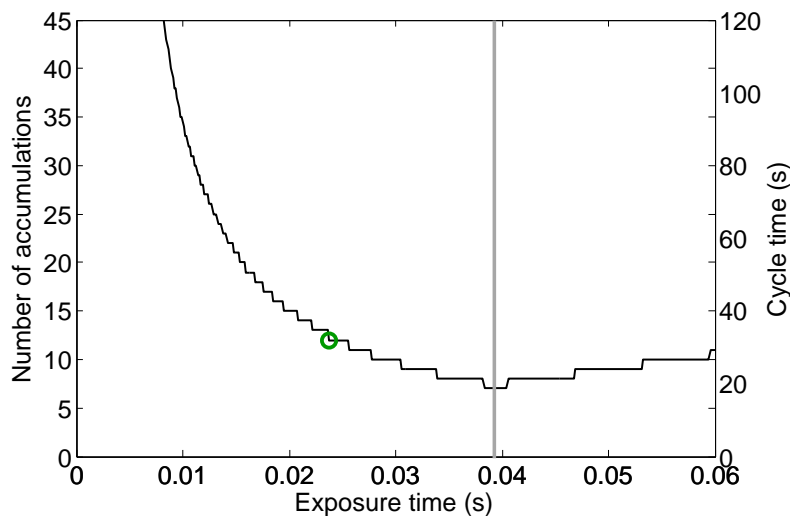


Figure 3.7. Cycle time and number of accumulations: dependence on exposure time. The circled mark shows the time at which 60 % of the FWC is filled. The initial values for sensitivity, read noise, and dark current were used, together with $FWC = 100 \text{ ke}^-$ and $1/T_{\text{acq}} = 10 \text{ fps}$. The vertical gray line indicates the saturation condition. It is located at a longer exposure time than in Figure 3.5 (left) because the FWC was smaller in that case.

This section proposes several synchronization alternatives and evaluates their effect on the overall performance.

A synchronization strategy comprises two elements: the order in which the polarization states, wavelength positions, and images are acquired to complete a cycle, which we call from now on *tuning* mode, and the scheme followed to coordinate the filtergraph and PMP transitions with the image acquisitions, which we will call *acquisition* mode. The first out of three tuning modes is the so-called *fast polarization* mode, which is represented in Fig. 3.8. In this mode one fixes first the wavelength λ and tunes over all polarization states $\{1, \dots, N_P\}$. At every polarization state, n images are acquired. This is repeated a number of times N_A/n to increase the SNR. Then one tunes the filtergraph to the next wavelength position and repeats the process. After having completed N_λ wavelength positions, a cycle is finished. The parameter n can be adjusted accordingly in the range $\{1, \dots, N_A\}$. This mode requires N_λ filtergraph transitions and $N_\lambda \cdot N_P \cdot N_A/n$ polarization changes. Therefore, it is more convenient when the PMP transitions are faster than the filtergraph ones. Since images taken at the same polarization and wavelength are accumulated, this mode requires a buffer memory with capacity for $2 \cdot N_P$ images, where the factor 2 comes from the two cameras. The next tuning mode is the *fast wavelength* mode, represented in Fig. 3.9. It is analogous to the previous one but, in this case, the wavelength positions are changed every n frames whereas the polarization states only change N_P times. In consequence, $N_\lambda \cdot N_P \cdot N_A/n$ wavelength transitions and N_P polarization transitions are needed. This mode is advantageous when the filtergraph is faster than the PMP. The *fast wavelength* mode would require a memory storing N_λ images at a time. Finally, the last tuning mode is the *intermediate* mode, depicted in Fig. 3.10. In this case one fixes the filtergraph at one wavelength and tunes the PMP over the N_P polarization states, acquiring n images at each state. When all states are covered, the filtergraph is tuned to the next wavelength and the polarization period is repeated as before. This is

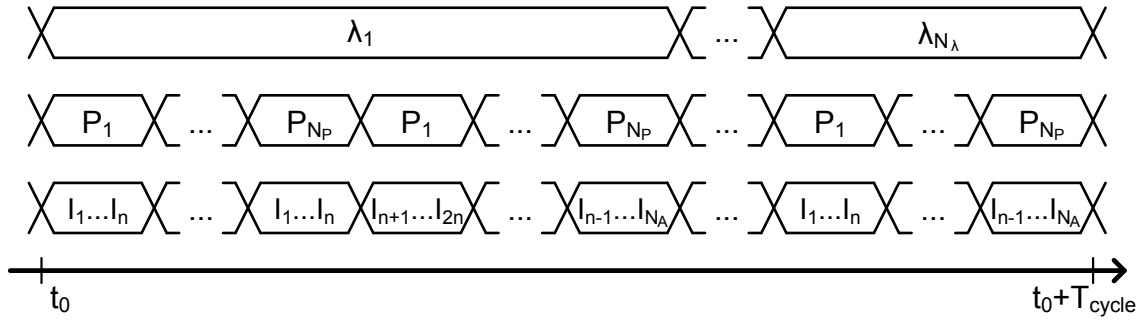


Figure 3.8. Fast polarization tuning mode: timing sketch.

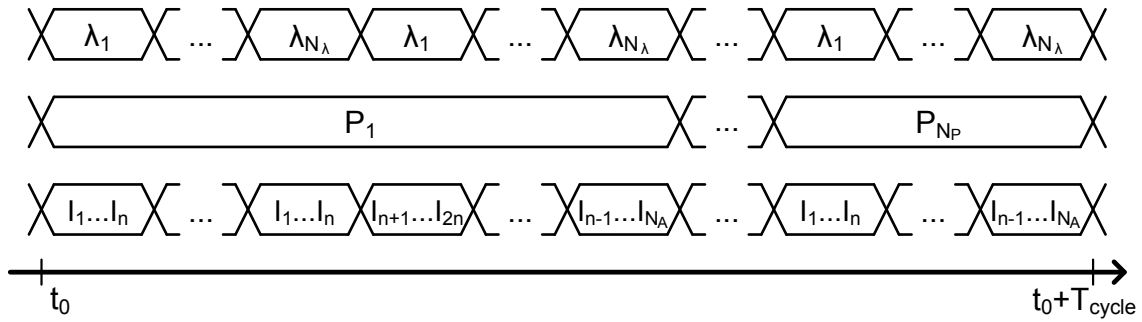


Figure 3.9. Fast wavelength tuning mode: timing sketch.

done for all wavelengths, and the whole process is repeated a number of N_A/n times to reach the desired SNR. This mode is the slowest because it requires $N_\lambda \cdot N_A/n$ wavelength transitions, and $N_P \cdot N_\lambda \cdot N_A/n$ polarization changes. The memory requirement for this mode is $N_\lambda \cdot N_P$ images, i.e., higher than in the previous modes. The advantage is that the different wavelength and polarization acquisitions are distributed more evenly over time.

Regarding the acquisition modes, Figure 3.11 depicts the three proposed options. The first row represents the filtergraph, the second the PMP, and the last three the cameras for each mode. The *continuous* mode assumes that the cameras are taking images continuously, independently of the wavelength or polarization condition. During every transition of the PMP there is one image exposed to that transition, which means that the polarimetric efficiencies are degraded. Section 3.4.3 tackles this issue. On the other hand, while the filtergraph is changing the affected images are discarded. This is the case because, in general, the filtergraph transitions are longer (see Appendix A) and the distortion they introduce seriously degrades the results. This mode turns out to be the faster when the number of wavelength transitions is small, but does not provide optimum polarimetric efficiencies. In the *triggered* mode, cameras only expose when both wavelength and polarization states are settled. Therefore there are gaps which length depends on the filtergraph and PMP's transition times. This mode provides maximum polarimetric efficiencies and avoids missing time because of frame discarding. However, the control of the cameras becomes more complex, the traffic load in the commanding link between DPU and FPA is higher, and the acquisition of frames is started and stopped regularly, which may induce small temperature and noise variations. Finally, the *discarding* mode runs the cameras continuously, but discards the images affected by both PMP and filtergraph's transitions.

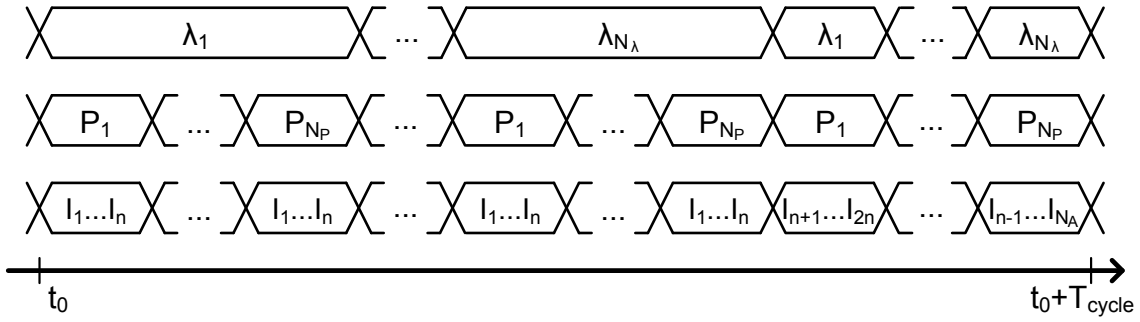


Figure 3.10. Intermediate tuning mode: timing sketch..

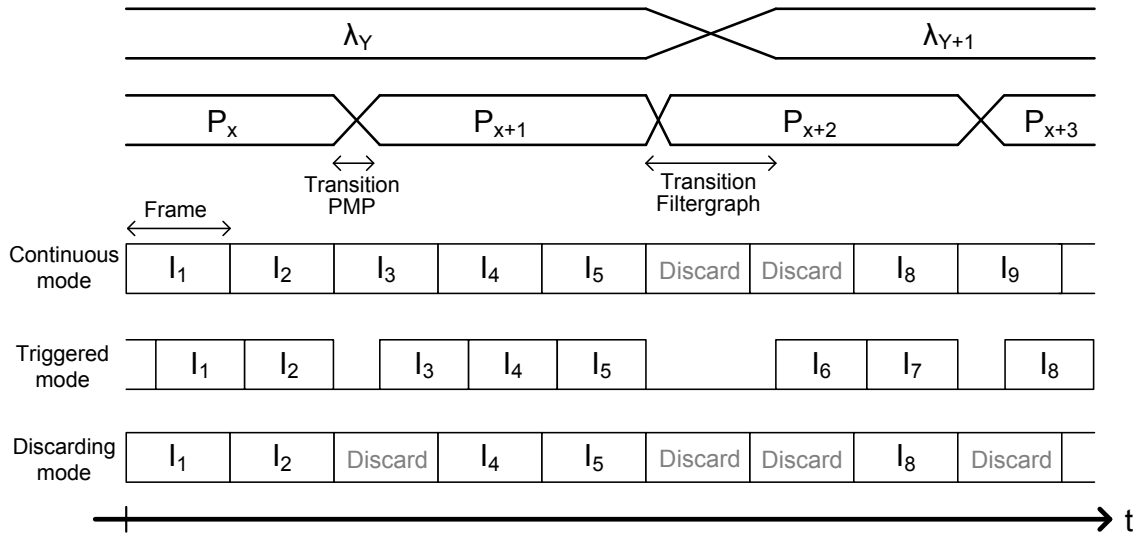


Figure 3.11. Acquisition modes. The transitions and states shown in this drawing are only for illustrative purposes, and do not follow any logic pattern.

This mode also offers optimum efficiencies, but it is the slowest one.

We analyze how the proposed tuning and acquisition modes affect the cycle time and the polarimetric modulation period, also abbreviated as modulation period. The modulation period is the time needed to complete one scan over the N_p polarization states, i.e., it is the time elapsed from the first image taken at N_1 to the first image taken at N_p . According to Feller (2011), this time must be shorter than 2 s to guarantee that the solar evolution does not introduce spurious polarimetric signal on the instrument's measurements. This effect is important only within one modulation period because even if the different modulation periods are added together, the spurious effect cancels out among periods. Figure 3.12 (left) shows the cycle time as a function of the parameter n for the ideal case and the rest of tuning modes. The values used for the filtergraph and PMP timing are described in Appendix A, and the *triggered* acquisition mode was employed. A higher value of n reduces the number of wavelength and/or polarization transitions, thus reducing the cycle time. In the ideal case, where transitions are instantaneous, this effect is almost non-existent. The *fast polarization* mode gives the best cycle times, though is only compliant with the requirement for $n > 2$. On the other side, the *fast wavelength* increases the cycle time considerably, and would require $n > 7$ to complete a cycle in less

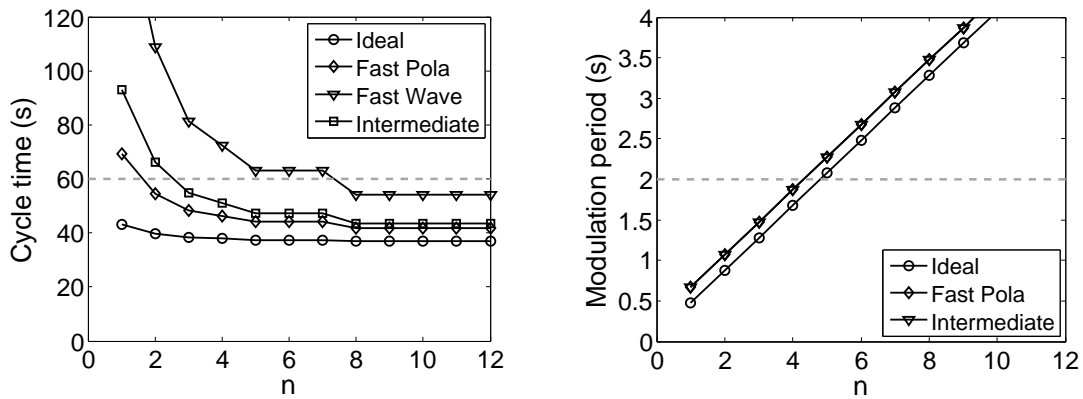


Figure 3.12. Influence of the tuning mode on the cycle time (left) and modulation period (right).

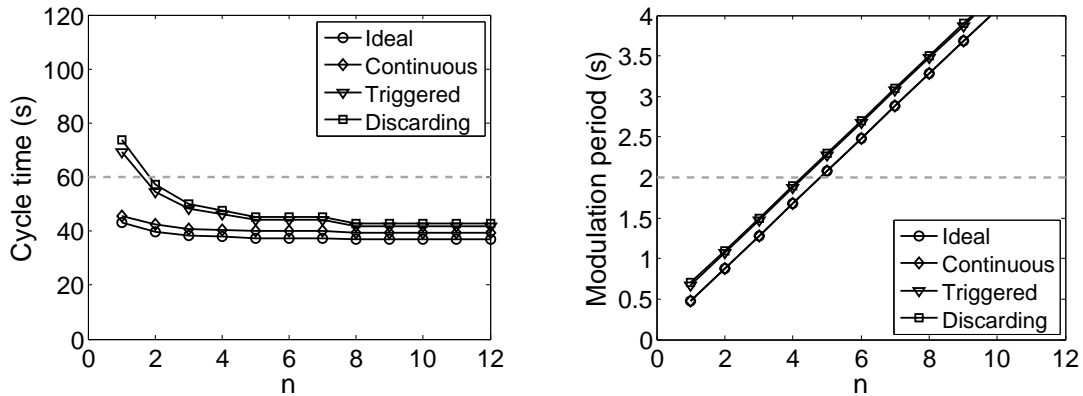


Figure 3.13. Influence of the acquisition mode on the cycle time (left) and modulation period (right).

than 60 s. The right plot displays the modulation period versus n and the tuning mode. The *fast wavelength* mode does not appear because it leads to modulation times close to the cycle time, which are far above the requirement. In this case, a higher n increases the modulation cycle, where $n < 4$ is the condition to fulfill the needed period. Both, *fast polarization* and *intermediate* give exactly the same modulation period. In conclusion, *fast polarization* with $n < 4$ is the best trade-off. In the same way, Figure 3.13 shows the same but versus the acquisition modes, assuming *fast polarization* tuning mode. The *continuous* mode is obviously the faster one, regarding both cycle and modulation period, whereas the *triggered* and *discarding* modes provide acceptable performance if $2 < n < 4$. In this case, the decision for the best option needs an analysis of the polarimetric efficiencies versus acquisition mode as follows in Section 3.4.3.

3.4.3 Shutter implications

Any noise on the accumulated images propagates to the retrieved Stokes parameters, hence to the polarimetric measurements, as defined by the polarimetric efficiency (see Section 2.1). The larger the efficiency ε_n , the less noisy the corresponding Stokes parameter I_n . This section analyzes how the efficiency is degraded because of the limited response times of the LCVR retarders in the PMPs. This degradation depends on the acquisition mode and on the camera shutter, which behaves either as a snapshot, where all the pixels are exposed to light at the same time, or as a rolling shutter, with rows at the top part of the image being exposed before rows at the bottom part (see Section 2.2). As for the tuning mode, this analysis employs the *fast polarization*. The *fast wavelength* mode would show very small degradation of the efficiencies because the number of polarization changes is also small. On its part, the *intermediate* mode would perform as the *fast polarization*.

As pointed out in the previous section, the *triggered* and *discarding* acquisition modes do not suffer from efficiency reduction. The reason is that these modes either do not take images during the LCVRs' transitions, or discard those frames. Therefore, they would lead to optimum efficiencies (Section 2.1):

$$\begin{pmatrix} \varepsilon_I \\ \varepsilon_Q \\ \varepsilon_U \\ \varepsilon_V \end{pmatrix} = \begin{pmatrix} 1 \\ 1/\sqrt{3} \\ 1/\sqrt{3} \\ 1/\sqrt{3} \end{pmatrix}. \quad (3.21)$$

In order to analyze how the LCVRs' transitions affect the *continuous* acquisition mode, Figure 3.14 shows the retardances of the LCVRs for two modulation periods. The graphs suppose a frame rate of 10 fps and the retardances and timing values given in Appendix A.

In case the camera has a snapshot shutter, two possible scenarios appear in the *continuous* acquisition mode:

1. At every modulation state, the readout is longer than the exposure time plus the LCVRs' transition time. Therefore, the exposure can take place during the period in which the modulation state is settled at its aimed value (end of each state in Fig. 3.14). In this scenario, transitions do not affect the exposures and the efficiencies are the optimum ones.
2. The exposure is longer than the stable period of each modulation state. The transitions, or a fraction, degrade the exposure, and therefore the efficiencies are reduced. This is the case for some of the transitions in Fig. 3.14. Figure 3.15 shows the efficiencies versus the parameter n for this scenario, assuming an exposure time of 20 ms and $N_A = 14$. The higher n , the lower the number of transitions, and thus the better the efficiencies. The degradation, even when $n = 1$, is mild because the exposure time is very short.

The *continuous* mode degrades the efficiency differently when a rolling shutter is employed. Since there are always some rows exposing during the acquisition time, and not all expose at the same time, the efficiencies differ from row to row. Figure 3.16 shows

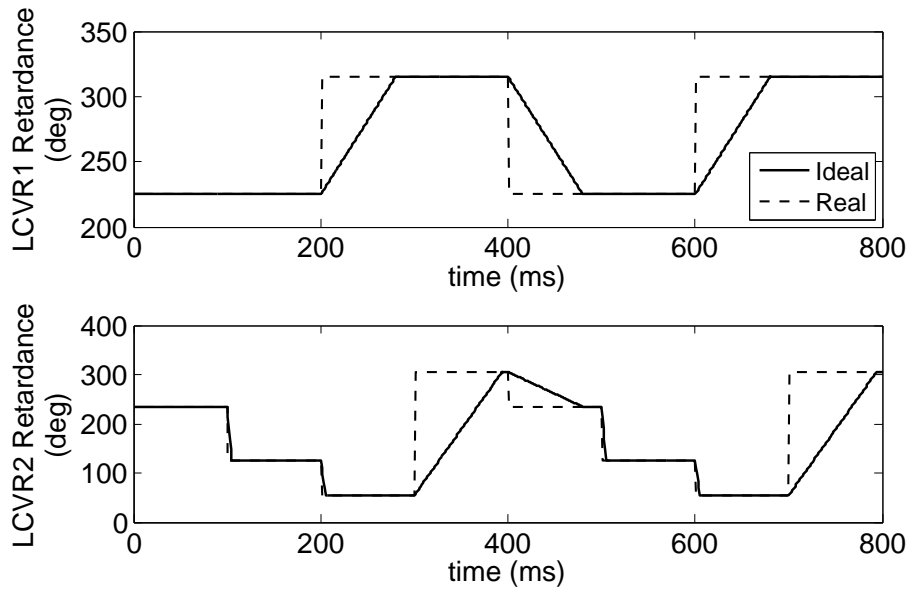


Figure 3.14. Polarization modulation packages: transitions. The ideal case assumes infinite response rates, whereas the real case is modeled using linear responses.

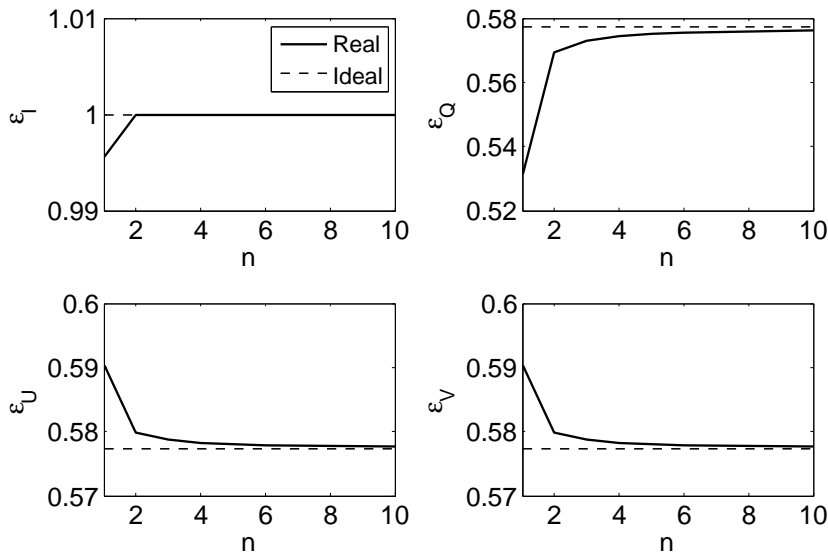


Figure 3.15. Polarimetric efficiency in continuous mode with snapshot shutter.

the polarimetric efficiencies of the four Stokes parameters in the same case of 20 ms exposure and $N_A = 14$, but with rolling shutter. The graphs display the efficiency in terms of the row number, from 0 to 2048, as a function of the parameter n . Firstly, the rows at the top of the sensor (top is 0), which are those more exposed to polarization transitions, suffer from efficiency reduction. On the other hand, the bottom part of the image, which correspond to the end of each state in Fig. 3.14, shows optimum efficiencies because the LCVRs have already reached their next state. As for the dependence on n , a higher value reduces the number of transitions, thus improving the averaged efficiencies.

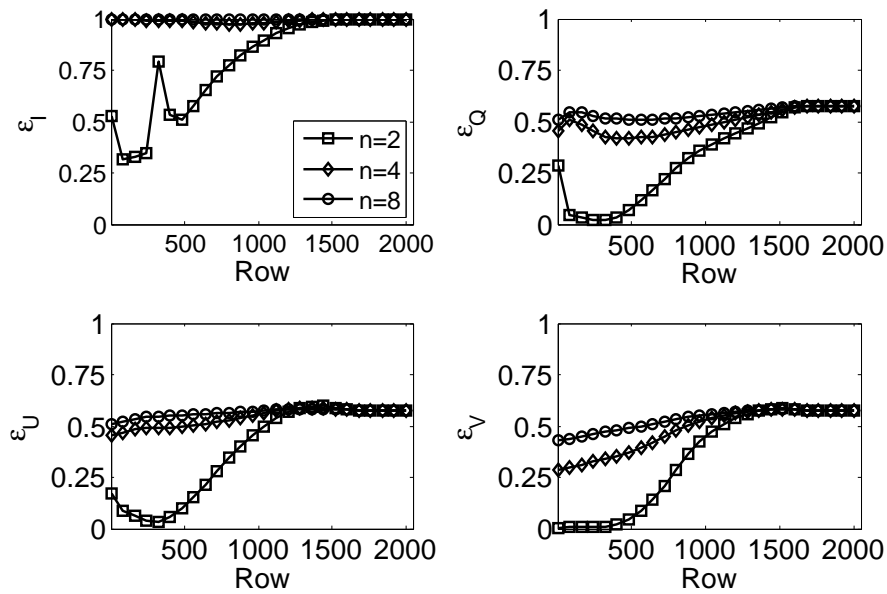


Figure 3.16. Polarimetric efficiency in continuous mode with rolling shutter.

In addition to the implication of the camera shutter on the PMPs synchronization, it may be important to assess whether the use of a rolling shutter may introduce smearing on the images. If $1/T_{\text{acq}}$ is the frame rate, the time difference between the start of the exposure on the first and last rows is T_{acq} . Therefore, any change faster than T_{acq} may blur the image. In case the exposure time is longer than T_{acq} , the smearing would be limited by this time and not by the effect of the rolling shutter. The instrument accumulates images taken within a modulation period, which means that if T_{acq} is shorter than a modulation period, the smearing because of the rolling shutter is negligible. Since the modulation period remains higher than 0.5 s (Fig. 3.12-3.13), and $T_{\text{acq}} = 100$ ms at 10 fps, the rolling shutter effect with respect to smearing of the image is not noticeable. Finally, according to Martínez-Pillet (2006) the camera shutter repeatability, measured as the fluctuations on the exposure times of a sequence of images, must be lower than a certain limit to guarantee that the differential imaging does not introduce spurious signals. PHI sets this limit to 10 ppm (parts per million) within a modulation period, which means that the exposure time of a sequence of images shall not fluctuate more than $5 \mu\text{s}$ per modulation period.

3.4.4 Discussion

The exposition and simulation results presented in the last three sections (3.4.1, 3.4.2 and 3.4.3) allow defining a concise set of requirements for the image sensor, inferring some specifications for the camera electronics, and identifying the best operating strategy for the instrument. Table 3.6 includes the set of specifications for the image sensor that allows reaching the needed scientific performance. The format comes from a top-level specification of the instrument, whereas the pixel size is a combination of an upper limit imposed by the optical design, and a lower limit derived from technological limitations of the sensor. This does not mean that smaller pixels are not possible, but they would hardly

Table 3.6. Requirements of the image sensor affecting instrument performance. Top part lists the key parameters, whereas the bottom part includes some secondary specifications that must be held within a reasonable range.

Parameter	Unit	Requirement	Source
Format	pixels	2048 × 2048	Table 3.4
Pixel size	μm^2	$\leq 18 \times 18$ $\geq 10 \times 10$	Optical design Tech. limits
Sensitivity @ λ_0	%	> 40	Fig. 3.6
Full well charge	ke^-	> 100	Fig. 3.5
Frame rate	fps	> 10	Fig. 3.5
Read noise	e^-	< 100	Fig. 3.6
Dark current @278 K	e^-/s	< 1000	Fig. 3.6
Shutter type		Snapshot or rolling	Section 3.4.3
Readout mode		Read while exposing	Section 3.4.1
Additional			
Non-linearity	%	< 2	
PRNU	%	< 5	
Crosstalk	%	< 10	
Image lag	%	< 1	
Power cons.	mW	< 500	

fulfill other specifications, for example the full well charge (see Chapter 4). As for the sensitivity, full well, frame rate, read noise, and dark current, they all derive from Fig. 3.5 and 3.6, with some margin added to take into account the increase in cycle time because of filtergraph and PMPs transitions, and the degradation due to radiation or ageing effects on the sensor. The margin is especially ample for the dark current because this parameter is usually severely affected by radiation (see Sections 2.3 and 6.4). Regarding the full well charge and the frame rate, the given values are the best compromise, but simulations suggest that a higher frame rate would allow a lower full well charge and viceversa. The shutter requirement depends on the acquisition mode, therefore both shutter options are possible but the rolling shutter would impose the *triggered* mode. To complete the definition, Table 3.6 includes some additional parameters that are not critical for the performance of the instrument but must be kept below certain limits before performance is affected.

The complete specification of requirements for the camera electronics can only be completed once the particular image sensor is selected. Therefore it will be detailed in Chapter 5. Table 3.7 merely lists those requirements directly derived from the image

Table 3.7. Requirements of the camera electronics affecting instrument performance.

Parameter	Unit	Requirement	Source
Dynamic range	dB	≥ 60	Eq. (3.22)
Pixel resolution	bits/pixel	≥ 10	Eq. (3.23)
Average pixel rate	Mpixels/s	≥ 41.9	Eq. (3.24)
Exposure time drift	μs	≤ 5	Section 3.4.3

sensor definition in Table 3.6, or discussed in previous sections. The dynamic range is given by the ratio between the maximum and minimum signal levels which, in this case, are the full well charge and the read noise:

$$DR(dB) = 20 \cdot \log \frac{FWC}{\sigma_{read}}. \quad (3.22)$$

The effective resolution of the ADC stage shall be such that it digitizes the entire dynamic range:

$$N_{\text{eff, bits}} = \lceil \log_2 DR \rceil, \quad (3.23)$$

where one must take into account the noise introduced by the digitization process. The total number of bits of the ADC can be higher than the effective resolution. Finally, the averaged pixel rate coming out of the sensor, hence of the camera, depends on the frame rate and the number of pixels as

$$P_{\text{rate}}(\text{pixels/s}) = \frac{N_{\text{row}} \cdot N_{\text{col}}}{T_{\text{acq}}}. \quad (3.24)$$

The optimum synchronization strategy among filtergraph, PMP, and camera, as well as the key performance parameters for PHI, are given in Table 3.8. The *triggered* acquisition mode is selected as the baseline because it yields optimum polarimetric efficiencies. However, the *continuous* mode is also an option, provided that a camera with snapshot shutter is available and the PMPs's transition times allow it. Depending on the final camera performance, the parameter n can be tuned to adjust the cycle time and modulation period.

3.5 Summary

The Solar Orbiter mission presents a challenging orbit around the Sun, with a closest point at Mercury's distance and a furthest point at about Earth's distance. This inner-heliospheric orbit leads to a harsh radiation environment, whereas the extreme variations in distance to our star result in severe thermal fluctuations. The spectro-polarimeter (PHI) on board the spacecraft demands the acquisition of many frames at different wavelength positions and polarization states in a short time. In this way it can achieve high polarimetric signal to noise ratios and efficiencies.

Table 3.8. Optimum operating mode of the PHI instrument according to the derived requirements. Any deviation, for instance in the image sensor, would lead to variations of this optimum operating point.

Parameter	Value	Source
Tuning mode	<i>Fast polarization</i>	Fig. 3.12
Parameter n	$2 \leq n \leq 4$	Fig. 3.12, 3.13
Acquisition mode	<i>Triggered (or continuous)^a</i>	Fig. 3.13
Accumulations	$N_A = 12$	Fig. 3.7
Cycle time (s)	$48 < T_{\text{cycle}} < 55$	Fig. 3.13
Modulation period (s)	$1 < T_{\text{mod}} < 1.8$	Fig. 3.13
Pol. SNR	$SNR(I^c) = 10^3$	Section 3.4.1
Pol. efficiency	$\varepsilon_1 = 1.0$ $\varepsilon_{2,3,4} = 1/\sqrt{3}$	Section 3.4.3

^aDepending on the shutter type and PMPs transition times

The environment of the mission on one hand, and the required scientific performance of the instrument on the other add a set of constraints to the camera subsystem. Simulations of the instrument running at different operating modes and with different cameras parameters provide an ideal tool to optimize the camera performance requirements, and its synchronization with instrument internal subsystems.

Next chapter makes use of the defined specifications for the image sensor and compares them with both the technological state of the art and with other solar spectropolarimeters that are in use.

4 Selection of the image sensor

Recent advancements on the performance of CMOS imagers place them in a competitive position with respect to CCDs, which, up to date, have been the preferred solution for scientific applications. Moreover, the CMOS inherent radiation tolerance, together with its low power consumption and control simplicity, makes this technology very attractive for space missions. This is particularly the case for Solar Orbiter because it is a medium-class mission, with limited power and mass budgets, and it will encounter a notably harsh radiation environment. Consequently, PHI aims at employing CMOS sensors on its focal plane assemblies.

This chapter reviews the state-of-the-art of CMOS image sensors (CISs), with a main focus on space technology, and examines detectors used in similar instruments. In addition, it assesses the suitability of off-the-shelf and technologically-viable custom sensors for the PHI instrument. Finally, a justified decision is taken, and the main characteristics of the selected sensor are exposed. The goal (g3) of the thesis is the author contribution presented here (see Section 1.1).

4.1 State-of-the-art

At present, the collection of active pixel sensors that have flown on board scientific spacecrafts is limited, the majority corresponding to infrared hybrid technologies. New missions often need to shape existing sensors to their needs, or to embark on fully custom developments, which leads to higher costs and risks, as well as to long production times. Two basic parameters drive the state-of-the-art of CISs: the CMOS process used to manufacture the device (feature size) and the pixel size. CMOS technology tends to scale down the feature size, which allows reducing physical dimensions and supply voltages, increasing operating frequency, and improving radiation tolerance against ionizing effects and latch-ups. On the other hand, miniaturization results in second order effects that affect the performance. In particular, smaller processes and lower voltages trigger new leakage current mechanisms (Roy et al. 2003), enhance noise contributions, and facilitate the occurrence of multiple single event upsets on digital circuits. These high order effects may be acceptable for standard processes but contribute significantly to quality degradation on high performance imagers (Theuwissen 2008). Hence, CMOS imagers employ processes that, though following the general reduction trend, are well behind the cutting-edge processes. For instance, state-of-the-art processes in 2012 for commercial microprocessors use 22 nm technology, whereas scientific imagers are fabricated in $0.18 \mu\text{m}$, which was the feature size for standard processes in 1999 (see technology roadmap in ITRS 2011).

The pixel size plays a key role in the sensor definition because it influences most of

Table 4.1. Comparison of CISs pixel architectures. This list is based on the most common architectures. The particular features of each pixel depend on its specific design and operating mode. The main disadvantage of the simple 3T is the high noise because double sampling is not possible. The 4T architecture solves this problem with the use of CDS. ([†]) means that the 5T pixel allows operating the sensor either with a snapshot shutter or with CDS, but not both at the same time. A 6T architecture would permit combining snapshot shutter and CDS, but with CDS it suffers from secondary effects (parasitic light sensitivity). Thus, it is usually operated with uncorrelated double sampling (*). Adding more transistors can solve this issue. See Holst and Lomheim 2007 (Ch. 4) or Janesick et al. 2002 for a deeper explanation and pixel schematics.

	3T	4T	5T	6T
Advantages	Simple (↑↑) Fill factor	Noise (CDS) Simple (↑)	Noise (CDS) [†] Snapshot [†]	Noise (CDS)* Snapshot
Disadvantages	Noise (↑↑) Rolling Image lag	Rolling Full well (↓)	Full well (↓↓) Fill factor (↓)	Full well (↓↓↓) Fill factor (↓↓) Radiation

its parameters. In general, pixel dimensions scale down along with the manufacturing process, which favors the design of highly integrated cameras with high resolution and low consumption at reduced costs. This inclination pushes both commercial imagers and scientific detectors. However, the latter show a moderate reduction tendency because of degradation on essential performance parameters as the pixel gets smaller. State-of-the-art pixel sizes on commercial mobile imagers range from 1 to 5 μm , while scientific pixels occupy between 10 and 18 μm . As a consequence of the size difference, the biggest scientific CISs hold 16 Mpixels and the majority show resolutions not exceeding 1 – 4 Mpixels. Higher resolutions are achieved using mosaics of smaller sensors, or stitching techniques (Hoffman et al. 2005).

From this point on, the discussion will focuss on scientific detectors. The spectral range aimed by each application influences the optimum type of detector technology. Current visible imagers are fabricated as monolithic or silicon hybridized chips, showing high sensitivity from 400 to 900 nm. Above those wavelengths, the infrared market is dominated by hybrid technologies, where HgCdTe sensors provide sensitivity to photons above 10 μm . Ultraviolet and vacuum UV (100 – 200 nm) sensors may require hybrid architectures using wide band-gap materials (AlGaIn) on the sensitive layer, or multi-channel plates coupled to silicon sensors to intensify UV photons (Huber et al. 2010, Ch. 25). Extreme ultraviolet sensitivity (10 – 100 nm) can be achieved on silicon via back-thinning processes (Waltham et al. 2007). Frontside illuminated sensors are the choice for applications demanding sensitivities not higher than 50 – 60 %, whereas backside devices reach above 80 %. The fill factor limits the sensitivity on front illuminated sensors. It gets worse as the pixel size decreases or the complexity of the pixel design increases, and is better for smaller CMOS processes.

Pixel types differ in their architecture, characterized by the number of transistors per pixel and by the photodiode structure. Complex architectures bring new functionalities, such as analog CDS or snapshot shutter, but reduce fill factor and radiation tolerance. Therefore, state-of-the-art space sensors restrict their complexity to 3 or 4 transistors per pixel, leaving 5T and 6T sensors for those cases in which specific requirements apply and

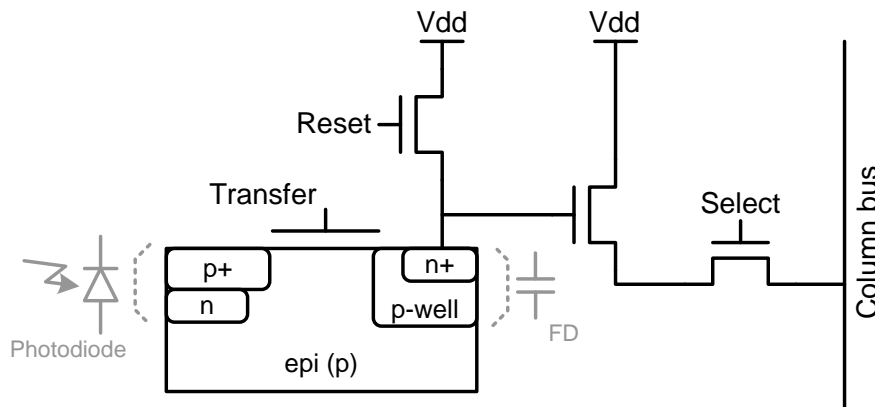


Figure 4.1. 4T pinned-photodiode CMOS sensor: pixel architecture. The transfer gate separates the photodiode from the floating diffusion node during integration, and transfers the integrated charge when the gate is closed. The reset gate, which is local for each pixel, erases any previous charge from the floating diffusion before the charge transfer. Finally, the pixel value is readout through an amplifier and an additional select gate. Reset and kTC noises can be removed via CDS because the reset value can be read just before transferring the charge to the FD, and then subtracted from the read pixel value.

the radiation environment allows it. Table 4.1 summarizes the key advantages and disadvantages of typical architectures from 3T to 6T. Recent sensors tend to employ 4T pinned photodiode designs (Fig. 4.1) that shield the photo-sensitive area from the surface, thus decreasing dark current and radiation induced interface traps. However, the pinned photodiode manufacturing process is rather complex compared to usual photodiodes designs.

Smaller pixel size and higher complexity confine the maximum charge capacity of a pixel. In contrast to CCDs, which can easily demonstrate full well capacities beyond 200 ke^- , present space CMOS imagers rarely exceed 100 ke^- . Some complex CMOS pixel architectures, such as capacitive trans-impedance amplifier (CTIA), reach higher full well charge (FWC) but worsen power consumption and radiation hardness (Hoffman et al. 2005). Dark current also depends on the pixel dimensions, as well as on the photodiode architecture. Values may vary severely from one sensor design to another, which means that some sensors must be operated at low temperature to reach acceptable dark current levels, while others can work at room temperature. Infrared sensors always require operation at low temperatures because their band-gap is very low. Therefore, thermal electrons can easily contribute to the signal. Read noise state-of-the-art values also vary significantly from one application to another. In those cases where readout rate can be low and the full well requirement is not very high, read noise can be reduced to about 1 e^- . However, if speed and charge capacity are important factors, read noise shows typical values between 40 and 100 e^- .

Regarding speed, high frame rate demands are addressed in two ways: increasing the number of outputs and the readout pixel rate. Sensors with resolutions larger than 1 Mpixel usually require more than one parallel output, often a few, in order to keep an adequate frame rate with the pixel rate within certain limits, thus preserving acceptable noise and image lag figures. Maximum pixel rates per output in modern sensors are in the range of 10 to 30 MHz. Above these frequencies, readout and digitization noise levels, ADC resolution, and power consumption are compromised. The fixed pattern

noise, which remains one of the disadvantages of CISs with respect to charge-coupled devices, worsens in sensors with many parallel outputs.

State-of-the-art specialized CISs processes have proven good spatial uniformities for resolutions up to 16 Mpixels, and allow integration of several on-chip circuitry. Scientific sensors, especially those designed for space, make a minimum use of the integration capabilities to avoid any performance reduction. For example, on-chip ADCs are not yet able of providing good results at resolutions above 10 – 12 bits. As additional functionality, present imagers can normally do windowing.

Among other features, radiation tolerance differentiates space sensors from the rest. State-of-the-art space CMOS imagers employ several techniques to enhance their tolerance against radiation. First, smaller processes lead to transistors with thinner gate oxides, which means that oxide traps are minimized and the susceptibility to ionizing radiation decreases. The limitation to this scaling effect arises from the oxides used in the shallow trench isolation (STI) structures, and from the fact that smaller features are usually accompanied by lower voltages. The oxides should not be reduced to guarantee isolation, while lower voltages are more susceptible to radiation induced threshold voltage changes. To overcome the effect of traps in the isolation oxides, transistors with circular shapes and p^+ guard rings structures are employed (Velazco et al. 2007, Ch. 7). Guard rings also protect against latch-ups. Pinned photodiodes provide shielding from the surface, acting as a barrier against interface defects and charge carrier traps. However, this advantage with respect to ionizing dose may be a counter measure against displacement damage (Goiffon et al. 2010). The parameters most affected by radiation are dark current, sensitivity, read noise, and power consumption. Others, such as non-uniformities and hot pixels, may also suffer from degradation. As for levels of tolerance, some CIS prototypes have demonstrated operability at Mrad(Si) doses (Eid et al. 2001; Bogaerts and Dierickx 2000). However, imagers compliant with scientific criteria rarely show tolerances above 200 krad(Si), usually being below 100 krad(Si). Susceptibility to displacement damage is normally limited, or tested, to an equivalent 10 MeV proton fluence of a few 10^{11} p^+ /cm² (e.g. Bogaerts et al. 2003 or Van Aken et al. 2009). Most of the modern CMOS imagers are immune to latch-ups, and their single event upset susceptibility highly depends on the additional circuitry of the sensor.

Table 4.2 shows a list of state-of-the-art sensors that may be suitable for PHI. It includes the six available visible CMOS imagers that best exhibit a resolution, radiation tolerance, full well, and frame rate compliant with the aimed specifications (Chapter 3). In addition, the last column (vendor 7) specifies the proposal of a customized development for this camera. This proposal has been defined taking into account what is technically viable without entailing major risks.

Future CISs for space scientific applications will probably continue pushing in the direction of increasing the number of pixels and decreasing the pixel size, while not disturbing the overall performance. More complex pixel architectures, such as 5T pinned photodiode or 6T, may find their way in demanding radiation environments, and may provide additional functionalities, snapshot shutter, and reduced noise features. The inclusion of on-chip ADCs with acceptable resolutions and sampling rate may substitute the usual concept of front-end electronics.

Table 4.2. Selection of CMOS sensors potentially suitable for PHI: main characteristics. Information has been collected from manufacturers' datasheets, published measurements, and direct communications. Some parameters are not available (N/A). Radiation values correspond to the levels up to which the sensors have been tested without major degradation. The last sensor (Vendor 7) is a new development proposal, where given parameters are goals.

Parameter	Vendor 1	Vendor 2	Vendor 3	Vendor 4	Vendor 5	Vendor 6	Vendor 7
Format (pixels)	1024 × 1024	1024 × 1024	2048 × 2048	2004 × 2058	2048 × 2048	2048 × 2048	2048 × 2050
Pixel size (μm^2)	15 × 15	18 × 18	12 × 12	14 × 14	18 × 18	10 × 10	10 × 10
CMOS Process (μm)	0.5	0.35	0.25	0.35	0.25	N/A	0.18
Illumination	Frontside	Frontside	Frontside	Frontside	Backside	Backside	Frontside
Pixel type	3T	3T	6T	6T	3T (Hybrid)	N/A (Hybrid)	4T
Frame rate / Nr. outputs (fps / -)	11 / 1	10 / 1	15 / 2	> 60 / 12	38 / 32	1.2 / 1	11 / 2
Spectral range (nm)				~ 400 - ~ 900			
Sensitivity @ 600 nm (%)	20	45	37	35	80	85	50
Full well charge (ke^-)	99	82	48	80	80	120	100
Dark current @ 293 K (e^-/s)	3135	200	6600	1225	~ 10 ⁵	N/A	200
Read noise @ 293 K (e^-)	47	35 - 50	65	60	30 - 60	100	60
Shutter type	Rolling	Rolling	Snapshot	Snapshot	Rolling	N/A	Rolling
Radiation tol. (TID) (krad(Si))	250	42	20	10	90	70	70
Radiation tol. (Protons) (p^+/cm^2)	2.4 · 10 ¹¹ @ 10,60 MeV	2 · 10 ¹¹ @ 10,60 MeV	Low	Not tested	N/A	N/A	10 ¹¹ @ 10 MeV
Radiation tol. (SEL) ($\text{MeV} \cdot \text{cm}^2/\text{mg}$)	> 127.8	> 110	> 120	Not tested	> 100	N/A	> 100
Power cons. (mW)	100	60	200	N/A	< 100	< 100	< 500
Status	Available	Available	Available	Available	Available	Available	Custom

Table 4.3. Image sensors employed in current solar magnetographs: main features. List includes in the following order: type of sensor, pixel format, pixel size, frame rate, full well charge, spectral range, illumination side, and shutter type. Section 2.1 provides more information about these instruments.

MDI (1995)	HMI (2010)	IMaX (2009)	CRISP (2008)	SP (2006)	TIP-II (2005)
CCD	CCD	CCD	CCD	CCD	CMOS hybrid
1024×1024	4096×4096	1024×1024	1024×1024	224×1024	1024×1020
$21 \mu\text{m}^2$	$12 \mu\text{m}^2$	$12 \mu\text{m}^2$	N/A	$12 \mu\text{m}^2$	$18 \mu\text{m}^2$
0.47 fps	0.43 fps	30 fps	35 fps	~ 21 fps	36 fps
450 ke^-	200 ke^-	170 ke^-	N/A	130 ke^-	320 ke^-
		$0.4 - 0.9 \mu\text{m}$			$0.9 - 2.5 \mu\text{m}$
Frontside	Frontside	Frontside	Backside	Frontside	Frontside
	Mechanical shutter (snapshot)				Rolling sh.

Currently-in-use space and ground-based solar magnetographs employ, almost exclusively, CCD imagers (Table 4.3). Only those instruments working in the infrared, as TIP-II does, are using CMOS hybrid technologies. However, TIP-II creates 1D magnetograms versus wavelength, which means that the impact of the rolling shutter and fixed pattern noise is not that severe as in 2D maps. The maturity of charge-coupled device (CCD) technology, together with the moderate radiation environments encountered by earth-orbiting missions like SDO (HMI) or Hinode (SP), motivated those decisions. All these imagers benefit from the high full well capacities provided by CCDs. Only the most recent instrument (HMI) demands a resolution higher than 1 Mpixel. As for the minimum rate required, it varies among instruments because it depends on several optical parameters, such as field of view or spatial resolution (Section 3.4). If one compares the characteristics of these imagers with the state-of-the-art space CISs, it comes clear that full well, as well as fixed pattern noise, are sacrificed for the sake of a better radiation tolerance, an electronic shutter, and lower consumption.

4.2 Assessment of alternatives

Both technical and non-technical aspects are considered during the evaluation of image sensor possibilities. The first step consists of comparing technical parameters to the list of requirements (Table 3.6) and radiation specifications (Fig. 3.2), and studying the impact on the instrument performance. The second step analyzes cost, risk, procurement time, and logistics. Previous section exposed the difficulties of finding an appropriate CMOS sensor for space applications, and provided a pre-selection of detectors to contrast with (Table 4.2).

The first two sensors, vendor 1 and vendor 2, use the most mature technology. This derives from their CMOS process sizes, which are larger than for the rest. They, especially Vendor 1, have demonstrated good response to high radiation doses after full qualification campaigns. The major drawback of these options lies in the resolution, which is only 1024×1024 . Since PHI baseline is a 2048×2048 sensor, these detectors would lead to either a reduction of the field of view by a factor of four, or a decrease in spatial resolution.

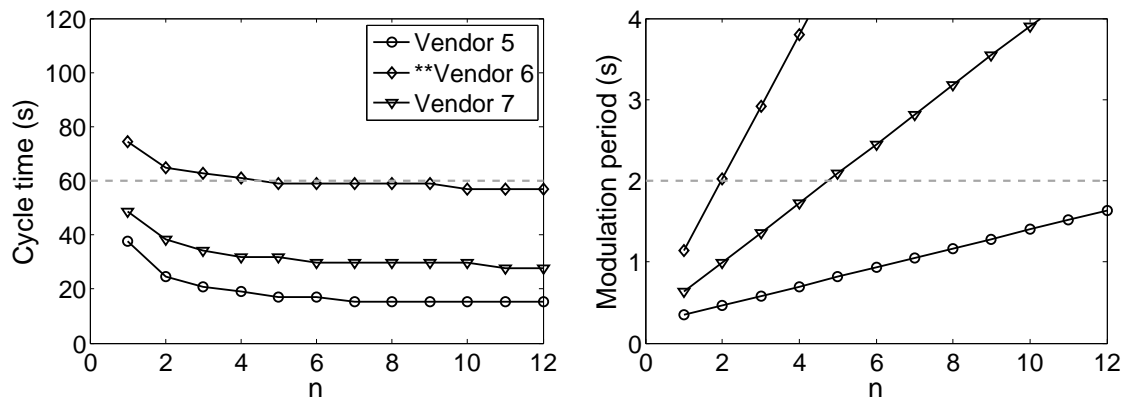


Figure 4.2. Influence of image sensors vendor 5, 6 and 7 on instrument performance: cycle time and modulation period. Parameter n was defined in Section 3.4.2. Dashed gray lines define the maximum allowed times. **This simulation assumes that vendor 6 sensor shows a frame rate of 5 fps. Tuning and acquisition modes as defined in Table 3.8 are employed.

Therefore, they are only considered a back-up solution, to be adopted in case no suitable 2048×2048 sensor rises.

Vendors 3 and 4 hold a 6T pixel architecture, which has the advantage of operating with snapshot shutter. Hence, they would allow running the instrument in continuous mode (see Section 3.4.3). However, the complex pixel architecture results in two disadvantages: sensitivity is reduced due to the fill factor and radiation tolerance is low. In particular, vendor 3 is a commercial sensor, which was not designed for space purposes, whereas vendor 4 was designed for low Earth orbit (LEO) missions. Results of radiation tests suggest that problems, especially artifacts and power deviations, start appearing in vendor 3 after a ionizing dose 20 krad(Si), which is far below the expected dose of the PHI camera. In addition, displacement damage was tested only up to low proton fluences. Vendor 4 sensor has proven good functionality up to 10 krad(Si) of ionizing dose, but it has not been tested further or against displacement damage. Besides, its architecture, together with the fact that low Earth orbits show typical total ionizing doses below 20 krad(Si) under 2 mm Al shielding (ESA PA 1993, Ch. 16), suggests that the tolerance to radiation of this sensor is insufficient for Solar Orbiter.

Vendor 5 is an off-the-shelf hybrid sensor which infrared version has flown already in Earth-orbiting scientific missions. It can deliver up to 38 fps via 32 parallel outputs, which can be controlled by an off-the-shelf rad-hard ASIC. Its high level of dark current requires operation at low temperature (below 240 K to reach levels lower than $400 e^-/s$). Radiation figures regarding displacement damage are confidential, thus user testing is recommended. Vendor 6 is not an off-the-shelf sensor, but a custom development for a mission that currently runs its implementation phase. Though some radiation parameters are confidential, the mission for which the sensor is intended (BepiColombo) will orbit Mercury, which means that its radiation environment will be very close to the one of Solar Orbiter. The primary shortcoming of this option is the frame rate, which is only of 1.2 fps. Hence PHI would require a partial redesign of the sensor to either increase the number of outputs or boost the readout frequency. The last option is vendor 7, which supposes a fully custom development. If one simulates the performance of the instrument for these

three alternatives (Fig. 4.2), vendor 5 shows a fulfillment of specifications well beyond requirements, vendor 7 is compliant with ample margins, and vendor 6 sits at the edge of the requirements assuming that 5 fps are reached after redesign.

New developments or partial redesigns always entail higher risk and procurement times than off-the-shelf products. This, joined to the typical fact that off-the-shelf costs shall be lower, makes new developments difficult and challenging. However, costs are not always higher for new developments, depending that on the company, heritage, and its interest on the aimed sensor. Finally, logistics difficulties are often related to geographical and political aspects. Consequently, vendor 7 leads to the highest risk and procurement time. However, in this case, vendor 7 presents the lowest cost and simplest logistics (Table 4.4). The partial redesign of vendor 6 results in an intermediate risk, but cost and logistics are demanding. Lastly, vendor 5 would minimize the risk and delivery time with a moderate sacrifice in cost and logistics with respect to vendor 7.

4.3 Decision and sensor description

The discussion and analysis of alternatives in the previous section classified vendor 5 and vendor 7 as the most appropriate candidates for the sensor selection. Disadvantages of vendor 5 arise in terms of confidentiality issues, which make the radiation levels for displacement damage and for the readout ASIC uncertain, as well as of logistics and cost. The cost becomes exceptionally high if parts for user radiation testing are required. On its part, vendor 7 has the disadvantages of running higher risks, demanding user radiation tests, and resulting in a comparably longer development time. In view of all collected information, we decide to weight cost and logistics against risk, and select vendor 7, the custom development, as the scientific image sensor for PHI.

The selected sensor, so-called ISPHI, is a development contracted with the Belgian company CMOSIS nv. It has a resolution of 2048×2050 pixels with a 10 by 10 μm pixel pitch. Each pixel comprises four transistors and a pinned photodiode, which provide low dark current and allow performing correlated double sampling to reduce reset and kTC noise. ISPHI is front-side illuminated and is manufactured in the Tower 0.18 μm CIS process. The device works with a main supply of 3.3 V. The rest of the performance goals were exposed in Table 4.2 (vendor 7).

Two main parts constitute the sensor architecture: pixel array and readout stages (Fig. 4.3). On the first part, externally applied signals control pixels exposure and operate the electronic rolling shutter. These external signals address the array rows, govern the pixel internal transistors (gates), and command the connection of pixel rows to the readout circuitry. After exposure, pixel signals are transferred to the parallel column amplifiers (column gain stage) in a two-rows at a time basis. Then, the two consecutive rows are multiplexed into four serial lines, the CDS correction is performed, and finally the four lines are multiplexed again into two external analog outputs. These two simultaneous outputs permit to readout the sensor at 11 fps using a 30 MHz clock, which takes into account the overhead times during the readout. The operation of the column amplifiers, multiplexing stages, and output stages is also commanded by external signals. A set of internal registers, controlled via a serial peripheral interface (SPI), configures different parameters of the readout stages. In addition to the external control signals and main

Table 4.4. Comparison of sensor alternatives: technical compliantness, risk, cost, procurement time, and logistics. Logistics considers difficulties emanating from confidentiality issues, ITAR restrictions, and others. Higher grade implies better technical requirements match, higher risk or cost, longer time, or more laborious logistics.

	Technical	Risk	Cost	Time	Logistics
Vendor 5	• • •	•	• •	• •	• •
Vendor 6	•	• •	• • •	• • •	• • •
Vendor 7	• • •	• • •	•	• • •	•

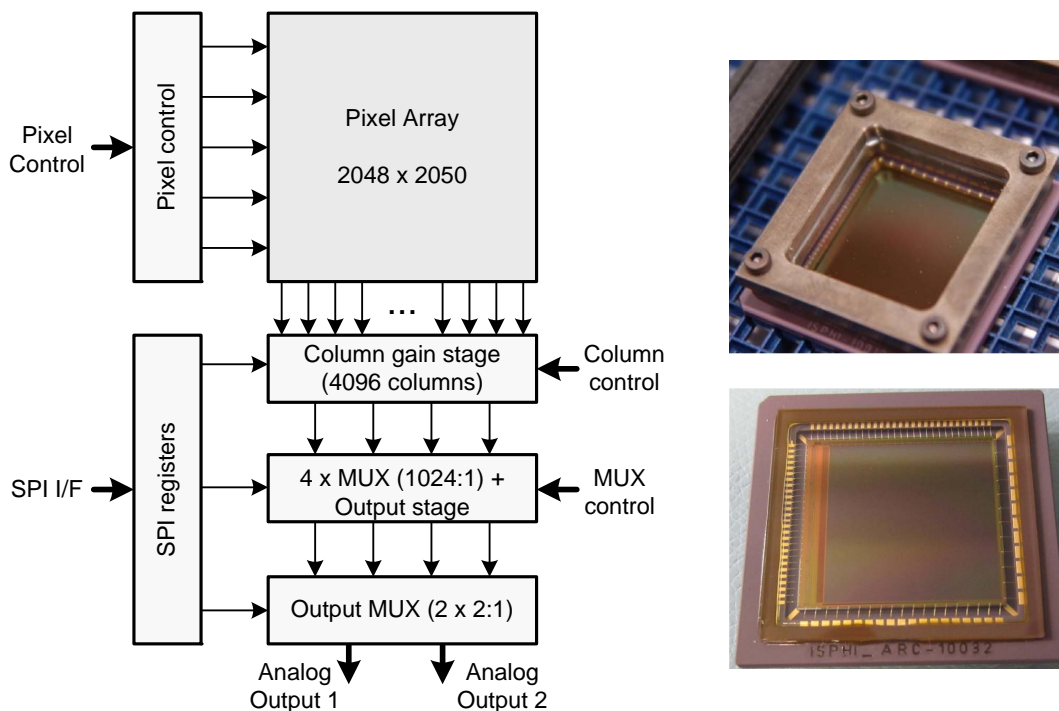


Figure 4.3. ISPFI sensor architecture identifying the external interfaces, the two analog outputs, and the readout stages (left). Rows from the pixel array shift to the column gain stage in two at a time basis, so that only 1024 rows are addressed. Right side shows a picture of the packaged sensor (top) and of the sensor die (bottom).

supply, the sensor requires eight tunable pixel supplies.

At design level, some of the measures discussed in Section 4.1 are taken towards a better radiation tolerance of the ISPFI. Firstly, a heavily doped p^+ layer on the pinned photodiode shields it from the surface, decreasing defects and traps induced by ionizing environments. Secondly, adequate transistors layout, in particular the use of circular transistors, mitigates the leakage effect due to ionizing induced charges. Moreover, the technology scaling down to $0.18 \mu\text{m}$ also helps to improve tolerance against ionizing radiation and latch-ups. Regarding protection against single event upsets on the internal registers, the sensor does not include any built-in redundancy.

The development plan for the sensor has an initial duration of 10 months, assuming

3 months of sensor design, 3 months of sensor manufacturing in the foundry, 1 month of wafers assembly on the packages, and 3 months of first testing and characterization. After that, radiation tests shall be performed with a duration of about 6 months. However, space qualification lies out of the contractor's responsibility. Even though the fundamental design and production tasks were carried out by CMOSIS, we supported the whole development, participating in the critical development decisions, and conducting the proper fulfillment of requirements.

Packaging of the sensor is also an ad-hoc design. In particular, the package is a ceramic 91-pins PGA with removable glass window (Fig. 4.3, right). Its manufacturing process takes about 4 months.

5 Design of the camera electronics

Following to the definition of the image sensor, the second essential piece of the camera is the front-end electronics, the concept of which was presented in Section 2.2.

This chapter defines the camera electronics functionality, describes its architectural design, and addresses the fulfilment of its performance requirements. The discussion primarily focuses on the digital control electronics, which is based on a field programmable gate array. The FPGA device and design solution, with emphasis on critical aspects and limitations, are described. Moreover, we propose a set of enhanced functionalities to be added to the control electronics. Finally, the impact of space radiation on the implemented design is covered.

The author original work in this chapter accomplishes the goal (g4) of the thesis and includes the major contributions (c2) and (c3). Details can be found in Section 1.1.

5.1 Functionality and architecture

The camera electronics must carry out a set of functions that, basically, turns the image sensor into an operable camera. Each of these functions shall demonstrate a minimum performance to both, fulfill the instrument's requirements and make the most of the image sensor's features. A descriptive list of those tasks follows:

1. Supply of the image sensor, which includes fixed bias voltages plus a set of eight tunable pixel supplies that optimize the performance.
2. Control of the image sensor at pixel array level. This task encompasses the generation of pixel signals to control the image exposure, as well as the sequential addressing of rows to govern the electronic shutter.
3. Readout of images from the sensor. It requires the control and clocking of the output stages of the sensor to produce an adequate stream of pixel data at its two analog outputs.
4. Communicate with the sensor via the provided SPI interface to write and read internal configuration registers.
5. Digitize the two sensor's outputs.
6. Transmit the digitized image through an external data interface.
7. Produce a set of housekeeping values, which shall contain information about camera temperatures, current consumptions, voltages, version, and internal status.

Table 5.1. Goal performance parameters for the camera electronics considering instrument and ISPHI requirements. FEE read noise refers to contributions to the read noise that arise from the camera electronics, like digitization noise. The peak pixel rate results from the maximum frequency of the two output channels of the sensor, which is 2×30 MHz (Section 4.3). The average pixel rate is the peak pixel rate but taking into account overhead times. See Section 3.4.4 for an explanation of how the rest of parameters are derived.

Parameter	Unit	Goal
FEE read noise	e^-	≤ 60
Dynamic range	dB	≥ 64.4
Pixel resolution	bits/pixel	≥ 11
Average pixel rate	Mpixels/s	≥ 46.2
Peak pixel rate	Mpixels/s	60
Exposure time drift	μs	≤ 5

8. Communicate with a control external interface to receive commands that configure and manage the overall functionality, and to transmit HK information.

The performance requirements of the camera were first defined in Chapter 3 assuming an image sensor with the minimum required features (Table 3.7). After selecting the ISPHI sensor in Chapter 4, see specifications in Table 4.2 (Vendor 7), we can refine those requirements to get the maximum out of the sensor's features (Table 5.1). Performance is specified in terms of maximum noise to assure that the sensor's read noise is not exceeded by the FEE noise, and of speed to achieve the desired frame rate. FEE read noise, dynamic range, and pixel resolution relate to the noise, whereas the pixel rates link to the speed, and the exposure time drift indicates accuracy.

The camera design concept follows a discrete electronics approach (see Section 2.2.2 for concept definitions). The high cost and long design time of an ASIC readout alternative are not reasonable for this single camera development. Thus, each module of the design block diagram is implemented with an individual component (Fig. 5.1). FPGA is the technology chosen to implement the digital control electronics. As discussed for the camera concept, a digital ASIC is not an option in terms of cost and scheduling, whereas an off-the-shelf and space qualified μ Processor does not meet the camera speed requirements (see Section 2.4 for technologies comparison). The camera works with an external 120 MHz clock provided by a crystal oscillator. The data stream consists of two 14-bits ADCs running at 30 Msps that digitize the analog outputs of the sensor and send the result to the control FPGA. The FPGA multiplexes both outputs into a single 60 MHz line, which is then sent to a serializer and transferred via a channel-link interface to the on-board processing unit. This interface allows sending data at rates above 1.5 Gbps over a serialized link using 3 + 1 differential pairs. An additional SPI interface running at 2.5 MHz permits receiving commands from the instrument control unit as well as sending out housekeeping information. The analog housekeepings are retrieved via two extra ADCs with integrated multiplexer that provide 16 analog channels. Finally, eight programmable digital-to-analog converters configure the pixel supplies, while a ninth one is

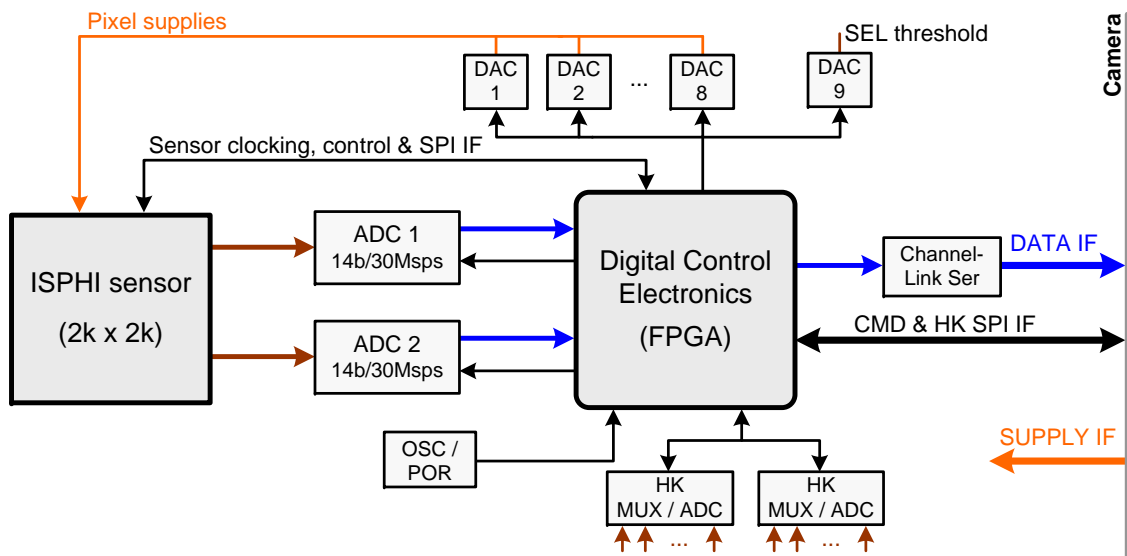


Figure 5.1. Block diagram of the camera electronics. Digital data stream is highlighted in blue, analog signals in brown, supplies in orange, and the rest of digital connections are black. Note that power connections other than the pixel supplies are not detailed.

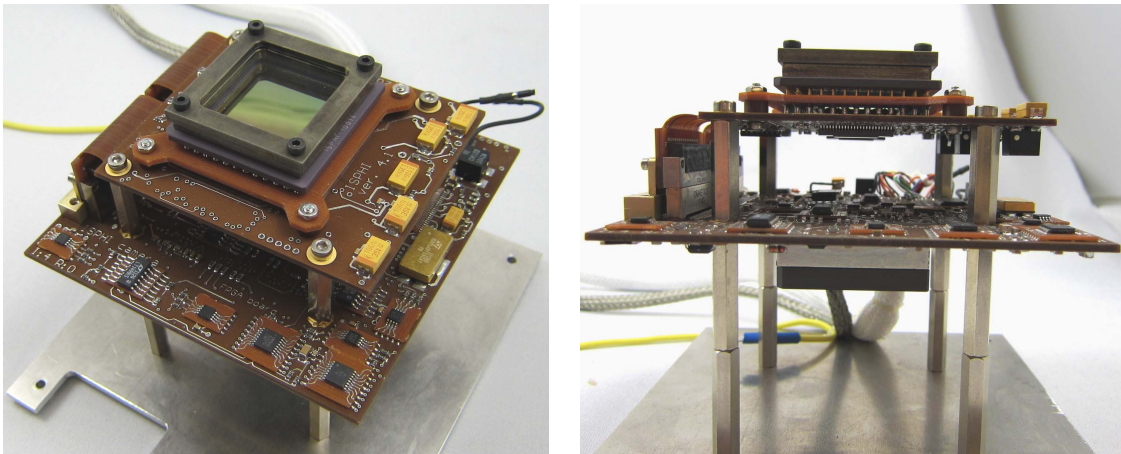


Figure 5.2. Pictures of the camera electronics: electrical model. All camera components are allocated within two boards: sensor board and FPGA board. The sensor board contains the ISPHI, which lies at the top of the camera, and the two analog-to-digital converters on the bottom part. Two flexible PCBs connect it with the FPGA board, which includes the FPGA (bottom part on the right side), DACs, housekeeping circuitry, channel-link serializer, and the external interfaces. Two cables come out of the FPGA board, one comprising data and commanding interfaces and the other the supply lines. The space between boards will accommodate the cold finger element at the bottom of the ISPHI.

employed to set the latch-up protection threshold (see Section 5.3.1). Figure 5.2 displays two pictures of the camera electronics including the ISPHI sensor.

From the camera block diagram, one can determine the specific tasks that the digital control electronics shall accomplish, and relate them to the list of camera functionalities given at the beginning of the section (Table 5.2). In addition to accomplishing those

Table 5.2. List of digital control electronics tasks.

ID	Task
1	Control and clocking of the sensor at pixel and readout levels, as well as communication with its SPI interface (camera tasks 2, 3, 4)
2	Generation of the ADCs sampling clocks at 30 MHz (linked to camera task 5)
3	Acquisition and synchronization of data from both ADCs at 30 MHz, and multiplexing of it into a single 60 MHz line. A low frame rate mode with ADCs running at 15 MHz shall also be supported (linked to camera task 5)
4	Communication with channel link serializer to transmit data up to 60 MHz (camera task 6)
5	Communicate with the external SPI interface at 2.5 MHz to receive commands and send housekeepings (camera task 8)
6	Management of commands and housekeepings (linked to camera functionalities 7, 8)
7	Control of HK-ADCs to retrieve analog housekeepings (camera task 7)
8	Control of DACs to tune the sensor's pixel supplies (linked to camera task 1)

tasks, the FPGA design shall guarantee the performance requirements previously showed in Table 5.1.

5.2 Digital control electronics

Previous section introduced the camera electronics and detailed the roles played by the digital control part. Hereafter we propose a design solution, analyze alternatives for the most demanding points, and report on the outcomes of the design.

5.2.1 FPGA device

The camera functionality is not foreseen to change during the mission, thus in-flight re-programmability of the field programmable gate array is not required. This fact motivates the use of antifuse FPGA technology, which shows high tolerance to radiation and reduces power consumption (see Section 2.4, Table 2.7, for a comparison of technologies). In particular, we decided to employ the *RTAX250* FPGA from Microsemi in a *CQ352* package. This family of devices has a long flight heritage and represents the state-of-the-art of space antifuse FPGAs. Its main features are (Microsemi RTAX datasheet 2012):

- Manufactured on 0.15 μm CMOS antifuse process.
- Radiation tolerance: $\text{TID} > 200 \text{ krad}(\text{Si})$, $\text{SEL-LET}_{\text{th}} > 117 \text{ MeVcm}^2/\text{mg}$, $\text{SEU-LET}_{\text{th}} > 37 \text{ MeVcm}^2/\text{mg}^1$.

¹Berg et al. (2011) and Rezgui et al. (2009) discuss the dependency of SEU LET_{th} and cross-section with frequency and circuitry features in the RTAX family.

- Built-in Triple Module Redundancy in all user flip-flops. No SET built-in mitigation is included.
- Differential IO capabilities (LVDS).
- Capacity of 1408 registers (R-cells) and 2816 combinatorial cells, each of which can implement above 4000 different 5-bits functions.

5.2.2 Architecture

In order to fulfill all assignments in Table 5.2, the control electronics design splits up into eight internal modules (Fig. 5.3). The *clocks manager* receives the 120 MHz clock from the external oscillator and generates the main clocks of the design: *pixel* clock at 30 MHz and *channel-link* clock at 60 MHz. When running at low frame rate, which is a mode controlled by the *Commands manager*, these clocks have frequencies of 15 MHz and 30 MHz, respectively. The *IO & POR manager* configures the type of every input/output of the FPGA and controls the overall power-on reset (POR) policy of the design. An asynchronous POR signal is applied externally.

The *ISPFI controller* manages the complete image sensor interface. First, it implements the SPI protocol via two shift-register structures to read and write registers on the sensor with a SPI clock running at 15 MHz (*SPI interface*). Second, it creates the signaling to reset, address, and transfer rows of pixels to the amplification stages of the sensor, thus managing the exposure time, the electronic shutter, and the correlated double sampling (*Pixel control*). Finally, it governs the readout of pixels via the adequate clocking of the output stages (*Readout control*). The *Commands manager* sets all configurable parameters, such as exposure time or readout rate, and commands the read/write of sensor registers. The *Data manager* creates the data path between the ADCs and the external channel-link interface. First, the *ADCs clocking* module generates the clocks needed to sample the analog outputs of the sensor. Then, the *Data acquisition* acquires the two data streams received from the ADCs and synchronizes them with the *channel-link* clock. After that, the *CL controller* multiplexes both data lines into a single stream and sends it to the channel-link serializer together with the needed control flags. The *ISPFI controller* sends synchronization flags to the *Data manager* to indicate when the image readout starts and ends.

All DACs are governed by the *DACs controller*, which implements the required SPI interface (master side) to communicate with the converters using a 15 MHz clock. In the same way, the *Housekeeping ADCs controller* manages the two external ADCs through another SPI interface (master side) also at 15 MHz, and retrieves the digitized analog-HK values, which are then sent to the *Commands manager*. The *SPI module* is the slave implementation of the serial peripheral interface that links the camera with the instrument's processing unit. The SPI clock runs at 2.5 MHz. The module is controlled by the *Commands manager*, and transmits all commands replies and housekeepings. On the other side, it receives commands and housekeeping requests. Apart from the clock synchronization and transmission/reception shift-registers, the module adds/checks the cyclic redundancy check (CRC) for all output/input SPI packages. Finally, the *Commands manager* is in charge of configuring and triggering the operation of all modules, as well as of the managing of analog and digital housekeepings.

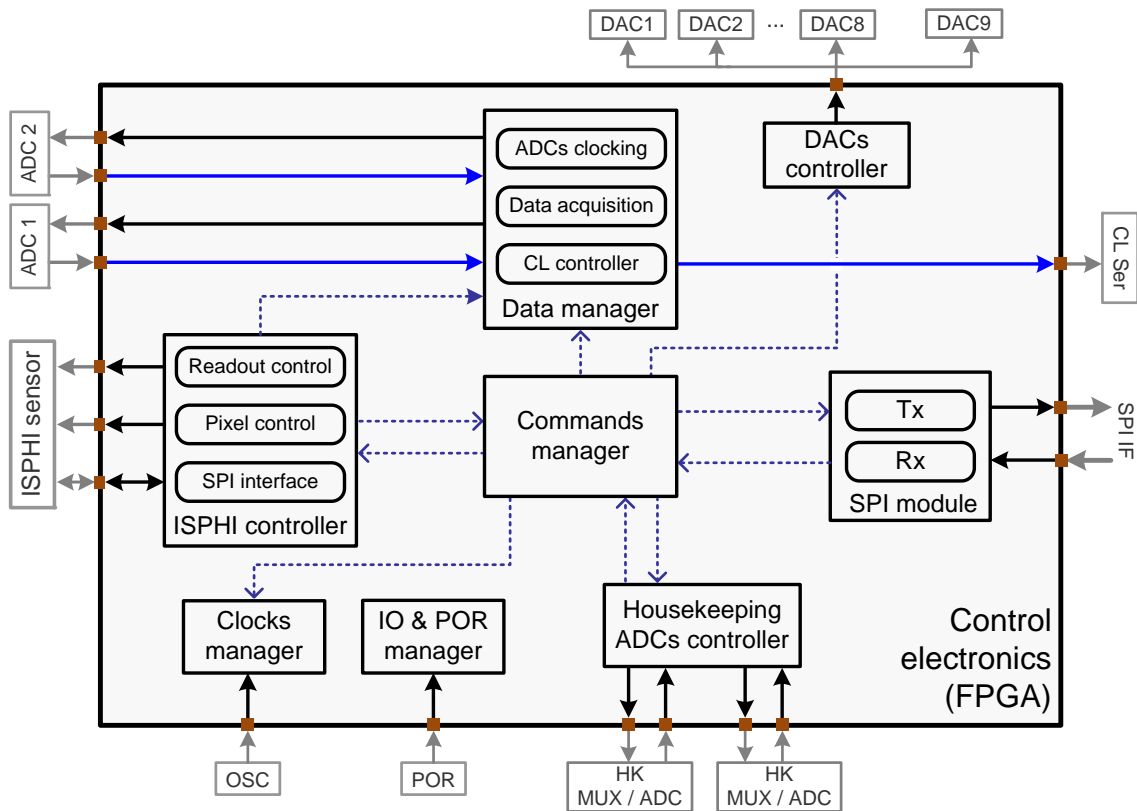


Figure 5.3. Reduced block diagram of the FPGA design. For simplicity, only connections of modules with external blocks and main inter-modules links are displayed.

5.2.3 Critical points

We identify two parts of the proposed architecture (Fig. 5.3) as critical to reach the performance specifications presented in Table 5.1: *ADCs clocking* and *Data acquisition*. Furthermore, the power-on reset policy is considered relevant for requiring particular implementation techniques. This section addresses and discusses specific design solutions for these critical points.

5.2.3.1 ADCs clocking

The digitization noise is the most significant contribution of the front-end electronics to the total read noise. Other sources, such as circuit crosstalk, grounding, or power supply noise, are usually minimized with an appropriate analog design and layout. Some noise components of the digitization stage, such as quantization noise or non-linearities, are inherent in the ADCs themselves. Therefore, one can overcome them via selecting a converter with enough effective number of bits (ENOB) at the desired sampling rate, 11 bits at 30 MHz in this case (Table 5.1). However, other noise sources originate from the clocking of the ADCs.

In particular, two parameters of the sampling clock have a crucial influence over the noise: the sampling instant and the jitter. The sampling instant is determined by the active edge of the sampling clock, and represents the actual time at which the analog

pixel is sampled. Sampling the signal too early, before it is settled, leads to spurious contributions from the previous sample (pixel), while a late sampling can interfere with the transition to the next sample. An optimum sampling instant, or window, shall be identified to assure minimal spurious contributions. As the sampling frequency increases, the optimum window becomes smaller. Furthermore, this optimum instant is a priori unknown for the sensor outputs and may show dependence on temperature and radiation dose, or may even vary from output to output. Therefore, a fixed pre-calibrated sampling instant may not be the best solution. On its part, the clock jitter causes random variations on the sampling edge from pixel to pixel, which degrade the dynamic range. To guarantee a non-degraded dynamic range in an N bits ADC, assuming a sinusoidal input signal of frequency f , the clock jitter (rms) shall fulfill (Kester 2005, Sect. 6.5):

$$t_j < \frac{1}{\pi \cdot f \cdot 2^{N+1}}. \quad (5.1)$$

A 30 MHz input signal in a 14 bits converter requires a maximum jitter of $t_j(14b) = 0.3$ ps, while the requirement for the needed 11 bits of effective resolution is relaxed to $t_j(11b) = 2.6$ ps. Ideally, ADCs should be clocked by a local oscillator located as close as possible to reduce jitter effects. However, the necessity of finding an optimum sampling point makes inviable the use of such a fixed clock. Fortunately, the outputs of an image sensor usually do not present large pixel to pixel variations, but a slow slew rate, which means that the jitter effect is smaller than that predicted for a sinusoidal input signal. If we compare the clocking requirements of all sensors presented in Chapter 4, the high readout frequency of the ISPHI imposes the hardest constraints. Finally, clock skew may also be a concern because it can compromise the synchronization when two or more ADCs present different skews in their sampling clocks. Next section will discuss synchronization strategies.

To tackle the finding of the optimum sampling instant and its potential variability, we propose to generate a tunable sampling point. This approach allows the user selecting the sampling point among a set of delayed versions of the clock via sending a command (Fig. 5.4). Thus, the camera can be calibrated to reach an optimum value. We limit the number of available points to eight, which implies a separation of $\Delta s = 4.17$ ns for a 30 MHz clock. The implementation of this solution on the control FPGA requires generating a set of delayed clocks and selecting the one with the desired active edge. These clocks can be created either using combinatorial logic that delays the input signal, i.e., a string of inverters, or employing a fast master clock that oversamples the clock to shift it. The main disadvantage of the first alternative is that controlling the combinatorial delays may be an unmanageable task, especially because they can show dependence with temperature. The second option provides deterministic edge positions, but requires the use of a high frequency clock. In particular, either using a clock eight times faster or employing both, rising and falling, edges of a four times faster clock would be needed. Although the design using both edges demands a careful control of the signals to avoid timing violations, a clock eight times faster (240 MHz) would consume more power and highly complicate the camera layout. Accordingly, the *main* clock of the design has a frequency of 120 MHz. Figure 5.5 shows the schematic used for that purpose. The proposed structure assumes that the *main* clock can freely sample the *p0* clock (*PixelCLK*) without any risk of metastability, which is reasonable because *PixelCLK* was previously derived, in

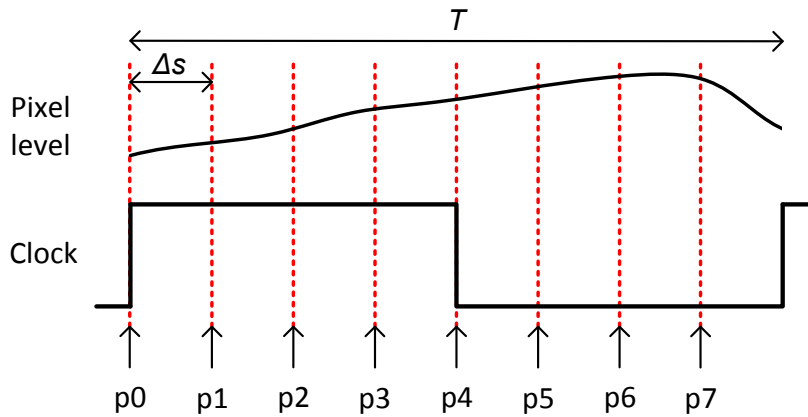


Figure 5.4. Tunable sampling point: concept. The clock represents a non-delay sampling clock which active edge (rising) matches the point p_0 . Each sampling point from p_1 to p_7 would lead to a sampling clock with its active edge delayed to meet that point. The signal above (pixel level) is the analog input to be sampled. The optimum sampling point for this example lies between p_5 and p_7 .

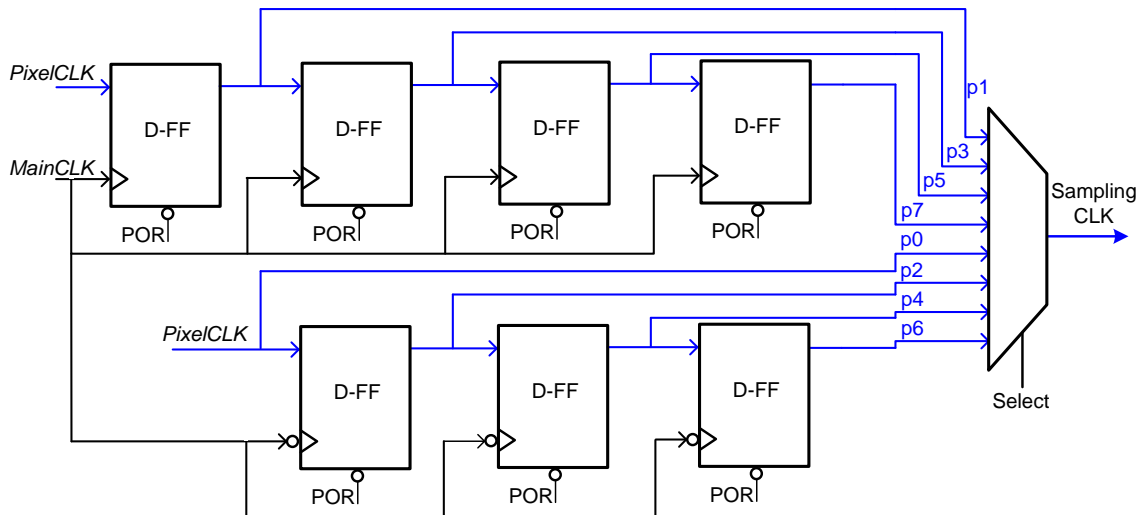


Figure 5.5. Tunable sampling point: schematic. *MainCLK* is the four times faster clock provided by the external oscillator, whereas *PixelCLK* represents the sampling clock at the original position p_0 .

the *Clocks manager* module, from that *main* clock. Any additional delay added between the generation of the clock in the FPGA and the input of the ADC, such as the FPGA output port or the propagation through the PCB, would affect equally all sampling points.

Applying the presented concept of sampling point, two solutions for the implementation of the ADCs clocking follow. The first one is a direct approach to solve the problem, whereas the second tries to optimize the critical parameters discussed above. Hereinafter we present their implementation, advantages, and disadvantages, while their performance after being tested in real hardware will be exposed in Chapter 6 (Section 6.1).

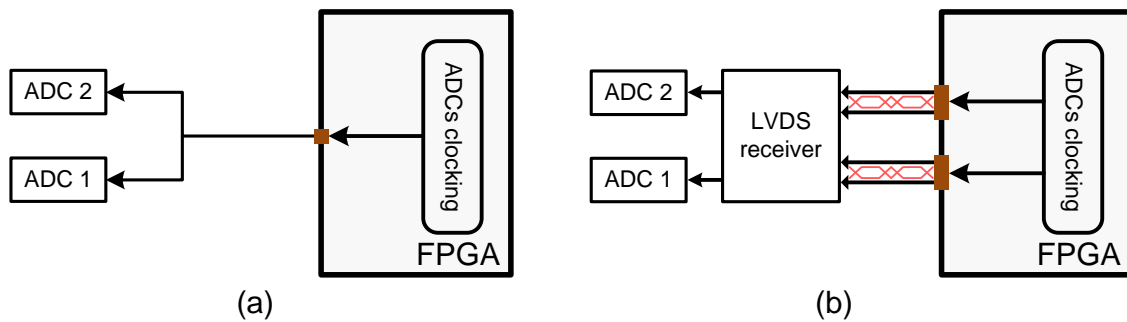


Figure 5.6. Simple (a) and proposed (b) solutions for ADCs clocking: comparison.

Simple clocking strategy This approach assumes that both sensor outputs present equal or very similar delays, and that the same happens to the sampling clock paths. Therefore, the same sampling clock can safely trigger both converters. In addition, to save FPGA output pins and to simplify the boards layout, a single output feeds both ADCs. Figure 5.6 (a) sketches this alternative. The main advantages are that the synchronization and multiplexing of data from the two ADCs is simple because both share the same sampling clock, and that the number of resources, pins, area, and power, is minimal. On the other hand, differences between the optimum points of both analog channels add noise to the readout process, and the transmission of the sampling clock from the FPGA to the converters may be susceptible to interferences and undesired reflections.

Proposed clocking strategy In this case, the sampling point of each ADC can be selected independently because two individual sampling clocks are generated (Fig. 5.6, b). Moreover, interferences on the clock transmission from the FPGA to the ADCs are reduced by using differential signaling (LVDS). The advantages of this solution are that differences between both analog channels can be overcome, and that routing-related noise sources are minimized. However, these benefits come at the expense of more FPGA pins (four instead of one), more complex layout, and the need of a differential, low jitter, receiver next to the converters. In addition, the synchronization and multiplexing stages for this approach become more complex (see next section).

In summary, while the first approach provides simplicity against performance, the second aims at optimum performance but becomes more complex. This second approach is only justified if the performance results of the first one are not satisfactory.

5.2.3.2 Data acquisition from ADCs: synchronization

Transferring the image data from the ADCs to the CL serializer through the FPGA requires three steps: retrieving the pixel data from the two converters, synchronizing these data streams with the *channel-link* clock, and multiplexing them into a single line in the *channel-link* clock domain. The digital data from the converters are synchronized with the falling edges of the sampling clocks, which are generated inside the FPGA. Thus, the first step is direct if the sampling clock and data propagation delays are small enough (Fig. 5.7). To guarantee proper operation even if those delays vary with operating conditions, the sampling point used to internally sample the digital data is uncoupled from the ADC sampling clock. For example, $SampCLK(p_i)$ may feed the ADC and $SampCLK(p_{i+1})$

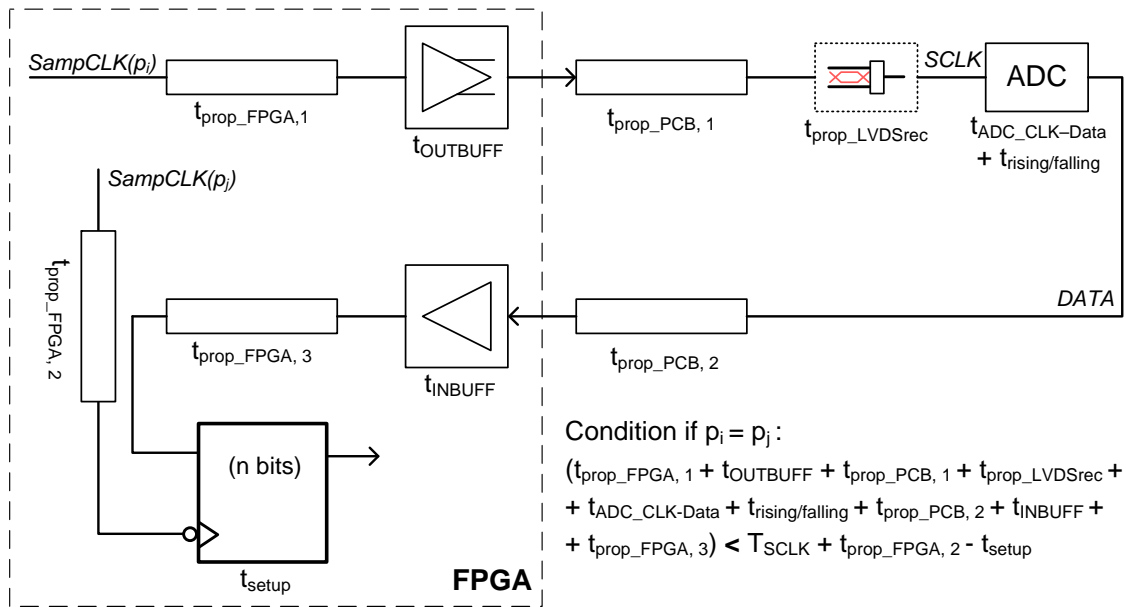


Figure 5.7. Sampling clock and ADC data delays from/to the FPGA. The condition below shall be fulfilled if the same clock ($SampCLK(p_i)$) feeds the ADC, and samples the digitized data inside the FPGA, i.e., if $p_i = p_j$.

register the digital data, so that an additional delay of Δs is allowed. After this step, two data buses are available in the domain of the sampling clocks. The third step is simple because the two data buses to multiplex already belong to the final clock domain. Finally, the primary difficulty emanates from the second step, which synchronizes data in the variable sampling clock domains with the doubled frequency *channel-link* clock. This process shall avoid sampling the data during the transition periods, which would lead to metastabilities², thus to wrong data. The synchronization process turns to be more or less complex depending on which of the solutions given in the previous section is adopted for the clocking of the ADCs. While the simple solution, where both ADCs share sampling clock, requires a single synchronization between the sampling clock and the *CL* clock, the proposed solution needs to synchronize two independent sampling clocks with the *CL* clock. These two independent synchronizations can make it difficult to multiplex the data buses into one line if they present a delay in clock cycles after synchronization. We present here a specific solution for the simple case, and evaluate a set of general solutions that can be applied to both, the simple and the proposed clocking strategies.

Synchronization of simple clocking: shifting of *CL* clock This special solution greatly simplifies the synchronization scheme when a single clock samples both converters. It consists of delaying the *channel-link* clock as a function of the selected sampling point, in the same way the sampling clock is delayed. Hence, the sampling clock and the *CL* clock are synchronous and digital data from the ADCs can be directly sampled using the *CL* clock. The implementation of this solution requires a schematic similar to the

²A metastability occurs if the input signal of a register changes just before or after the active edge of the clock, hence provoking an instability. The minimum times before and after the active edge in which the input signal must be stable are the setup and hold times of the registers.

one used to generate the sampling clock (Fig. 5.5), but applied to the double frequency *CL* clock. In this case, since *MainCLK* has double the frequency of the input *CLCLK*, only four versions of the clock can be generated. Therefore, the schematic is reduced to three D-flip-flops plus a four-inputs multiplexer. The only remaining concern of this solution are the control flags that indicate the start and end of frames to the *CL controller*. These flags are generated using the non-delay version (*p0*) of the clocks, and now has to be sampled by any delayed version of *CL* clock. However, since both the delayed and non-delayed clocks are internally generated using the *main* clock, the flags can be freely sampled if they fulfill $t_{\text{prop}} < \Delta s - t_{\text{setup}}$, where t_{prop} is the propagation delay of the flags inside the FPGA, Δs is the minimum delay between adjacent sampling points, and t_{setup} is the registers set-up time. The disadvantage of this solution is that the clock provided to the channel-link serializer changes phase every time the sampling point changes. This situation makes the internal phase-lock loop of the serializer to re-synchronize and lose its output clock for some time. However, the sampling point shall only be changed during calibration and the serializer can be powered-down and powered-up every time this operation is performed. On the other hand, the main advantage is related to the amount of extra resources needed to acquire the ADCs data, which is reduced to the three registers and multiplexer required to delay the *CL* clock, apart from the data registers to sample the input data bus.

Synchronization of proposed clocking The following paragraphs discuss the concept, advantages, and disadvantages of three approaches proposed to solve the general synchronization problem. The first solution employs the clock relation between domains to simplify the synchronization, while the last two options assume that sampling and *main* clocks belong to completely asynchronous domains. In all three cases, the synchronization structure adds extra delays to the data streams. To guarantee that the control flags sent by the sensor controller, such as start and end of frame, are in phase with the acquired data in the *channel-link* clock domain, as well as to adjust the ADC delay, a parameter called *pipeline delay* is introduced. This parameter, selectable by command, permits delaying the cycle at which the data in the CL domain starts being sent to the serializer.

Approach 1: Mesochronous structure As previously discussed, the sampling clock is a delayed version of the *pixel* clock. Thus, these two signals are not asynchronous but mesochronous (Dally and Poulton 1998, Ch. 10), i.e., they have the same frequency and different phase. In addition, the sampling clock, the *pixel* clock, and the *channel-link* clock are originally derived from the same *main* clock of the design. Therefore, if one uses the clocks just after being created and before any multiplexing or input/output stage, and takes care of the timing violations, it shall be possible to produce a synchronization signal that allows sampling the ADC data using the *channel-link* clock. Figure 5.8 shows the proposed structure. All sampling clocks before multiplexing, as well as the *channel-link* clock before entering any clock routing resource, belong to the *main* clock domain. The first FF and gate at the top detect the falling edge of the sampling clock (point *i*), whereas the two subsequent gates plus the second FF keep the detection signal active until a rising edge on *CL* clock occurs. Given that *CL* clock is generated on the rising edges of the *main* clock, if the propagation plus multiplexing delay of the enable signal fulfills $t_{\text{prop+mux}} < (T_{\text{mainCLK}}/2 - t_{\text{setup}} + t_{\text{prop_CLCLK}})$, with $t_{\text{prop_CLCLK}}$ the propagation delay

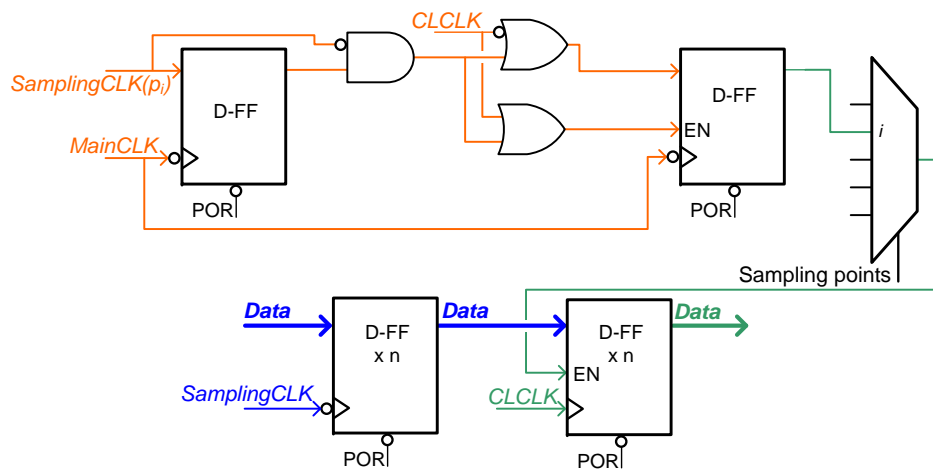


Figure 5.8. Data synchronization using mesochronous structure. Blue signals are in the sampling clock domain ($freq = f$), orange in the main clock ($freq = 4f$), and green in the final channel-link clock domain ($freq = 2f$). The top part generates an enable signal to safely sample the data from the ADCs using the channel-link clock. This enable signal shall be generated per sampling point, with the appropriate one being selected to sample the data. Data registers are displayed at the bottom row. They consist of n registers each, with n being the number of data bits.

of $CLCLK$ from its generation point, it can directly feed the enable pin of the bottom FFs that sample the data into the CL domain. In principle, the top part of the structure needs to be replicated for every sampling point, and then selected, while the bottom part is instantiated for each ADC, i.e., twice. Each ADC has an associated sampling clock with a given sampling point. However, since the frequency of the CL clock is only twice the one of the sampling clocks, each group of four sampling clocks will generate the same enable signal. Thus, the top part of the structure can be replicated only twice. The data from two sampling clocks with different phases may be synchronized in different cycles of the CL clock, which may mismatch the pixels after multiplexing. To solve this point, an additional delay of one CL clock cycle can be added to the synchronized data before multiplexing. This delay is controlled via commanding, but has default values associated to each sampling point, which, in principle, should not change. In total, this structure requires $8 \cdot 2 + 2 \cdot n = 46$ registers per ADC, where the first 8 is the number of sampling points and $n = 15$ for a 14 bits ADC plus overflow flag. Applying the reduction of the top part of the structure from 8 to 2 replications, resources diminish to $2 \cdot 2 + 2 \cdot n = 34$ registers per ADC.

Approach 2: Double flopping A common structure to synchronize signals between asynchronous clock domains is the double flopping (Kilts 2007, Ch. 6). This structure employs a brute-force method to minimize the probability of metastability, i.e., maximize the mean time between failures, during the synchronization process (Stephenson et al. 2009). Since the main clock is four times faster than the sampling clock, it can be used to generate an enable signal that detects the rising edges of the sampling clock via double flopping (Fig. 5.9). This enable signal can now sample data using the main clock. Once the data belong to the main clock domain, since this clock runs twice faster than the CL clock, it can generate a two-cycles wide enable signal that allows sampling the

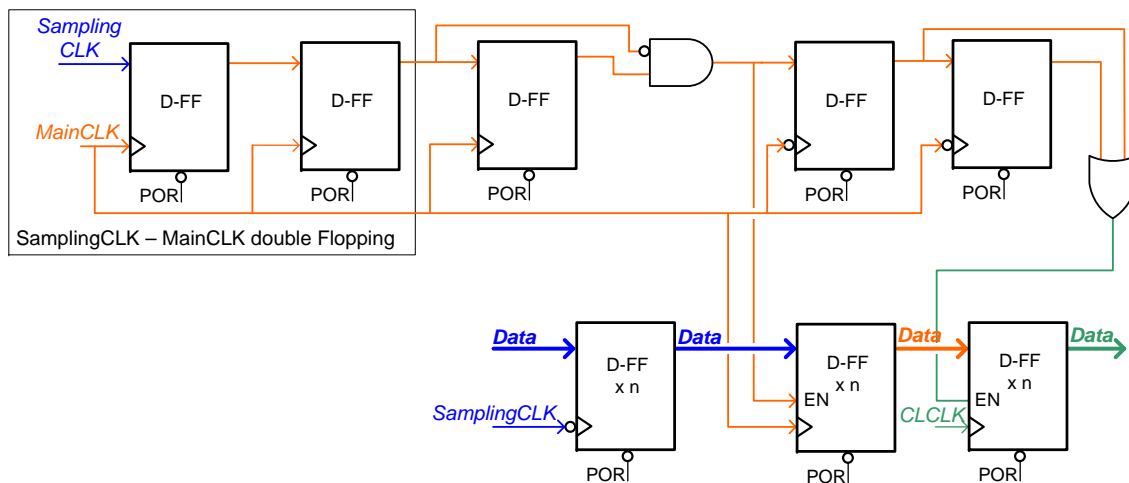


Figure 5.9. Data synchronization using double flopping. Colors follow the same coding as in Fig. 5.8. The FF and gate after the double flopping generate the enable signal to sample the data using the *main* clock, whereas the two subsequent clocks widen this enable signal to be used with the *CL* clock.

data in the *CL* clock domain. The first set of data registers could have been avoided by detecting the falling edge of the sampling clock and directly registering the input data bus using the *main* clock. However, since the sampling clock that really generates the data bus in the ADCs is affected by some propagation delays with respect to the existing inside the FPGA, sampling first with the internal sampling clock is safer. This double flopping scheme applied to the camera synchronization shall be duplicated to allow synchronizing both ADCs when the sampling points are different. It requires $5 + 3 \cdot n$ per ADC, which amounts 94 registers for two 14 bits plus overflow. Apart from the high amount of required resources, this complex solution is not totally free of metastabilities. In addition, the double flopping structure presents an uncertainty of ± 1 clock cycle (Kilts 2007, Ch. 6), which means that it is not possible to determine the exact *main* clock cycle in which the sampling edge will be detected. This is not a problem for synchronizing a single ADC channel since it just adds an extra delay, but it complicates the later multiplexing of the two channels because they can be unpredictably unpaired.

Approach 3: Dual-port memory Another classical method to pass data between asynchronous clock domains is using a memory that allows writing and reading with different clocks. The most common alternative employs an asynchronous FIFO controller (Dally and Poulton 1998, Ch. 10; Kilts 2007, Ch. 6). However, we propose a simplified architecture to directly use the dual-port memory elements of the FPGA (Fig. 5.10), and avoid implementing a FIFO controller, which adds complexity, or using the built-in one, which is not radiation tolerant. The memory block shall be deep enough to guarantee that data being read is not being written simultaneously. The control flag (*fr_start*) can be synchronized with both clock domains, as explained for the shifting *CL* clock alternative, and not only enables but also resets the counters. The counter on the write side starts at the address zero, whereas the counter on the read side starts some positions further to avoid overlapping. The previously introduced *pipeline delay* parameter allows adjusting

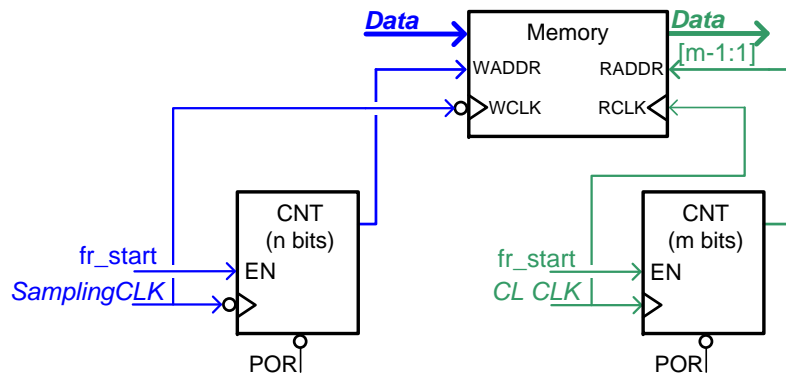


Figure 5.10. Data synchronization using dual-port memory. Since the *channel-link* clock has double the frequency of the sampling clock, the number of bits must fulfill $m = n + 1$, so that both counters scan the complete memory during the same period.

the moment at which the data in the CL domain starts being valid. This parameter may change if the sampling point does so. The synchronization structure shall be duplicated to synchronize data from both ADCs. This solution is free of metastabilities and limits the number of registers to the $n + m$ required by the counters. It uses SRAM memory blocks that are not radiation tolerant by design. The EDAC core (Microsemi EDAC 2012), which needs above 90 registers for a single implementation, could be employed to assure the integrity of the stored data. However, since the data stored in the memory is rapidly readout and it represents pixel values that are not highly critical, scrubbing is not necessary and the EDAC algorithm might be omitted if it is considered that the SEU rate is very low compared to the rate at which pixels are readout.

In summary, the first synchronization alternative (shifting of *CL* clock) is the most efficient in terms of resources, and is free of any metastability. However, it can only be applied if the simple clocking strategy is employed. To face the proposed clocking scheme, which uses separate sampling points per ADC, the first solution is the preferred one because it takes advantage of the internal clocks relations to reduce the number of resources required, though the design requires special care to guarantee the timing constraints. The other two alternatives, which concept can be applied to any general asynchronous problem, increase the number of required resources. In addition, the double flopping does not eradicate the probability of metastability, whereas the memory alternative either demands many resources to mitigate the radiation effects, or is susceptible to them. Chapter 6 (Section 6.1) will present and compare the results of the implemented alternatives.

5.2.3.3 Reset policy

The power-on reset of the camera electronics has two purposes. First, it keeps the FPGA in reset state until other external components, especially the crystal oscillator, are initialized. Second, it ensures that the FPGA is in a known initial state after switching on. An improper reset policy or design of the reset circuitry may lead to irregular malfunctioning of the system.

Three aspects define the reset policy: whether the reset is synchronous or asynchronous, if it is global for the whole design or local, and the way of resetting different

clock domains. A review of all those points, as well as an assessment of their advantages and disadvantages can be found in Cummings et al. (2003). Kilts (2007), in Section 2.4, analyzes the impact of the reset policy on area occupation. Hereafter, we focus on presenting and justifying the policy proposed for the digital control electronics that is subject of study.

The external POR signal the FPGA receives is fully asynchronous. The optimum reset solution avoids the two problems associated with asynchronous resets, i.e., metastability during the release and de-assertion at different times for different flip-flops, but still benefit from the two asynchronous advantages, i.e., immediate response and independency of the clocks. The design creates an internal reset signal that shows an asynchronous assertion and a synchronous de-assertion. This signal is generated via a double flopping structure, as suggested by Cummings et al. (2003). Synchronization is carried out for each one of the three main clock domains of the design: *main* clock, *channel-link* clock, and *pixel* clock. Therefore, each part of the design is reset using the signal corresponding to its clock domain to avoid any metastability during de-assertion. Finally, the reset signal shall be distributed across the device. Given that the vast majority of the design modules belong to the *pixel* clock domain, this reset signal travels using a dedicated routing resource, which is hardwired over the whole FPGA array and provides low skew and low propagation delay. Thus, $POR_{Pixel\ CLK}$ is global but does not consume extra resources. On their part, the CL and main domains are smaller. Their reset signals can just be replicated to reduce the fan-out and distributed locally over different modules. Figure 5.11 shows the general scheme. The disadvantage of this policy is that different clock domains start operating after reset at different times because they are synchronized with different clocks. However, this does not cause any problem because critical inter-domain signals are synchronized before being used and the rest of signals are not critical.

5.2.4 Limitations

This section studies which factors limit the camera performance and identifies constraints arising from the proposed control electronics design.

Pixel rate Provided that image sensor and analog-to-digital converters can withstand higher operating rates, the pixel rate would be limited by the frequency of pixel and sampling clocks. Table 5.3 shows the result of the worst case static timing analysis of the implemented design, using the *mesochronous structure* as synchronization strategy. A proper design requires the frequencies being below the maximum speeds derived from this analysis to prevent from timing violations. In addition, frequency ratios among different clocks shall be preserved. Thus, the actual limitation comes from the *main* clock, which must run four times faster than the *pixel* clock, and twice than the *channel-link* clock. Therefore, the maximum frequencies are: $f_{Main\ CLK} = 153.1\text{ MHz}$, $f_{CL\ CLK} = 76.5\text{ MHz}$, and $f_{Pixel\ CLK} = 38.2\text{ MHz}$, which would lead to a frame rate of 14 fps after taking into account readout overheads. In case the number of sampling points is reduced from eight to four, the limitation is not the *main* clock but the *CL* clock, and the *pixel* clock could reach its maximum frequency in Table 5.3, which would result in a frame rate above 30 fps. A direct consequence of this increase in speed is an overall increase in noise. For example,

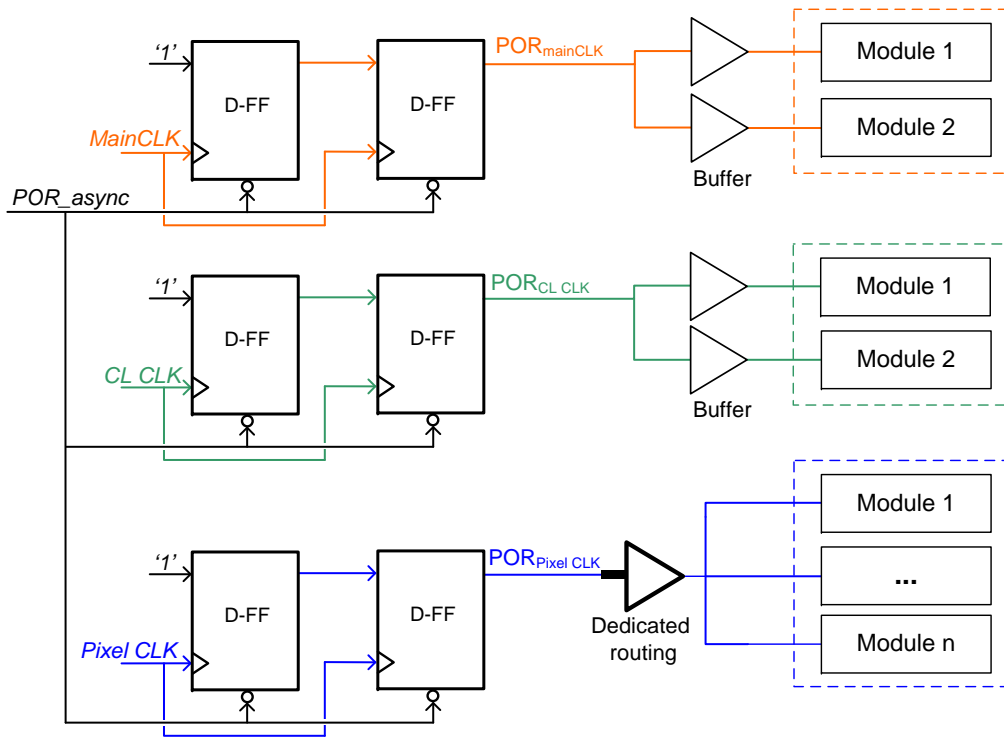


Figure 5.11. Power-on reset policy. Each clock domain holds its own reset signal. First stages contain the FFs that synchronize the reset de-assertion.

Table 5.3. Result of the Static Timing Analysis for the proposed FPGA design (worst case). Second column indicates the maximum frequency that would guarantee no timing violation in the implemented design, whereas the third one shows the default values for the camera.

Clock	Max frequency (MHz)	Def frequency (MHz)
Main CLK	153.1	120
CL CLK	181.2	60
Pixel CLK	83.3	30

digitization noise increases due to the higher jitter requirement associated to the faster readout. In addition, the power consumption of the camera would increase.

Output channels A second way of boosting the frame rate of the camera is via increasing the number of analog channels that come out of the image sensor. Assuming that the sensor can accommodate more outputs and that more converters are added to the electronics, the limitation lies in the FPGA area utilization, its number of input/outputs, and the power consumption, as well as in the external channel-link interface. Firstly, adding more channels requires more synchronization and acquisition modules, a more complex multiplexing stage for the different data streams, and more input/output pins. Table 5.4 details the area consumption in terms of flip-flops and the number of FPGA pins required for the proposed design, and estimates the case of increasing the number of channels to

Table 5.4. Digital control electronics design area and pin occupation (left). Right side shows an estimation of the total occupations in case the number of outputs of the sensor increases from two to four and eight, respectively. The area is estimated as the number of flip-flops because this is the limiting factor compared to the required combinatorial blocks.

Module	# FFs	# Pins		
Data manager	237	58		
Clocks manager	18	1		
Commands manager	220	–		
DACs controller	58	19		
SPI module	335	8		
HK ADCs controller	28	7		
IO & POR manager	6	1		
ISPHI controller	245	38		
Total	1162	132		

4 outputs		8 outputs	
# FFs	# Pins	# FFs	# Pins
1312	166	1612	234

four and eight, which would yield 22 and 44 fps, respectively. The area capacity of the selected *RTAX250* FPGA, with 1408 registers, is enough to easily implement the design for two channels. The four channels case would also fit but occupying more than 90% of the resources, while implementing the eight outputs case requires the use of a larger control device. In the same way, the number of user pins of the device package, which limit is 198, allows holding the two and four outputs design, but not the eight one, which needs a larger package. The advantage of increasing the number of channels with respect to speeding up the pixel rate is that the readout noise is not degraded. However, channel to channel differences contribute to the fixed pattern noise of the images. Moreover, the increase in power consumption is higher because additional discrete converters shall be added to the camera design. Finally, the channel-link interface would need either to be supplied with a faster clock or duplicated if its maximum bandwidth is exceeded.

Exposure time drift This requirement sets the maximum variation of the exposure time between modulation periods, which last a minimum of 0.5 s (see Section 4.2), to 5 μ s. The repeatability in frequency of the *main* clock provided by the oscillator ultimately drives the drift of the exposure time over a certain period. Crystal oscillators normally guarantee repeatabilities over a year or a wide range of temperatures better than 10 ppm, which means that a 120 MHz clock would deviate $\Delta = 83.3$ fs. Other factors that may influence the drifting of the exposure time, such as propagation delays dependence on temperature or radiation, present variations of the order of nanoseconds within long periods of time. Therefore, the exposure time drift requirement does not impose any difficulty to the design. In general, any camera with an electronic shutter control shall easily be compliant with the stability requirements, which, on the other hand, may be hard to reach with a mechanical shutter.

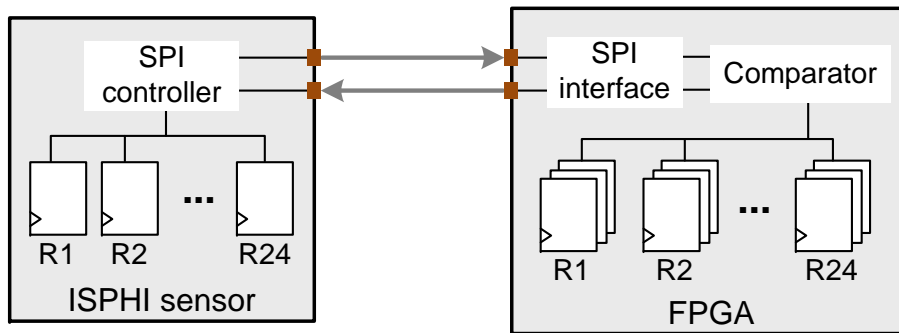


Figure 5.12. Image sensor protection against SEU: remote TMR.

Noise Given the proposed camera design, the noise mainly depends on the frequency at which the image is readout. Figures regarding the noise features that the overall design achieves as a function of frequency will be given in Chapter 6 (Section 6.1).

5.3 Enhanced functionality

This section introduces three additional features that improve or complement the basic camera specification. Two of them aim at protecting the image sensor against radiation, whereas the last one adds an extra operating mode to the default sensor operation.

5.3.1 Image sensor protection

5.3.1.1 Single event upsets

As most modern CMOS sensors, the ISPHI includes a set of internal registers that configure gains, reference voltages, and other parameters. Cost and size restrictions do not allow to harden these registers against radiation, which means that they are susceptible to single event upsets. This vulnerability does not exist in CCDs because they do not include built-in circuitry with registers.

To improve the tolerance of the sensor against SEUs, we propose to employ the TMR-protected registers of the FPGA to store a safe copy of all sensor's registers. The values stored on the sensor can be regularly read using the provided SPI interface (see Section 4.3), and compared with the values remotely saved on the FPGA. In case a discrepancy is found, the error is logged and that register is re-written with the correct value from the protected registers. This remote-TMR protection does not prevent the sensor from upsets, but automatically corrects them, thus avoiding functional interruptions due to upsets (SEFIs). Moreover, it allows logging errors and identifying register failures during radiation testing. Figure 5.12 displays the concept of the protection. The solution is similar to the scrubbing widely used to, for example, periodically update memory elements in SRAM FPGAs (Ostler et al. 2009), but customized and applied to the image sensor.

The drawback of the solution is the time gap introduced by the read, comparison, and write processes, which take about $14 \mu\text{s}$ and that shall not be done in parallel with the data acquisition to avoid additional noise contributions. However, the checking periodicity can be adjusted to reach a compromise between reliability and cadence. By default, the

system checks the status of the registers after every image acquisition. An additional mode permits to directly re-write all sensor registers, without performing a pre-check of the actual value. Chapter 6 (Section 6.4) presents the results during testing of this solution in a radiation facility.

5.3.1.2 Single event latch-ups

The ISPHI sensor is protected against latch-ups by design. However, the drastic consequences a SEL would have on the instrument motivate to additionally protect the sensor at camera level. This protection consists of monitoring the sensor's current consumption via an analog comparator integrated in the camera boards. In case the sensor consumption exceeds a given threshold, the FPGA receives a notifying flag. Immediately after the flag is asserted, the FPGA shall command a power down of main and secondary sensor supplies, disable the pixel supplies via DACs commanding, and stop the sensor clocking and signaling. Once the camera is in latch-up state, with the sensor off, it waits for a post-SEL switch on command to return to normal operation. During the post-SEL switch on, the inrush current of the sensor may momentarily exceed the latch-up threshold. Therefore, the protection mechanism shall consider this effect via adding an appropriate delay to prevent false SEL detections. The comparing threshold (SEL threshold) is configured by the FPGA via the DAC9 (Fig. 5.3), which allows compensating for possible consumption deviations due to aging or radiation effects. Given the criticality of this protection, it can be enabled or disabled by the user.

5.3.2 Snapshot shutter operating mode

The advantages and disadvantages of using either a rolling or snapshot shutter in the PHI cameras were analyzed in Section 3.4.3. We concluded that both solutions fulfill the minimum instrument requisites, but a snapshot shutter would allow running the acquisition in *continuous* mode, hence reducing the total cycle time. In Chapter 4 we justified the selection of a rolling-shutter image sensor as the most appropriate for PHI. This section analyzes a way of modifying the sensor operation so that it performs as if it would allow snapshot shutter exposures.

The pixel architecture of a 4T pinned-photodiode sensor, as the one used in the ISPHI, was shown in Fig. 4.1, where two memory elements are distinguished: photodiode and floating diffusion (FD). Table 5.5 (left) lists the steps required to operate the rolling shutter and the steps to implement the modified snapshot shutter (right). This emulated snapshot shutter provides an almost simultaneous exposure to light of all pixels of the array. However, it presents some disadvantages derived from the 4T pixel architecture:

- Correlated double sampling is not possible because the floating diffusions are used to store the image data, instead of the reset levels.
- Exposure time does not start at the same time for all rows, but there is a difference given by the fast reset and transfer operations, which take about 3 ms for the ISPHI sensor.
- The frame rate is reduced because read while exposing is not possible due to the fast reset.

Table 5.5. Rolling and snapshot shutter with 4T pinned-photodiode pixels: steps.

Rolling shutter	Snapshot shutter
Reset row 0	Fast reset of all rows (sequentially) (Start exposure of all rows)
Reset level stored in FD (Start exposure of row 0)	
Reset row 1	... wait exposure time ...
Reset level stored in FD (Start exposure of row 1)	
... wait exposure time ...	Fast transfer of pixel values to FDs (sequentially)
Readout FD reset values of row 0 Transfer integrated value to FD Readout FD	
Readout FD reset values of row 1 Transfer integrated value to FD Readout FD	Sequential readout of all FDs (reset level readout after pixel level)
...	

If one combines the modified snapshot shutter with a mechanical shutter that blocks the light during the fast reset and transfer, the exposure to light can be completely simultaneous for all rows. Nevertheless, the mechanical shutter would reduce the repeatability of the exposures and would require a motor controller.

Given all the disadvantages derived from the snapshot shutter operation, this solution would not improve the overall performance of PHI.

5.4 Assessment of radiation effects

All components in the camera electronics are exposed to some level of radiation that may affect their functionality and performance. Given the complexity of the digital control electronics, understanding how radiation influences the FPGA and the implemented design is vital to assure the success of the instrument. This section analyzes those radiation-induced effects. First, we explore the long-term effects caused by ionizing radiation. Second, we discuss the single event effects triggered by energetic particles and heavy ions. Finally, some mitigation techniques are proposed to deal with the most critical hazards.

5.4.1 Long-term effects

Ionizing radiation tests performed with the RTAX family of FPGAs demonstrate radiation tolerance with minimum degradation up to doses in the range of 200 to 300 krad(Si) (Wang 2007; Huang and Wang 2012). Hereafter we assess the impact of damage in every potentially degraded parameter: current consumption, propagation delay, input/output levels, transition times, and clocks, including jittering and duty cycle.

Current consumption As occurs in most CMOS circuits when exposed to ionizing radiation, the RTAX devices show an increase in current consumption with increasing dose. The power increment for the *RTAX250S* device after 300 krad(Si) irradiation is about 154 mW before annealing, and 57 mW after annealing (Wang 2007). These factors do not prevent the correct operation of the camera if they are taken into consideration while estimating the margins of the power budget.

Propagation delay The delay signals experience after passing through combinatorial blocks and propagating between consecutive flip-flops normally varies with induced radiation. RTAX test reports claim that these variations, after annealing, are always below 10 %, with most of the cases below ± 2.5 %, and only one irradiated sample out of sixteen (RTAX1000S) showing 6.2 % deviation. To assess whether this degradation can cause malfunctioning of the proposed design, one shall compare the worst case of degradation with the results of the static timing analysis given in Table 5.3. If one adds the extra propagation delay to the periods associated with the maximum frequencies in that table, the resulting frequencies shall still be higher than the goal operating ones (right column):

$$\frac{1}{f_{\max}} + \Delta t_{\text{prop}} < \frac{1}{f_{\text{goal}}}, \quad (5.2)$$

where t_{prop} is the delay associated to the most restrictive propagation path. Otherwise, a timing violation can occur. The most demanding case is the *main* clock, which maximum frequency is 153.1 MHz, i.e., the associated period is 6.53 ns. The static timing analysis calculates this period taking into account not only propagation delays but also setup times. After correcting from the setup time, the propagation delay becomes 6.22 ns. An increase of 10 % plus the same setup time results in 7.15 ns, which gives a maximum frequency of 139.8 MHz. Thus, the goal frequency of 120 MHz is still reachable after the worst-case delay degradation. The same can be checked for the *channel-link* and *pixel* clocks. In case the propagation delay decreases instead of increasing, the condition to be guaranteed is that the propagation delays shall still be longer than the hold time of the flip-flops. Using static timing analysis results for minimum delays, we obtain that the margin is more than enough to deal with a 10 % of delay decrease. Another consequence of the increase in propagation delay is that the sampling clocks experience a shift in time. Therefore, if the shift is large enough it may deviate the sampling point from its optimum position. However, since the camera provides a selectable sampling point and all points are equally shifted, high deviations could be corrected by selecting a more appropriate point.

Input/Output levels Both the threshold voltage of the FPGA inputs and the low and high levels of its outputs suffer from small variations after radiation. To cope with that, the output levels and input thresholds of all subcomponents that interface with the digital control electronics must exhibit enough margin. Since the variations lie well below 10 %, this margin is easily guaranteed.

Transition times The time it takes for the signals at the output of flip-flops to change from low to high and viceversa determines the slew rate. The effect of a slower slew rate is particularly important for the generated sampling clocks. Ideally the edges of the clocks

have infinite slope, which makes them immune to the addition of random noise. As the edge becomes slower, any noise contribution can alter the exact point in time at which the clock exceeds the threshold, thus leading to a contribution to the jitter. Since that jitter is a key parameter to keep the camera read noise under specifications, any degradation is relevant. Fortunately, RTAX radiation tests did not lead to any degradation of the transition times (Wang 2007).

Clocks: jittering and duty cycle We analyze potential degradations on the most critical clocks of the design: the sampling clocks. The direct relation of the jitter with the camera read noise was already discussed in Section 5.2.3. On its part, the duty cycle shall be as close to 50 % as possible to achieve optimum performance of the analog to digital converters (Kester 2005, Sect. 3.2). The camera employs track and hold ADCs, which means that a duty cycle other than 50 % makes either the tracking or holding stage shorter than normal. Therefore, the effective sampling frequency would be the one correlated to the shortest half of the cycle and the noise would increase. There is no evidence of long-term degradation of jitter or duty cycle in antifuse FPGAs when exposed to ionizing radiation. In particular, RTAX test reports and related publications do not address these effects. However, variations on jitter after ionizing dose are known to affect other components, such as phase-locked loops (PLLs) (Zhu 2008, pp. 72-73). In this case, we do not employ any PLL to generate the sampling clocks, and the jitter degradation of the crystal oscillator is minimal. As for duty cycle degradation, it has been only reported in commercial flash FPGAs (Kastensmidt et al. 2011).

5.4.2 Single event effects

Exceeding the criticality of long-term effects, SEEs have become the major concern when operating digital circuits in environments with high radiation levels. Although RTAX devices are radiation tolerant by design, under certain circumstances some effects can still appear and endanger the regular behavior of the design. Here, we review the potential effects, their significance, and assess how they may impact the camera design.

Destructive events Latch-ups (SEL) are the most common destructive events. The chosen FPGAs are tolerant to the events up to linear energy transfers above 100 MeVcm²/mg, thus they are considered to be immune by design.

Upsets in sequential logic These upsets occur when a particle passes through the area where a sequential block is located and alters its logic value. The RTAX FPGAs use local triple module redundancy in all user FFs, which means that each of them comprises three FFs sharing inputs, clock, and enable signals, and an output voter that decides in favor of the majority. Using this approach, devices are protected against single upsets in the registers. However, two cases remain unprotected: if the upset occurs in the output voter and if multiple upsets affect the same cell simultaneously. Consequently, devices show high tolerance against upsets, but are not completely immune. Although the upset cross-section of fully sequential blocks should not depend on operating frequency, the output voter induces this frequency dependence (Rezgui et al. 2009). At a certain LET, the higher

the frequency the larger the probability of upset. Most of the camera blocks, including the critical control modules, work in the *pixel* clock domain, which runs at a maximum frequency of 30 MHz. The high frequency domains at 60 and 120 MHz only perform data path and sampling tasks, thus being less critical in case an upset arises. Within the control modules, finite state machines (FSMs) are especially critical because an upset in the state register may send the machine to an invalid state and block its operation if it is not properly protected. The next subsection discusses the FSM protection. The image sensor latch-up protection and biasing are also of special concern because an upset on their circuitry may either prevent the turning off of the sensor in case of SEL, or apply improper bias voltages to the imager.

Upsets due to transients Single event transients (SETs) happening in combinatorial logic or routing nets can be latched by a sequential block and provoke upsets. Transient induced SEUs occur if the incident particle induces sufficient charge to produce a glitch that lasts long enough as to be sampled by the subsequent flip-flop. This type of upsets highly depends on the characteristics of the combinatorial circuit, such as net fanouts and number of combinatorial stages, as well as on the operating frequency (Berg et al. 2011). The local TMR protection is not able of mitigating transients because all three flip-flops receive the same inputs and all sample the same radiation-induced transients. These upsets have the same impact on the design than those induced in the sequential logic. In addition, a transient in the reset routing network may cause an undesired partly or complete reset of the design.

Clock upsets: glitch and jitter If a single event transient affects a global clock network, upsets can be generated in all or part of the flip-flops that belong to that clock domain. Two types of clock upsets can be induced: glitch and jitter (Steifert et al. 2005). The glitch upset is a transient in the clock signal that propagates into the clock input of one or more flip-flops and creates false samplings of the input data. Therefore, incorrect data may appear at the output of the FFs. Rezgui et al. (2009) study the worst-case susceptibility of dedicated routing resources in RTAX FPGAs to glitch upsets. On its part, jitter upsets occur if radiation injects charge in a clock node close to the clock edge, thus randomly shifting the edge and producing jitter in the sampling. As a result, data may be sampled too early and a timing setup violation may take place. The jitter upset only affects paths which timing is close to the maximum, so that a small shift in the clock edge may sample the transition of the input data. This case is unlikely in the camera design because, as derived from the static timing analysis (Table 5.3), there is a margin between default and maximum frequencies.

5.4.3 Mitigation techniques

Once the previous sections identified the most critical parts of the design, hereafter we discuss a set of techniques to minimize the impact of the radiation-induced effects on those parts.

Several finite state machines control the sequential execution of tasks on the digital control electronics. For example, the readout and exposure sequence of the image sensor or the cyclic redundancy checking of the SPI communication are partly governed by

FSMs. To prevent the FSMs to change state after a SEU alters one bit on the state registers, we codify the states using a *one-hot* encoding instead of a sequential one. This encoding maps the valid states so that only one bit of the state vector can be active at a time. If there is a bit flip after a SEU, either two bits are active or all are inactive, thus the error can be detected and the machine can be sent to a safe state and automatically recovers the functionality. The case of multiple upsets affecting the same state vector could not be detected and may provoke a jump to another valid state, but not to an invalid one. Therefore, this encoding guarantees that the machine does not get stuck after a single upset. The implementation of the *one-hot* encoding requires N registers to map N machine states, whereas the sequential encoding only requires $\log_2(N)$ registers to map the same number of states. On the other hand, the *one-hot* case uses less decoding resources to jump from one state to the next because a single active bit defines the current status.

The image sensor latch-up protection and biasing were also identified as critical, especially in the case of single event transients, for which the FPGA does not include protection. Since the sensor latch-up flag and the DACs triggering run at low frequency, the induced transients can be filtered via a guard gate as suggested by Rezgui et al. (2007) for flash FPGAs, without risk of causing timing violations. Using this measure, only those transients that last long enough as to avoid being filtered could induce an upset. However, the probability of occurrence of those cases is very low as to include additional mitigation methods.

Finally, transients affecting the reset routing network may cause a partial or complete reset of the design. If there is a complete reset, the current operation stops but the camera status remains being known. However, a partial reset can lead to an state where some modules are waiting for inputs from others that have been reset, thus reaching a blocking situation. To avoid these situations, the main reset of the design was routed via a dedicated low skew routing resource, which are considered hardened by design. In case a transient occurs, the very low skew of the network assures that every flip-flop is reset and the partial blocking situation is avoided. The camera design uses the dedicated routing network to distribute the reset in most of the design (*pixel* clock domain), and normal routes for the *channel-link* and *main* clock domains. Nevertheless, as mentioned before, the last domains only contain data path circuitry, which would not induce any blocking situation if partially reset.

5.5 Conclusions

As primary tasks, the camera electronics controls the image sensor via signaling, clocking, and biasing, and digitizes the pixel data through analog to digital converters. In addition, it provides commanding and data communication links to the instrument main unit and is in charge of acquiring, collecting, and distributing housekeeping values. The digital control electronics manages all above-mentioned tasks, thus playing a key role in the accomplishments of the camera specifications. The digital design is based on an antifuse field programmable gate array because it yields the best compromise on cost, time, reliability, and performance.

Apart from the basic functionality, the FPGA design is driven by the optimization of two main performance parameters: digitization noise and speed, which shall assure the

readout noise and frame rate specifications of the camera, respectively. One can minimize the digitization noise via controlling the sampling position and jittering of the FPGA generated sampling clocks. To tackle the first point we propose the use of a flexible sampling point that allows optimizing the sampling even if there are environmental dependencies. The second point is addressed via comparing two alternatives, a straight forward solution and a proposed optimized one, which adds complexity but is expected to produce better noise figures. Test results will be discussed in Chapter 6.

Another critical point of the design is the data acquisition from the two analog to digital converters, synchronization, and posterior multiplexing into a single data line. Four synchronization strategies applied to this particular problem have been described and compared. Two of them are selected as the preferred ones depending on the used clocking strategy. We propose the so-called *shifting of the CL clock* solution in case the straight forward clocking strategy is employed, and the *mesochronous structure* if the proposed optimum clocking strategy is implemented.

The limitations analysis of the FPGA design suggests that it could drive a camera with an improved sensor running at up to 14 or 22 fps if the clock frequency or the number of outputs increases, respectively.

Two enhanced functionalities were added to the design. First, to overcome the lack of protection of the image sensor against single event upsets, we introduced a mechanism that prevents the camera from single event functional interruptions via a remote triple modular redundancy of the internal sensor's registers. In addition, the current consumption of the sensor is continuously being compared with a given threshold to automatically switch off the sensor in case of latch-up. The second enhanced functionality is related to the shutter. Although the image sensor presents a rolling shutter, one can modify the clocking and signaling scheme of the sensor to make it performing as if it would be a true snapshot shutter sensor. The drawbacks of this operating mode include an increase in noise and a decrease in frame rate.

Regarding radiation effects, long-term degradation does not impose a performance or functionality risk to the camera design. On the other hand, since the employed FPGA only includes built-in protection against single event upsets on sequential blocks, single event transients represent some risk. Control finite state machines, sensor latch-up protection, and sensor biasing are identified as the critical modules of the design, to which additional mitigation techniques shall be applied. Additionally, the reset network also requires special measures.

Finally, the design alternatives introduced in this chapter as well as the compliantness of the camera performance shall be evaluated and tested using the real camera. Next chapter will address those points, including:

- Sampling point testing and evaluation of ADCs clocking approaches.
- Post-testing comparison of proposed synchronization alternatives.
- Overall noise measurements.
- Test of image sensor protections against SEU and SEL.

6 Camera tests and space qualification

After having derived the camera performance and environmental requirements in Chapter 3, described the selected image sensor in Chapter 4, and presented the camera electronics design in Chapter 5, this chapter discusses test and qualification results that interrelate those previous chapters. First, we evaluate the performance of the camera electronics and the usefulness of its optimizations. Second, the selected image sensor is characterized and, in third place, its radiation tolerance is assessed. Finally, all results are compiled and compared with other scientific cameras in space.

The author original work in this chapter accomplishes the goals (g5) and (g6) of the thesis and includes the major contribution (c4). See Section 1.1 for details.

Ample parts of Section 6.4 have been literally published in proceedings of the Society of Photo optical Instrumentation Engineers under the following reference:

J. Piqueras, K. Heerlein, S. Werner, R. Enge, U. Schühle, J. Woch, T. De Ridder, G. Meynants, B. Wolfs, G. Lepage, and W. Diels, "*CMOS sensor and camera for the PHI instrument on board Solar Orbiter: evaluation of the radiation tolerance*", High Energy, Optical, and Infrared Detectors for Astronomy V, Editors: Andrew D. Holland and James W. Beletic, Proc. SPIE 8453, 845314 (2012), doi:10.1117/12.925403.

6.1 Electrical tests

This section assesses the performance of camera electronics and image sensor in terms of read noise, dynamic range, and operating frequency. Furthermore, we discuss the outcome of testing the clocking schemes and synchronization strategies proposed in the previous chapter. Finally, we quantify the power consumption of camera and sensor under different operating conditions.

6.1.1 Camera read noise and pixel sampling

Chapter 5 presented the camera requirements with respect to front-end electronics noise, speed, and dynamic range (see Table 5.1). The concept of flexible sampling point was proposed to optimize the pixel sampling on high speed sensors and the digitization noise was identified as one of the main sources of FEE noise. In addition, two ADC clocking schemes were presented as design solutions.

Two aspects motivate the sampling point concept: finding the instants at which the analog pixel outputs are settled and compensating for deviations due to environmental conditions (temperature and radiation). Figure 6.1 proves the usefulness of the concept through the projection of an optical target on the sensor. Electrical transitions from one

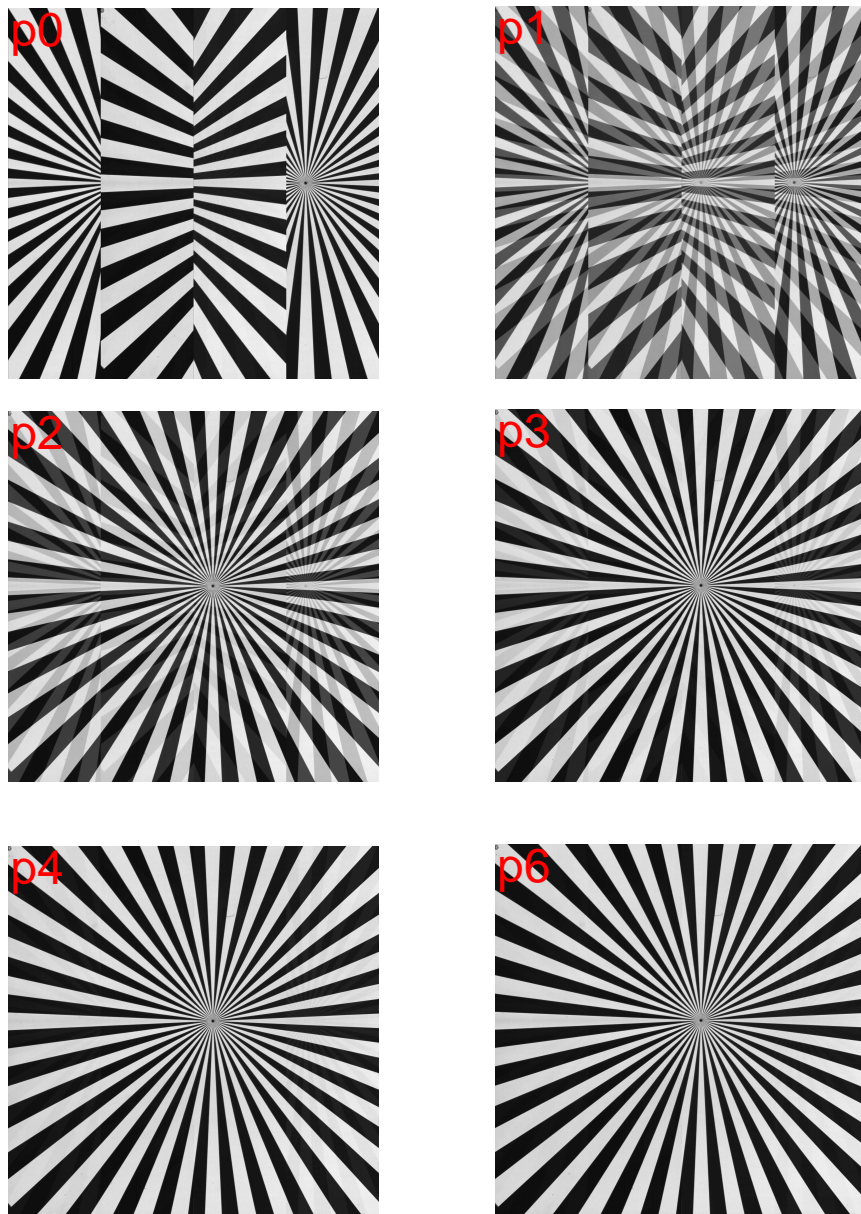


Figure 6.1. ISPHI star-target image versus sampling instant. Early sampling points (e.g., p_0) result in corrupt images because pixels are sampled before they have appeared at the sensor's outputs. Therefore, digitized samples correspond to the previous pixels, which because of the output multiplexing of the sensor belong to different quadrants of the image (Fig. 4.3). Points from p_1 to p_4 sample the transition from previous to current pixels, with p_5 to p_7 samples being free of previous pixel spurious contributions. Both ADCs share the same sampling point in these images.

pixel to the following are not sharp in time because of the limited current of the output drivers and the load capacitances, which comprise ADC inputs and PCB tracks. Thus, the delay applied to the sampling instant shall be enough to avoid spurious contributions from previous pixels (points p_5 to p_7 are optimum in this case). As anticipated, tem-

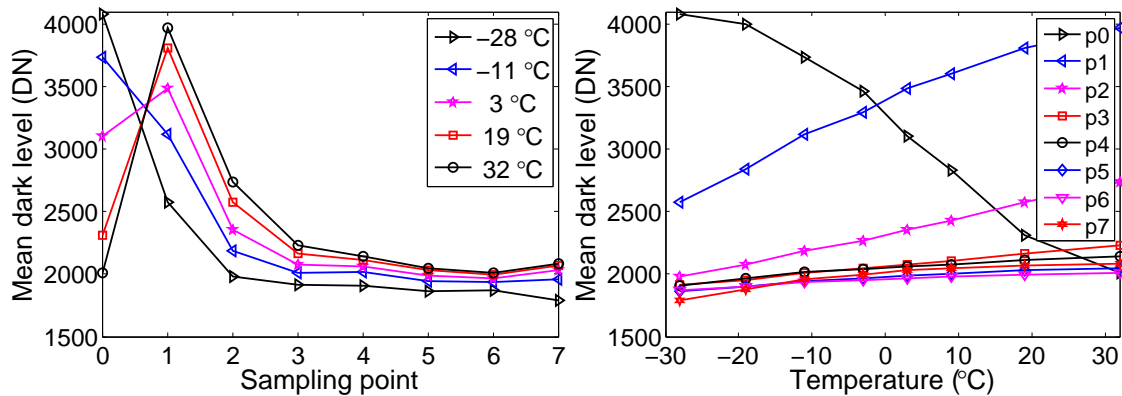


Figure 6.2. Effect of the sensor operating temperature on the optimum sampling point. The mean level of a dark image does not fluctuate severely when pixels are sampled in their settled region (e.g., p_4 to p_6). On the other hand, sampling closer to the transition region of the pixels leads to higher mean levels because of the combined contributions of previous and current pixel. Left graph shows how the transition region between two consecutive pixels (level peak) varies with temperature. Right plot represents the same idea but displaying the smooth evolution of each sampling point dark level with temperature. During this test the ISPHI sensor was cooled down via a cold finger attached to its bottom side, whereas the rest of camera electronics, which is separated from the cold element, only suffered from minimal temperature variations.

perature variations modify the position of the sampling points with respect to the pixel outputs (Fig. 6.2). Low temperatures (below -10 °C) show high mean dark levels, which correspond to the transition unstable region, at earlier sampling points than high temperatures do (Fig. 6.2, left plot). As temperature increases, the transition from previous to current pixel changes from point p_0 to p_1 (Fig. 6.2, right plot). Thus, we conclude that higher temperatures increase the delay of the analog output channels of the sensor (Fig. 6.3). Although Figure 6.2 suggests that points p_3 to p_7 can safely sample the pixels, independently of the temperature, it shall be noted that a small increase in the mean dark level is seen as a noticeable ghosting in the images if the target is not homogeneously dark (Fig. 6.1) and, hence, increases the overall image noise. Consequently, the modest delays caused by the operating temperature can have a negative impact on the overall noise of the camera system if the sampling point is not adjusted accordingly. Moreover, this test evaluated only the effect of temperature variations on the image sensor, but it is known (see Section 3.2.2) that the rest of front-end electronics components, such as the FPGA that generates the sampling clocks, will undergo severe temperature gradients during the mission that also alter the clocks sampling instants.

Static tests with the camera electronics have allowed evaluating the digitization noise at two operating frequencies and employing the two studied clocking strategies: simple and proposed (Fig. 6.4). The test setup consists of an emulator board with the same pin-out as the ISPHI sensor package that is plugged in the sensor board of the camera. This board feeds the ADCs with different combinations of fixed voltages. Ideally, if fixed voltages are applied to the converters, all sampling instants should lead to the same level of digitization noise. However, this is not the case if interferences or additional sources of noise affect the system. The simple clocking strategy presented in Section 5.2.3.1 results in a noise pattern caused by interferences and potential reflections in the ADCs clock dis-

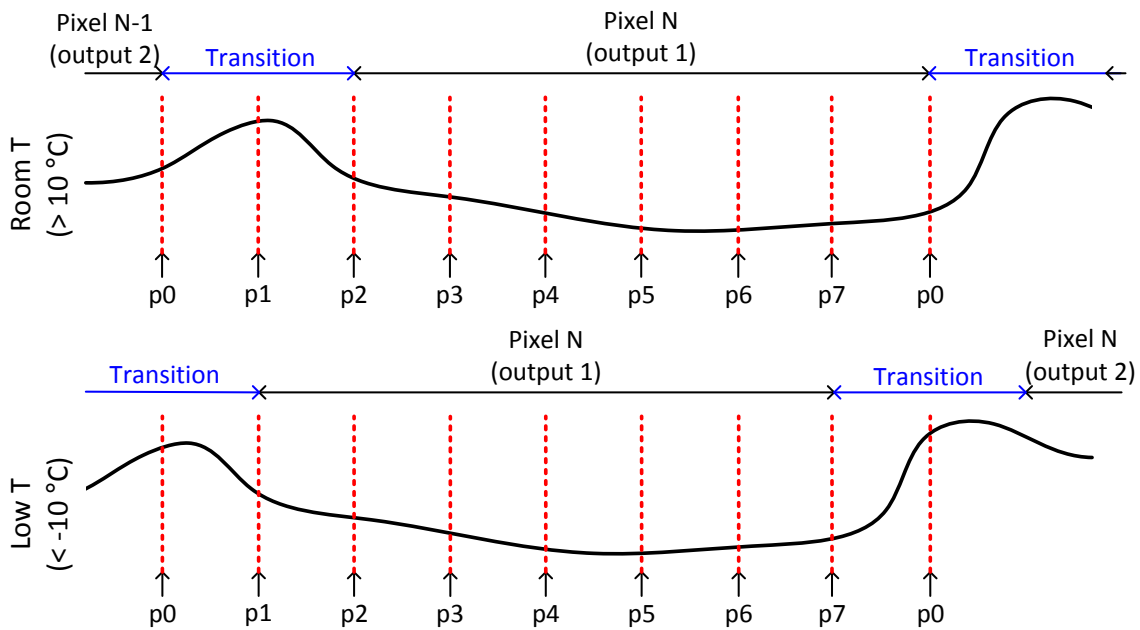


Figure 6.3. Interpretation of the temperature effect on the sampling point. Higher temperatures add higher delays to the analog pixel output of the sensor.

tribution (Fig. 6.4, b). As a result, the measured digitization noise shows a dependency on the sampling point and, in most cases, is higher than the required one even at half frequency (Fig. 6.4, a). Given that the interference pattern in (b) is fix under same operating conditions, one can remove it via subtraction of two consecutive frames. The resulting noise, after being compensated from the increase factor due to the subtraction, is then very close to the camera specifications at full speed and does not show a strong dependency on the sampling point (Fig. 6.4, c). Finally, the proposed sampling strategy leads to noise figures well below the required limit (Fig. 6.4, d). In consequence, the proposed sampling scheme, where clocks are independent for each converter and distributed via differential signaling, is more adequate to assure the minimum noise requirements of the camera. The same test could have been repeated but employing dynamic voltage patterns at the input of the ADCs to evaluate a worst case of noise measurement. However, this dynamic mode, which is controlled by a clock, introduced additional interferences in the emulator board, with the results being non-representative of the real noise. Therefore, the dynamic noise measurements were carried out using the sensor.

One can measure the overall read noise of the camera system via acquiring dark images at very short exposure times. Either the variation of level of individual pixels during a long sequence of images is calculated and then averaged across pixels, or consecutive dark images are subtracted to remove the fixed pattern noise contributions and the variation across pixel of the resulting image is computed. Figure 6.5 shows the results for each sensor output of the ISPHI and at two different operating frequencies (right plot). Outputs 1 and 2 correspond to ADC 1 whereas 3 and 4 are digitized by ADC 2. The optimum sampling point p_6 has been used for the acquisitions. The results are well within specifications for both image sensor and camera electronics.

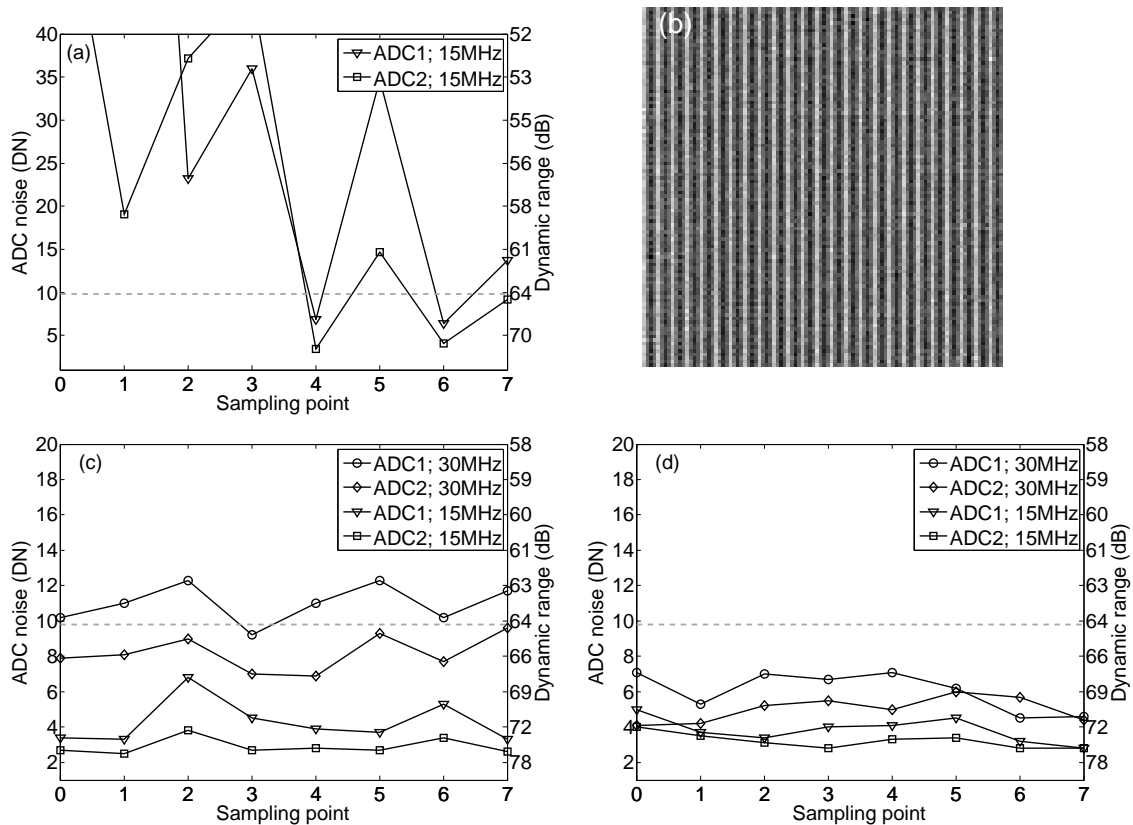


Figure 6.4. Digitization noise versus sampling scheme. The noise is measured within consecutive samples via applying fixed low-noise voltages to the analog inputs of each ADC. Plot (a) shows the noise, and corresponding dynamic range, measured at the lower camera frequency (15 MHz) and employing the simple ADC clocking strategy. Graph (b) displays the interference pattern that results from the simple clocking strategy and leads to the high noise plotted in (a). Ideally pattern (b) should be fully uniform. The same measurements for the simple strategy but after removing the fixed interference pattern, via subtraction, are shown in graph (c). Finally, plot (d) represents the noise and dynamic range measurements using the proposed clocking strategy (see Section 5.2.3.1). The dashed gray line indicates the noise/dynamic range requirement for the camera system.

6.1.2 Data acquisition and synchronization

Section 5.2.3.2 described the main issues associated to the FPGA retrieving of digitized data from the analog-to-digital converters. In particular, that section discussed the necessity of delaying the clocks used to sample the analog data on the converters before sampling the digitized pixels and presented a set of solutions to synchronize the data streams from both ADCs into a common clock domain.

The pixel readout frequency at full speed is high enough as to be able of falsifying the digital pixel acquisition because of delays associated to propagation of ADC output data and sampling clocks (see Fig. 5.7). Therefore, to avoid spurious pixels, the clock used to acquire the digitized data inside the FPGA shall present an additional delay with respect to the sampling clock (Fig. 6.6). At room temperature, a delay of $2 \Delta s$ is sufficient, with Δs being the separation between contiguous sampling points. Given that the set of

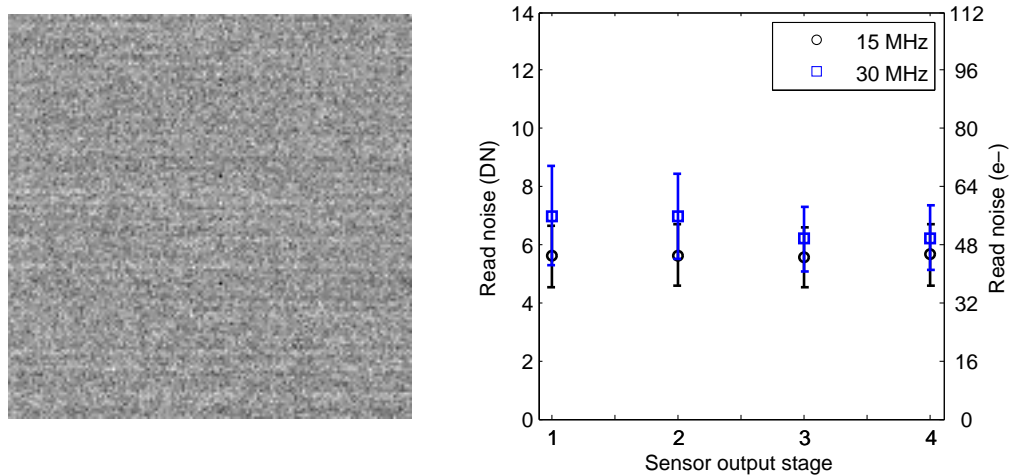


Figure 6.5. Overall camera read noise versus frequency at room temperature. This measurement includes both image sensor and camera electronics contributions. Left side shows a dark image taken with very short exposure time after being corrected from fixed pattern noise via subtraction (30 MHz). Therefore, the noticeable spatial noise is read noise. Right graph plots the read noise figures calculated for each output stage of the sensor (1 to 4) and at maximum and half operating frequencies. The right axis translates the ADCs digital numbers to electrons using the conversion gain that will be estimated in Section 6.2.

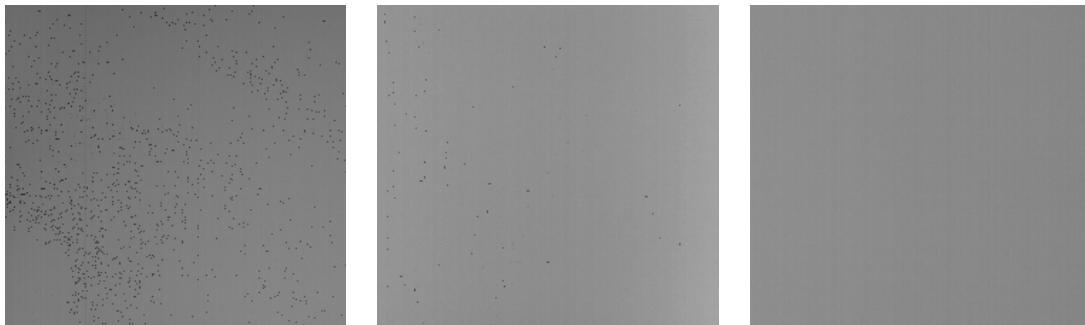


Figure 6.6. Acquisition of digitized pixels at room temperature. Wrong pixels appear if ADCs outputs are sampled using the same clock internally generated to sample the analog pixels, i.e., $SampCLK(p_i)$ (left image). Delaying the sampling clock by one discrete step, i.e., $SampCLK(p_{i+1})$, results in a smaller number of corrupt pixels (central image), whereas using a clock delayed by two discrete steps, i.e., $SampCLK(p_{i+2})$, produces no wrong pixels (right image).

delays that affects the ADC data and clock signals depends on operating temperature, the compensating clock delay must be flexible during the mission.

We have tested three out of the four synchronization strategies presented in the previous chapter: *shifting of CL clock*, *mesochronous structure*, and *double flopping*. The last strategy, *dual-port memory*, was not implemented because the preceding ones were successful and its testing would not add any special advantage. The *shifting of CL clock* approach, which applies only to the case of simple clocking strategy of the ADCs, provided an easy and successful way of synchronizing the data. However, as described in

Table 6.1. Camera power consumption versus operating mode and frequency.

Pixel frequency (MHz)	Operating mode	Power cons (W)
15	Stand-by	1.03
	IS biased	1.38
	Acquiring	1.70
30	Stand-by	1.13
	IS biased	1.55
	Acquiring	1.94

Chapter 5, the phase of the channel-link clock changes every time either the sampling clock or the operating frequency is varied, which results in a temporal loss of the CL synchronization after one of those changes. All subsequent images after the loss are correctly acquired. The *mesochronous structure* worked properly for all combinations of sampling points. The adjusting of ± 1 clock cycle between the data retrieved from each ADC, which may be needed when each ADC channel uses a different sampling clock, showed a logical dependence on the employed sampling points. Finally, the *double flopping* synchronization also ran correctly. Nevertheless, the test required the manual adjusting of the ± 1 data clock cycle for each ADC. This adjusting did not show a predictable dependence on the sampling point, though it was kept fixed during the whole one-hour acquisition test. Metastabilities during the sampling of the data by the first FF provoke that unpredictability. In conclusion, the *mesochronous structure* is the preferable solution because it performs successfully without manual adjustments, employs a relatively low number of resources, and allows using the low-noise clocking strategy for the analog-to-digital converters.

6.1.3 Power consumption

Both cost of space missions and thermal stability of spacecrafts become negatively affected when the power consumption of onboard instruments exceeds the allocated budget. Therefore, designers shall keep this factor below strict margins. The camera operating mode and the pixel frequency influence the power consumption of camera electronics and image sensor (Table 6.1). The pixel frequency has a direct impact on the consumption of the whole readout chain, including image sensor, FPGA, analog-to-digital converters, and channel-link serializer. Power increases likewise as the ISPHI is biased and images are being acquired, which is the most demanding operating mode.

The power consumption of the FPGA can be minimized via applying appropriate design techniques. For instance, stand-by consumption decreases if control electronics disables the clocking of the analog-to-digital converters. In the same way, flip-flops shall include enable signals so that only FFs directly involved in acquiring images consume dynamic power during acquisition.

Table 6.2. Electro-optical characterization: summary of measurements. The characterization was carried out employing the camera model with the proposed clocking strategy, the mesochronous synchronization strategy, at full speed (11 fps, full frame), sampling point p_5 on both ADCs, and a science grade ISPHI sensor. Test column specifies which section covers the test method and results for each parameter.

Parameter	Unit	Test
Conversion gain	DN/e^-	Section 6.2.1
Non-linearity	%	Section 6.2.1
Full well charge	e^-	Section 6.2.1
Read noise	e^-	Sections 6.1.1, 6.2.1
Dark current	e^-/s	Section 6.2.2
DCNU	%	Section 6.2.2
Offset FPN	e^-	Section 6.2.2
PRNU	%	Section 6.2.3
Sensitivity	%	Section 6.2.3

6.2 Electro-optical characterization

Most of the electro-optical parameters of the camera exclusively depend on the performance of the image sensor (see Table 2.4). However, it is of vital importance for the outcome of the instrument to properly characterize them and understand their behavior under appropriate operating conditions. This section covers the analysis and presentation of results for all parameters summarized in Table 6.2.

6.2.1 Conversion gain and linearity

Test setup and data set Environmental conditions were room temperature and air pressure. A halogen lamp plus a 550 nm optical filter and a set of lenses provided uniform illumination over the sensor's sensitive area (flat-field). Lamp intensity was kept fixed during the test and exposure time varied from the shortest one ($\approx 90 \mu s$) to well beyond saturation (≥ 1 s) in $N_{t_{exp}} = 20$ steps. At each exposure time, $N_{im} = 60$ consecutive images were acquired.

Analysis method

1. Conversion gain is estimated using two different methods: photon transfer curve (PTC) linear and PTC non-linear estimation. A concise explanation and comparison of these and other methods can be found in Bohndiek et al. (2008), and a detailed description of the PTC analysis in Janesick (2007), Ch. 4-5. These methods also allow deriving read noise and full well charge.
2. Non-linearity requires correcting the image levels at each exposure time from the offset fixed pattern noise. Then the average image level is plotted versus exposure time and the best linear fit to this curve is calculated. Deviations of the real curve from the fitting indicates the non-linearity. The maximum signal level at which that non-linearity exceeds 2% defines the linear full well charge (Table 3.6).

Results Once the offset FPN contribution is removed, the most significant noise contributor to the total camera noise changes with signal level. This allows defining four noise regimes: readout, shot, fixed pattern noise, and saturation (Fig. 6.7, left). The readout regime appears at very low signal levels (S), where the shot noise \sqrt{S} is negligible. Since the readout noise is independent of the signal, it appears as a horizontal line at the readout noise level ($\sigma_{\text{read}} = 6.013$ DN) in the PTC diagram. As signal increases the shot noise starts influencing the total noise, which results in the shot regime. Given that the shot noise follows a Poisson distribution, the slope in log scale is $1/2$. From the shot noise to signal relation the conversion gain can be obtained as explained in Janesick (2007), Ch. 4-5, leading to the values shown in Fig. 6.7 (right). The third regime is dominated by signal dependent fixed pattern noise, which increases linearly with slope = 1. Finally, the image sensor reaches its maximum full well charge and saturates. This condition defines the fourth regime, where noise rapidly decreases or increases with signal depending on the saturation differences among pixels. The saturation full well charge can then be retrieved as $FWC_{\text{sat}} = 11700$ DN. Using the right graph and taking the more accurate non-linear estimation of the conversion gain, noise levels and low signals can be converted with $C_g(N) = 0.119$ DN/ e^- , whereas for higher signal levels we shall use $C_g(S) = 0.1175$ DN/ e^- . As a result, the camera's read noise becomes $\sigma_{\text{read}} = 50.53$ e^- and the saturation full well $FWC_{\text{sat}} = 99575$ e^- .

Once the conversion gain is known, the linearity of the camera response to light as well as an accurate value of the linear full well charge, i.e., the point at which non-linearity exceeds a defined threshold, can be calculated. Saturation curves provide a visual measurement of the linear response as well as a starting point to compute the non-linearity via curve fitting (Fig. 6.8, left). The linearity deviations lead to a linear full well charge given by the intersection of curves with the 2% criterion on the right graph, resulting in $FWC_{\text{linear}} = 95250 \pm 250$ e^- . This value is slightly below the 10^5 e^- specification.

6.2.2 Dark current and offset FPN

Test setup and data set The experiment took place in a vacuum chamber with controlled temperature at the bottom side of the image sensor via a cold finger element. The environment was completely dark. Temperature was scanned from -40 °C to $+30$ °C in steps of $\Delta T \approx 10$ °C, leading to N_T temperature points. At each temperature, exposure time varied from the shortest one to above 1 min in $N_{\text{exp}} = 25$ steps, taking $N_{\text{im}} = 25$ images per exposure time.

Analysis method

1. At each temperature T_i with $i = \{1, \dots, N_T\}$, compute bias image $\mathbf{I}_{\text{bias}}(T_i)$ via averaging pixel by pixel the N_{im} frames taken with the shortest exposure time (t_0). $\mathbf{I}_{\text{bias}}(T_i)$ only contains offset FPN contribution because read noise is removed via averaging.
2. Repeat the averaging process of the previous step for the rest of exposure times t_j , with $j = \{1, \dots, N_{\text{exp}} - 1\}$. Resulting images $\bar{\mathbf{I}}_{\text{dark}}(T_i, t_j)$ are free of read and dark shot noise.

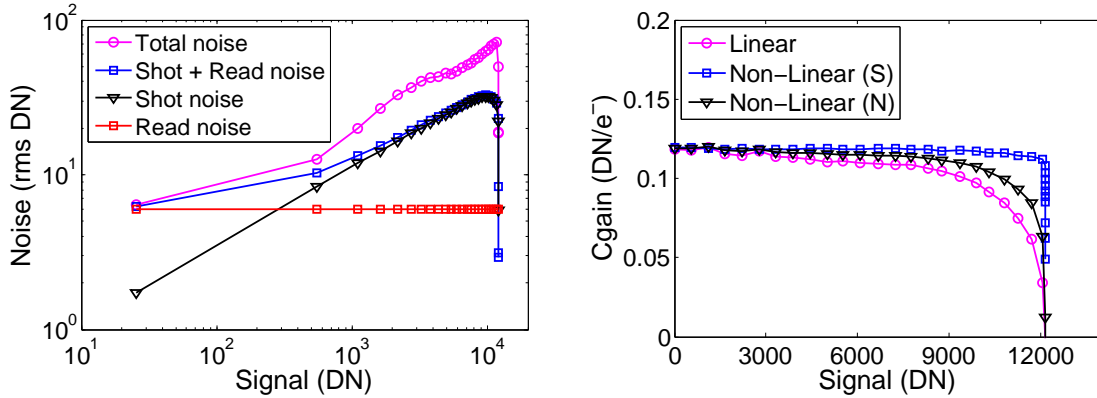


Figure 6.7. Photon transfer curves and conversion gain. The PTC curves detail the noise components of the camera as a function of the signal from dark level until saturation (left plot). At very low signal levels, read noise dominates the total noise. As signal increases, photon shot noise, which shows a slope of 1/2, starts modulating the total noise until the fixed pattern noise contribution takes over for higher signal levels (slope becomes 1). Finally, the sensor reaches saturation and the noise dependencies with signal fall off. The conversion gain derived from the shot noise PTC curve shows a small dependency on signal level because of the intrinsic non-linearity of CIS sensors (see Janesick 2007, Ch. 7). The non-linear estimation method compensates for that non-linearity and provides more accurate conversion gain values for converting low signals (noise, N) and higher signals (S) (right plot).

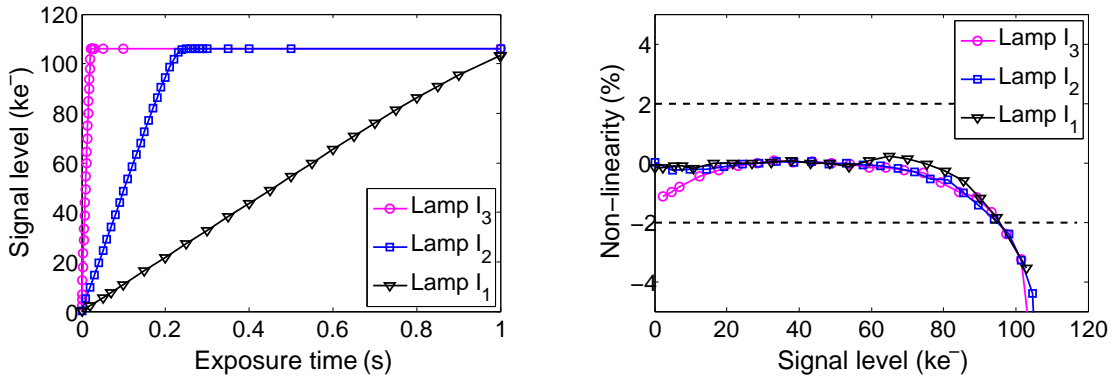


Figure 6.8. Saturation curves and linearity. Under flat and fixed illumination conditions, the camera responses linearly to increasing exposure time from darkness until saturation. Stronger light intensities lead to steeper slopes and earlier saturation (left plot, variation from I_1 to I_3). The non-linearity on the saturation curves is displayed in the right graph, with the dashed horizontal lines being the indicators of maximum allowed non-linearity, i.e., linear full well charge condition. The conversion gain factor derived from Fig. 6.7 have been used to translate the shown signal levels to electrons.

- Each averaged dark frame is corrected from bias via subtraction to remove the offset FPN: $\bar{I}_{\text{dark-offset}}(T_i, t_j) = \bar{I}_{\text{dark}}(T_i, t_j) - I_{\text{bias}}(T_i), \forall i, j.$

- Dark current rates in DN/s arise from the slopes of the curves $\bar{S}_{\text{dark-offset}}^{(\bar{x}, \bar{y})}(T_i, t_j)$

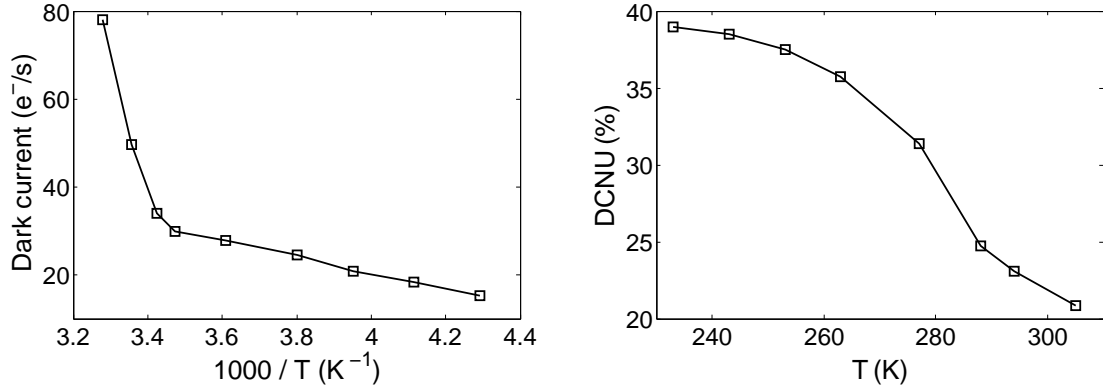


Figure 6.9. Dark current and DCNU versus temperature. Rate of thermal current generation shows two regimes (left plot). At high temperatures - above 290 K - dark current rapidly increases as temperature does, with the DC level doubling every ≈ 8 K, whereas at lower temperatures the generation slows down. Conversely, dark current non-uniformity relative to dark current decreases at higher temperatures because of the high levels of DC (right graph).

versus t_j at each temperature T_i , where $\bar{S}_{\text{dark-offset}}^{(\bar{x}, \bar{y})}(T_i, t_j)$ is the mean pixel value in $\bar{I}_{\text{dark-offset}}(T_i, t_j)$ calculated across a selected area of the image (\bar{x}, \bar{y}) . The conversion gain calculated in Section 6.2.1 allows translating the results to e^-/s .

5. Dark current non-uniformity is the slope of the curves $\sigma_{S_{\text{dark-offset}}^{(\bar{x}, \bar{y})}}(T_i, t_j)$ versus t_j , where the standard deviation instead of the mean value is calculated in this case. The results at each temperature T_i are normalized by the dark current rate to get the DCNU expressed in %. Bad pixels are identified as those deviating more than 10 times the standard deviation from the mean value, and are not taken into account for the DCNU calculation.
6. The offset FPN at each temperature is $\sigma_{S_{\text{bias}}^{(\bar{x}, \bar{y})}}(T_i)$. Depending on the area of the image used to compute the offset FPN, it is *global* if pixels come from the whole array, *local* per output stage if pixels belong to a single output stage of the ISPHI, or *column* if pixels come from the same image column. Results are translated from *DN* to e^- using the conversion gain factor.

Results The mechanism that dominates the thermal generation of dark current in the sensor changes depending on the operating temperature range (Fig. 6.9, left). Three main mechanisms contribute to dark current generation: surface, depletion, and diffusion (Janesick 2001, Section 7.1.1). Given that pinned photodiodes, such as the one used in the ISPHI, reduce the surface thermal generation, only depletion and diffusion participate in the dark current response versus temperature. In particular, diffusion dominates at higher temperatures (Blouke 2012), where dark current level doubles every ≈ 8 K, while depletion takes over below 290 K, with a rate of $\approx 2.67 e^-/s/K$. At room temperature, the sensor shows a dark current level of about $60 e^-/s$, which is well below the instrument requirement (Table 3.6) and the sensor specification (Table 4.2).

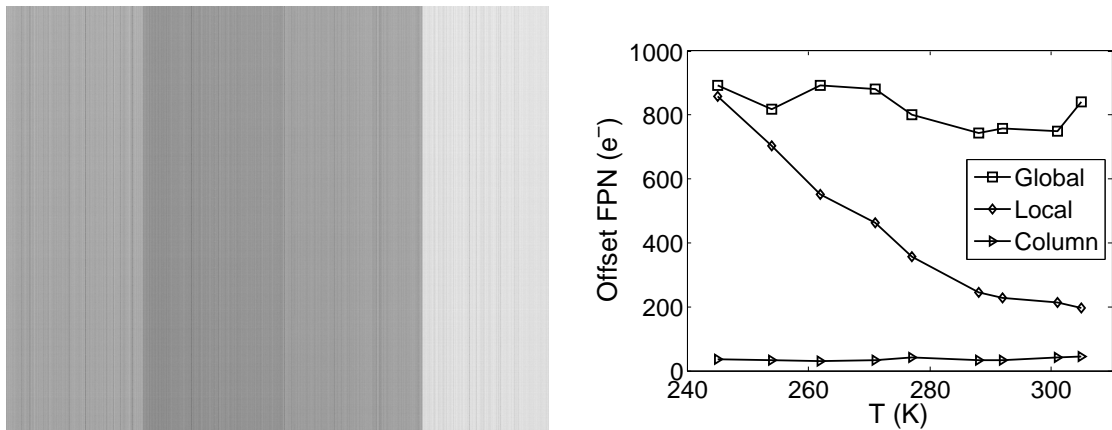


Figure 6.10. Offset fixed pattern noise versus temperature. Left image is a dark frame that shows the two main contributors to the offset FPN: vertical quarters that globally divide the image, which originate from the output stages of the sensor, and local column to column variations that arise from the column gain stage of the ISPFI (see architecture in Fig. 4.3). Sensor’s column gain stage shows a dependency on temperature that modulates the *Local* FPN, whereas the *global* contribution does not show such an explicit tendency (right plot). *Column* FPN remains below the readout noise level for the whole temperature range.

Spatial non-uniformities on the dark current are higher at higher temperatures if they are calculated in absolute terms. Dark current levels decrease with temperature at a faster rate than non-uniformities do. Therefore, when those non-uniformities are normalized by the dark current level, lower temperatures result in larger relative non-uniformities (Fig. 6.9, right).

All three contributors to the offset FPN do not show the same trend with temperature (Fig. 6.10). *Column* FPN keeps constant with temperature and is at the level of the readout noise of the sensor. Therefore, this component would not dominate the image pattern even if global and local FPN would not exist. *Local* FPN increases as temperature decreases, which suggests that column amplifiers and related circuitry vary their performance with temperature. At temperatures below 245 K the *local* FPN reaches the values of the dominant contributor, the *global* FPN. Finally, the overall offset FPN is dominated by differences among the four output stages of the sensor. It shows a reduced variability with temperature that can be related to deviations on the pixel sampling (see Fig. 6.2). All offset FPN contributions can be removed from images via subtraction of an averaged bias image taken at the appropriate temperature: $I_{\text{bias}}(T_i)$.

6.2.3 Sensitivity and PRNU

Test setup and data set These measurements were carried out under vacuum conditions and with a controlled temperature of $T = +10^\circ\text{C}$. A Xenon lamp followed by an integrating sphere and a filter wheel provides uniform illumination at the selected wavelength over the sensor’s sensitive area. The wavelength varies from $\lambda_1 = 300\text{ nm}$ to $\lambda_{N_\lambda} = 1\ \mu\text{m}$ in $N_\lambda = 8$ steps. A calibrated Silicon photodiode placed at the same distance from the source than the camera allows taking reference measurements to compare with.

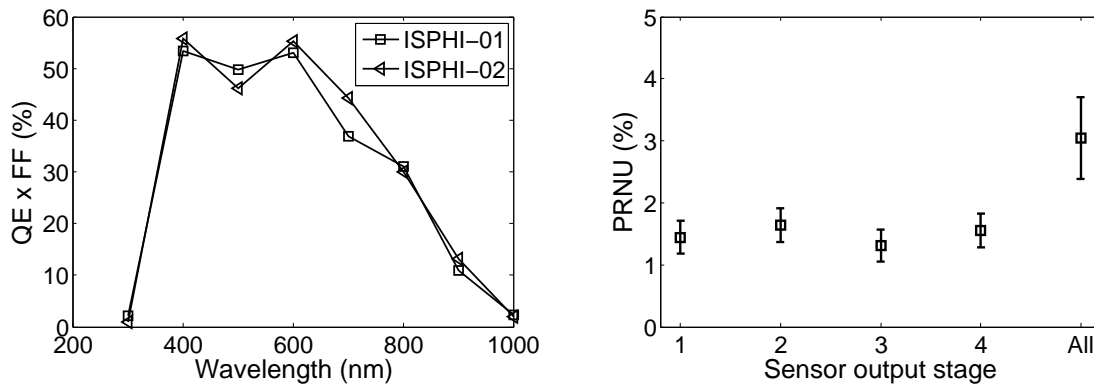


Figure 6.11. Sensitivity versus wavelength and PRNU. ISPHI’s sensitivity reaches values above 45% in the visible range and drops as light goes into the ultraviolet and near-infrared regions of the spectrum (left plot). Variability from sensor to sensor occurs because of differences in flatness and wafer positions during manufacturing. Pixel response non-uniformity lies within the 5% upper requirement both, locally per sensor output and globally when measured over pixels from different outputs (right plot). Error bars indicate variations among different ISPHI devices.

At each wavelength position, exposure time varies from $\approx 90 \mu\text{s}$ to 5 s in $N_{t_{\text{exp}}} = 20$ steps. $N_{\text{im}} = 10$ frames are acquired at each exposure time.

Analysis method

1. Averaged sensitivity is calculated via comparison of the sensor’s response at each wavelength to the one of the calibrated photodiode. The quantum efficiency transfer method, which is explained elsewhere (e.g., Janesick (2001), Section 2.4), has been employed.
2. Pixel response non-uniformity is computed at the 600 nm wavelength according to the criterion and procedure given in EMVA (2010). *Global* PRNU refers to the whole array of pixels, whereas *local* PRNU is calculated for each output stage of the sensor.

Results Quantum efficiency by fill factor product in the ISPHI follows the behavior expected from a Silicon photodiode. Maximum sensitivity lies at visible wavelengths, with fast decreasing in the UV wing, and slower drop towards the near-IR side, where at $1 \mu\text{m}$ the sensitivity is below 5% (Fig. 6.11, left). At the desired wavelength of 617.3 nm sensitivity falls in the 50 – 55% range, which is within specifications.

Local pixel response non-uniformity keeps within 1 – 2% range, which can arise from variations introduced on the silicon wafer during processing or even from non-uniformities on the illumination setup. If pixels from the whole sensor array are considered, the global PRNU results in 3 – 4% (Fig. 6.11, right), which means within camera specifications (see Table 3.6).

6.3 Overall qualification strategy

Every component of the camera shall undergo a set of qualification tests to assure its durability and performance from launch until the end of the mission. The characteristics of these tests are defined by mission's properties and component's nature. If a particular component already passed a qualification process, led by the manufacturer or another project, that fulfills the requirements of the mission, it is considered as a qualified part and the process does not need to be repeated. All electronic components within the designed camera are qualified parts except for the image sensor. Therefore, only the image sensor requires a qualification strategy.

The ISPHI qualification plan comprises the following tests:

- Ionizing and non-ionizing radiation to prove tolerance to space environment (see next section).
- Thermal-vacuum cycling to verify resistance to extreme temperatures and gradients. See MIL-STD-883 (2010) method 1010.8 for details.
- Life / reliability to assure proper operation under specified conditions during the mission lifetime. See MIL-STD-883 (2010) method 1005.9 for details.
- Vibration / mechanical shock to prove that the sensor can survive launch mechanical forces. See MIL-STD-883 (2010) methods 2007.3 and 2002.5 for details.
- Bond strength to prove that bond connections between sensor's die and package can withstand certain level of stress. It is a destructive test. See MIL-STD-883 (2010) method 2011.8 for details.

From the above-mentioned plan, this work only covers the radiation tests, which are discussed in the next section. Apart from the components testing, some additional tests, such as vibration, may be required at camera (subsystem) level.

6.4 Image sensor radiation tests

The radiation tolerance of the sensor is a key aspect to classify the device as suitable, or not, for space missions. This section describes the radiation campaigns carried out during the sensor qualification, and reports on the results concerning the three potential radiation effects: total ionizing dose (TID), displacement damage (DD), and single event effect (SEE).

6.4.1 Campaigns

We planned all campaigns to cover radiation levels that are representative of the Solar Orbiter mission specification (Table 6.3). In addition, we followed the European standards to define biasing, rates, and rest of irradiation conditions (ESCC22900 2007; ESCC25000 2002).

Table 6.3. Summary of Solar Orbiter radiation specification. Given values of TID and NIEL assume an aluminum shielding of thickness as indicated in the second column. Figure 3.2 in Chapter 3 showed a more detailed definition of the expected radiation environment, whereas the complete specification can be found in Sørensen (2010).

Requirement		Unit	Value
Total ionizing dose	1 mm Al	krad(Si)	150
	2 mm Al		74
Proton fluence	10 MeV	p ⁺ /cm ²	3.8 · 10 ¹¹
	60 MeV		2.6 · 10 ¹⁰
NIEL equivalent 10 MeV proton fluence	1 mm Al	p ⁺ /cm ²	3.6 · 10 ¹¹
	2 mm Al		1.8 · 10 ¹¹
SEL LET threshold	-	MeV cm ² /mg	60

The total ionizing dose test was carried out using a Cobalt-60 source, which decays emitting gamma rays of 1.17 and 1.33 MeV. It took place in 2011 at the Cyclotron Research Center in Louvain-La-Neuve (Belgium). Three unbiased and two biased devices underwent different levels of TID up to a maximum of 154 krad(Si), and went through post-irradiation annealing phases at both room and high temperatures (Table 6.4). The devices under test were at room temperature through the whole irradiation stage (Fig. 6.12). A monitoring system continuously recorded the current consumption of the biased sensors supplies, both during irradiation and annealing. All five sensors, plus a reference one, were characterized before the campaign, at each one of the five irradiation steps, before annealing, and after each annealing period. The characterization comprised the acquisition of dark and flat-field images at different exposure times, and a set of star targeted images. All measurements were carried out at room temperature, using a halogen lamp and a green filter ($\lambda = 550$ nm). Therefore, the characterization outcome included: dark current (DC), dark current non-uniformity (DCNU), offset fixed-pattern noise (FPN), read noise, relative sensitivity at 550 nm, pixel response non-uniformity (PRNU), conversion gain, linearity, image appearance, and power consumption.

To test for displacement damage, protons of three energies, 10.6, 15 and 20 MeV, irradiated three unbiased sensors at fluences up to $4 \cdot 10^{11}$ p⁺/cm² (Table 6.4). This campaign took place in 2011 at the IPNAS institute of the University of Liège (Belgium). The test was carried out in vacuum and at room temperature (Fig. 6.13), with the glass window of the sensors being exchanged for a thin kapton foil to avoid proton attenuation. Same conditions used for annealing of the TID unbiased devices apply to the post-irradiation annealing phase after the proton campaign. As for the pre- and post-characterization, identical measurements as in the TID campaign were taken, but the intermediate steps in this case were at three different fluences. During the analysis of the results, SRIM software (Ziegler 2011) allowed calculating the proton induced ionizing dose as explained in Gomes and Shea (2011), thus permitting, together with the Cobalt-60 results, to discern between ionizing and non-ionizing effects.

Finally, the last campaign pre-evaluated the sensor susceptibility to single event effects using a CASE system at ESTEC (Netherlands), in 2012 (Nickson 2011). The

Table 6.4. Overview of radiation campaigns.

Total Ionizing Dose						
Source	Samples	Dose rate (rad(Si)/hr)	Dose (krad(Si))		Annealing 21°C (hrs)	Annealing 100°C (hrs)
Cobalt-60	1 biased, 1 unbiased	482	88.3		192	168
Cobalt-60	1 biased, 1 unbiased	482	108		192	168
Cobalt-60	1 unbiased	900	154		192	168
Proton Displacement Damage						
Energy (MeV)	Samples	Flux (p ⁺ /cm ² /s)	Fluence (p ⁺ /cm ²)	Ion Dose (krad(Si))	Annealing 21°C (hrs)	Annealing 100°C (hrs)
10.6	1 unbiased	3 · 10 ⁸	4 · 10 ¹¹	213.2	168	168
15	1 unbiased	4 · 10 ⁸	3 · 10 ¹¹	122	168	168
20	1 unbiased	4 · 10 ⁸	2 · 10 ¹¹	65	168	168
Single Event Effects						
Source	Samples	Average LET (MeV cm ² /mg)	Estimated fluence (ions/cm ²)		Annealing 21°C (hrs)	Annealing 100°C (hrs)
Cf-252	1 operating	43	1.44 · 10 ⁶		168	168

Californium-252 source produces fission fragments, α particles, and neutrons. Only fission fragments, which represent about 3% of the decay, are useful for SEE testing. These fragments show an energy distribution with maximums at 78.7 and 102.5 MeV, and lead to an average linear energy transfer of 43 MeV cm²/mg. The range on Silicon is limited to about 13 μ m (Blandford and Pickel 1985), and the generated beam spot is smaller than the sensor's sensitive area. However, it allows both, validating the test equipment before using it on the heavy-ions cyclotron, and pre-assessing the device tolerance to SEEs. The irradiation took place in vacuum, at room temperature, and with the sensor protective window removed (Fig. 6.14). The evaluated device was operating in a dark environment during the eight hours of irradiation. At the same time, all images were recorded together with a complete set of housekeepings indicating health status of the complete camera system. The sensor SEU and SEL protection mechanisms were enabled during part of the testing (Section 5.3.1).

All devices employed for the radiation evaluation were selected from the same batch of potential flight sensors. However, no special attention was paid to their performance or number of artifacts.

6.4.2 Results

Hereafter we trace the performance of the ISPHI sensor during irradiation with Cobalt-60, protons, and Californium-252, as well as during the post-irradiation annealing phases.

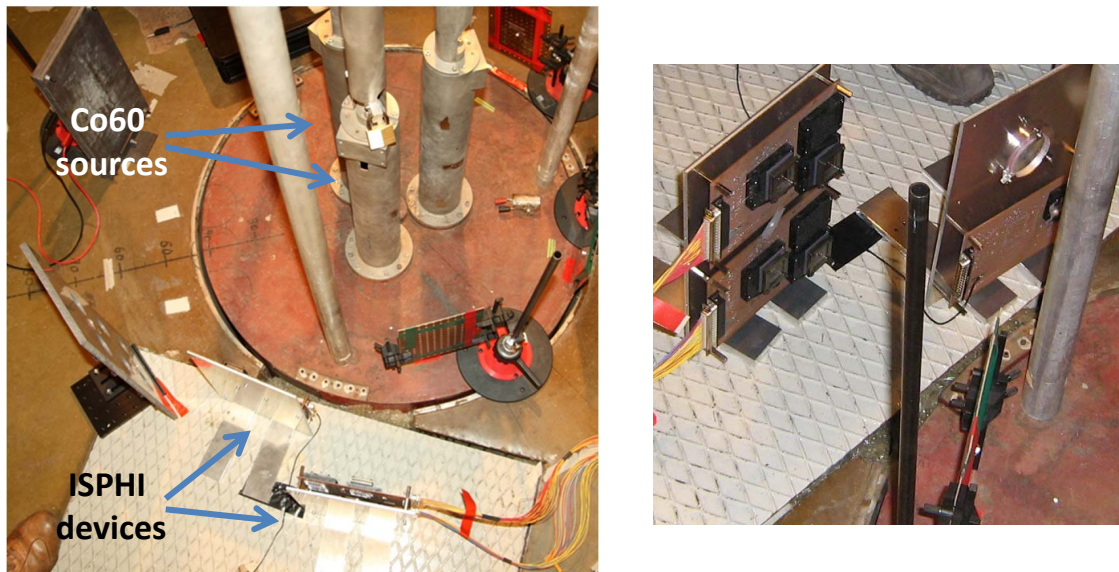


Figure 6.12. Total ionizing dose radiation campaign: setup. Three cobalt-60 radioactive sources lie in the rods located at the center of the irradiation room, with the devices under test (DUTs) surrounding them (left picture). The distance between the devices and the sources determines the dose rate. Three test boards with biasing capabilities hold the ISPHI sensors during irradiation (right picture).



Figure 6.13. Displacement damage radiation campaign: setup. A beam line communicates the cyclotron, where the protons are generated, with a small vacuum chamber where the DUT is located (left picture shows beam line and chamber). Right photo displays the open chamber. Protons enter the chamber through the right aperture and hit the device located on the left side.

6.4.2.1 Cobalt-60 total ionizing dose

Outcome of the cobalt-60 campaign indicates that the sensor is radiation tolerant up to 75 krad(Si). Below this dose, both biased and unbiased devices show moderate degrada-

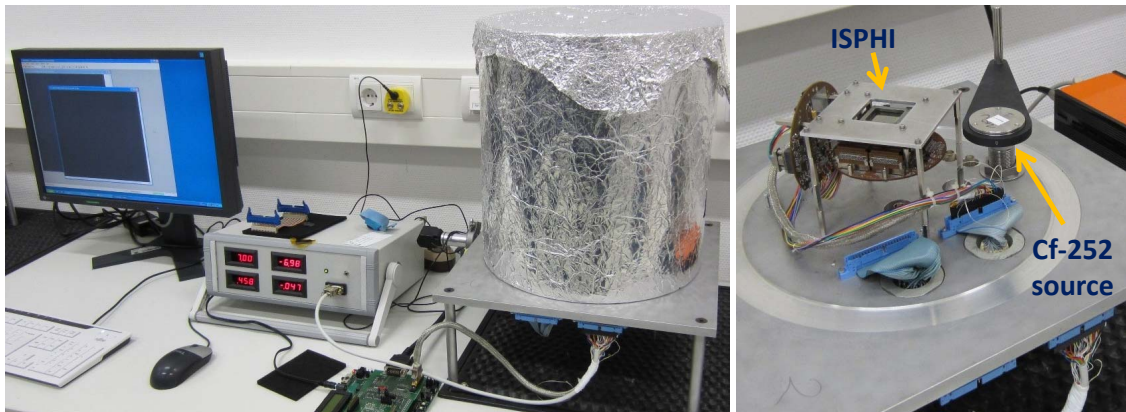


Figure 6.14. Single event effects radiation campaign: setup. The camera electronics and sensor to be irradiated are placed inside a vacuum jar together with the Californium-252 source. Aluminum foil covers the jar to guarantee dark exposures during irradiation (left photo). Camera power supply and control computer are displayed on the left side. Right picture shows a view of the jar interior. The source lies on a rotating bar that allows placing it just over the sensor, which is plugged in the camera electronics. An aluminum plate protects the rest of camera components from being irradiated.

tion on dark current, dark current non-uniformity, and sensitivity, whereas biased devices also show an increase in current consumption. After annealing (detailed further below), all the above-mentioned parameters significantly recuperate. The rest of measured features, i.e., pixel response non-uniformity, conversion gain, linearity, and offset fixed pattern noise, remain unaltered.

Doses higher than 75 krad(Si) lead to row defects on biased devices, while unbiased sensors simply extend the moderate degradation seen at lower doses. These defects mostly emerge as completely dark lines, though in some cases exhibit a whiter shade than their surrounding rows. Number of defects trends towards boosting exponentially as dose increases. The damage turns out to be non-permanent, since annealing at room temperature partially recovers it, and the high temperature baking fully heals it (Fig. 6.15). Given that defects affect complete individual rows and that each row address corresponds in reality to two consecutive rows (Fig. 4.3), the damage must be located after the row decoding circuitry and before the pixels themselves. In particular, the vulnerable points are the signal drivers that connect the control signals to all pixels in each individual row. Despite the defects, all devices were functional during the whole test.

Dark current increase is the most common effect on CMOS imagers exposed to ionizing dose, being the result of induced trapped charges and interface traps (Goiffon et al. 2009; Rao et al. 2008; Goiffon et al. 2010). During irradiation, biased and unbiased devices show a similar tendency, increasing dark current at a rate of about $5.5 \text{ e}^-/\text{s}/\text{krad}$ at low doses, and at $1.38 \text{ e}^-/\text{s}/\text{krad}$ for doses above 55 krad(Si). The annealing phase at room temperature decreases the dark current to values fairly close to the initial ones, whereas the annealing at high temperature does not cause a significant effect (Fig. 6.16, left). Figure 6.16 (right) displays dark current distributions at different doses, where the dark current increase appears as the right-shift of the quasi-Gaussian curves, and the DCNU as the widened distributions. The non-uniformity increases with dose at a rate of about

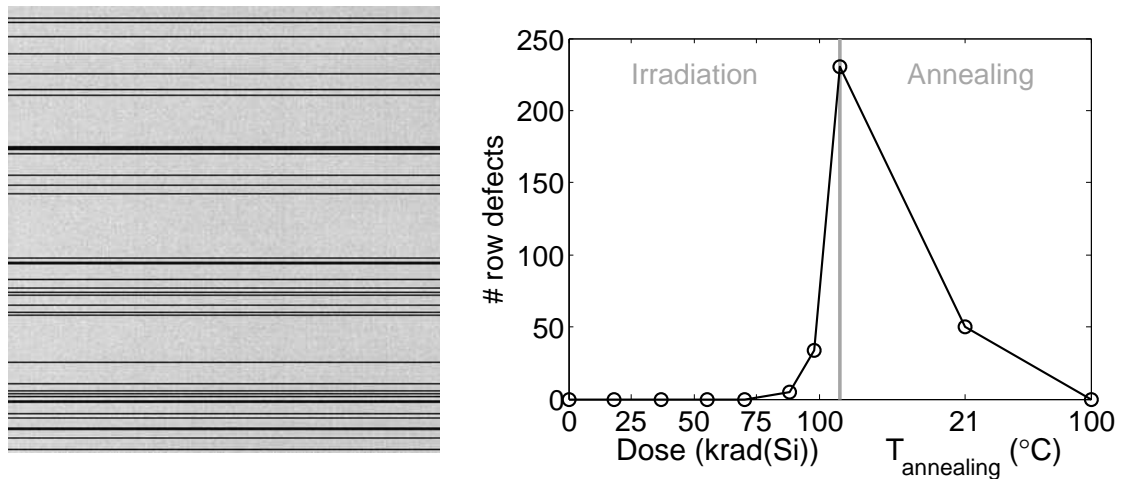


Figure 6.15. Image appearance after TID exposure. Row defects appear on biased devices after 75 krad(Si) of TID. The amount of defects increases exponentially with accumulated dose, decreasing after annealing at room temperature, and vanishing after annealing at 100 °C (right plot). Left image is a flat field taken at 108 krad(Si), showing more than 200 black rows.

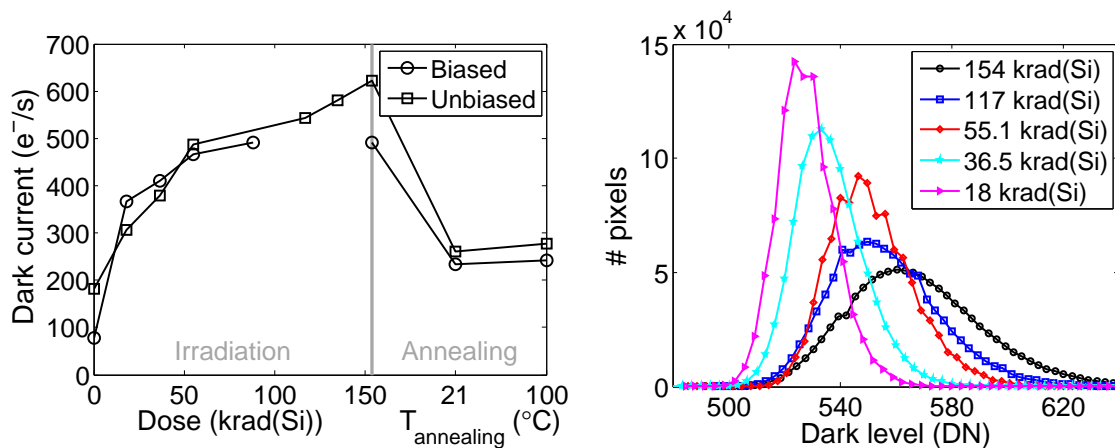


Figure 6.16. Dark current after TID exposure. Dark current varies as a function of total ionizing dose and annealing in a similar way for biased and unbiased devices (left graph). The right side displays dark distributions for an unbiased device with 5 s exposure time from 18 to 154 krad(Si), showing both the increase in dark level and dark current non-uniformity.

0.5 e⁻/s/krad, and does not recover after annealing.

Sensitivity, especially at short wavelengths (400–700 nm), decreases after TID mainly because of recombination centers generated on the oxide interface and silicon bulk of the pixel (Goiffon et al. 2009). However, another mechanism, which results from changes on optical properties of the multi-layered stack above the pixels, may also contribute to sensitivity reduction (Rao et al. 2008). Since our characterization did not comprise a complete spectral response analysis, changes on signal level at a fixed wavelength and illumination conditions were taken as estimations of this parameter. Results suggest that there is a decrease of sensitivity of about 12% after 154 krad(Si) at 550 nm. In addition,

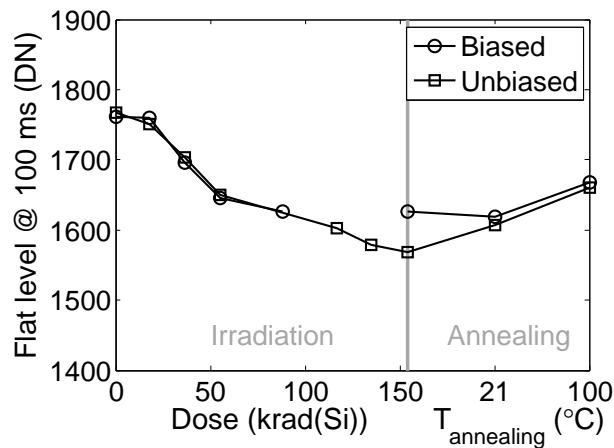


Figure 6.17. Signal level of flat images taken under the same illumination conditions at 550 nm, and with an exposure time of 100 ms. The biased device was irradiated up to 88.3 krad(Si), whereas the unbiased one continued until 154 krad(Si). Biased correction is not included on the Y-axis level.

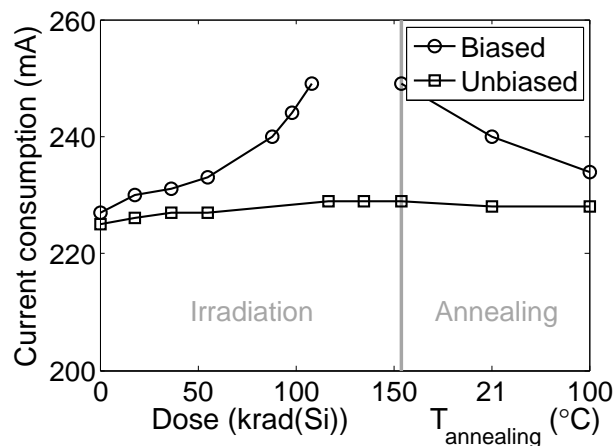


Figure 6.18. Current consumption for the complete camera versus irradiation dose and annealing. Since only the image sensor was irradiated, variations correspond to changes on the sensor's power consumption. Total ionizing dose affects differently power consumption on biased and unbiased devices.

devices response does not depend upon bias conditions, and they partially recover after annealing at high temperature (Fig. 6.17).

Ionizing radiation shifts the threshold voltage of MOS transistors, increasing the leakage current of n-channel ones when they are off (Ma and Dressendorfer 1989). This leakage results in a growth of the sensor's power consumption. Our measurements confirm this variation on consumption for devices biased during irradiation, but this is not the case for unbiased sensors (Fig. 6.18). The consumption increases at 0.96 mW/krad up to 75 krad(Si), and starts boosting rapidly (4.1 mW/krad) for higher doses. The annealing stage leads to a partial recovery, so that a final deviation of less than 3% remains.

6.4.2.2 Proton displacement damage

High fluence of protons produced severe and permanent degradation on some of the sensor's parameters, whereas others were only temporarily affected, and the rest remained unchanged. Among the severely damaged features are dark current and dark current non-uniformity. On its part, temporarily affected parameters include read noise, pixel response non-uniformity, sensitivity, full well charge, and power consumption.

Exposure of electronic devices to protons results not only in displacement damage due to non-ionizing interactions, quantified as non-ionizing energy loss (NIEL), but also in damage because of accumulated total ionizing dose. In this section, we make use of the gamma irradiation results for unbiased devices (Section 6.4.2.1) together with the calculated proton induced ionizing dose (Table 6.4) to distinguish between displacement damage and TID effects.

Irradiations at different proton energies, in the range from 10.6 to 20 MeV, and at the same fluence led to similar degradation levels. This is because protons with energies in such a small range produce similar NIEL, thus comparable displacement damage. In general, lower energies produce higher non-ionizing energy loss and therefore a higher degradation, as shown by Bogaerts et al. (2003) or Van Aken et al. (2009), whereas higher energies provide larger penetration depths.

Dark current and dark current non-uniformity, which despite substantial post-annealing recovery remain significantly degraded, are the parameters of most concern for the sensor qualification. As expected (Bogaerts et al. 2003), dark current increases linearly with proton fluence, and thus with NIEL, following

$$\Delta D_c(E) = k(E) \cdot \frac{F}{10^{10}}, \quad (6.1)$$

where F is the increase in fluence expressed in p^+/cm^2 and $k(E)$ the damage factor for each energy in $\text{e}^-/\text{s}/\text{p}^+/\text{cm}^2$. From Fig. 6.19 (left), the annealing phase decreases the dark current in similar steps for room and high temperature, resulting on a final value that is still more than two orders of magnitude higher than the initial one. The damage factors during irradiation are $k(10.6 \text{ MeV}) = 4381$, $k(15 \text{ MeV}) = 4694$ and $k(20 \text{ MeV}) = 6524$. At the same time the average dark current rises, its non-uniformity increases considerably, widening the dark distribution as the fluence goes up (Fig. 6.19, right). This DCNU also recovers with annealing, especially at high temperature, but does not reach the shape of the initial distribution. Devices did not show any further improvement, neither in DC nor in DCNU, after additional self-annealing of five months plus annealing of six months at room temperature. Therefore, we consider the induced radiation effect as permanent. If one compares the results in Fig. 6.19, where the accumulated ionizing dose reaches more than 120 krad(Si) for proton energies of 10.6 and 15 MeV, to those presented in Fig. 6.16 for unbiased devices up to 154 krad(Si), it becomes clear that the ionizing contribution to the degradation after proton testing is negligible. Since all measurements took place at room temperature, lowering the operating temperature may be a way of coping with the high levels of dark current. Figure 6.20 shows how both dark current and dark current non-uniformity improve at lower temperatures. In addition, the PHI instrument aims at relatively low exposure times, which eases the impact of high dark current contributions.

Read noise also exhibits a steady rise with proton fluence followed by a nearly com-

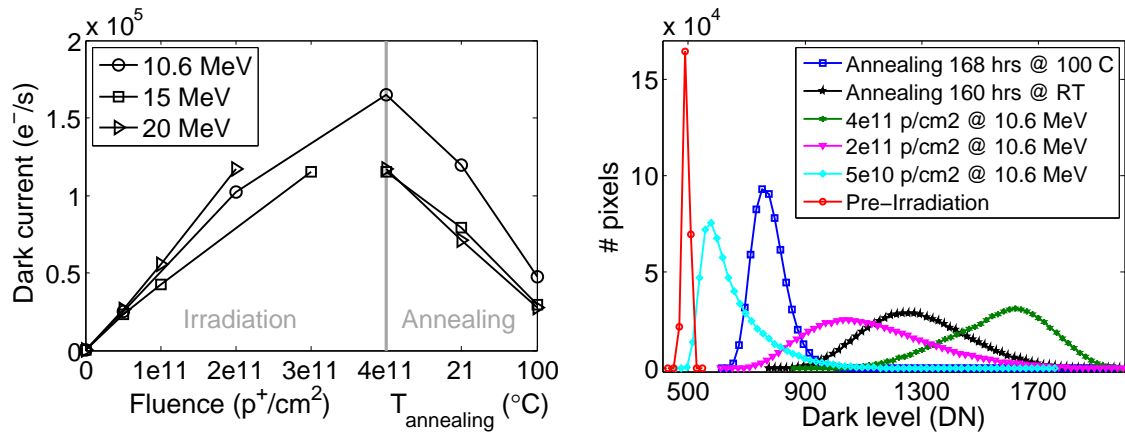


Figure 6.19. Dark current increase due to proton irradiation is similar for 10.6 and 15 MeV protons and slightly higher for 20 MeV, whereas the recovery after annealing is comparable for the three proton energies (left plot). The dark current distributions at 10.6 MeV is shown on the right graph for an exposure time of 200 ms.

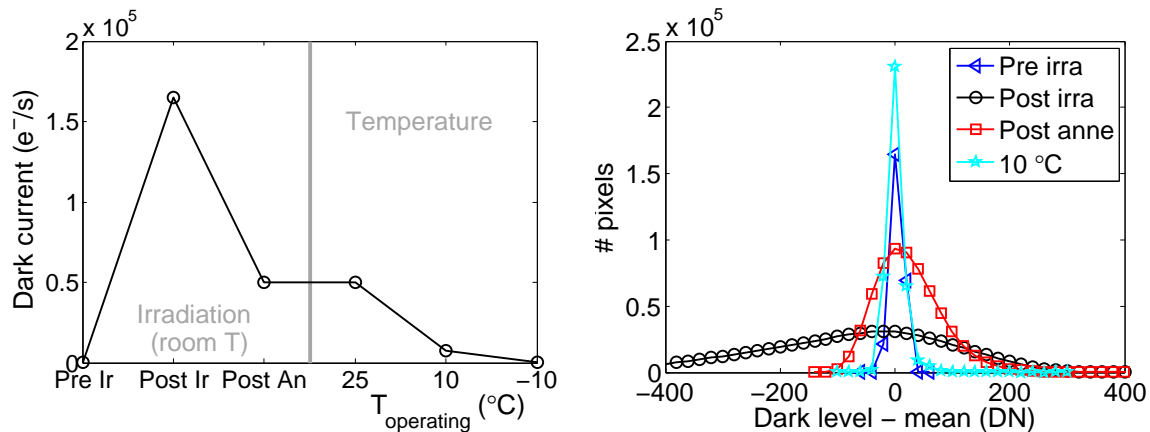


Figure 6.20. Dark current on the 10.6 MeV proton irradiated device decreases as temperature does, reaching at -10°C a level close to the pre-irradiated one at room temperature: $571\text{ e}^{-}/\text{s}$ versus $306\text{ e}^{-}/\text{s}$ (left graph). Right plot displays the dark distributions centered around zero, which widen after irradiation and narrow as temperature decreases. Therefore, at 10°C the irradiated sensor shows a distribution comparable to the pre-irradiation one.

plete cure after annealing (Fig. 6.21). Since gamma irradiation did not affect this parameter, the observed effect shall be attributed to displacement damage. Variation from initial to final value is about $1 - 2\text{ e}^{-}$, which stays within acceptable limits.

Signal level under flat illumination provides an indication of sensitivity changes on the sensor. Figure 6.22 (right) shows the decrease in signal level after different proton fluences, and the later recovery with room and high temperature annealing, which sets final values to about the same levels they had before irradiation. Comparing this sensitivity reduction to the one observed after the gamma campaign (Fig. 6.17), one observes that the decrease is higher after proton testing, but recovery is weaker after TID. The exact mechanism triggering these sensitivity changes is not totally clear (Bogaerts et al. 2003).

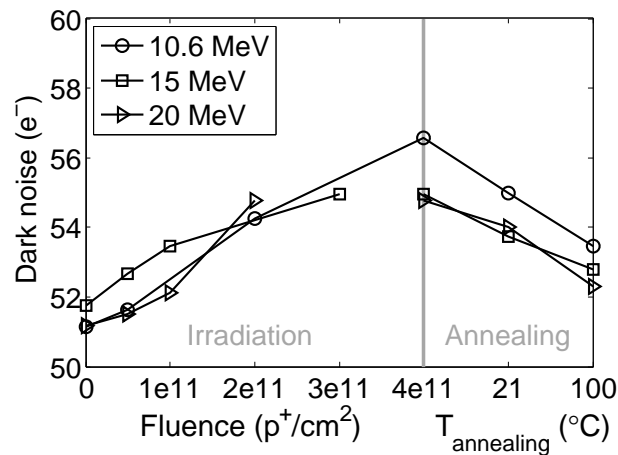


Figure 6.21. Read noise dependence on proton fluence and energy, as well as on annealing. The measured post-annealing read noise is slightly higher than the initial values.

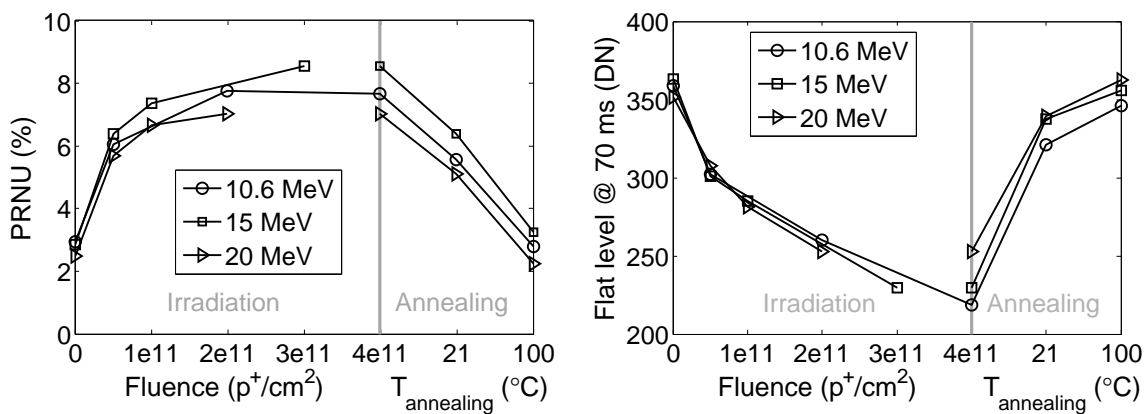


Figure 6.22. PRNU and sensitivity after proton irradiation. Pixel response non-uniformity variation with respect to proton fluence and energy, as well as annealing. The PRNU value is calculated according to the criterion given in EMVA (2010) (left plot). Signal level of flat images taken under the same illumination conditions at 550 nm, and with an exposure time of 70 ms, which corresponds to about half full well of the sensor (right graph). Given levels are corrected from dark contribution.

Furthermore, an absolute spectral response measurement of the sensor before and after irradiations may help on the analysis. This task is part of the near future work.

Spatial uniformity on the pixel responses diminishes as well after proton irradiation (Fig. 6.22, left). PRNU doubles after the first fluence ($5 \cdot 10^{10} \text{ p}^+/\text{cm}^2$), and then the effect starts saturating. Annealing completely heals the PRNU damage. Since no PRNU degradation was seen after the gamma campaign, this effect is entirely caused by displacement damage.

Full well charge suffered from reduction during irradiation but recovered almost completely after the two phases of annealing at room and high temperature. The net reduction stays below 4 %.

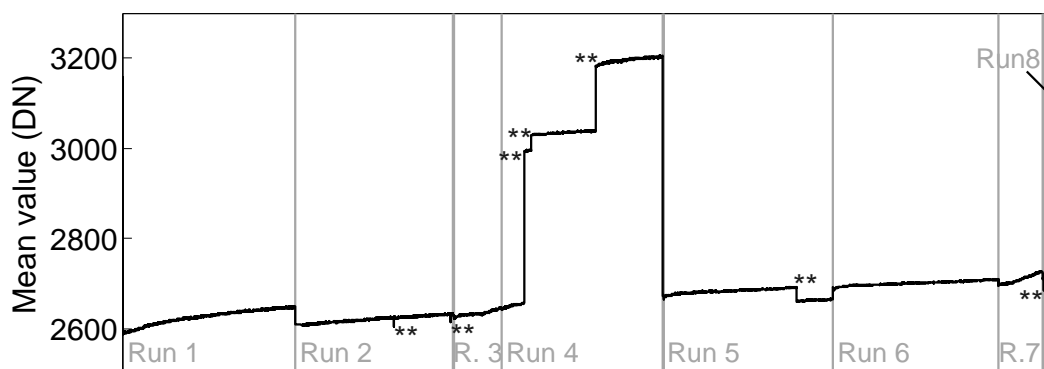


Figure 6.23. The mean value of the sequence of images taken during the live test is plotted versus the irradiation run. Double asterisks (**) represent changes due to single event effects (SEE), most of them identified as single event upsets (SEU). The recovery at the end of run 4 and run 5 is because of a power cycling of the sensor, whereas recoveries on run 2 and 8 occur automatically because of the remote TMR functionality of the camera (see section 5.3.1).

6.4.2.3 Californium-252 single event effects

Live monitoring of dark images and camera housekeepings allowed detecting and identifying several single event effects during eight hours of irradiation with the Cf-252 source. No single event latch-up occurred for the whole campaign. Conversely, seven single event effects were detected and identified as single event upsets (SEU). From these events, four happened while the camera SEU recovery system (remote TMR, see Section 5.3.1) was disabled, thus resulting on single event functional interruptions (SEFI). The rest of events were automatically corrected and just provoked single wrong frames. Moreover, single event transients continuously generated randomly distributed white dots, caused by direct ionization, on the dark frames. The occurrence of events depends on the position of the source over the sensor. SEUs only appeared with the source located either at the center or at the right edge of the device, confirming that no internal registers are located on the left side.

Figure 6.23 displays a continuous monitoring of the dark mean value for all frames acquired during irradiation. Abrupt changes on mean level are caused by single event upsets that modify some sensor settings. A monitoring of the standard deviation would also allow detecting the same number of sudden changes. Depending on which register is hit by the incident particle, the effect becomes more or less notorious. During runs 2 and 8 the camera recovery system was activated, therefore the duration of the single event effect is limited to a single acquisition. On the other hand, runs 4 and 5 do not include automatic recovery, resulting on setting changes that last until the end of the run, point at which the camera is power cycled. Run 4 shows two additional singularities. First, there is an accumulation of effects, and second, the first and last events produce sudden decrease and increase in power consumption, respectively (Fig. 6.24). The continuous retrieving of housekeepings allowed the identification of the exact location of some events. For example, the event on run 8 was caused by an upset on the sensor register that sets the reference voltage of the pixel outputs. Later tests have confirmed that a variation on this register leads to an offset modification of the sensor outputs, hence changing the image mean level.

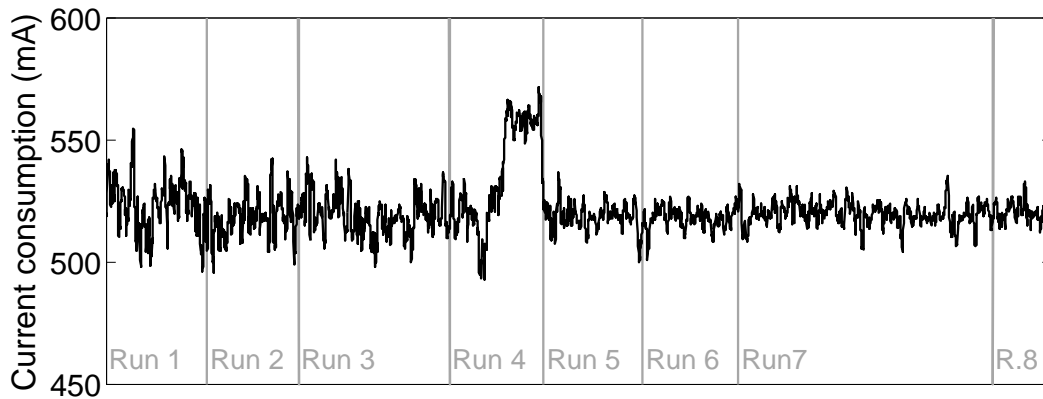


Figure 6.24. Live monitoring of the camera current consumption during Cf-252 irradiation of the sensor. Every vertical line demarcates a run, after which the radioactive source is moved away and placed above the sensor again to start the next run. The continuous high frequency variation is because of the camera acquisition cycle and not caused by changes induced by radiation.

Apart from transient effects, heavy ions and Cf-252 irradiation can also lead to long-term effects because of induced ionizing dose. One can already anticipate this effect on the continuously monitored dark mean level, where there is a smooth increase over time (Fig. 6.23). The pre- and post-irradiation measurements as well as the annealing stage confirm this trend.

Once the camera electronics and setup has been successfully tested, including the camera protection against upsets (Section 5.3.1), next step is to evaluate the sensor sensitivity to heavy ions accelerated by a cyclotron. We plan to use a high linear energy transfer (LET) and low penetration ion cocktail to irradiate at different LETs. This test will allow calculating the SEU saturated cross section of the ISPHI.

6.5 Discussion

Through this chapter we have characterized alternatives for the clocking of the analog to digital converters, the retrieving of digitized data, and the synchronization of sensor, ADCs, control electronics, and output data link. The electrical and electro-optical characteristics of camera and image sensor have been measured, and the radiation tolerance of the image sensor evaluated.

Three factors support adding flexibility to the active edge of the pixel sampling clocks while reading out at high frequency (30 MHz) and operating the camera in harsh environments (Solar Orbiter). First, finding an optimum point at which pixels are settled and spurious contributions from previous and next pixels fade, thus avoiding ghosting artifacts. Second, temperature gradients modify the delays associated to the outputs of the image sensor and alter the optimum sampling instant. Third, radiation can also vary the positions of the sampling points via affecting the timing properties of control electronics, ADCs, and image sensor. Operating the camera at a lower readout frequency, i.e., 15 MHz for the ISPHI, diminishes the need of flexible sampling points because the stable sampling periods are longer and timing changes on the electronics have a low impact. In

Table 6.5. Camera and IS performance: Comparison with requirements. Requirements column refers to the instrument requirements presented in Table 3.6, whereas ISPFI specifications are the sensor development goals shown in Table 4.2 (Vendor 7). Finally, the results column indicates the outcome of the electrical and electro-optical characterization of the camera.

Parameter	Unit	Requirement	ISPFI specification	Result
Frame rate	fps	≥ 10	11	11
Read noise	e^-	≤ 100	60	52 ± 5
Dark current @ 293 K	e^-/s	$\leq 10^3$	200	≈ 35
Sensitivity @ 600 nm	%	≥ 40	50	50 ± 5
PRNU	%	≤ 5	–	< 3.5 (global)
Non-linearity	%	≤ 2	≤ 2	≤ 2
Full well charge	e^-	$\geq 10^5$	10^5	95250 ± 250
Dynamic range	dB	≥ 60	64.44	65.62
Power consumption	mW	≤ 500	≤ 500	1940 ^a

^aValue for the complete camera electronics plus image sensor.

addition, milder and more steady environments assure stable timing properties and also eliminate the need of clocks adjusting.

Camera data converters must be clocked separately and differential signaling shall be employed to carry clocks from the control electronics to the ADCs. Otherwise, dynamic range and noise requirements are not met at high frequency even if the induced interference pattern is removed via post-processing of the images. At half operating frequency (15 MHz), the simple clocking approach meets the noise requirements if the interference pattern is removed via subtraction of images. Digital data streams from the converters can be successfully synchronized with the FPGA and the channel-link interface using different structures. However, the mesochronous approach presented in Chapter 5 provides the preferred solution regarding implementation resources and reliability.

All camera parameters fulfill the instrument requirements and the sensor specifications except for the full well charge, which is slightly lower than desired (Table 6.5). This modest deviation of FWC does not impede the successful performance of the instrument as suggested by the instrument simulation that were presented in Chapter 3 (Fig. 3.5). Power consumption is not detailed for the image sensor but given for the complete camera. The value below 2 W is within the PHI budget.

The ISPFI sensor has been subjected to radiation tests of total ionizing dose, proton displacement damage, and single event effects. The sensor is radiation tolerant up to 75 krad(Si) of TID, and shows temporal damage (recovered after annealing) at higher doses if the sensor is biased during irradiation. Proton irradiation significantly degrades dark current and dark current non-uniformity even after annealing, whereas other parameters, such as dark noise, sensitivity, and PRNU, only suffer from minor degradation. The dark current deterioration can be overcome via operating the sensor at low temperatures,

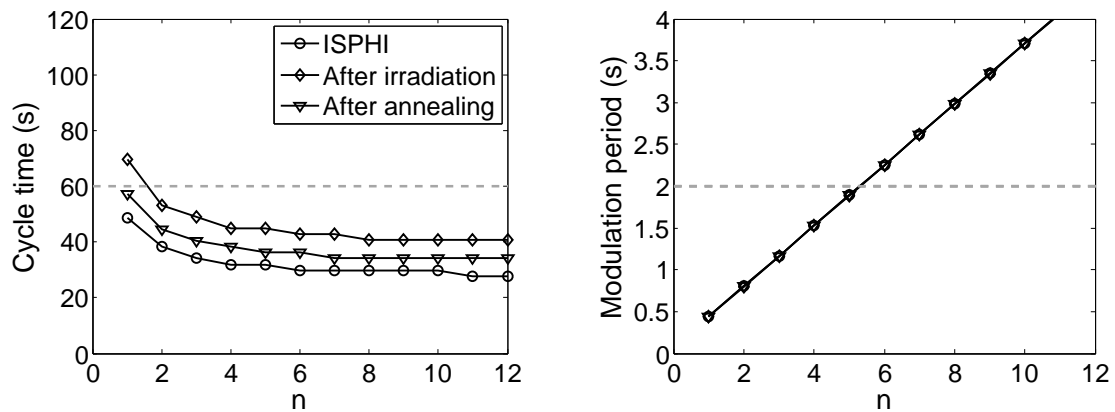


Figure 6.25. PHI performance before, during, and after sensor irradiation. ISPHI plot assumes the measured camera performance (Table 6.5, Results), after irradiation includes degradation up to 75 krad(Si) of TID and up to $2 \cdot 10^{11} \text{ p}^+/\text{cm}^2$ proton fluence, and after annealing refers to the high temperature recovery phase. Parameter n was defined in Section 3.4.2. Dashed gray lines define the maximum allowed times. Tuning and acquisition modes as defined in Table 3.8 are employed.

with 263 K being the temperature at which irradiated devices after annealing show the same behavior than non-irradiated ones at room temperature. In addition, the irradiated sensors underwent high proton fluences that correspond to the expected environment for the spacecraft. The instrument environment is expected to withstand lower non-ionizing doses. The SEE pre-assessment with Cf-252 have allowed validating the setup to be used in a heavy ions cyclotron facility, and it did not cause any latch-up on the system. Contrarily, seven single event upsets were detected, which permitted successfully testing the camera SEU recovery mechanism (remote TMR). In conclusion, three recommendations arise from the radiation assessment: (1) in-flight annealing can help the image sensor recover from long-term degradation effects, (2) low temperature operation of the ISPHI ($< 263 \text{ K}$) is needed to keep the dark current within reasonable margins, and (3) the remote triple module redundance implemented in the control electronics prevents single event functional interruptions on the sensor and unnecessary power cycling. As a result of the radiation tests, additional shielding to reduce the levels of radiation on the image sensor is not necessary provided that the own camera housing exceed a thickness of 2 mm aluminum or equivalent, which is guaranteed by design.

The performance of the instrument is affected by the degradation of the image sensor after irradiation and recovery after the annealing phases (Fig. 6.25). The reference plot (ISPHI) includes the sensor's properties after being characterized. After annealing the instrument's requirements are fulfilled for all values of the parameter n , but the cycle time increases by about 14 %.

6.5.1 Comparison with scientific cameras in space

The sampling, digitization, and synchronization of analog pixels from image sensors become more critical as the readout frequency increases. The design of the PHI camera, which has a pixel frequency of 30 MHz, has demanded special measures to optimize the

sampling point and to implement a proper synchronization approach. These difficulties do not exist in cameras with slower pixel frequencies, as occurs with most of the currently in-flight space cameras (Table 6.6). The shown cameras either do not require a faster readout or cannot exceed a readout frequency of 2.5 MHz while keeping the noise within specifications. A higher number of outputs on the detector also complicates the acquisition at high speed. From the table, only the first camera system comprises a sensor with more than two analog outputs.

The thermal environment for spacecrafts that orbit around the Earth or other planets, around the Sun at a fixed distance, or around small bodies is, in general, more stable than the one for missions which distance to the Sun varies significantly within their lifetime. This eases the optimization of the instrument under the expected operating conditions.

All instruments studied in Table 6.6 employ charge-coupled devices instead of CMOS imagers because they are exposed to relatively low radiation levels and APS were not mature enough at the time of their development phases. Most of those cameras are surrounded by protective shielding to reduce the received radiation dose and guarantee the survival of the sensors. Since CCDs do not include on-chip control or configuration registers, single event upsets are not a concern for those camera systems. Therefore, protective measures, such as triple modular redundancy, are not necessary. On the other hand, the clocks used to operate CCD-based cameras must be carefully generated and calibrated to optimize the camera performance. This aspect complicates the design of CCD controllers.

Table 6.6. Characteristics of in-use space cameras: selection of three solar cameras (HMI, SP, and SECCHI), one planetary imager (VMC), and two small bodies cameras (OSIRIS and DFC). Launch years are indicated in the *Year* row. Given ionizing radiation doses correspond to missions' levels. Basic information about the compared instruments and their camera systems can be found in Schou et al. (2012) for HMI, Tsuneta et al. (2008) for SP, Waltham and Eyles (2007) for SECCHI, Keller et al. (2007) for OSIRIS, Markiewicz et al. (2007) for VMC, and Sierks et al. (2011) for DFC.

Instrument	HMI	SP	SECCHI	OSIRIS	VMC	DFC
Mission	SDO	Hinode	STEREO	Rosetta	Venus Express	Dawn
Year	2010	2006	2006	2004	2005	2007
Type	CCD	CCD	CCD	CCD	CCD	CCD
Pixel size	12×12	12×12	13.5×13.5	13.5×13.5	9×9	14×14
Format	4096×4096	224×1024	2048×2048	2048×2048	1032×1024	1024×1024
Pixel frequency	2	2.5	1	0.65	2.09	1
Frame rate / Nr. outputs	$0.43 / 4$	$\sim 21 / 2$	$\sim 0.23 / 1$	$0.29 / 2$	$\sim 2 / 1$	$0.83 / 1$
Full well charge	200	130	200	100	30	270
Read noise	16	100	20	7	100	34
ADC resolution	14	12	16	2×14	14	14
Dark current	10 (213 K)	600 (273 K)	$8 \cdot 10^3$ (293 K)	200 (293 K)	817 (293 K)	333 (293 K)
Spectral range	400 – 800	400 – 800	$450 - 750^a$	250 – 1000	345 – 1030	400 – 1050
Peak sensitivity	< 50	< 50	< 95	< 80	< 40	< 20
Orbit	Earth (GEO)	Earth (LEO)	Sun (1 AU)	Comet ^b	Venus	Asteroids ^c
Radiation tol. (TID)	(krad(Si)) < 30	< 30	< 30	< 20	< 20	< 20

^aRange refers to the visible channel of the instrument.

^bOrbit around the comet 67P / Churyumov - Gerasimenko.

^cOrbits around the asteroids Vesta and Ceres.

7 Concluding remarks

This thesis has tackled the definition, design, development, and qualification of a new camera electronics and a new detector with the purpose of optimizing them for space solar instruments. In particular, it has been applied to the PHI Polarimetric and Helioseismic Imager, which will operate as a remote sensing instrument on the Solar Orbiter spacecraft. We commenced studying the instrument's scientific needs and mission's characteristics to establish the camera requirements. Camera specifications were then related to filtergraph and polarizer timing properties to evaluate their combined influence on the PHI performance, which allowed elaborating and determining the most appropriate strategy to tune those subsystems while acquiring images. Based on a comprehensive review of the state-of-the-art of image sensors and a comparison with the defined camera requirements, the development of a custom Active Pixel Sensor (or CMOS imager) was adopted as solution. The principal demands for the new image sensor were: fast readout (high frame rate), high full well capacity, and sufficient radiation tolerance. The digital control electronics of the camera was designed, based on an antifuse FPGA, to drive the target image sensor, clock the analog to digital converters, and interface with the main unit of the instrument. A flexible sampling and acquisition technique has been proposed and implemented to deal with the highly variable mission environment and the high readout rate while minimizing the camera noise. The camera characterization has demonstrated that the noise is limited by the CMOS sensor if the sampling parameters are calibrated according to operating frequency and environment, and that the manufactured detector fulfills the instrument's needs. Furthermore, achieved camera characteristics were compared with other in-flight camera systems and proved to be especially demanding with respect to speed and radiation tolerance. Finally, three campaigns of radiation tests assessed space degradation on the sensor and confirmed the fulfillment of the camera requirements under the mission's environment, provided that in-flight annealing and low operating temperatures can be guaranteed. Moreover, the campaigns proved the usefulness of the implemented sensor's protection against single event upsets.

In Chapter 1, we have linked four primary contributions to the primary goals of this work. Now we can review these contributions as follows:

(c1) *Optimum strategy to synchronize camera, filtergraph, and polarizers.*

The defined *Fast polarization* tuning mode, where the polarizers sequentially scan all polarization states at each filtergraph position before the next wavelength is selected, provides the optimum synchronization strategy when combined with the *triggered* acquisition mode, where each sequence of frames is requested individually from the camera. The introduced parameter n , which indicates the number

of sequential images to be acquired each time a given polarization state and wavelength position are fixed, adds flexibility to both optimization and camera requirements, thus permitting to reach the desired performance with a wider diversity of configurations. This *Fast polarization - triggered* configuration results in maximum polarization efficiencies, with cycle time and modulation periods varying within acceptable ranges depending on n , and while keeping the polarimetric signal to noise ratio within specification. The camera shutter plays a significant role in determining the optimum operating strategy. The proposed approach allows using both rolling or snapshot shutters. However, snapshot shutters allow running the image acquisition in *continuous* mode, thus reducing the total cycle time but slightly degrading the polarimetric efficiencies. Even though the optimum strategy may vary if polarizers or filtergraph change properties, the optimization procedure presented here would still be applicable.

(c2) *Reduction of camera noise at high readout frequencies in variable radiation and thermal environments.*

Fast readout reduces the optimum time interval at which the output pixels can be sampled. Moreover, that sampling window varies, in turn, with temperature and radiation exposure because of changes in the timing properties of electronic components. We have proven those changes with temperature in the output delays of the image sensor. Pre-calibrating an adequate sampling instant does not solve the problem and leads to spurious noise contributions. The sampling approach proposed here overcomes both issues, small sampling window and variability, via allowing the user to finely adjust the sampling instant at any time. In addition, that optimum sampling point can be optimized independently for different readout channels, hence accounting for differences between sensor's outputs and analog to digital converters. That independent optimization complicates the data acquisition and multiplexing. However, acquisition strategies have been reviewed and evaluated during this work to implement the best solution. The proposed sampling approach reduces the camera readout noise at the maximum readout frequency of PHI (2×30 MHz) and assures that the camera electronics contribution to the overall noise is below the detector's dark temporal noise. The main limitation of this flexible solution, which is implemented in the control FPGA, arises from the need of adjusting the sampling parameters of the camera via user commanding in case of severe environmental variations. This limits the camera autonomous operation, but shall only be required occasionally.

(c3) *Protection of the camera against functional interruptions caused by space radiation.*

Internal registers on CMOS imagers are often susceptible to single event upsets because on-chip mitigation measures raise both cost and development time. The implemented remote triple modular redundancy uses the TMR protected registers of the control FPGA to store a safe copy of the sensor registers and overwrites them in case a discrepancy caused by an ionizing particle is detected. Radiation tests have shown how the PHI camera automatically recovers from single event upsets when the remote TMR protection is enabled, thus preventing single event functional interruptions that occur when the protection is deactivated. The checking periodicity of

internal and remote registers can be adjusted. However, registers cannot be updated while an image is being acquired to avoid spurious noise contributions. Therefore, the protection does not assure the absence of single corrupt images after a SEU, but guarantees that SEUs do not provoke functional interruptions.

(c4) *Testing and analysis of radiation effects on custom CMOS image sensor.*

ISPHI, the custom image sensor developed for PHI, is functional after being subjected to ionizing and non-ionizing radiation doses at levels above the expected ones for the Solar Orbiter mission. Performance parameters are degraded, especially dark current and dark current non-uniformity, but still within specifications if the detector operates below a temperature of 263 K. Displacement damage caused by protons is the effect that produces most of the performance reduction on the detector. Post-irradiation annealing has proved to considerably heal some of the deteriorated parameters. Thus, in-flight annealing is recommended to reduce sensor degradation during the phases in which the instrument does not carry out observations. We consider that additional shielding to specifically protect the image sensor is not needed for PHI. Among all instrument parameters, the total cycle time is the one most influenced by the sensor degradation after irradiation, increasing it by about 14 %.

Most of the contributions of this thesis can be applied to solar instruments other than PHI as well as to areas other than solar polarimetry. The study of how camera parameters as well as subsystems synchronization influence the polarimetric outcomes of the instrument can easily be adapted to future solar observatories. In the same way, the sampling point and synchronization approaches to reduce noise without decreasing the frame rate could be scaled to future and faster scientific cameras by increasing the frequency of the main camera clock or the number of digitization channels. Radiation mitigation measures, irradiation and annealing findings, together with the custom developed APS itself can also serve future space projects.

Various results of this thesis provoke new questions that instigate further investigations or analyses. (1) The proposed approach to perform an optimal sampling of the pixels under different environments or operating conditions requires manually adjusting the sampling parameters after relevant changes (Chapters 5 and 6). An algorithm could be derived and implemented, e.g., in the flight software, to auto-calibrate those parameters periodically or every time the surrounding conditions vary. (2) Our theoretical study on how the rolling shutter influences the operation of the instrument in the *continuous* acquisition mode shows fluctuations on the polarimetric efficiencies within the image rows (Chapter 3). This behavior can be reproduced in the laboratory with the polarizers and it can be assessed whether they could be dynamically tuned to compensate for such fluctuations. Lastly, (3) the next steps on the camera development for PHI, which are planned, include the single event effects testing on a heavy ions accelerator, the reliability and mechanical qualification tests mentioned in Section 6.3, and the selection of the ISPHI flight sensors after carefully characterizing the available samples (Chapter 6).

APS-based cameras have a good prospect of replacing charge-coupled devices as the preferred solution in scientific imagers. In space, this allows medium and harsh environments eliminating shield layers from image sensors, while in extreme radiation atmospheres, e.g., Jovian orbits, one can benefit from notable reductions in shielding. Next

generations of CMOS imagers shall push toward combining snapshot shutter features with high tolerances against radiation, thus providing future space observatories with better temporal resolution.

A Detailed specification of PHI

This appendix complements the description of PHI given in Chapter 3 and provides those inputs used for the calculations presented in Section 3.4 that were not detailed there. Some of the figures given here correspond to measured values, whereas others are the best estimations available at the time of writing. Moreover, all these parameters may change with temperature and exposure to radiation. The presented values assume the expected operating conditions with respect to temperature, but do not consider degradation due to radiation.

Table A.1 gives the optical transmissions of the optics unit's submodules, leading to a total transmittance of 8.1 %. The absorption line observed by PHI is plotted in Fig. A.1, where the vertical lines are the spectral positions selected by the filtergraph. The continuum point is placed on the red side of the line, outside of its influence, whereas the other points lie equidistant from the line center. Table A.2 contains the exact wavelength positions as well as the tuning speed of the filtergraph. Finally, Table A.3 includes the polarization positions, given as the retardances ρ and σ of the two polarizers accommodated in one PMP, and the response times needed to change from one position to the following one.

Table A.1. Transmissions of the PHI optical subsystems.

Parameter	Symbol	Unit	Value
Entrance window	τ_{window}	%	80
Mirrors	τ_{mirrors}	%	88.6
Lenses	τ_{lenses}	%	81.7
Filtergraph	$\tau_{\text{filtergraph}}$	%	35
PMP	τ_{PMP}	%	90.3
Pol. beamsplitter	$\tau_{\text{Pol-BB}}$	%	49
Non-pol. beamsplitter	$\tau_{\text{nPol-BB}}$	%	90
Total	τ	%	8.1

Table A.2. Tuning speed and exact wavelength positions of the spectral tuning of PHI.

Parameter	Symbol	Unit	Value
Tuning speed	$R_{\text{filtergraph}}$	nm/s	0.05021
Position 1	$\lambda_1 = \lambda^c$	nm	617.3741
Position 2	λ_2	nm	617.3201
Position 3	λ_3	nm	617.3271
Position 4	λ_4	nm	617.3341
Position 5	λ_5	nm	617.3411
Position 6	$\lambda_6 = \lambda_{N_\lambda}$	nm	617.3481

Table A.3. Retardance values and response times of the polarizer used for the polarimetric tuning of PHI.

Parameter	Symbol	Unit	Value
Vector mode - $N_p = 4$			
Position 1	P_1	deg	$\rho = 225$ $\sigma = 234.74$
Position 2	P_2	deg	$\rho = 225$ $\sigma = 125.26$
Position 3	P_3	deg	$\rho = 315$ $\sigma = 54.74$
Position 4	P_4	deg	$\rho = 315$ $\sigma = 305.26$
Response time 1	$P_1 \rightarrow P_2$	ms	5
Response time 2	$P_2 \rightarrow P_3$	ms	94
Response time 3	$P_3 \rightarrow P_4$	ms	94
Response time 4	$P_4 \rightarrow P_1$	ms	80
Longitudinal mode - $N_p = 2$			
Position 1	P_1	deg	$\rho = 360$ $\sigma = 90$
Position 2	P_2	deg	$\rho = 360$ $\sigma = 270$
Response time 1	$P_1 \rightarrow P_2$	ms	94
Response time 2	$P_2 \rightarrow P_1$	ms	5

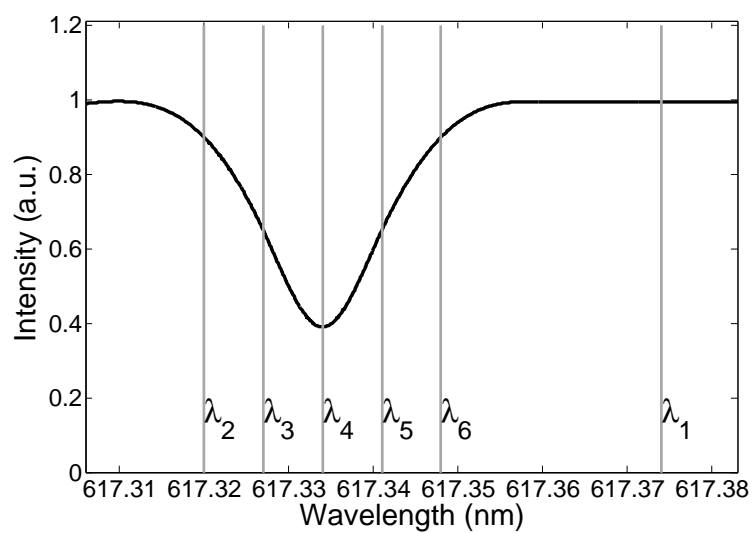


Figure A.1. Profile of the FeI spectral line used by PHI. Vertical lines indicate the filtergraph positions from λ_1 (in the continuum) to λ_{N_1} .

Acronyms

ADC	Analog to digital converter	FD	Floating diffusion
APS	Active pixel sensor	FDT	Full disk telescope
ASIC	Application-specific integrated circuit	FEE	Front-end electronics
AU	Astronomical unit	FF	Fill factor
CASE	Californium-252 assessment of single-event effects	FF	Flip-flop
CCD	Charge-coupled device	FIFO	First in, first out
CDS	Correlated double sampling	FOV	Field of view
CIS	CMOS image sensor	FPA	Focal plane assembly
CL	Channel link	FPGA	Field programmable gate array
CME	Coronal mass ejection	FPN	Fixed pattern noise
CMOS	Complementary metal-oxide-semiconductor	fps	Frames per second
CPLD	Complex programmable logic device	FSM	Finite state machine
CRC	Cyclic redundancy check	FWC	Full well charge
CTIA	Capacitive trans-impedance amplifier	FWHM	Full width at half maximum
CVCM	Collected volatile condensable material	GAM	Gravity assist maneuver
DAC	Digital to analog converter	GCR	Galactic cosmic ray
DC	Dark current	GEO	Geostationary earth orbit
DCNU	Dark current non-uniformity	GPU	Graphics processing unit
DD	Displacement damage	HI	Heavy ion
DFC	Dawn framing camera	HK	Housekeeping
DN	Digital number	HMI	Helioseismic and magnetic imager
DPU	Digital processing unit	HRT	High resolution telescope
DSP	Digital signal processor	HVPS	High voltage power supply
DUT	Device under test	IMaX	Imaging magnetograph experiment
EDAC	Error detection and correction	IS	Image sensor
EM	Electromagnetic	ISPHI	Image sensor for PHI
ENOB	Effective number of bits	ISS	Image stabilization system
EUV	Extreme ultraviolet	ITAR	International traffic in arms regulation
		LCVR	Liquid crystal variable retarder
		LEO	Low Earth orbit
		LET	Linear energy transfer

Acronyms

LUT	Look-up table	SDO	Solar dynamics observatory
LVDS	Low-voltage differential signaling	SECCHI	Sun earth connection coronal and heliospheric investigation
MDI	Michelson doppler imager	SEE	Single event effect
NIEL	Non-ionizing energy loss	SEFI	Single event functional interruption
NIR	Near infrared	SEL	Single event latch-up
OSIRIS	Optical, spectroscopic, and infrared remote imaging system	SEP	Solar energetic particle
OTP	One-time programmable	SET	Single event transient
PAL	Programmable array logic	SEU	Single event upset
PCB	Printed circuit board	SNR	Signal to noise ratio
PGA	Pin grid array	SOHO	Solar and heliospheric observatory
PHI	Polarimetric and helioseismic imager	SPI	Serial peripheral interface
PLA	Programmable logic array	SO	Solar orbiter
PLD	Programmable logic device	SRAM	Static random access memory
PLL	Phase-locked loop	SST	Swedish solar telescope
PMP	Polarization modulation package	SWAP	Sun watcher using APS detectors and image processing
POR	Power-on reset	s/c	Spacecraft
ppm	Parts per million	TID	Total ionizing dose
PROBA	Project for onboard autonomy	TIP	Tenerife infrared polarimeter
PRNU	Pixel response non-uniformity	TMR	Triple modular redundancy
PTC	Photon transfer curve	VMC	Venus monitoring camera
QE	Quantum efficiency	VTT	Vacuum tower telescope
rms	Root mean square		
ROIC	Readout integrated circuit		

Bibliography

- Bagnasco, G., October 2011, Experiment Interface Document: Part A, *SO project document*, SOL-EST-RCD-0500, Issue 2, Rev. 8
- Beletic, J., Blank, R., Gulbransen, D., Lee, D., Loose, M., Piquette, E., Sprafke, T., Tennant, W., Zandian, M., and Zino, J., 2008, Teledyne Imaging Sensors: infrared imaging technologies for astronomy and civil space, *High Energy, Optical, and Infrared Detectors for Astronomy III, Proc. SPIE*, Vol. 7021, pp. 70210H, doi:10.1117/12.790382
- Berg, M., Kim, H., Friendlich, M., Perez, S., Seidlrnk, C., Label, K., and Ladbury, R., 2011, SEU Analysis of Complex Circuits Implemented in Actel RTAX-S FPGA Devices, *IEEE Trans. Nuclear Science*, Vol. 58, Issue 3, pp. 1015-1022, doi:10.1109/TNS.2011.2128886
- Bigas, M., Cabruja, E., Forest, J., and Salvi, J., 2006, Review of CMOS Image Sensors, *Microelectronics Journal*, Vol. 37, Issue 5, pp. 433-451, doi:10.1016/j.mejo.2005.07.002
- Bignami, G., Cargill, P., Schutz, B., and Turonon, C., 2005, Cosmic Vision: Space Science for Europe 2015-2025, *ESA publication*, Vol. BR-247, Issue 1
- Blandford, J. and Pickel, J., 1985, Use of Cf-252 to determine parameters for SEU rate calculation, *IEEE Trans. Nuclear Science*, Vol. NS-32, pp. 4282-4286
- Blouke, M.M., 2012, Diffusion dark current in front-illuminated CCDs and CMOS image sensors, *Sensors, Cameras, and Systems for Industrial and Scientific Applications XIII, Proc. SPIE*, Vol. 8298, pp. 829809, doi:10.1117/12.920463
- Bohndiek, S.E., Blue, A., Clark, A.T., Prydderch, M.L., Turchetta, R., Royle, G.J., and Speller, R.D., 2008, Comparison of Methods for Estimating the Conversion Gain of CMOS Active Pixel Sensors, *IEEE Sensors Journal*, Vol. 8, No. 10, pp. 1734-1744, doi:10.1109/JSEN.2008.2004296
- Bogaerts, J. and Dierickx, B., 2000, Total dose effects on CMOS active pixel sensors, *Proc. SPIE*, Vol. 3965, pp 157-167, doi:10.1117/12.385432
- Bogaerts, J., Dierickx, B., Meynants, G., and Uwaerts, D., 2003, Total Dose and Displacement Damage Effects in a Radiation-Hardened CMOS APS, *IEEE Trans. Electron Devices*, Vol. 50, pp. 84-90, doi:10.1109/TED.2002.807251

- Carter, W., Duong, K., Freeman, R.H., Hsieh, H., Ja, J.Y., Mahoney, J.E., Ngo, L.T., and Sze, S.L., 1986, A user programmable reconfiguration gate array, *Proc. IEEE Custom Integrated Circuits Conference*, pp. 233-235
- Collados, M., 1999, High Resolution Spectropolarimetry and Magnetography, *Third Advances in Solar Physics Euroconference: Magnetic Fields and Oscillations, ASP Conf. Ser.*, Vol. 184, pp. 3-22, ISBN: 1-58381-010-2
- Collados, M., Lagg, A., Díaz-García, J.J., Hernández-Suárez, E., López-López, R., Páez-Mana, E., and Solanki, S.K., 2007, Tenerife Infrared Polarimeter II, *The Physics of Chromospheric Plasmas, ASP Conf. Ser.*, Vol. 368, pp. 611
- Cummings, C.E., Golson, S., and Mills, D., 2003, Asynchronous & Synchronous Reset Design Techniques - Part Deux, *Synopsys User Group (SNUG)*, Boston
- Dale, C., Marshall, P., Cummings, B., Shamey, L., and Holland, A., 1993, Displacement Damage Effects in Mixed Particle Environments for Shielded Spacecraft CCDs, *IEEE Trans. Nuclear Science*, Vol. 40, Issue 6, pp. 1628-1637, doi:10.1109/23.273497
- Dally, W.J. and Poulton, J.W., 1998, *Digital Systems Engineering*, Cambridge University Press, Cambridge, ISBN: 9780521592925
- De Groof, A., Berghmans, D., Nicula, B., Halain, J.P., Defise, J.M., Thibert, T., and Schühle, U., 2008, CMOS-APS Detectors for Solar Physics: Lessons Learned during the SWAP Preflight Calibration, *Solar Physics*, Vol. 249, Issue 1, pp. 147-163, doi:10.1007/s11207-008-9175-y
- Del Toro-Iniesta, J.C., 2003, *Introduction to Spectropolarimetry*, Cambridge University Press, Cambridge, ISBN: 9780521036481
- Del Toro-Iniesta, J.C. and Collados, M., 2000, Optimum Modulation and Demodulation Matrices for Solar Polarimetry, *Applied Optics*, Vol. 39, Issue 10, pp. 1637-1642, doi:10.1364/AO.39.001637
- Del Toro-Iniesta, J.C. and Martínez-Pillet, V., 2011, Diagnostics for spectropolarimetry and magnetography, *Physics of Sun and Star Spots: Proc. IAU Symposium*, No. 273, pp. 37-43, Cambridge University Press, Cambridge, doi:10.1017/S1743921311014979
- Drobnes, E., Littleton, A., Pesnell, W.D., Beck, K., and Buhr, S., 2012, *The Solar Dynamics Observatory*, Springer, USA, ISBN: 9781461436720
- Eid, E., Chan, T.Y., Fossum, E.R., Tsai, R.H., Spagnuolo, R., Deily, J., Byers, W.B., and Peden, J.C., 2001, Design and characterization of ionizing radiation-tolerant CMOS APS image sensors up to 30 Mrd (Si) total dose, *IEEE Trans. Nuclear Science*, Vol. 48, Issue 6, pp. 1796-1806, doi:10.1109/23.983133
- European Machine Vision Association, 2010, Standard for Characterization of Image Sensors and Cameras, *EMVA Standard 1288*, Issue 3

- ESTEC product assurance and safety, automation and informatics departments, 1993, The Radiation Design Handbook, *ESA publications*, ESA-PSS-01-609, Issue 1, Noordwijk (NL), ISSN: 0379-4059
- European Space Components Coordination, 2007, Total Dose Steady-State Irradiation Test Method, *ESCC basic specification* No. 22900, Issue 3, Noordwijk (NL)
- European Space Components Coordination, 2002, Single Event Effects Test Method and Guidelines, *ESCC basic specification* No. 25000, Issue 1, Noordwijk (NL)
- European Space Components Coordination, 2011, Techniques for Radiation Effects Mitigation in ASICs and FPGAs, *ESCC Handbook*, Draft, Revision 6, Noordwijk (NL)
- Fernández-Rico, J. and Pérez-Grande, I., 2012, SO/PHI Optics Unit Thermal Analysis, *PHI instrument technical note*, SOL-PHI-IDR-SY4000-TN-8, Issue 2
- Fernández-León, A., Pouponnot, A., and Habinc, S., 2002, ESA FPGA task force: Lessons learned, *Proc. Military and Aerospace Programmable Logic Devices (MAPLD) 2002 conference*
- Feller, A., 2011, Effect of Pointing Errors and Solar Evolution on Polarimetric Accuracy, *PHI instrument technical note*, SOL-PHI-MPS-SY1300-TN-2, Issue 1 Rev. 2
- Gandorfer, A., Povel, H.P., Steiner, P., Aebersold, F., Egger, U., Feller, A., Gisler, D., Hagenbuch, S., and Stenflo, J.O., 2004, Solar polarimetry in the near UV with the Zurich Imaging Polarimeter ZIMPOL II, *Astronomy & Astrophysics*, Vol. 422, pp. 703-708, doi:10.1051/0004-6361:20040254
- Gandorfer, A., Solanki, S.K., Woch, J., Martínez-Pillet, V., Álvarez-Herrero, A., and Appourchaux, T., 2011, The Solar Orbiter Mission and its Polarimetric and Helioseismic Imager (SO/PHI), *Journal of Physics: Conf. Ser.*, Vol. 272, Issue 1, pp. 012086, doi:10.1088/1742-6596/271/1/012086
- Goiffon, V., Estribeau, M., and Magnan, P., 2009, Overview of ionizing radiation effects in image sensors fabricated in a deep sub-micrometer CMOS imaging technology, *IEEE Trans. Electron Devices*, Vol. 56, pp. 2594-2601, doi:10.1109/TED.2009.2030623
- Goiffon, V., Virmontois, C., Magnan, P., Cervantes, P., Corbiere, F., Estribeau, M., and Pinel, P., 2010, Radiation damages in CMOS image sensors: testing and hardening challenges brought by deep sub-micrometer CIS processes, *Proc. SPIE*, Vol. 7826, pp. 78261S, doi:10.1117/12.868443
- Gomes, J. and Shea, H.R., 2011, Displacement damage effects in silicon MEMS at high proton doses, *Proc. SPIE*, Vol. 7928, pp. 79280G, doi:10.1117/12.873546
- Henney, C.J., Keller, C.U., and Harvey, J.W., 2006, SOLIS-VSM Solar Vector Magnetograms, *Solar Polarization 4, ASP Conf. Ser.*, Vol. 358, p. 92
- Hoffman, A., Loose, M., and Suntharalingam, V., 2005, CMOS Detector Technology, *Experimental Astronomy*, Vol. 19, Issue 1-3, pp. 111-134, doi:10.1007/s10686-005-9013-2

- Holmes-Siedle, A. and Adams, L., 2002, *Handbook of radiation effects*, Oxford University Press, Oxford, ISBN: 9780198507338
- Holst, G.C. and Lomheim, T.S., 2007, *CMOS/CCD Sensors and Camera Systems*, SPIE press book, Washington, ISBN: 9780819467300
- Howell, S. B., 2006, *Handbook of CCD Astronomy*, Cambridge University Press, Cambridge, ISBN: 9780521617628
- Huang, C.K. and Wang, J.J.: Microsemi Corporation, 2012, Total Ionizing Dose Test Report: RTAX1000-CQ352, *Product test report*
- Huber, M., Pauluhn, A., Culhane, J., Timothy, J., Wilhem, K., and Zehnder, A., 2010, Observing Photons in Space, *ISSI scientific report series, ESA/ISSI*, Noordwijk (NL), ISBN: 9789292219383
- ITRS, 2011, International Technology Roadmap for Semiconductors, www.itrs.net
- Janesick, J. and Blouke, M., 1987, Sky on a chip: the fabulous CCD, *Sky and Telescope Magazine*, Vol. 74, Issue 3, pp. 238-242
- Janesick, J., 2001, *Scientific Charge-Coupled Devices*, SPIE press book, Washington, ISBN: 9780819436986
- Janesick, J., Gunawan, F., Dosluoglu, J., Tower, J., and Mccaffrey, N., 2002, Scientific CMOS Pixels, *Experimental Astronomy*, Vol. 14, Issue 1, pp. 33-43, doi:10.1023/A:1026128918608
- Janesick, J., Andrews, J., and Elliott, T., 2006, Fundamental Performance Differences between CMOS and CCD imagers: Part I, *High Energy, Optical, and Infrared Detectors for Astronomy II, Proc. SPIE*, Vol. 6276, pp. 62760M, doi:10.1117/12.678867
- Janesick, J., Andrews, J., Tower, J., Grygon, M., Elliott, T., Cheng, J., Lesser, M., and Pinter, J., 2007, Fundamental Performance Differences between CMOS and CCD imagers: Part II, *Focal Plane Arrays for Space Telescopes III, Proc. SPIE*, Vol. 6690, pp. 669003, doi:10.1117/12.740218
- Janesick, J., 2007, *Photon Transfer*, SPIE press book, Washington, ISBN: 9780819467225
- Kastensmidt, F.L., Fonseca, E.C.P., Vaz, R.G., Goncalvez, O.L., Chipana, R., and Wirth, G.I., 2011, TID in Flash-Based FPGA: Power Supply-Current Rise and Logic Function Mapping Effects in Propagation-Delay Degradation, *IEEE Trans. Nuclear Science*, Vol. 58, pp. 1927-1934, doi:10.1109/TNS.2011.2128881
- Keller, H.U., Barbieri, C., Lamy, P., Rickman, H., Rodrigo, R., Wenzel, K.P., Sierks, H., A'Hearn, M.F., Angrilli, F., Angulo, M., Bailey, M.E., Barthol, P., Barucci, M.A., Bertaux, J.L., Bianchini, G., Boit, J.L., Brown, V., Burns, J.A., Büttner, I., Castro, J.M., Cremonese, G., Curdt, W., Da Deppo, V., Debei, S., Cecco, M.D., Dohlen, K., Fornasier, S., Fulle, M., Germerott, D., Gliem, F., Guizzo, G.P., Hviid, S.F., Ip, W.H.,

- Jorda, L., Koschny, D., Dramm, J.R., Kührt, E., Küppers, M., Lara, L.M., Llebaria, A., López, A., López-Jimenez, A., López-Moreno, J., Meller, R., Michalik, H., Michelena, M.D., Müller, R., Naletto, G., Origné, A., Parzianello, G., Pertile, M., Quintana, C., Ragazzoni, R., Ramous, P., Reiche, K.U., Reina, M., Rodríguez, J., Rousset, G., Sabau, L., Sanz, A., Sivan, J.P., Stöckner, K., Tabero, J., Telljohann, U., Thomas, N., Timon, V., Tomasch, G., Wittrock, T., and Zaccariotto, M., 2007, OSIRIS - The Scientific Camera System Onboard Rosetta, *Space Science Reviews*, Vol. 128, Issue 1-4, pp. 433-506, doi:10.1007/s1121400691284
- Kester, W., 2005, *The Data Conversion Handbook*, Elsevier (Newnes), Norwood (USA), ISBN: 9780750678414
- Kilts, S., 2007, *Advanced FPGA design*, John Wiley & Sons, New Jersey (USA), ISBN: 9780470054376
- Kosugi, T., Matsuzaki, K., Sakao, T., Shimizu, T., Sone, Y., Tachikawa, S., Hashimoto, T., Minesugi, K., Ohnishi, A., Yamada, T., Tsuneta, S., Hara, H., Ichimoto, K., Suematsu, Y., Shimojo, M., Watanabe, T., Shimada, S., Davis, J.M., Hill, L.D., Owens, J.K., Title, A.M., Chulhane, J.L., Harra, L.K., Dopschek, G.A., and Golub, L., 2007, The Hinode (Solar-B) Mission: An Overview, *Solar Physics*, Vol. 243, Issue 1, pp. 3-17, doi:10.1007/s11207-007-9014-6
- Kuon, I. and Rose, J., 2007, Measuring the Gap Between FPGAs and ASICs, *IEEE Trans. Computer-Aided Design of Integrated Circuits and Systems*, Vol. 26, pp. 203-215, doi:10.1109/TCAD.2006.884574
- Kuon, I., Tessier, R., and Rose, J., 2008, FPGA Architecture: Survey and Challenges, *Foundations and Trends in Electronic Design Automation*, Vol. 2, pp. 135-253, doi:10.1561/10000000005
- Loose, M., Lewyn, L., Durmus, H., Garnett, J., Hall, D., Joshi, A., Kozlowski, L., and Ovsiannikov, I., 2003, SIDECAR Low-power control ASIC for focal plane arrays including A/D conversion and bias generation, *Instrument Design and Performance for Optical/Infrared Ground-based Telescopes, Proc. SPIE*, Vol. 4841, pp. 782-794, doi:10.1117/12.462601
- Ma, T.P. and Dressendorfer, P.V., 1989, *Ionizing Radiation Effects in MOS devices and circuits*, John Wiley & Sons, Canada, ISBN: 0-471-84893-X
- Magnan, P., 2003, Detection of visible photons in CCD and CMOS: A comparative view, *Nuclear Instruments and Methods in Physics Research*, Vol. 504, Issue 1-3, pp. 199-212, doi:10.1016/S0168-9002(03)00792-7
- Manuzzato, A., 2009, *Single Event Effects on FPGAs*, PhD Thesis, University of Padova (I)
- Marsden, R. and Müller, D., 2011, SO Definition Study Report (Red Book), *ESA publication*, ESA/SRE(2011)14, Issue 1

- Markiewicz, W.J., Titov, D.V., Ignatiev, N., Keller, H.U., Crisp, D., Limaye, S.S., Jaumann, R., Moissl, R., Thomas, N., Esposito, L., Watanabe, S., Fiethe, B., Behnke, T., Szemerey, I., Michalik, H., Perplies, H., Wedemeier, M., Sebastian, I., Boogaerts, W., Hviid, S.F., Dierker, C., Osterloh, B., Böker, W., Koch, M., Michaelis, H., Belyaev, D., Dannenberg, A., Tschimmel, M., Russo, P., Roatsch, T., and Matz, K.D., 2007, Venus Monitoring Camera for Venus Express, *Planetary and Space Science*, Vol. 55, Issue 12, p. 1701-1711, doi:10.1016/j.pss.2007.01.004
- Martínez-Pillet, V., Collados, M., Sánchez-Almeida, J., González, V., Cruz-Lopez, A., Manescau, A., Joven, E., Paez, E., Diaz, J., Feeney, O., Sánchez, V., Scharmer, G., and Soltau, D., 1999, LPSP & TIP: Full stokes polarimeters for the Canary islands observatories, *High Resolution Solar Physics: Theory, Observations and Techniques, Proc. 19th Sacramento Peak Summer Workshop, ASP Conf. Ser.*, Vol. 183, p. 264, ISBN: 1-58381-009-9
- Martínez-Pillet, V., 2006, Instrumental approaches to magnetic and velocity measurements in and out of the ecliptic plane, *Proc. 2nd Solar Orbiter workshop*, ESA SP-641 (CD-ROM), Noordwijk (NL)
- Martínez-Pillet, V., Del Toro-Iniesta, J.C., Álvarez-Herrero, A., Domingo, V., Bonet, J.A., González-Hernández, L., López-Jiménez, A., Pastor, C., Gasent-Blesa, J.L., Mellado, P., Piqueras, J., Aparicio, B., Balaguer, M., Ballesteros, E., Belenguer, T., Bellot-Rubio, L.R., Berkefeld, T., Collados, M., Deutsch, W., Feller, A., Girela, F., Grauf, B., Heredero, R.L., Herranz, M., Jerónimo, J.M., Laguna, H., Meller, R., Menéndez, M., Morales, R., Orozco Suárez, D., Ramos, G., Reina, M., Ramos, J.L., Rodríguez, P., Sánchez, A., Uribe-Patarroyo, N., Barthol, P., Gandorfer, A., Knoelker, M., Schmidt, W., Solanki, S.K., and Vargas-Domínguez, S., 2011, The Imaging Magnetograph eXperiment (IMaX) for the Sunrise Balloon-Borne Solar Observatory, *Solar Physics*, Vol. 268, Issue 1, pp. 57-102, doi:10.1007/s11207-010-9644-y
- Maxfield, C., 2004, *The Design Warrior's Guide to FPGAs*, Elsevier, Oxford, ISBN: 0-7506-7604-3
- Microsemi Corporation, 2010, Radiation-Tolerant ProASIC3 FPGAs Radiation Effects, *Product test report*
- Microsemi Corporation, 2012, CoreEDAC v2.1, *Handbook*, Revision 1
- Microsemi Corporation, 2012, RTAX-S/SL and RTAX-DSP Radiation Tolerant FPGAs, *Product datasheet*, Revision 15
- Microsemi Corporation, 2012, SmartFusion Customizable System-on-Chip (cSoC), *Product datasheet*, Revision 8
- Mohammadzadeh, A., Duzellier, S., Hopkinson, G., Mangeret, R., Poivey, C., Cueto Rodríguez, J., and Mattsson, S., 2003, Radiation Engineering Methods for Space Applications, *RADECS short course*, Noordwijk (NL)

- Müller, D., Marsden, G., Cyr, O.C.St., and Gilbert, H.R., 2012, Solar Orbiter - Exploring the Sun-Heliosphere connection, *Solar Physics*, Online version, Springer, doi:10.1007/s11207-012-0085-7
- Murdin, P., 2001, Encyclopedia of Astronomy and Astrophysics, *Nature Publishing*, Online version: eaa.crcpress.com
- Nickson, B., 2011, CASE system, <https://escies.org/webdocument/showArticle?id=252&groupid=6>
- Ortiz, A. and van der Voort, L.H.M. Rouppe, 2010, Spectropolarimetry with CRISP at the Swedish 1-m Solar Telescope, Magnetic coupling between the Interior and Atmosphere of the Sun, *Astrophysics and Space Science Proc.*, pp. 150-155, Springer, Berlin, doi:10.1007/978-3-642-02859-5_11
- Ostler, P.S., Caffrey, M.P., Gibelyou, D.S., Graham, P.S., Morgan, K.S., Pratt, B.H., Quinn, H.M., and Wirthlin, M.J., 2009, SRAM FPGA Reliability Analysis for Harsh Radiation Environments, *IEEE. Trans. Nuclear Science*, Vol. 56, Issue 6, pp. 3519-3526, doi:10.1109/TNS.2009.2033381
- Piqueras, J., Heerlein, K., Werner, S., Enge, R., Schühle, U., Woch, J., De Ridder, T., Meynants, G., Wolfs, B., Lepage, G., and Diels, W., 2012, CMOS sensor and camera for the PHI instrument on board Solar Orbiter: evaluation of the radiation tolerance, *High Energy, Optical, and Infrared Detectors for Astronomy V, Proc. SPIE*, Vol. 8453, pp. 845314, doi:10.1117/12.925403
- Rao, P.R., Wang, X., and Theuwissen, A.J.P., 2008, Degradation of CMOS image sensors in deep-submicron technology due to γ -irradiation, *Solid-State Electronics*, Vol. 52, Issue 9, pp. 1407-1413, doi:10.1016/j.sse.2008.04.023
- Rezgui, S., Wang, J.J., Tung, E.C., Cronquist, B., and McCollum, J., 2007, New Methodologies for SET Characterization and Mitigation in Flash-Based FPGAs, *IEEE Trans. Nuclear Science*, Vol. 54, Issue 6, pp. 2512-2524, doi:10.1109/TNS.2007.910126
- Rezgui, S., Wang, J.J., Sun, Y., D'Silva, D., Cronquist, B., and McCollum, J., 2009, SET characterization and mitigation in RTAX-S antifuse FPGAs, *Proc. of the 2009 IEEE Aerospace conference*, Vol. 1, pp. 1-14, doi:10.1109/AERO.2009.4839515
- Roy, K., Mukhopadhyay, S., and Mahmoodi-Meimand, H., 2003, Leakage Current Mechanisms and Leakage Reduction Techniques in Deep-Submicrometer CMOS circuits, *Proc. IEEE*, Vol. 91, Issue 2, pp. 305-327, doi:10.1109/JPROC.2002.808156
- Sasso, C., Lagg, A., and Solanki, S.K., 2006, Milne-Eddington inversions of the He I 10830 Å Stokes profiles: Influence of the Paschen-Back effect, *Astronomy & Astrophysics*, Vol. 456, pp. 367-371, doi:10.1051/0004-6361:20065257
- Scherrer, P.H., Bogart, R.S., Bush, R.I., Hoeksema, J.T., Kosovichev, A.G., Schou, J., Rosenberg, W., Springer, L., Tarbell, T.D., Title, A., Wolfson, C.J., Zayer, I., and MDI engineering team, 1995, The Solar Oscillations Investigation - Michelson Doppler Imager, *Solar Physics*, Vol. 162, Issue 1-2, pp. 129-188, doi:10.1007/BF00733429

- Schou, J., Scherrer, P.H., Bush, R.I., Wachter, R., Couvidat, S., Rabello-Soares, M.C., Bogart, R.S., Hoeksema, J.T., Liu, Y., Duval, T.L., Akin, D.J., Allard, B.A., Miles, J.W., Rairden, R., Shine, R.A., Tarbell, T.D., Title, A.M., Wolfson, C.J., Elmore, D.F., Norton, A.A., and Tomczyk, S., 2012, Design and Ground Calibration of the Helioseismic and Magnetic Imager (HMI) Instrument on the Solar Dynamics Observatory (SDO), *Solar Physics*, Vol. 275, Issue 1-2, pp. 229-259, doi:10.1007/s11207-011-9842-2
- Shurcliff, W.A., 1962, *Polarized Light: Production and Use*, Harvard University Press, Massachusetts
- Sierks, H., Keller, H.U., Jaumann, R., Michalik, H., Behnke, T., Bubenhausen, F., Büttner, I., Carsenty, U., Christensen, U., Enge, R., Fiethe, B., Gutiérrez-Marqués, P., Hartwig, H., Krüger, H., Kühne, W., Maue, T., Mottola, S., Nathues, A., Reiche, K.U., Richards, M.L., Roatsch, T., Schröder, S.E., Szemerey, I., and Tschentscher, M., 2011, The Dawn Framing Camera, *Space Science Reviews*, Vol. 163, Issue 1-4, pp. 263-327, doi:10.1007/s11214-011-9745-4
- Simms, L.M., 2010, *Hybrid CMOS SiPIN Detectors as Astronomical Imagers*, PhD Thesis, Stanford University (USA)
- Socas-Navarro, H., Trujillo-Bueno, J., and Landi-Degl'Innocenti, E., 2004, Signatures of Incomplete Paschen-Back Splitting in the Polarization Profiles of the He I λ 10830 Multiplet, *Astrophysical Journal*, Vol. 612, pp. 1175-1180, doi:10.1086/422580
- Sørensen, J., 2010, Solar Orbiter Environmental Specification, *SO project document*, TEC-EES-03-034/JS, Issue 3
- Steifert, N., Shipley, P., Pant, M.D., Ambrose, V., and Gill, B., 2005, Radiation-induced clock jitter and race, *Proc. 43rd Annual International Reliability Physics Symposium*, pp. 215-222, doi:10.1109/RELPHY.2005.1493087
- Stephenson, J., Chen, D., Fung, R., and Chromczak, J., 2009, Understanding Metastability in FPGAs, *Altera white paper*, v1.2
- Stettler, M., Caffrey, M., Graham, P., and Krone, J., 2004, Radiation effects and mitigation strategies for modern FPGAs, *Proc. 10th Workshop on Electronics for LHC and Future Experiments*, pp. 112-116
- Stix, M., 2002, *The Sun: An introduction*, Springer, Berlin, ISBN: 3-540-42886-0
- Theuwissen, A., 2008, CMOS image sensors: State-of-the-art, *Solid-State Electronics*, Vol. 52, Issue 9, pp. 1401-1406, doi:10.1016/j.sse.2008.04.012
- Tsuneta, S., Ichimoto, K., Katsukawa, Y., Nagata, S., Otsubo, M., Shimizu, T., Suematsu, Y., Nakagiri, M., Noguchi, M., Tarbell, T., Title, A., Shine, R., Rosenberg, W., Hoffman, C., Jurcevich, B., Kushner, G., Levay, M., Lites, B., Elmore, D., Matsushita, T., Kawaguchi, N., Saito, H., Mikami, I., Hill, L.D., and Owens, J.K., 2008, The Solar Optical Telescope for the Hinode Mission: An Overview, *Solar Physics*, Vol. 249, Issue 2, pp. 167-196, doi:10.1007/s11207-008-9174-z

- USA Department of Defense, 2010, Test Method Standard: Microcircuits, *Standard for Military and Aerospace electronic systems MIL-STD-883*, Issue H, Columbus (USA)
- Van Aken, D., Hervé, D., and Beaumel, M., 2009, Total Dose, Displacement Damage and Single Event Effects in the Radiation Hardened CMOS APS HAS2, *Proc. SPIE*, Vol. 7474, pp. 74741C-74741C-12, doi:10.1117/12.829983
- Velazco, R., Fouillat, P., and Reis, R., 2007, *Radiation Effects on Embedded Systems*, Springer, Dordrecht (NL), ISBN: 978-1-4020-5645-1
- Waltham, N. and Eyles, C., 2007, Design, development and performance of the STEREO SECCHI CCD cameras, *Solar Physics and Space Weather Instrumentation II, Proc. SPIE*, Vol. 6689, pp. 668908-668908-15, doi:10.1117/12.733835
- Waltham, N., Pryderch, M., Mapson-Menard, H., Pool, P., and Harris, A., 2007, Development of a thinned back-illuminated CMOS active pixel sensor for extreme ultraviolet spectroscopy and imaging in space science, *Nuclear Instruments and Methods in Physics Research*, Vol. 573, Issue 1-2, pp. 250-252, doi:10.1016/j.nima.2006.10.259
- Wang, J.J., 2003, Radiation Effects in FPGAs, *Proc. 9th Workshop on Electronics for LHC Experiments*, pp. 34-43
- Wang, J.J.: Microsemi Corporation, 2007, Total Ionizing Dose Test Report: RTAX250, *Product test report*
- Woch, J. and PHI team, 2012, PHI Experiment Interface Document: Part B, *PHI instrument document*, SOL-PHI-MPS-SY1400-IF-2, Issue 2
- Wong, H., Betz, V., and Rose, J., 2011, Comparing FPGA vs. Custom CMOS and the impact on Processor Microarchitecture, *Proc. 19th ACM/SIGDA International Symposium on Field Programmable Gate Arrays*, pp. 5-14, doi:10.1145/1950413.1950419
- Xilinx Corporation, 2010, Space-grade Virtex-4QV Family Overview, *Product specification*, DS653, Version 2.0
- Zhu, P., 2008, *Design and characterization of phase-locked loops for radiation tolerant applications*, PhD Thesis, Southern Methodist University (USA)
- Ziegler, J.F., 2011, Stopping and range of ions in matter, www.srim.org

Acknowledgements

This PhD thesis results from the work I have carried out during the past years at the Max-Planck-Institute for Solar System Research, in Katlenburg-Lindau. Numerous people have contributed to it in one or another way, or have supported me along this path.

In the first place, I feel indebted to Joachim Woch and Udo Schühle for having allowed me to perform my dissertation in this field, as well as for having made me constantly think that my work was following the correct direction. Joachim's continuous support and sensible way of facing difficulties were really valuable. Udo did always find the time to discuss and review my written work, and provided me with remarkably useful suggestions. I am also very grateful to Prof. Harald Michalik. He generously accepted me as PhD student and gave me key advices to shape and refine this thesis.

My thanks go to Sami Solanki for kindly making space in his tight agenda to become referee and committee member of this thesis, and for actively supporting the instrumentation development on the solar group that he leads. I am grateful to Prof. Karl-Heinz Glaßmeier for agreeing to chair my disputation. I also appreciate the efforts of Dieter Schmitt to efficiently coordinate the IMPRS research school.

There are two persons without whom I would have never embarked on this doctorate: Valentín Martínez Pillet and Ezequiel Ballesteros Ramírez. Valentín deserves a really big thanks because he devised the framework of this dissertation, introduced me to solar polarimetry, and kept showing interest about the ongoing status of my PhD studies. Ezequiel revealed to me the foundations of a doctorate in instrumentation and firmly encouraged me to start one, which I do truly appreciate. Besides, I want to express my gratitude to José Carlos del Toro Iniesta for his assistance with understanding polarimetry, and to Johann Hirzberger for providing me with quick and solid answers to my science-related questions.

I am very fortunate to have formed part of the MPS *Labor*, and especially of the *PHI FPA* team, where I always felt fully integrated and found a stimulating and warm working environment. Stephan Werner has contributed to many of the results of this work and has prepared most of the setups without which those results would not have come into being. I am deeply thankful to him not only for his openness and willingness to arrange new measurements, but also for the pleasant atmosphere of our office. Klaus Heerlein was at all times available to start interesting discussions and is one of the key architects of the great environment of the team: thank you. Rainer Enge and Michael Sperling amazed me from the very beginning with their easiness to build *ready-to-flight* electronics. They have kept constantly open to design changes and improvements, this I highly appreciate. I also thank Tanja Macke for having made my bureaucratic life much easier.

For their support and fruitful discussions during the radiation tests, as well as for the notable information they have shared, I am grateful to Ali BenMoussa and Samuel Gissot.

I cannot forget the enjoyable time spent with some of my fellows at the IMPRS and MPS. In particular, with Karsten Schindler, with whom I had many refreshing and *recherche* conversations and who enlighten me on more than one matter; with Farhad Shakeri for amusing and shortening our daily Göttingen-Lindau journeys; with Fátima Rubio for being on all occasions attentive and ready to give a hand; and with Julia Thalmann for keeping accessible to solve my regulatory doubts and for her pleasant company. In addition, I had lots of fun with Jeff Lee, enjoyed many dinners and excursions with Yeon Joo, formed an amiable community with Vali, joined football games and *Brocken* hikes with Wieland, and had diverting experiences with Maria, David, Kok Leng, Maria A., Juan S., Chemedá, Lucas, and of course, the whole Friday Evening Beer (FEB) team.

A very special and well deserved thanks go to Mari C for her endless support and patience, and for having been such an exceptional life companion. The last words of this thesis are dedicated to my parents, whose support and faith in my decisions have guided me, and to my brother, who was always a source of inspiration to me: *¡gracias!*

Curriculum Vitae and publications

Name Juan José Piqueras Meseguer
Date of birth 19 May 1984
Place of birth Molina de Segura, Murcia (Spain)
Citizenship Spanish

Education

2002 - 2007 Universidad Politécnica de Cartagena (Spain)
Electronics engineer (*telecommunications*). Thesis: "Astronomical image acquisition and real-time processing system based on FPGA"

2007 - 2009 Universidad de La Laguna (Spain)
Master of Advanced studies (*Diploma de Estudios Avanzados*). Thesis: "Hardware implementation of the re-focussing mechanism of plenoptic images"

2009 - 2013 Technische Universität Braunschweig (Germany)
PhD thesis under the *International Max Planck Research School (IMPRS) on Physical Processes in the Solar System and Beyond* program

Professional experience

06/2006 - 09/2006 Instituto de Astrofísica de Canarias (Spain)
Summer internship. Project: Real-time adaptive optics

09/2007 - 06/2008 Instituto de Astrofísica de Canarias (Spain)
Electronics fellowship. Project: FastCam

06/2008 - 09/2009 Instituto de Astrofísica de Canarias (Spain)
Electronics and quality control engineer. Project: IMaX / Sunrise

10/2009 - present Max-Planck-Institut für Sonnensystemforschung (Germany)
Research assistant / Electronics engineer. Project: PHI / Solar Orbiter

Publications

- Piqueras, J.**, Heerlein, K., Werner, S., Enge, R., Schühle, U., Woch, J., De Ridder, T., Wolfs, B., Lepage, G., and Diels, W., 2012, CMOS sensor and camera for the PHI instrument on board Solar Orbiter: evaluation of the radiation tolerance, *High Energy, Optical, and Infrared Detectors for Astronomy V, Proc. SPIE*, Vol. 8453, pp. 845314, doi:10.1117/12.925403
- Martínez-Pillet, V., del Toro-Iniesta, J.C., Álvarez-Herrero, A., Domingo, V., Bonet, J.A., González-Fernández, L., López-Jiménez, A., Pastor, C., Gasent-Blesa, J.L., Mellado, P., **Piqueras, J.**, Aparicio, B., Balaguer, M., Ballesteros, E., Belenguer, T., Bellot-Rubio, L.R., Berkefeld, T., Collados, M., Deutsch, W., Feller, A., Girela, F., Grauf, B., Heredero, R.L., Herranz, M., Jerónimo, J.M., Laguna, H., Meller, R., Menéndez, M., Morales, R., Orozco Suárez, D., Ramos, G., Reina, M., Ramos, J.L., Rodríguez, P., Sánchez, A., Uribe-Patarroyo, N., Barthol, P., Gandorfer, A., Knoelker, M., Schmidt, W., Solanki, S.K., and Vargas-Domínguez, S., 2011, The Imaging Magnetograph eXperiment (IMaX) for the Sunrise Balloon-Borne Solar Observatory, *Solar Physics*, Vol. 268, Issue 1, pp. 57-102, doi:10.1007/s11207-010-9644-y
- Femenía, B., Rebolo, R., Pérez-Prieto, J.A., Hildebrandt, S.R., Labadie, L., Pérez-Garrido, A., Béjar-Sánchez, V., Díaz-Sánchez, A., Villó, I., Oscoz, A., López, R., Rodríguez, L.F., and **Piqueras, J.**, 2011, Lucky Imaging Adaptive Optics of the brown dwarf binary GJ569Bab, *Monthly Notices of the Royal Astronomical Society*, Vol. 413, Issue 3, pp. 1524-1536, doi:10.1111/j.1365-2966.2011.18226.x
- Labadie, L., Rebolo, R., Villó, I., Pérez-Prieto, J.A., Pérez-Garrido, A., Hildebrandt, S.R., Femenía, B., Díaz-Sánchez, A., Béjar, V.J.S., Oscoz, A., López, R., **Piqueras, J.**, and Rodríguez, L.F., 2011, High-contrast optical imaging of companions: the case of the brown dwarf binary HD 130948BC, *Astronomy & Astrophysics*, Vol. 526, id.A144, doi:10.1051/0004-6361/201014358
- Labadie, L., Rebolo, R., Femenía, B., Villó, I., Díaz-Sánchez, A., Oscoz, A., López, R., Pérez-Prieto, J.A., Pérez-Garrido, A., Hildebrandt, S.R., Béjar-Sánchez, V., **Piqueras, J.**, and Rodríguez, L.F., 2010, High spatial resolution and high contrast optical speckle imaging with FastCam at the ORM, *Ground-based and airborne inst. for astronomy III, Proc. SPIE*, Vol. 7735, pp. 77350X, doi:10.1117/12.857998
- Rodríguez-Ramos, L.F., Martín, Y., Díaz J.J., **Piqueras, J.**, García-Jiménez, J., and Rodríguez-Ramos, J.M., 2010, FPGA-based real time processing of the Plenoptic Wavefront Sensor, *Proc. 1st AO4ELT conference: Adaptive Optics for Extremely Large Telescopes*, id.07010, doi:10.1051/ao4elt/201007007
- Rodríguez-Ramos, L.F., Martín-Hernando, Y., Díaz-García J.J., **Piqueras-Meseguer, J.J.**, and Rodríguez-Ramos, J.M., 2009, The Plenoptic Camera as a wavefront sensor for the European Solar Telescope (EST), *Astronomical and Space Optical Systems, Proc. SPIE*, Vol. 7439, pp. 74390I-74390I-9, doi:10.1117/12.828578
- Rodríguez-Ramos, L.F., Díaz-García J.J., **Piqueras-Meseguer, J.J.**, Martín-Hernando, Y., and Rodríguez-Ramos, J.M., 2008, FPGA-based slope computation for ELTs adaptive optics wavefront sensors, *Adaptive Optics Systems, Proc. SPIE*, Vol. 7015, pp. 701530-701530-11, doi:10.1117/12.787412

- Oscosz, A., Rebolo, R., López, R., Pérez-Garrido, A., Pérez, J.A., Hildebrandt, S., Rodríguez-Ramos, L.F., **Piqueras, J.J.**, Villó, I., González, J.M., Barrena, R., Gómez, G., García, A., Montañés, P., Rosenberg, A., Cadavid, E., Calcines, A., Díaz-Sánchez, A., Kohley, R., Martín, Y., Peñate, J., and Sánchez, V., 2008, FastCam: a new lucky imaging instrument for medium-sized telescopes, *Ground-based and Airborne Instrumentation for Astronomy II, Proc. SPIE*, Vol. 7014, pp. 701447, doi:10.1117/12.788834
- Rodríguez-Ramos, L.F., **Piqueras-Meseguer, J.J.**, Martín-Hernando, Y., Oscosz, A., and Rebolo, R., 2008, Real-time lucky imaging in FastCam project, *Ground-based and Airborne Instrumentation for Astronomy II, Proc. SPIE*, Vol. 7014, pp. 701449, doi:10.1117/12.787403
- Piqueras, J.**, Rodríguez-Ramos, L.F., Martín, Y., and Martínez-Álvarez, J.J., 2008, FastCam: Real-Time Implementation of the Lucky Imaging Technique using FPGA, *Proc. 4th Southern Conference on Programmable Logic*, Vol. 1, pp. 155-160, doi:10.1109/SPL.2008.4547748
- Gago, F., Rodríguez-Ramos, L., Herrera, G., Gigante, J., Alonso, A., Viera, T., **Piqueras, J.**, and Díaz, J.J., 2007, Tip-Tilt Mirror Control Based on FPGA for an Adaptive Optics System, *Proc. 3rd Southern Conference on Programmable Logic*, Vol. 1, pp. 19-26, doi:10.1109/SPL.2007.371718

Conference contributions

- Piqueras, J.**, Heerlein, K., Werner, S., Enge, R., Sperling, M., Schühle, U., and Woch, J., 2012, Assessing effects of space radiation on the image sensor for SO/PHI, Poster, *Rocks'n'stars conference*, Göttingen (DE)
- Piqueras, J.**, Heerlein, K., Werner, S., Enge, R., Schühle, U., Woch, J., De Ridder, T., Wolfs, B., Lepage, G., and Diels, W., 2012, CMOS sensor and camera for the PHI instrument on board Solar Orbiter: evaluation of the radiation tolerance, Oral presentation, *SPIE Astronomical Instrumentation conference*, Amsterdam (NL)
- Blanco, J., Martínez, V., Feller, A., Hirzberger, J., and **Piqueras, J.**, 2012, Software simulator for SO/PHI: SOPHism, Poster, *5th Solar Orbiter workshop*, Brugge (B)
- Piqueras, J.**, Rodríguez-Ramos, L.F., Martín, Y., and Martínez-Álvarez, J.J., 2008, FastCam: Real-Time Implementation of the Lucky Imaging Technique using FPGA, Oral presentation, *4th Southern Conference on Programmable Logic*, Bariloche (Argentina)